

University of Southampton Research Repository ePrints Soton

Copyright © and Moral Rights for this thesis are retained by the author and/or other copyright owners. A copy can be downloaded for personal non-commercial research or study, without prior permission or charge. This thesis cannot be reproduced or quoted extensively from without first obtaining permission in writing from the copyright holder/s. The content must not be changed in any way or sold commercially in any format or medium without the formal permission of the copyright holders.

When referring to this work, full bibliographic details including the author, title, awarding institution and date of the thesis must be given e.g.

AUTHOR (year of submission) "Full thesis title", University of Southampton, name of the University School or Department, PhD Thesis, pagination

UNIVERSITY OF SOUTHAMPTON
Faculty of Engineering, Science and Mathematics
School of Engineering Sciences

LIGHT TRAPPING IN FLUORESCENT SOLAR COLLECTORS

by
Nazila Soleimani

Thesis for the Doctor of Philosophy
March 2012

UNIVERSITY OF SOUTHAMPTON
ABSTRACT
FACULTY OF ENGINEERING, SCIENCE AND MATHEMATICS
SCHOOL OF ENGINEERING SCIENCES
MATERIALS RESEARCH GROUP
Doctor of Philosophy
LIGHT TRAPPING IN FLUORESCENT SOLAR COLLECTORS
by Nazila Soleimani

A fluorescent solar collector (FSC) is an optoelectronic waveguide device that can concentrate both diffuse and direct sunlight onto a solar cell which is then converted to electricity. Fluorescent collectors offer the potential to reduce the cost of crystalline silicon (c-Si) solar cells, but so far their effectiveness has been demonstrated only theoretically.

The major problems in the device obtaining high practical efficiency are photon transport losses and material instability. This aim of this research is to increase the fundamental understanding of photon transport losses in fluorescent collectors, and to explore the method in overcoming the losses in fluorescent solar collectors.

This thesis presents the theoretical and experimental results obtained during the development and characterisation of fluorescent collectors, a thin film c-Si solar cell used to detect photons from the fluorescent solar collector.

A method for preparing fluorescent collector plates was by spin-coating dye-doped PMMA (Polymethylmethacrylate) on glass slides (BK7 glass). An optical characterisation technique for determining reabsorption loss of the fluorescent collectors was developed and used to evaluate the performance of the fluorescent collector base on laser dyes. The validity of this approach was verified by comparing the results with theoretical solutions, derived using a model adapted from the Weber and Lambe, and the modified Weber and Lambe, theories.

Different losses in the FSC are studied in this work and we investigate the effect of surface scattering in a realistic FSC. To characterise the photon transport inside the collector, we monitor the angular distribution of a collimated light beam, which enters the collector from the edge, after propagation and total internal reflection. We find that the surface scattering process is described well by Fraunhofer diffraction at surface inhomogeneities of a size, roughly 11 μm .

The major losses in FSC are found to be caused by the surface roughness, which increases the probability of the escape cone losses in FSC from the top surface. This loss can be suppressed to less than 2% using an index matching planarisation layer. The influence of the bulk and surface scattering on the performance of the FSC are presented in this work, which were compared with the experiment and theory.

The angular dependence of the edge fluorescence was studied in this work, and it showed the edge fluorescence decreases by increasing the detection angle, and the value of reabsorption also decreases by increasing the detection angle, up to 20° , before increasing again.

It was shown, also, that the quasi blackbody function agrees well with angular dependence of the edge fluorescence spectral, divided by the $\cos(\text{detection angle})$ region where the absorption and fluorescence band of the dye overlap. Also, the modified Weber and Lambe theory for the angular dependence of the fluorescence agreed well with the experimental results.

Contents

Academic Thesis: Declaration Of Authorship.....	16
Acknowledgements	18
List of Symbols	19
List of Abbreviations	22
Introduction.....	24
Aims and objectives	26
Thesis outline.....	28
Chapter 1	30
The role of solar radiation in the design of solar cells	30
Introduction.....	30
1.1.The solar spectrum.....	31
1.2. The solar constant	34
1.3. Solar intensity at the Earth's surface.....	34
1.4. Direct and diffuse radiation.....	35
1.5. Solid angle	35
1.6. Blackbody	36
1.7. Fluorescence	37
1.8. Effective temperature of fluorescence radiation (Kennard-Stepanov).....	39
Conclusion	40
Chapter 2	41
Principles of Solar Cell Operation.....	41
Introduction.....	41
2.1. The ideal solar cell	41
2.2. I-V characterisation of silicon solar cell	42
2.3. Solar cell characteristic in practice	45
2.4. Depletion layer of an abrupt p-n junction	45
2.5. Generation of electron-hole pairs.....	51
2.6. The quantum efficiency and spectral response	55
Conclusion	56
Chapter 3	57
Scattering theory	57

Introduction.....	57
3.1. Radiance and Irradiance for a laser beam	58
3.2. Scattering coefficient and the scattering efficiency	58
3.3. Mie scattering.....	60
3.4. Scattering in particles that are very large compared to the wavelength.....	65
3.5. Bi-directional surface distribution function	69
3.6. Radiation exchange within a spherical enclosure	70
Conclusion	71
Chapter 4	72
Fluorescent Solar Collectors	72
Introduction.....	72
4.1. Overview of a fluorescent solar collector	72
4.2. Weber and Lambe model for luminescent collector for solar radiation.....	73
4.2.1. Modified Weber and Lambe model for non-ideal coupling.....	75
4.3. Photon flow diagram.....	77
4.4. Solar absorption	78
4.5. Self absorption effect R, \bar{R}	78
4.6. Spectroscopic measurement of reabsorption losses	80
Conclusion	81
Chapter 5	82
Fabrication and Characterisation of Fluorescent Solar Collectors.....	82
Introduction.....	82
5.1. Spin coating processing stages.....	83
5.1.1. Stage one.....	83
5.1.2. Stage two.....	84
5.1.3. Stage three.....	85
5.2. Process trend charts.....	86
5.3. Fluorescent material.....	87
5.4. FSC (Fluorescent Solar Collector) preparation.....	89
5.4.1. Poly (methyl methacrylate) PMMA sample preparation	90
5.5. Con-focal laser sensor.....	90
5.5.1. XYRIS 4000 CL (or WL) system example.....	91

5.6. Scanning Electronic Microscopy (SEM)	93
5.7. Thickness measurement of transparent thin film by multiple interferencetechnique	95
5.7.1. Determination of film thickness.....	95
5.8. Taylor Hobson form Talysurf 120 stylus profiler	100
5.9. Characterisation techniques	102
5.9.1. Absorbance measurement	102
5.9.2. Fluorescence measurement	103
5.9.3. Front–face fluorescence detection	103
5.9.4. Edge fluorescence detection.....	104
5.9.5. Edge fluorescence detection in different angles.....	105
5.10. Photon collection efficiency and optical efficiency measurement.....	107
Conclusion	108
Chapter 6	109
Scattering measurement setup and integrating sphere measurement	109
Introduction.....	109
6.1. Transmittance measurement in double beam mode	109
6.2. Reflectance measurement in double beam mode	112
6.3. Total integrated scattering (TIS)	114
6.4. Scattering coefficient measurement with an integrating sphere.....	118
6.5. Roughness measurement using the angular dependence method.....	119
Conclusion	122
Chapter 7	123
The role of light scattering in the performance of Fluorescent Solar Collectors.....	123
Introduction.....	123
7.1. Theoretical Model and Photon Balance and scattering in the Collector	123
7.2. Photon collection efficiency with bulk scattering in the Batchelder model.....	126
7.3. Number of emitted photons.....	127
7.4. Photon flux in the edge of the fluorescent solar collector.....	129
7.5. Goniometer setup	130
7.5.1. Laser beam radius measurement	131
7.5.2. Photodiode calibration	132
7.5.3. Goniometer calibration	133

Conclusion	136
Chapter 8	137
Results and discussion	137
Introduction.....	137
8.1. Scattering measurement of FSC by photon emission from the edge	137
8.2. Modelling the intensity of scattered light by diffraction.....	143
8.3. Effect of the roughness on the performance of FSC	147
8.4. TracePro modelling.....	150
8.5. Scattering measurement in Perspex /Acrylic sample	153
8.6. Bi-directional surface distribution function from collector edges	155
8.7. Results and discussion from experiment.....	156
8.8. Scattering efficiency measurement	160
Conclusion	160
Chapter 9	162
Angular Dependence of edge fluorescence	162
Introduction.....	162
9.1. Fluorescence measurement	162
9.2. Edge fluorescence detection.....	163
9.3. Determination of the first-generation fluorescence spectra	164
9.4. The effective temperature measurement	168
9.5. Chemical potential of the angular dependence of edge fluorescence	169
9.6. Modified Weber and Lambe for the edge fluorescence detected at different angles from one edge of the collector	173
Conclusion	174
Chapter 10	176
Conclusion and suggested future works	176
Conclusion	176
10.1. Future work.....	178
References	180
Appendix 1.....	184

List of figures

Figure 1: A C-Si solar cell is coupled to one edge of the fluorescent collector.	25
Figure 2: Diagrammatic representation of the scattering, absorption and transmission of incident solar radiation on its passage down through the Earth's atmosphere.	31
Figure 3: Air masses of 0, 1, 1.5 and 2.	32
Figure 4: Spectra irradiance for Earth (AM0) and global and direct + circumsolar (AM1.5) [16].	33
Figure 5: Scatterometer layout and solid angle.	36
Figure 6: Electronic transition energy level diagram [18].	37
Figure 7: The equivalent circuit of an ideal solar cell (full line). Non-ideal components are shown by the dotted line. I_{01} is the current passed through the first diode, I_{02} is the current passed through the second diode, and I is the current passed through the series resistance (R_s).	42
Figure 8: (a) Current-voltage characteristics of a mono-silicon solar cell under dark and illumination. (b) Inversion of (a) about the voltage axis.	43
Figure 9: (a) Space-charge calculated from equation (18). (b) Electric field calculated from equation (20). (c) Voltage across a p-n junction calculated from equation (25). Curves for an abrupt p-n junction in silicon at 300 K, and the density of donor ($N_D = 10^{16}\text{cm}^{-3}$) and acceptor ($N_A = 10^{16}\text{cm}^{-3}$) (More detail in Appendix 1).	47
Figure 10: Debye length for silicon in doping density of more than 10^{16}cm^{-3} (calculated from equations (21) and (22)).	49
Figure 11: A p-n junction formed by bringing the isolated p-type and n-type regions together. Also shown is the corresponding energy-band diagram at thermal equilibrium which is an amended version of figure 9c to indicate the relevant quantities [27].	50
Figure 12: Generation rate of electron-hole pairs, calculated from equation (37) as a function of distance into the cell when illuminated by sunlight.	52
Figure 13: Scattering of light in a particle as a sphere.	59
Figure 14: Diffraction by a large body with geometrical shadow area A.	67
Figure 15: BRDF and BTDF geometry in a glass substrate.	69
Figure 16: Radiation exchange within an enclosure of diffuse surfaces.	70

Figure 17: Schematic of a luminescent solar collector. The solar radiation is normally incident upon the collector surface, which is in the xy plane. A perfect reflecting mirror is placed in $y=0$ and the photocell is at $y=L$	73
Figure 18: Collector structure and escape cones. θ_c is the critical angle for total internal reflection.	75
Figure 19: Comparison of reabsorption probabilities calculated from Weber and Lambe's theory and the Modified Weber and Lambe's theory.	76
Figure 20: Photon flow diagram for a single dye FSC. Light from the sun is partially reflected, partially absorbed by the dye ensemble, and partially transmitted through the FSC plate. Emission is geometrically divided between the critical escape cone, and light trapped by total internal reflection. Light can be recycled into the dye ensemble by self absorption. Collected light is called collection efficiency, or Q_c , and can be converted into electricity by a photovoltaic cell (PVC)[50].	77
Figure 21: Stage one: dynamic dispense solution is spread on the substrate.	83
Figure 22: Stage two: the spin coater accelerates to its final speed and the solution is spun-off of the substrate.	85
Figure 23: Stage three: excess solvent evaporates.	86
Figure 24: Effect of different parameters on the spin coating process [54].	87
Figure 25: Absorbance and fluorescence of RB in ethanol from PhotochemCAD [55].	87
Figure 26: The chemical structure of RB and its important absorbance and fluorescence properties, from PhotochemCAD [55].	88
Figure 27: Absorbance and fluorescence of F Red305 in Dichloromethane (DCM) solution [58].	88
Figure 28 :The chemical structure of F Red305 and its important absorbance and fluorescence properties, from BASF Colorants for Plastics [58].	89
Figure 29: Schematic of the confocal operation principal. A collimator lens is oscillated over the sensors gauge range with the highest received intensity reflection corresponding to the surface height.	91
Figure 30: XYRIS 4000 CL-25 mm XYZ motion system- the CL sensor has an integrated microscope video camera, to assist in targeting the system.	92
Figure 31: Thickness measurement of RB, spin coated on top of glass, using the XYRIS 4000CL (area $3\text{mm} \times 3\text{mm}$). The sample thickness is approximately $25.9\mu\text{m}$	92
Figure 32: JSM 5910 scanning electron microscope.	93
Figure 33: SEM of RB spin coated on top of glass from the edges.	94

Figure 34: DFT of single layer film in Matlab, and the peak corresponding optical thickness, D , of the film, the duration of the signal equal to 1000 in this example.	97
Figure 35: Thickness measurement for PMMA dissolved in Toluene (0.5gr:5ml) and spin coated on top of silicon.	99
Figure 36: Thickness measurement for PMMA dissolved in DCM (0.5gr:5ml) and spin coated on top of silicon.	99
Figure 37: RB in DCM ($C=2.61 \times 10^{-3}$ mol/L), spin coated on top of silicon with different rotational speeds and measured using Avantes, SEM and Confocal laser, the error bars presenting an uncertainty of 14.26%.	100
Figure 38: Contact profilometers for measuring the thin film thickness	101
Figure 39: The optical arrangement for absorbance measurement.	102
Figure 40: Setup for front Fluorescent Detection.	104
Figure 41: Setup for Edge Fluorescent Detection.	104
Figure 42: Setup for Edge Fluorescent Detection (a) the sample was illuminated from the top and detected from the edge at 0° to 45° (b) sample rotated 90° , illuminated from the top, and detected from the edge at 0° to 45° . 0° was chosen to be in the middle of the sample.	106
Figure 43: Integrating spheres in double beam mode for transmittance measurements.	110
Figure 44: Comparison between the total transmittance (TT) and diffuse transmittance (DT) of PMMA spin coated on top of the BK7 glass at different wavelengths.	111
Figure 45: Comparison between the diffuse transmittance (DT) of PMMA spin coated on top of the BK7 glass and BK7 glass at different wavelengths.	111
Figure 46: Comparison between the total reflectance measurement (RT) and diffuse reflectance (RD) of PMMA spin coated on top of the BK7 glass and BK7 glass at different wavelengths.	114
Figure 47: Comparison between diffuse reflection (RD), total reflection (RT) with TIS of reflection of PMMA spin coated on top of the BK7 glass and BK7 glass at different wavelengths.	115
Figure 48: Comparison between diffuse transmittance (TD), total transmittance (TT) with TIS of transmittance of PMMA spin coated on top of the BK7 glass and BK7 glass at different wavelengths. .	116
Figure 49: Comparison between rms of forward and back scattering of PMMA spin coated on top of the BK7 glass and BK7 glass at different wavelengths.	117
Figure 50: AFM imaging from the top surface.	117

Figure 51: Scattering coefficient measurement from the surface and bulk, with the integrating sphere of dye (F305) mixed with PMMA and PMMA spin coated on top of the BK7 glass.	118
Figure 52: Angular dependence of reflection of I/I_0 for different incident angles in 670 nm.	120
Figure 53: BRDF measurement for incident angle of 10° , 20° , 30° and 40° . The wavelength of incidence was 670 nm.	120
Figure 54: BRDF in different positions of the surface (a) roughness was calculated to be $0.030 \mu\text{m}$; (b) roughness was calculated to be $0.0109 \mu\text{m}$; (c) roughness was calculated to be $0.014 \mu\text{m}$	122
Figure 55: Schematic diagram of a fluorescent collector, showing the double escape cone with apex angle, θ_c . In the simplified theory used in this paper, rays (A) form the photon flux N_{loss}^o , which escapes from the front face of the collector, and rays (B) contribute to the flux N_{work}^o which illuminates the solar cell.	124
Figure 56: Two energy levels in equilibrium. A is the ground state level and B is the excited state level.	127
Figure 57: Schematic of the experimental setup for the measurements of scattering.	130
Figure 58: Irradiance intensity of the laser beam in different positions fitted with a Gaussian beam.	131
Figure 59: Spectral responsivity of DH-Si photodiode compared to calibration data, SM05PD1A mounted Si-photodiode, and a silicon photocell power meter sensor.	133
Figure 60: Particle size measurement of 2wt% aqueous suspension PMMA, with an average diameter of $2 \mu\text{m}$, and compared with Mie scattering theory for spheres of different diameter. The error of this measurement was fixed at 0.6, with circles indicating the experimental results.	134
Figure 61: Particle size measurement of PMMA, with a diameter of $6 \mu\text{m}$, and compared with Mie scattering theory for spheres of different diameter. The error of this measurement was fixed at 0.6, and the circles indicate the experimental results.	135
Figure 62: Image of sphere on top of the substrate, with an optical microscope (diameter 6-7 μm).	135
Figure 63: PMMA spin coated glass, illuminated with laser light from one edge, and the scattered light detected from another edge at different angles, $\theta_1=15^\circ$ and $N=14.21\text{mm}$, $M=11.79 \text{ mm}$. The error in this experiment was 0.6, which was the width of the laser beam.	138
Figure 64: A comparison of I/I_0 at a wavelength of 670 nm, detected over a range of angles, with illumination from three different incident angles. The incident position labelled 'right' indicates that the light illuminated the edge to the PMMA side of the glass, while the incident position labelled 'left' indicates that the edge was illuminated from the opposite side. The incident laser beam is labelled 'Gaussian'.	141
Figure 65: The angular dependence of I/I_0 for different incident angles for a 670 nm incident light, (a) incident through the glass part, and (b) incident through the PMMA part.	142

Figure 66: Intensity of scattered light at an incident angle of 0° and 35°	143
Figure 67: PMMA spin coated on top of the glass, illuminated with laser light from one edge at an incident angle of 15° , the scattered light detected from another edge at different angles. The roughness from spin coated PMMA was assumed to have the circular shadow when the laser hit it.	143
Figure 68: Normalised angular dependence of irradiance of scattering at 15° incident angles in PMMA side for 670 nm. The solid line was fitted by using equation 171, circles indicating the experimental results.	144
Figure 69: Comparison of irradiance of scattering (a) and normalised irradiance (b) of scattered light in wavelengths of 670,633,532,401 nm, detected over a range of angles with illumination from 15° incident angles. The incident position labelled 'right' indicates that the light illuminated the edge to the PMMA side.	146
Figure 70: Comparison of the intensity of scattered light at a wavelength of 670 nm, detected over a range of angles with illumination from 15° incident angles, once when the PMMA top surface is covered with the optical gel (circles, blue), and once without optical gel (diamonds, green). The incident laser beam is labelled 'Gaussian'.....	147
Figure 71: Collection efficiency (left) for the FSC as a function of $\alpha_e L$, calculated using the modified Weber and Lamb model equation (172), for a perfectly smooth surface ($\Delta\theta=0$, closed dots), and a surface roughness characterised by $\Delta\theta=1.5^\circ$ (open dots). The absolute scattering loss (triangles, blue). and the relative scattering loss (diamonds, red) are normalised to the result for $\Delta\theta=0$. The absolute (triangles, blue) and relative scattering loss (diamonds, red) at $\alpha_e L = 10^{-2}$ as a function of the 1/e half-width of the diffraction cone are shown on the right.	149
Figure 72: Gaussian laser beam in a wavelength of 0.670 μm , illuminated at (a) 45° through the PMMA part of the sample; (b) incident at 45° through the glass part of the sample, or incident at 35° through the glass or PMMA part of the sample; (c) incident at 15° through the PMMA part of the sample; and (d) incident at 15° through the glass part of the sample, or 0° through the glass. The graphs are plotted on a log scale.	153
Figure 73: Angular dependence of I/I_0 for a perspex/acrylic fluorescent sample, with unknown dye concentration at different incident angles for a 670 nm incident light. The experimental data was fitted with a Gaussian (solid line) beam.	154
Figure 74: Scattering phase function for the perspex/ acrylic fluorescent sample, measured with the laser at a wavelength of 670 nm, and compared with Mie scattering theory for different sphere sizes. The error of this measurement was fixed at 0.6, which is the width of the laser beam, while circles indicate the experimental results.	155
Figure 75: BTDF measurement in polished and ground edges of BK7 glass.	156
Figure 76: Typical edge fluorescence spectra of Rhodamine B collectors.	157

Figure 77: Edge fluorescence spectra, normalised to coincide with the first generation fluorescence spectrum in the low-absorption, long-wavelength region. The area between the first fluorescence and edge fluorescence is equal to the probability of reabsorption, R .	158
Figure 78: Reabsorption probability for thin film collectors for different absorption of RB in the film compared to the W&L model.	159
Figure 79: Short circuit current detected with a solar cell for different edge fluorescence.	159
Figure 80: Typical flux of edge fluorescence spectra of F305 ($C=6.5 \times 10^{-4}$ mol/L) in an excitation wavelength of 550 nm, with the sample illuminated from the top and detected from one edge at different angles.	163
Figure 81: Typical flux of edge fluorescence spectra of F305 ($C=6.5 \times 10^{-4}$ mol/L) in an excitation wavelength of 550 nm, the sample rotated to 90° , illuminated from the top, and detected from one edge at different angles.	164
Figure 82: Absorbance of spin coated F305 on top of the glass substrate, for 6 different concentrations.	165
Figure 83: Top fluorescence spectra for various concentrations of spin coated F305, on top of the glass substrate.	165
Figure 84: Fluorescence spectra detected from the front surface of fluorescence collectors at various concentrations of spin coated F305 on top of the glass substrate. The spectra were normalised to unity at their peak.	166
Figure 85: The spectra of spin coated F305 on top of the glass substrate with concentration of $C=5 \times 10^{-6}$, fitted with the Gaussian.	167
Figure 86: Edge fluorescence spectra of spin coated F305, mixed with PMMA on top of the glass substrate with concentration of $C=5 \times 10^{-6}$, normalised to coincide with the first generation fluorescence spectrum in the low-absorption, long-wavelength region. The area between the first generation fluorescence and edge fluorescence is equal to the probability of reabsorption, R .	168
Figure 87: Kennard-Stepanov relation applied to the spectra of spin coated F305, mixed with PMMA on top of the glass substrate, with a concentration of $C=5 \times 10^{-6}$ mol/L.	169
Figure 88: Spectral responsivity of the edge of a silicon solar cell.	170
Figure 89: Edge fluorescence of F305, with concentration of $C=5 \times 10^{-6}$ mol/L, spin coated on top of the glass substrate and detected at different angle, compared with the Blackbody curve. In the spectral region where reabsorption affects photon transport, the edge fluorescence spectrum resembles a quasi-blackbody function.	171
Figure 90: Edge fluorescence of F305, with concentration of $C=5 \times 10^{-6}$ mol/L, spin coated on top of the glass substrate and detected at different angles, divided by $\cos(\text{angle of detection})$, compared with the	

Blackbody curve. In the spectral region where reabsorption affects photon transport, the edge fluorescence spectrum resembles a quasi-blackbody function. (b)Log plot of (a). 172

Figure 91: Reabsorption probability for thin film collectors at different detection angles of ROT305, with a concentration of $C=5\times 10^{-6}$ mol/L, compared to the modified W&L model. 174

Figure 92: AFM-scan of opal surface with hexagonally packed PMMA-spheres [72]. 179

List of tables

Table 1: Standard reflectance in different wavelengths(R_{std})[32].	112
Table 2: Distance from the incident beam inside the glass for different incident angles. The error in this calculation is 0.6, which is the width of the laser beam.	139
Table 3 : Beam width for different angles of incidence.	143

Academic Thesis: Declaration Of Authorship

I, Nazila Soleimani, declare that the thesis entitled

LIGHT TRAPPING IN FLUORESCENT SOLAR COLLECTORS

declare that this thesis and the work presented in it are my own and has been generated by me as the result of my own original research.

I confirm that:

1. This work was done wholly or mainly while in candidature for a research degree at this University;
2. Where any part of this thesis has previously been submitted for a degree or any other qualification at this University or any other institution, this has been clearly stated;
3. Where I have consulted the published work of others, this is always clearly attributed;
4. Where I have quoted from the work of others, the source is always given. With the exception of such quotations, this thesis is entirely my own work;
5. I have acknowledged all main sources of help;
6. Where the thesis is based on work done by myself jointly with others, I have made clear exactly what was done by others and what I have contributed myself;
7. Either none of this work has been published before submission, or parts of this work have been published as: [please list references below]:

Signed:

.....
.....

Date:

.....
.....

Book

Danos L, Kittidachan.P, Parel T.S, Fang L, Soleimani N., Meyer T.J.J, Markvart T.

Photon frequency management materials for efficient solar energy collection

Solar Energy Laboratory, Engineering Materials, School of Engineering Sciences, University of Southampton, SO17 1BJ, UK. (under review).

Journal Articles

1. Knabe.S, Soleimani.N, Markvart.T, Bauer G.H, Efficient light trapping in fluorescence solar collector by 3D photonic crystal, *Physica Status Solidi (RRL) - Rapid Research Letters* 4 (2010) 118-120.
2. Markvart.T, Danos.L, Fang.L, Parel.T and Soleimani.N, Photon frequency management for trapping & concentration of sunlight, *RSC Advances*(2011) 10.1039/c2ra01160c.
3. Soleimani.N, Knabe.S, Bauer.G.H, Markvart.T, Muskens.O.L, The role of light scattering in the performance of fluorescent solar collectors (*Journal of photonic for energy* -accepted).

Conference Articles

- 1.Soleimani.N, Kittidachan.P.,Meyer.T, Danos.L and Markvart.T. The rule of fluorescent collector edge on fluorescent solar collector performance. *Proceedings of 4th Photovoltaic Science Application and Technology, PVSAT4_0.17* Bath,UK.
2. Soleimani.N and Markvart.T, The effect of collector edge on photon collection efficiency of fluorescence solar collector.*PVSAT5* UK.
3. Soleimani.N, Danos.D, Meyer.T.,Markvart.T. Photon collection efficiency of fluorescent solar collectors.2008,14 PG conference(Southampton University).
4. Soleimani.N, .Markvart.T. Modelling the Scattering inside of fluorescent solar collector with Ray tracing techniques 2009, 15 PG conference (Southampton University).
5. Soleimani.N, Knabe.S, Markvart.T, Bauer.GH , Modelling the scattering inside a fluorescence solar collector by ray tracing. *PVSAT6*, Southampton UK.

Acknowledgements

It is my pleasure to acknowledge Dr Otto Muskens for kindly helping me with Scattering Theory and measurement, and for supporting me during my PhD; Professor T. Markvart for the many helpful discussions about all aspects of this report, and funding support; Dr S. Boden for helping me with the integrating sphere, scattering measurement and proofreading; A. Ghiass for helping me with the Lab View programming; my colleagues and co-workers; Dr T.J.J. Meyer for his help with collector designs with TracePro; Dr L. Danos for technical support in the laboratory; and Dr R. Greef for his help with measurement of the reflectivity of silver mirrors;

Dr S. Knabe for helping me with measurement of the angular dependence of scattering; Professor J. McBride and Dr I. Fitri for helping me with the film thickness measurements.

The help and support of all material group members, and the school of Engineering and Science, especially Professor P.A. Reed and A. Plutino, should be acknowledged, as should Professor D. Bagnall for letting me use the integrating sphere in the ECS optical laboratory.

I would also like to thank the industry for cooperating with us, and Andrew Knight and Sandra White (TracePro) for the free programme license.

I would like to thank Dave, Rob, Eric, Chris, Erik, Brian and Gwyneth for always providing me with excellent technical and administrative support, and my friends, Dr L. Armstrong and Dr A. Camerlingo, as well as my family for supporting me through my difficult times.

List of Symbols

Symbol	Description	Unit
A	area	cm^2
h	Planck constant	$\text{m}^2 \text{kg} / \text{s}$
c	speed of light	m/sec
Ω	solid angle	sr
Σ	Stefan-Boltzmann constant	$\text{Wm}^{-2}\text{K}^{-4}$
ν	frequency	Hz
E	energy	eV
ϵ	permittivity	F/m
E_{fn}	electron quasi-Fermi energy level	eV
E_{fp}	hole quasi-Fermi energy level	eV
E	electric field	V/cm
G	electron and hole generation rate per unit volume	photons/ $\text{cm}^3 \cdot \text{s}$
I_{sc}	short circuit current	A
J_{sc}	short circuit current density	A/cm^2
J_n	electron current density	A/cm^2
J_p	hole current density	A/cm^2
K	Boltzmann's constant	J/K
n	density of electrons per unit volume	cm^{-3}
N_D	donor density	cm^{-3}
N_A	acceptor density	cm^{-3}
ρ_a	density of holes per unit volume	cm^{-3}
q	electronic charge	C

V	voltage	V
V _{oc}	open circuit voltage	V
μ_n	electron mobility	cm ² /(V·s)
μ_p	hole mobility	cm ² /(V·s)
λ	wavelength of light	μm or nm
α	absorption coefficient	cm ⁻¹
ϕ_f	fluorescence quantum yield	%
η	efficiency	%
Q_A	absorption efficiency	%
Q_C	collection efficiency	%
Φ	photon flux	
θ_c	critical angle	°
FF	fill factor	
n	refractive index or density of electrons per unit volume	
ϕ_0	potential charge	
ϕ	polar angle	
G	geometric gain	
P	fraction of photons emitted through the critical angle or power	
$r(\alpha)$	re-absorption probability at wavelength	
R	reflectance or re-absorption probability	
T	transmittance and temperature	
T _D	diffuse transmittance	
R _D	diffuse reflectance	
η_{ext}	extinction scattering efficiency	
η_{bk}	back scattering efficiency	

η_{sca}	scattering efficiency	
C_{sca}	scattering cross section	
ρ_a	particles per unit of the volume	number of particles/m ³
P_i	power of incident	W
μ_s	scattering coefficient	mm ⁻¹
μ_a	absorption coefficient	mm ⁻¹
I_s	scattering irradiance	W/m ²
I_0	incident irradiance	W/m ²
T^*	effective temperature	K
I_p	photo current	A
τ_{rad}	radiative lifetime of dye	ns
τ_{pe}	photon emissions lifetime	ns
N^*	number of molecules in the excited state	
μ_{flux}	chemical potential of the flux	eV
$SR_{pv}(\lambda)$	spectral response	A/W ⁻¹
$\rho(\theta)$	phase function scattering	
$f_l(\nu)$	emissive power	W/Hz
δ	roughness	nm

List of Abbreviations

AM	Air Mass
c-Si	Crystalline Silicon
EQE	External Quantum Efficiency
FC	Fluorescent Collector
FSC	Fluorescent Solar Collector
IQE	Internal Quantum Efficiency
OD	Optical Density
PMMA	Poly-methylmethacrylate
PV	Photovoltaic
BSDF	Bi-directional Surface Distribution Function
BRDF	Bidirectional Reflectance Distribution Function
BTDF	Bidirectional Transmittance Distribution Function
SDF	Scattering Distribution Function
$f_e(\lambda)$	Scaled edge fluorescence spectrum
$f_1(\lambda)$	First generation front fluorescence or emission power
F305	Lumogen Frot 305
RB	Rhodamine B
I-V	Voltage Current characteristic
K-S	Kennard-Stepanov
NPL	National Physics Laboratory
W&L	Weber and Lambe
MW&L	Modified Weber and Lambe
R6G	Rhodamine 6G

RB Rhodamine B

F305 Lumogen dye from BASF [Frot 305]

Introduction

Solar cells convert sunlight directly into electricity. They are made of semiconducting materials such as silicon, the same material used in computer chips, and are often used to power calculators and watches. The solar energy excites an electron from the valence band to the conduction band, allowing the electrons to flow through the material to produce electricity. This process of converting light (photons) to electricity (voltage) is called photovoltaics (for a detailed description, see chapter 2).

Photovoltaic conversion of solar energy is one of the most promising ways of meeting the increasing energy demands of the future, in a time when conventional sources of energy are being depleted. In terms of human lifespan, the remaining lifetime of the Sun, at approximately 5 billion years, until the fusion of hydrogen stops, is effectively infinite. Furthermore, it appears that major advances in the understanding and fabrication of semiconductor devices over the past 30 years have paved the way for photovoltaics to make a significant contribution to the energy of the future [1].

Photovoltaics dates back to 1839 [2], when French physicist Antoine-Cesar, together with his son Alexandre Edmond Becquerel, observed that shining light on an electrode submerged in a conductive solution would create an electric current. Albert Einstein's interpretation of the photoelectric effect was one of the most crucial landmarks in the development of modern physics. It was in one of his three papers, published in 1905- a remarkable year for physics, that Albert Einstein introduced the idea of the photon to explain the photoelectric effect experiment. It was for this work that he was awarded a Nobel Prize in 1921. In the photoelectric effect, light shines on a metal plate, causing electrons to be knocked loose (ejected) from the plate. The kinetic energy of the fastest electrons ejected by the light can be measured as voltage.

The first solid state material (selenium) exhibiting the photo electric effect was discovered in 1873 by Willoughby Smith. William Shockley's theory of the p-n junction, in 1949, and the realisation of the junction transistor, in 1951, produced immediate visions of a fantastic future for solid-state electronic devices. In 1950, the American, Russell Ohl, invented a silicon solar cell. Improved solar cells became a reliable source of electricity for satellites, however, their price horrified electric utilities so they were only used when cheaper alternatives were unavailable

At the present time, solar cells are expensive when compared to fossil fuel energy. One solution would be photovoltaic modules integrated into the fabric of buildings, reducing the marginal cost of photovoltaic energy to a minimum. The aim of this work is to reduce the cost of crystalline silicon solar cells by using fluorescent collectors (figure 1).

In a fluorescent concentrator, dyes absorb radiation and emit light with a longer wavelength. Most of the emitted light is 'totally internally reflected' and therefore trapped and guided to the sides of the collector where it can be utilised by solar cells. Research these days is aimed at cost saving, by replacing expensive solar cells with cheaper fluorescent material.

The FSC has been researched over three decades, but the expected high efficiency of the device has not yet been realised due to different losses. In recent years, the performance of dye materials has been improved [1, 2], and the research in this field has stimulated, and gained increasing attention from, various research groups [3-11].

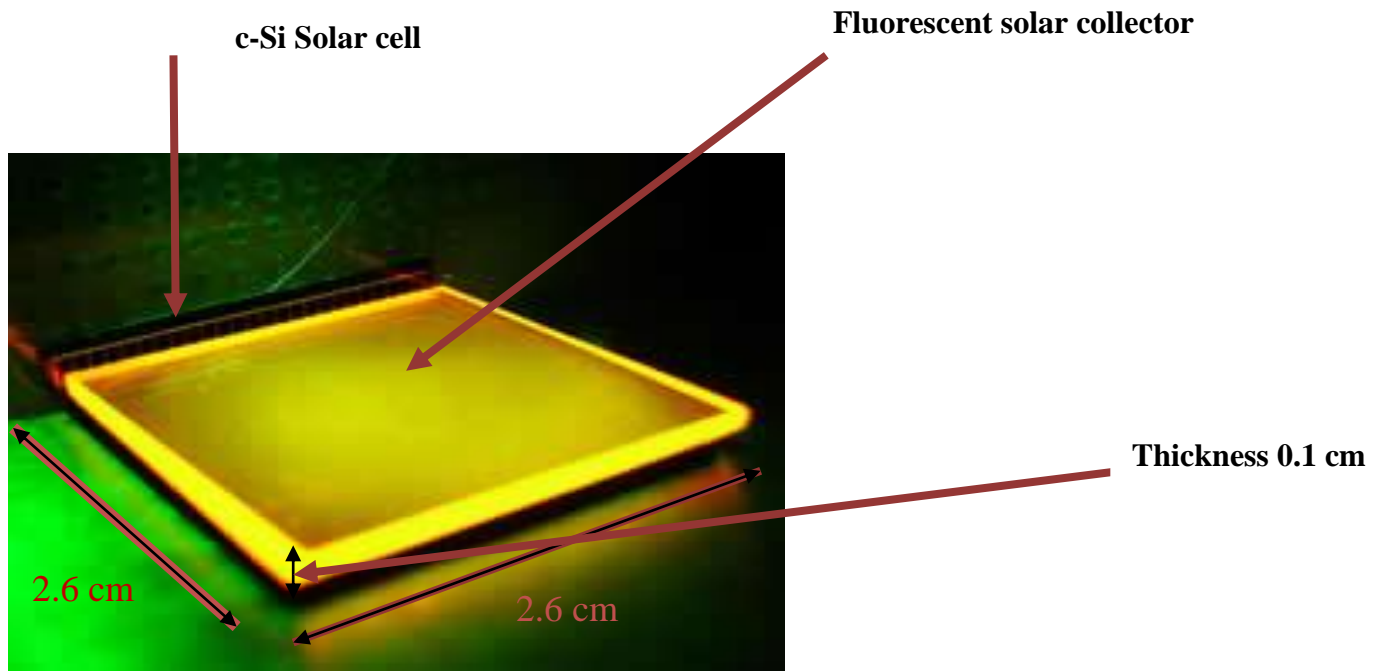


Figure 1: A C-Si solar cell is coupled to one edge of the fluorescent collector.

Aims and objectives

The aim of this report is to make an in-depth study of fluorescent collectors, focusing on a detailed description of losses that limit their operation. To accomplish this aim, the research has pursued the following objectives:

- Fabrication of fluorescent collectors by spin coating of dye-doped PMMA on glass, using different techniques for thickness measurement.
- Characterisation of fabricated fluorescent collectors by using a spectrometer.
- New theory in FSC when we have the bulk and surface scattering.
- Equipment setup for measuring the angular dependence of scattering in fluorescent solar collector.
- Roughness measurement in FSC by using different techniques (AFM, integrating spheres, angular dependence).
- Measuring and modelling the scattering of light in the collector by ray tracing.
- Reabsorption study of angular dependence of edge fluorescence, the chemical potential of the edge fluorescence flux incident on the solar cell.

A particular focus of the study was to determine the scattering contributions in FSC by using the angle dependence of light, internally reflected in the FSC. The cause of the scattering in spin coated dye, on top of the glass collector, is identified to be roughness from the top surface, rather than bulk losses. This loss can be suppressed using an index-matching planarization layer.

Reflection and transmittance measurements are in double beam mode, with an integrating sphere, as well as roughness measurement of the fluorescence solar collector with AFM, total integrated scattering, angular dependence measurement and a comparison of the results with each other.

The effect of the angular dependence of the edge fluorescence on reabsorption probability, and the chemical potential of the edge fluorescence flux incident on the solar cell, were studied in this work, and it was shown that the value of reabsorption was decreased by increasing the detection angle, up to 20°, before increasing again at larger angles. Further, the quasi-blackbody function agreed well with the angular dependence of the edge fluorescence spectral, divided by the $\cos(\text{detection angle})$ region, where the absorption and fluorescence band of the dye overlap.

Also, the modified Weber and Lambe theory for the angular dependence of the fluorescence agreed well with the experimental results.

Thesis outline

This thesis is based on two main research streams. The first stream, constituting chapters 1 and 2, is the role of the solar radiation in the design of solar cells, and the principles of solar cell operation. The second stream, in chapter 3 through 10, presents studies and experiments focused on scattering and fluorescent solar collectors.

The detailed structure of this thesis is as follows:

Chapter 1: An introduction to the fundamental principles of solar radiation, and the solar spectrum.

Chapter 2: P-N junction solar cells- describes the operation of P-N junction solar cells, presenting an overview of the properties of the semiconductors that are important in the design and operation of solar cells.

Chapter 3: Mie scattering theorem, and Fraunhofer diffraction in far-field, Bi-directional surface distribution function (BSDF) and the theory of the integrating sphere, based on radiation exchange within an enclosure of diffuse surfaces.

Chapter 4: Fluorescent solar collectors, the literature review on the subject of FSCs, including the history, operation principles, and self absorption.

Chapter 5: Experimental procedures- describes the methodology for fabrication of fluorescent solar collectors and the different methods for measuring film thickness, with different thickness limits, and the details of the characterisation techniques.

Chapter 6: Reflection and transmittance measurements in double beam mode with an integrating sphere, as well as a roughness measurement of the fluorescence solar collector with AFM, total integrated scattering, angular dependence measurement, and a comparison of the results with each other.

Chapter 7: New theory, based on the effect of the bulk scattering in the performance of the FSC. Introduces the experimental setups for measuring the scattering inside the fluorescence solar collector, as well as the setup of the angular dependence of scattering.

Chapter 8: New theory, based on the effect of the surface scattering in the performance of the FSC. Investigates the influence of the surface and bulk scattering, and the edge roughness on the performance of the FSC, comparing the theoretical results with experimental results, and ray tracing simulations (TracePro programme).

Chapter 9: Effect of the angular dependence of the edge fluorescence on the probability of reabsorption, and the chemical potential of the edge fluorescence flux incident on the solar cell.

The Modified Weber and Lambe model for angular dependence of the edge fluorescence was introduced, and used to calculate the reabsorption probability of the fluorescence solar collector.

Chapter 10: Conclusion of the thesis and suggested future work for increasing the optical efficiency of FSC.

Chapter 1

The role of solar radiation in the design of solar cells

Introduction

This chapter gives an introduction to the fundamental principles of solar radiation, black body radiation, fluorescence spectroscopy and the effective temperature of fluorescence radiation, or the Kennard-Stepanov law.

Energy is emitted from the Sun in the form of electromagnetic radiation, which drives the Earth's climate and environmental systems [12]. Thus, the Earth's atmosphere, oceans and land surface are heated by absorption of a fraction of the short wave solar radiation that is incident upon them. This radiation is subsequently emitted at longer wavelengths causing the atmosphere to be heated further, depending on the balance between the rates at which it absorbs and emits long wave radiation [13]. The resulting spatial difference in atmospheric heating generates momentum in the air mass, which, among other things, produces winds on the Earth surface [14]. Incident solar radiation, in conjunction with air temperature, also plays a key role in the growth and development of vegetation through the process of photosynthesis [15]. The amount of solar radiation incident on the Earth's surface varies with spatial location and the time of day and year. The spatial variation is a function of the difference in latitude and various properties of the local terrain, such as its altitude, gradient and aspect, while the temporal variation is governed by the angle of the Sun above the horizon, the turbidity of the atmosphere and the degree of cloud cover.

The solar irradiance (namely the global, or total) values are given in Watt per square metre (W/m^2) and is made up of 'diffuse' and 'direct' irradiance. Direct irradiance is that which arrives at the Earth's surface from the direction of the Sun, and is dominated by the direct solar beam [15]. Diffuse irradiance is that which arrives from all other directions in the hemisphere above the surface, having been scattered out of the direct solar beam by clouds, gases and particulate matter within the atmosphere, or having been reflected from surrounding areas of terrain [15].

Global (or total) irradiance is the sum of the direct and diffuse components (figure 2). An inclined surface, at an angle to the horizontal plane, may also receive radiation reflected from the ground.

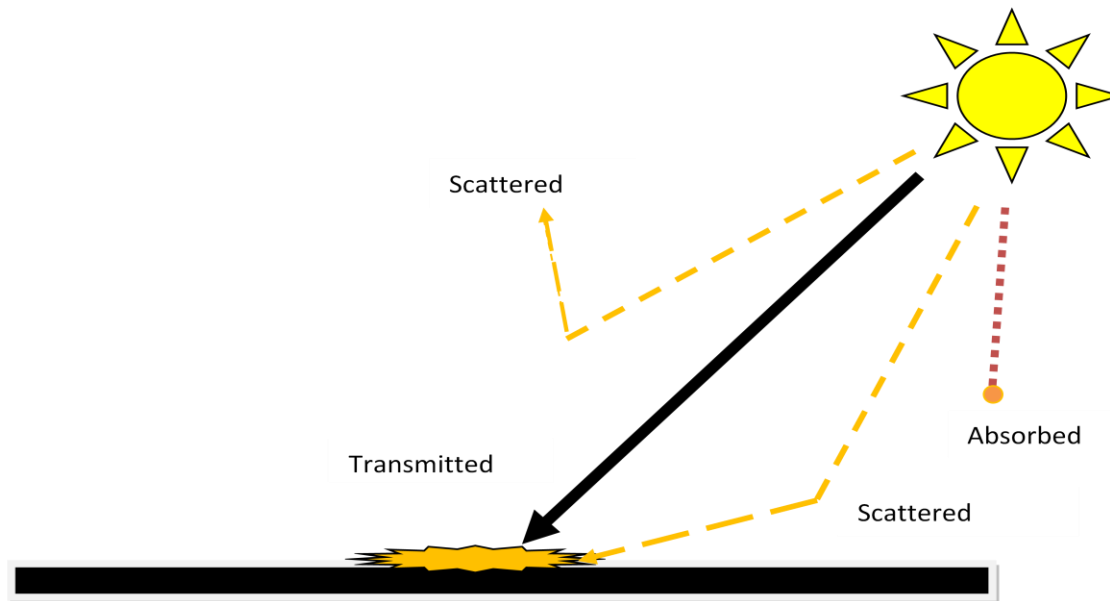


Figure 2: Diagrammatic representation of the scattering, absorption and transmission of incident solar radiation on its passage down through the Earth's atmosphere.

1.1. The solar spectrum

Absorption and scattering levels change as the constituents of the atmosphere change. Clouds are the most familiar cause of change, as they are able to block most of the direct radiation. Seasonal variations and trends in the thickness of the ozone layer have an important effect on terrestrial ultraviolet levels. Meanwhile, the ground level spectrum also depends on how far the Sun's radiation must pass through the atmosphere. With the Sun overhead, direct radiation reaching the ground passes straight through the entire atmosphere- we call this radiation "Air Mass 1 Direct" (AM 1D) radiation, and for standardisation purposes, we use a sea level reference site. Likewise, the global radiation with the Sun overhead is called "Air Mass 1 Global" (AM 1G) radiation. As it passes through no air mass, the extraterrestrial spectrum is called the "Air Mass 0" spectrum. The atmospheric path for any zenith angle is simply described relative to the overhead air mass

in figure 3. The actual path length can correspond to air masses of less than 1 (high altitude sites) to very high air mass values, just before sunset.

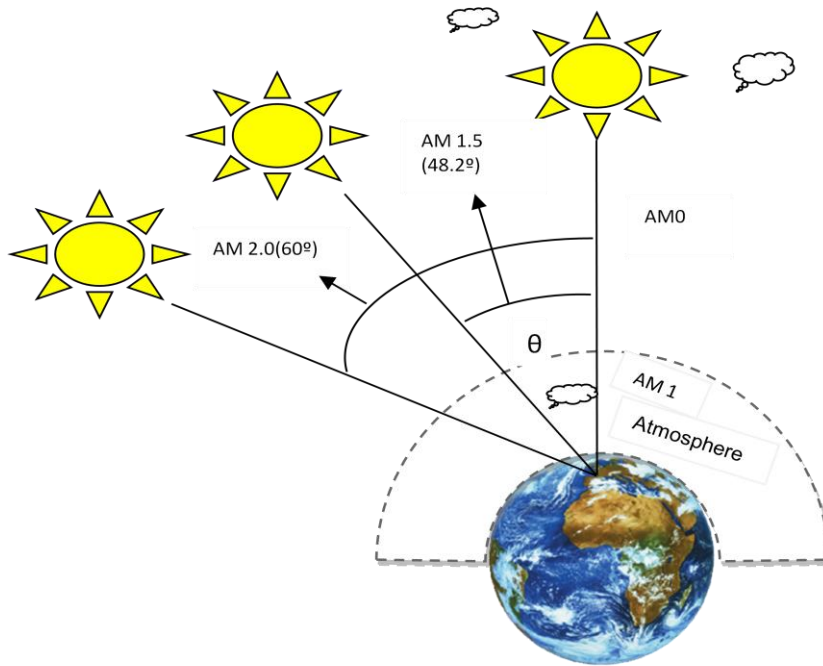


Figure 3: Air masses of 0, 1, 1.5 and 2.

The path length in units of air mass, changes with the zenith angle. Air Mass (AM) is defined as the amount of atmosphere through which the solar radiation has travelled and is related to the amount of absorption.

$$AM \approx \frac{1}{\cos \theta}, \quad (1)$$

where θ is the angle of the Sun to the vertical with the Sun directly overhead the illuminating spectra at the Earth's surface, and would be AM1. Outside the atmosphere, the spectra is AM0, while AM1.5 reference (sometimes called "standard") spectra are used to report PV cell performance measurements.

The reference spectra, accepted as spectral irradiance standards by the American Society for Testing and Materials, are the 'global' and 'direct normal' AM1.5 spectra. This means that the irradiance on the PV device includes direct solar radiation from the Sun's disk, plus sky and ground-reflected radiation (diffuse), incident on a flat plate device (cell, collector, etc). The

global and direct normal AM1.5 spectra have different spectral distributions, as shown in figure 4, and for easy comparison between photovoltaic cells, the efficiencies are reported under standard reporting conditions of AM1.5 Global at 1000 W/m^2 . When the Sun is directly overhead (at zenith), the path length is 1.0 (AM1.0). AM 1.0 is not synonymous with solar noon as, in most seasons and locations, the Sun is usually not directly overhead at that time. When the angle of the Sun from the zenith (i.e. the zenith angle) increases, the air mass increases also, so that at about 48.2° from the vertical, the air mass is 1.5, and at 60° , the air mass is 2.0. With longer path lengths, there is more scattering and absorption of solar radiation by atmospheric constituents, such as air molecules, aerosols (fine solid particles or liquid droplets in a gas), and water vapour. The combined effect is an attenuation of the incident solar radiation as it passes down through the atmosphere, the degree of which depends on the composition of the atmosphere, measured in terms of its gaseous constituents and aerosol content, as well as the path length that the solar radiation has to travel through to the ground. On the other hand, the amount of aerosols within the atmosphere, sometimes referred to as the aerosol mass loading, varies considerably from one location to another, and over relatively short periods of time. As we can see in the AM1.5 direct and circumsolar spectrum (figure 4), we have spikes in the infrared region, caused by the water drop in atmosphere, as they absorb the radiation from the Sun that reaches the atmosphere in the infrared region of the spectrum.

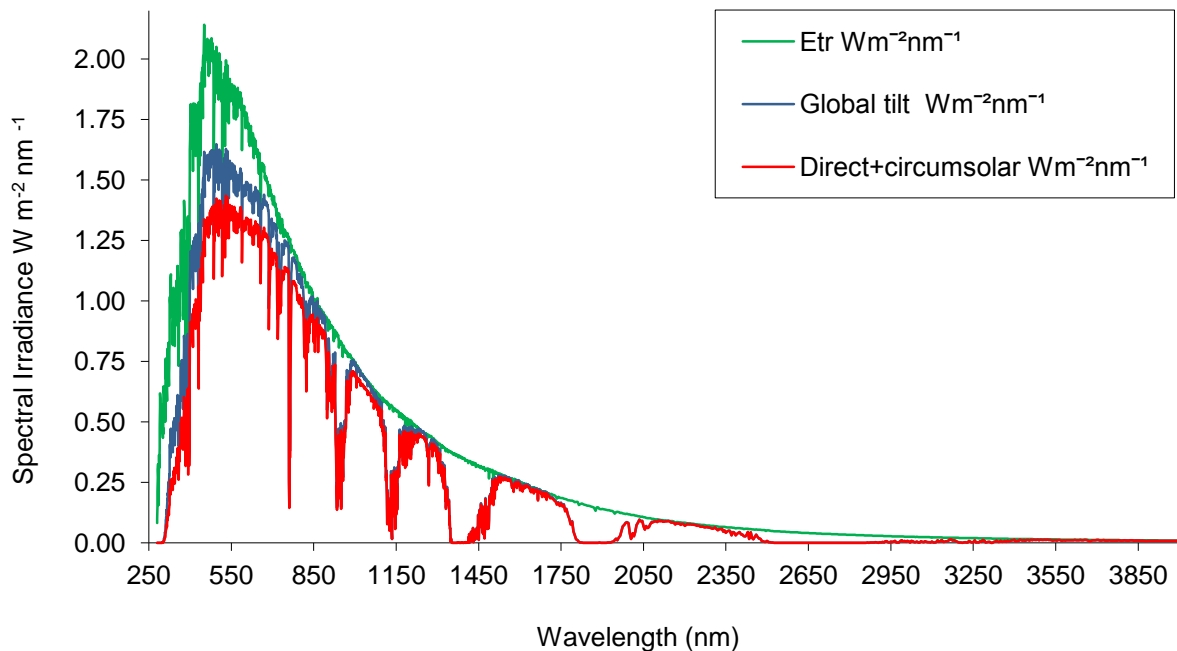


Figure 4: Spectra irradiance for Earth (AM0) and global and direct + circumsolar (AM1.5) [16].

1.2. The solar constant

This is the radiant power per unit area, perpendicular to the direction of the Sun's rays outside the Earth's atmosphere, where, at the mean, the Earth's distance is essentially constant. This radiation intensity is referred to as the solar constant, or alternatively, air mass zero (AM0) radiation.

The presently accepted value of the solar constant, in photovoltaic work, is 1.353 kW/m^2 .

This value has been determined by taking a weighted average of measurements made by equipment mounted on balloons, high altitude aircraft, and spacecraft. Knowledge of the exact distribution of the energy content in sunlight is important in solar cell work because these cells respond differently to different wavelengths of light.

1.3. Solar intensity at the Earth's surface

Rayleigh scattering, or scattering by molecules in the atmosphere. This mechanism attenuates sunlight at all wavelengths, but is most effective at shorter wavelengths.

2. Scattering by aerosols and dust particles.

3. Absorption by the atmosphere and its constituent gases; oxygen, ozone, water vapour, and carbon dioxide, particularly.

The most important parameter that determines the total incident power, under clear conditions, is the length of the light path through the atmosphere. This is shortest when the Sun is directly overhead.

The easiest way to estimate the air mass is to measure the length of the shadow, S , cast by the vertical structure of height, h .

$$\text{Air mass} = \sqrt{1 + \left(\frac{S}{h}\right)^2}, \quad (2)$$

with increasing air mass, and while other atmospheric conditions remain constant, the energy reaching the Earth is attenuated at all wavelengths.

1.4. Direct and diffuse radiation

The composition of terrestrial sunlight is further complicated by the fact that, as well as the component of radiation direct from the Sun, atmospheric scattering gives rise to a significant indirect or diffuse component. Even in clear, cloudless skies, the diffuse component can account for 10-20% of the total radiation received by a horizontal surface during the day.

For less sunny days, the percentage of diffuse radiation on a horizontal surface generally increases, and for days on which there is a notable lack of sunshine, most of the radiation will be diffuse. For days approaching sunny weather, about one-half of this radiation level is received, with around half of this being diffused.

Diffused sunlight has a different spectral composition to direct sunlight generally, being richer in shorter (or blue) wavelength, giving rise to future variability in the spectral composition of light received by a solar cell system.

Uncertainty in the distribution of diffuse radiation from different directions in the sky introduces other uncertainties when calculating radiation levels on an inclined surface, when compared with data generally recorded on a horizontal surface.

Photovoltaic systems based on concentrated sunlight can generally only accept rays spanning a limited range of angles.

1.5. Solid angle

The solid angle, Ω , is the two-dimensional angle in a three-dimensional space that an object subtends at a point. It is a measure of how large that object appears to an observer, looking from that point, and can be found as the area of the detector divided by the square of the distance between the illuminated spot, and the detector surface (figure 5).

$$\Omega = \text{Area of detector} / L^2 \quad (3)$$

The SI units of solid angles are 'steradian' (abbreviated "sr")

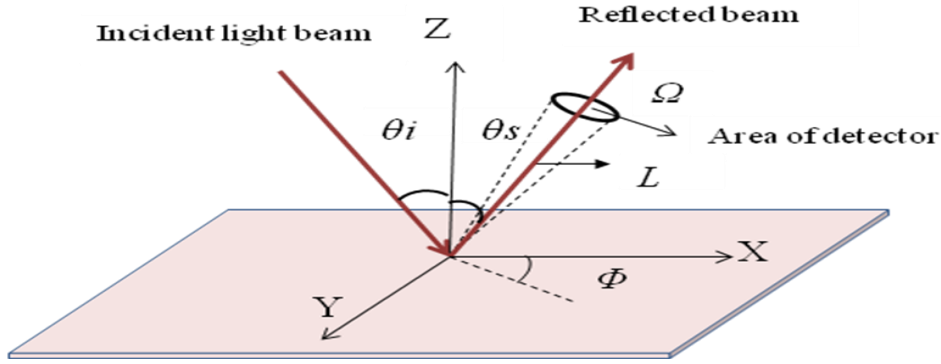


Figure 5: Scatterometer layout and solid angle.

1.6. Blackbody

The Sun emits energy in the form of electromagnetic radiation over a continuous range of wavelengths, known as the electromagnetic spectrum. Its behaviour in this respect is similar to that of a perfect ('blackbody') radiator at a temperature of approximately 6000K [17]. By definition, blackbody radiators absorb, and subsequently emit, all of the radiation incident upon them. The amount of energy emitted by a blackbody radiator varies with wavelength according to Planck's equation. The spectrum of radiation is denoted by $I(\nu, T)$, which is a function of frequency, ν . Planck's law is written as a unit of power (W) received per unit of area (m^2) into solid angle (sr) per unit of frequency interval:

$$I(\nu, T) = \frac{2h\nu^3}{c^2} \frac{1}{\exp\left(\frac{h\nu}{kT}\right) - 1} \quad Wm^{-2}sr^{-1}Hz^{-1}, \quad (4)$$

where h, c, k are: the Planck constant, the speed of light and the Boltzmann's constant respectively, and T is the absolute temperature.

Planck's law is also sometimes written in terms of the spectral energy density per unit volume of thermodynamic equilibrium cavity radiation. The law is thus written:

$$u(\nu, T) = \frac{4\pi}{c} I(\nu, T) = \frac{8h\nu^3}{c^3} \frac{1}{\exp\left(\frac{h\nu}{kT}\right) - 1}, \quad (5)$$

which contains units of energy per unit volume, per unit frequency (joule per cubic meter per hertz). Integrated over frequency, this expression yields the total energy density.

The total amount of power emitted per unit area of the surface of a black body is directly proportional to the fourth power of its absolute temperature:

$$l, \text{ is given by the Stefan-Boltzmann equation: } l = \sigma T^4, \quad (6)$$

where σ is the Stefan-Boltzmann constant ($\sigma = 5.67 \times 10^{-8} \text{ Wm}^{-2}\text{K}^{-4}$), and l is the total power radiated per unit area.

1.7. Fluorescence

Fluorescence [18, 19] is a spectroscopic method, whereby the molecules are excited by irradiation at a certain wavelength and emit radiation of a different wavelength. As shown in figure 6, when light with a particular wavelength is absorbed by a molecule (i.e., excitation), the electronic state of the molecule changes from the ground state to one of many vibrational levels. The excited electronic state is usually the first excited singlet state, S_1 (figure 6), where, once the molecule is in this excited state, relaxation can occur via several processes. Fluorescence is one of these processes, and results in the emission of light.

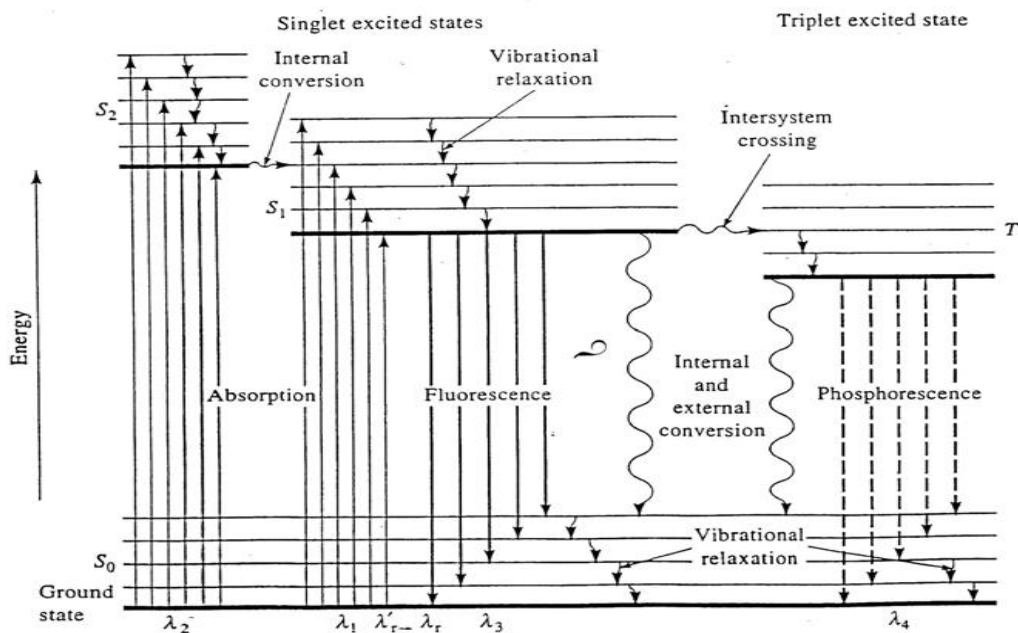


Figure 6: Electronic transition energy level diagram [18].

Following absorption, a number of vibrational levels of the excited state are populated.

Molecules in these higher vibrational levels then relax to the lowest vibrational level of the excited state (vibrational relaxation), and from this level, several processes can cause the molecule to relax to its ground state. The most important pathways are:

1. Fluorescence: corresponds to the relaxation of the molecule from the singlet excited state to the singlet ground state with emission of light. The wavelength (and thus the energy) of the light emitted is dependent on the energy gap between the ground state and the singlet excited state. The fluorescence energy is always less than the absorption energy for a given molecule, therefore the emitted light is observed at longer wavelengths than the excitation

2. Phosphorescence: this is the relaxation of the molecule from the triplet excited state to the singlet ground state with emission of light, and unlike fluorescence, a phosphorescent material does not immediately re-emit the radiation it absorbs. The slower time scales of the re-emission are associated with forbidden energy state transitions in quantum mechanics. As these transitions occur very slowly in certain materials, absorbed radiation may be re-emitted at a lower intensity for up to several hours after the original excitation.

3. Intersystem Crossing: in this process, if the energy states of the singlet state overlaps those of the triplet state, as illustrated in figure 6, vibrational coupling can occur between the two states. Molecules in the single excited state can cross over to the triplet excited state. The molecular spin state for Intersystem Crossing changes, and the energy remains the same.

4. Internal Conversion: direct vibrational coupling between the excited electronic states and the ground state (vibronic level overlap) and quantum mechanical tunnelling (no direct vibronic overlap but small energy gap) are internal conversion processes. Internal conversion is also sometimes called "radiation-less de-excitation", because no photons are emitted. The molecular spin state for internal conversion remains the same, whereas it changes for intersystem crossing. The energy of the electronically excited state is given off to vibrational modes of the molecule, or phonons, and the excitation energy is transformed into heat.

5. Collisional deactivation (external conversion): leads to non-radioactive relaxation.

Fluorescence intensity may also be reduced or eliminated if the luminescence molecule forms ground, or excited state complexes (quenching).

The quantum yield, or quantum efficiency, for fluorescence is therefore the ratio of the number of molecules that are luminescent to the total number of excited molecules.

1.8. Effective temperature of fluorescence radiation (Kennard-Stepanov)

The Kennard–Stepanov relation is a general relationship between the shapes of the absorption and the fluorescence spectra of a homogeneous substance.

For systems with one excited electronic state, and under conditions of excited-state thermal equilibrium, the Kennard–Stepanov (KS) relation predicts a linear relationship between absorption, emission, and temperature [20, 21, 22]

$$f_e(\nu) = \ln\left(\frac{c^2 f_1(\nu)}{8\pi h \nu^3 \text{abs}(\nu)}\right) = -\frac{h\nu}{kT} + D(T), \quad (7)$$

where $f_1(\nu)$ is the emissive power in W/Hz , ν is the frequency of electromagnetic radiation, T is the ambient temperature, and k is Boltzmann's constant. The term $D(T)$ is independent of frequency. $\text{abs}(\nu)$ is the absorption cross-section at energy, ν , and can be determined using the Beer-Lambert law, as shown in equation 8.

$$\text{abs}(\nu) = \frac{-\log\left(\frac{I}{I_0}\right)}{Cl}, \quad (8)$$

where I is the intensity of the light transmitted through a reference sample, I_0 is the intensity of incident, l is the path length, and C is the concentration.

The Kennard-Stepanov law is generally used to characterise the effective temperature of fluorescence.

It is important in the KS relation that the absorption and emission are held in the same energy level. In practice the optimal region is the region where the absorption and fluorescence bands overlap [21].

In this application, the general focus has been on the fit of experimental data to the linear function of frequency, suggested by equation 7, to see how well the results of the excited state attained thermal equilibrium before emission.

It has been observed, experimentally, that equation 7 often holds, even when the temperature, T , is unequal to the temperature of the emitting substance. For this reason, the T^* is adopted for the

effective temperature, to characterise the relationship between the absorption and emission process.

The Kennard-Stepanov spectral temperature is defined in terms of the slope of $f_l(\nu)$ [21]:

$$T^* = \frac{-k}{h} \frac{d}{d\nu} \ln\left(\frac{c^2}{8\pi h} \frac{f_l(\nu)}{\nu^3 \text{abs}(\nu)}\right)^{-1}, \quad (9)$$

This equation transforms the experimental $f_l(\nu)$ into a spectrum. In practice, T^* is found from the inverse slope of the regression line through $f_e(\nu)$, for a series of data points, centred at frequency, ν . In Stepanov's version of the theory, the relationship will hold if two conditions are satisfied: firstly, that the equilibrium is in an excited state, and secondly, that non-exciting absorption is achieved, due to transitions between the two vibrational levels of the ground state being negligible [21,22]. The effective temperature was used to calculate the chemical potential of the flux in the following chapter, indicating the specific temperature at which the flux reached the thermal equilibrium after reabsorption and re-emission events, described by Planck's law [22].

Conclusion

This chapter has presented the standard solar irradiance spectra- AM1.5, the estimate of global radiation (direct plus diffuse), and the temporal variation of incident solar radiation spectra, AM1.5, used for charting the performance of photovoltaic devices where the Sun delivers 1000 Wm^{-2} to the Earth.

The chapter reviewed the physics of fluorescence dye and the Planck Law, as well as the theory of Kennard–Stepanov, which was also explained and used in the following chapters.

Chapter 2

Principles of Solar Cell Operation

Introduction

A semiconductor solar cell is a device consisting of a large p-n junction area. The sunlight is absorbed by these materials and the solar energy excites an electron from the valance band to the conduction band, allowing the electrons to flow through the material, thus producing electricity. The process of converting light (photons) to electricity (voltage) is called photovoltaic [23].

Photovoltaic conversion of solar energy is one of the most promising methods of meeting the increasing energy demands of the future, at a time when conventional sources of energy are being depleted. Today, the direct conversion of light into electricity (photovoltaics), is becoming accepted as an important form of power generation. The aim of this chapter is to highlight those properties of semiconductors that are important in the design and operation of solar cells.

2.1. The ideal solar cell

An ideal solar cell can be represented by a current source connected in parallel with a rectifying diode, as shown in the figure 7, the corresponding I - V characteristic is described by the Shockley solar cell equation [24, 25].

$$I = I_{ph} - I_0 \left(e^{\frac{qV}{k_B T}} - 1 \right), \quad (10)$$

Where the k_B is the Boltzman constant, T is the absolute temperature, q (>0) is the electron charge, and V is the voltage at the terminal of the cell. I_{sat} is the diode saturation current.

The solar cell in the dark is simply a semiconductor current rectifier, or diode. In an ideal situation, the short circuit current, I_{sc} , is equal to photo-generated current, I_{ph} , and the open circuit voltage, V_{oc} , is given by:

$$V_{OC} = \frac{k_B T}{q} \ln\left(1 + \frac{I_{ph}}{I_{sat}}\right), \quad (11)$$

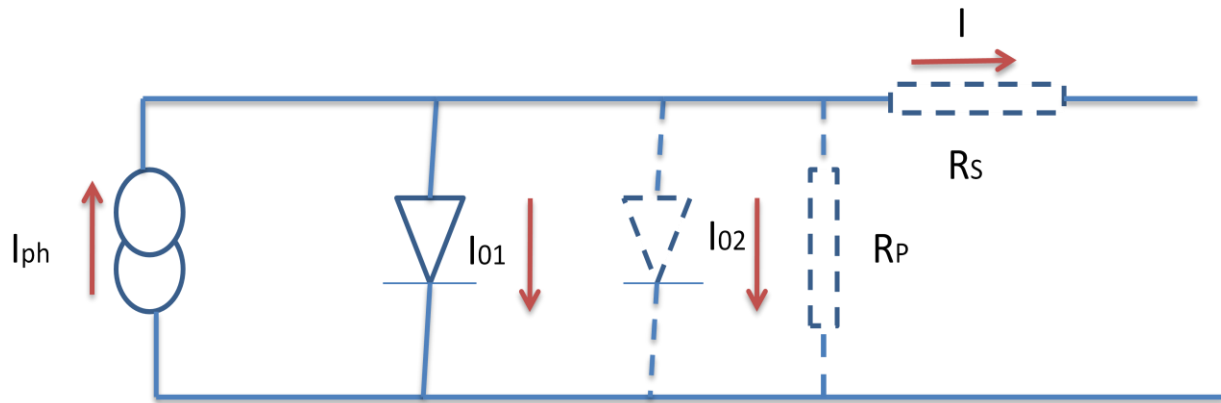


Figure 7: The equivalent circuit of an ideal solar cell (full line). Non-ideal components are shown by the dotted line. I_{01} is the current passed through the first diode, I_{02} is the current passed through the second diode, and I is the current passed through the series resistance (R_s).

2.2. I-V characterisation of silicon solar cell

A plot of equation 10 is given in figure 8(A). The curve passes through the fourth quadrant and, therefore, power can be extracted from the device. By properly choosing a load, close to 80% of the product, $I_{sc} V_{oc}$, can be extracted (I_{sc} is the short circuit current, and V_{oc} is the open circuit voltage of the cell; the shaded area is the maximum power rectangle). The $I-V$ curve is more generally represented by figure 8(B), which is an inversion of figure 8(A) above the voltage axis. In figure 8(B) the quantities, I_m and V_m , correspond to current and voltage, respectively, for the maximum power output.

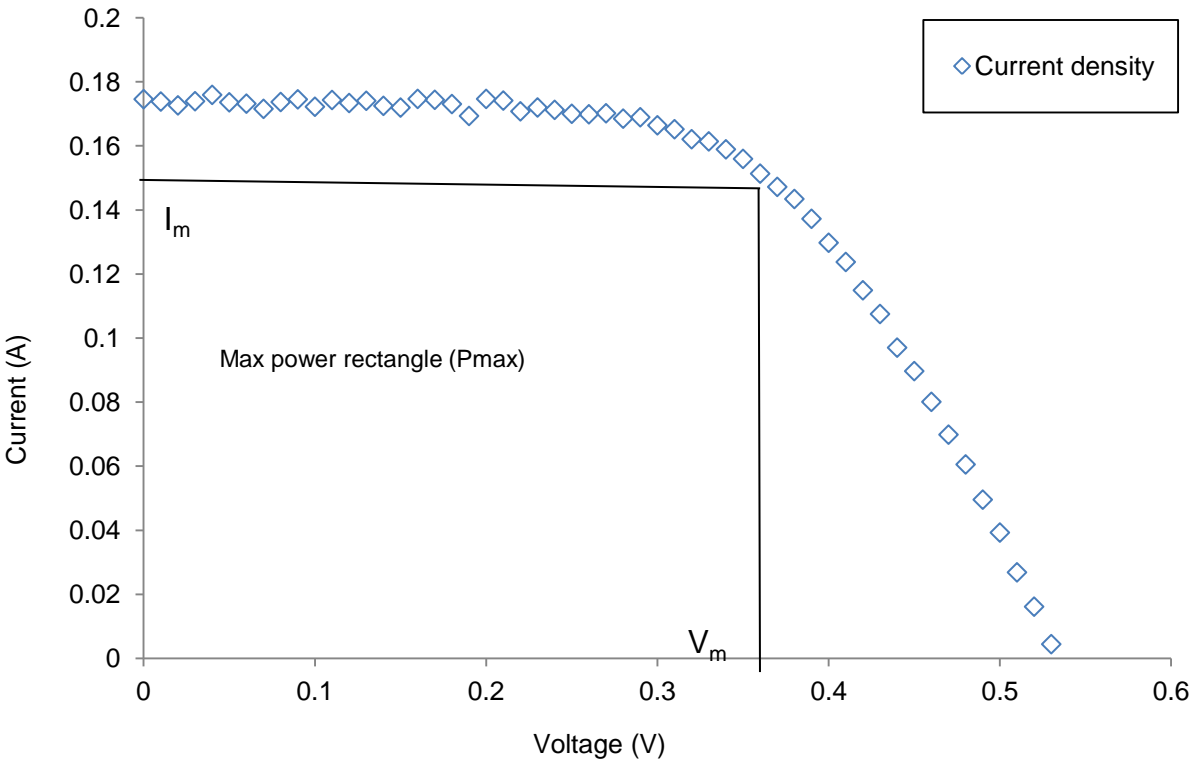
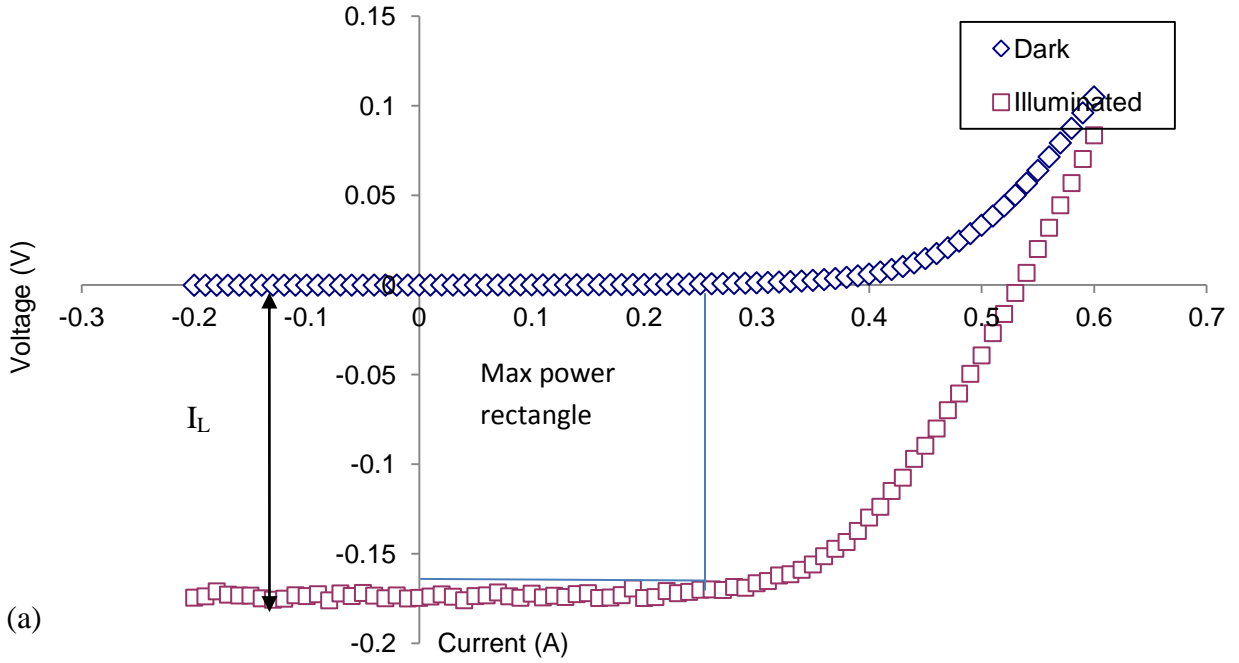


Figure 8: (a) Current-voltage characteristics of a mono-silicon solar cell under darkn and illumination. (b) Inversion of (a) about the voltage axis.

No power is generated under a short or open circuit, and the maximum power, P_{max} , produced by the device is reached at a point where the product, $I-V$, is at a maximum. This is shown, graphically, in figure 8(B), where the position of the maximum power point represents the largest area of the rectangle. One usually defines the fill factor (FF) by:

$$P_{max} = V_m I_m = FF V_{oc} I_{sc}, \quad (12)$$

where V_m and I_m are the voltage and current at the point of maximum power.

The efficiency, η , of the solar cell is defined as P_{max} , produced by the cell at the maximum power point under standard test conditions, divided by the power of the radiation incident upon it.

$$\eta = \frac{P_{max}}{P_{in}} = \frac{FF V_{oc} I_{sc}}{P_{in}}, \quad (13)$$

The fill factor FF of a solar cell with the ideal characteristic will be furnished by the subscript 0. It cannot be determined analytically but it can be shown that FF_0 depends only on the ratio

$$v_{oc} = V_{oc} / k_B T, \quad (14)$$

FF_0 is determined, to an excellent accuracy, by the approximate expression

$$FF_0 = \frac{v_{oc} - \ln(v_{oc} + 0.72)}{v_{oc} + 1}, \quad (15)$$

The $I-V$ characteristics of an ideal solar cell complies with the superposition principle: the functional dependence can be obtained from the corresponding characteristic of a diode in the dark through a shifting of the diode characteristic along the current axis, by I_{ph} , as is shown in figure 8A.

Most frequent test conditions have an irradiance of 100 mWcm^{-2} , a standard reference of AM1.5 spectrum, and a temperature of 25°C . The use of this standard irradiance value is particularly convenient, since the cell efficiency is then numerically equal to the power output from the cell in mWcm^{-2} . Other test conditions are sometimes adopted for cells which operate in different environments, for example, cells which power satellites and operate under the AM0 spectrum.

2.3. Solar cell characteristic in practice

An ideal solar cell may be modelled by a current source in parallel with a diode. The I - V characteristic of a solar cell, in practice, usually differs to the ideal characteristic, while a two-diode model is used to fit an observed curve with the second diode. The solar cell may also contain series (R_s) and parallel (or shunt, R_p) resistance, leading to a characteristic of the form:

$$I = I_{ph} - I_{01} \left\{ \exp\left(\frac{V + IR_s}{k_B T}\right) - 1 \right\} - I_{02} \left\{ \exp\left(\frac{V + IR_s}{2k_B T}\right) - 1 \right\} - \frac{V + IR_s}{R_p}, \quad (16)$$

where the light generated current, I_{ph} , may, in some instances, depend on the voltage (as shown in figure 7 by the dotted lines). The effect of the series resistance on the fill factor can be allowed for by writing:

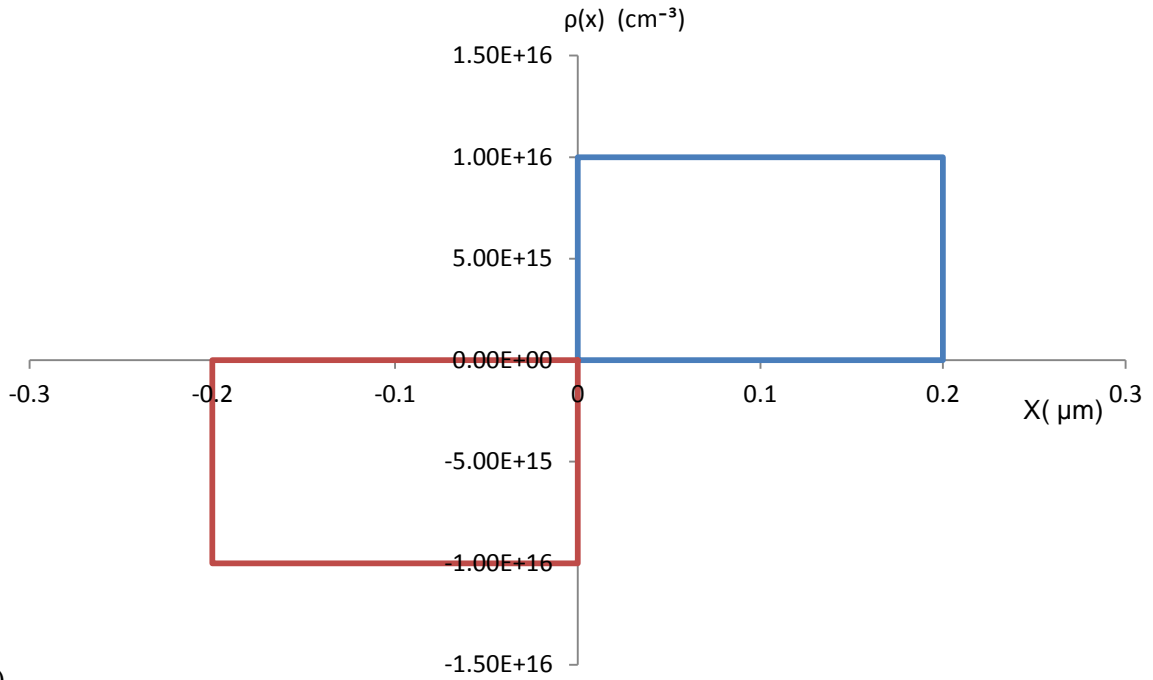
$$FF = FF_0(1 - r_s), \quad (17)$$

where the $r_s = R_s I_s / V_{oc}$. An analogous expression also exists for the parallel resistance.

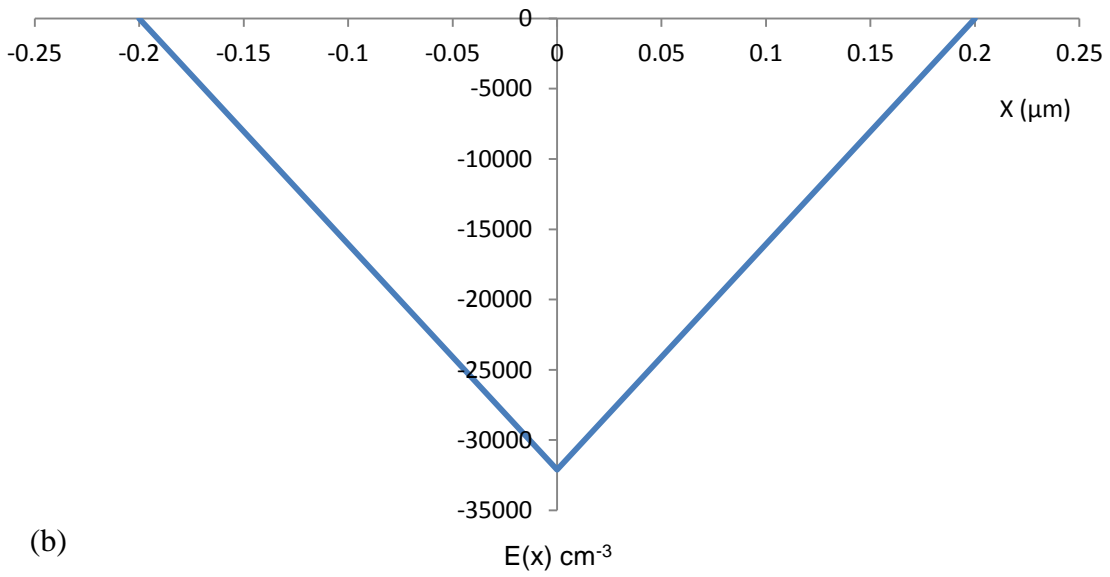
The series resistance usually arises from the resistance of the cell material to current flow, particularly through the front surface to the contacts, and from resistive contacts. Series resistance is a particular problem at high current densities, for instance, under concentrated light. The parallel, or shunt, resistance arises from leakage of current through the cell, around the edges of the device and between contacts of different polarity, and is a problem in poorly rectifying devices.

2.4. Depletion layer of an abrupt p-n junction

A simple model for the space-charge region, an approximation of the exhaustion region, was introduced by Shockley, that assumes a rectangular charge density distribution, as shown in figure 9.



(a)



(b)

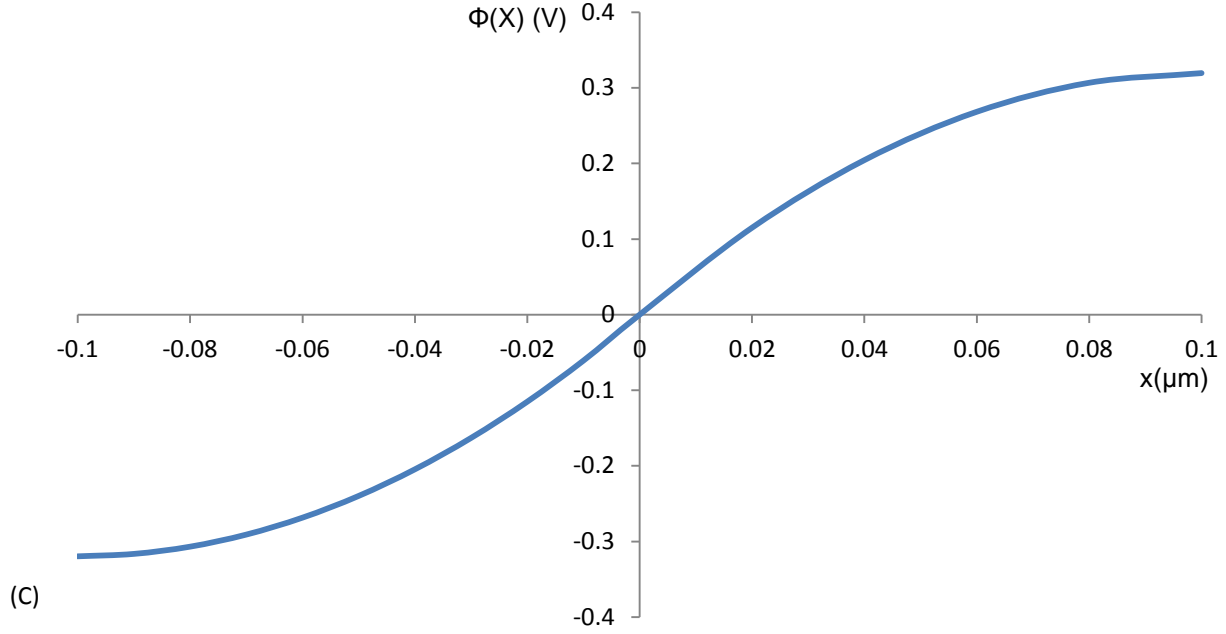


Figure 9: (a) Space-charge calculated from equation (18). (b) Electric field calculated from equation (20). (c) Voltage across a p-n junction calculated from equation (25). Curves for an abrupt p-n junction in silicon at 300 K, and the density of donor ($N_D = 10^{16} \text{cm}^{-3}$) and acceptor ($N_A = 10^{16} \text{cm}^{-3}$) (More detail in Appendix 1).

The space-charge region is depleted of mobile charge carriers and hence the space-charge density here is given by:

$$\begin{aligned} \rho(x) &= -qN_A & (-W_p \leq x \leq 0) \\ \rho(x) &= +qN_D & (0 \leq x \leq W_n), \end{aligned} \quad (18)$$

The electrical field in the space-charge region can be found by integrating Poisson's equation, from $x = 0$ to the edges of the depletion region, with the constant charge densities. This gives Poisson's equation:

$$\frac{d^2 \phi_0(x)}{dx^2} = -\frac{dE}{dx} = -\frac{\rho_0(x)}{\epsilon_0 \epsilon_s}, \quad (19)$$

where ϕ_0 is electrical potential, E is electrical field, $\rho_0(x)$ is space-charge density, and $\epsilon_0 \epsilon_s$ is the permittivity of free space and static permittivity of a medium.

$$\begin{aligned}
E(x) &= -\frac{qN_A}{\epsilon_0\epsilon_s}(W_p + x) & (-W_p \leq x \leq 0) \\
E(x) &= -\frac{qN_D}{\epsilon_0\epsilon_s}(W_n - x) & (0 \leq x \leq W_n),
\end{aligned} \tag{20}$$

Figure 9(b) shows the linear dependence of the electric field on the position in the space-charge region. The electric field vanishes outside this region. The Debye length (L_D) is defined as:

$$L_D^p = \left(\frac{\epsilon_0\epsilon_s kT}{q^2 N_A}\right)^{1/2}, \tag{21}$$

$$L_D^n = \left(\frac{\epsilon_0\epsilon_s kT}{q^2 N_D}\right)^{1/2}, \tag{22}$$

The electric field can be expressed as

$$\begin{aligned}
E(x) &= -\frac{V_{th}}{(L_D^p)^2}(W_p + x) & (-W_p \leq x \leq 0) \\
E(x) &= -\frac{V_{th}}{(L_D^n)^2}(W_n - x) & (0 \leq x \leq W_n),
\end{aligned} \tag{23}$$

where the so called thermal voltage, V_{th} , is defined by:

$$V_{th} = \frac{kT}{q}, \tag{24}$$

The Debye length is a characteristic length of the junction, and at thermal equilibrium, the depletion layer width of the abrupt junction is about $8L_D$ for silicon [26]. The Debye length is shown in figure 10 for typical doping densities $\geq 10^{16} \text{ cm}^{-3}$.

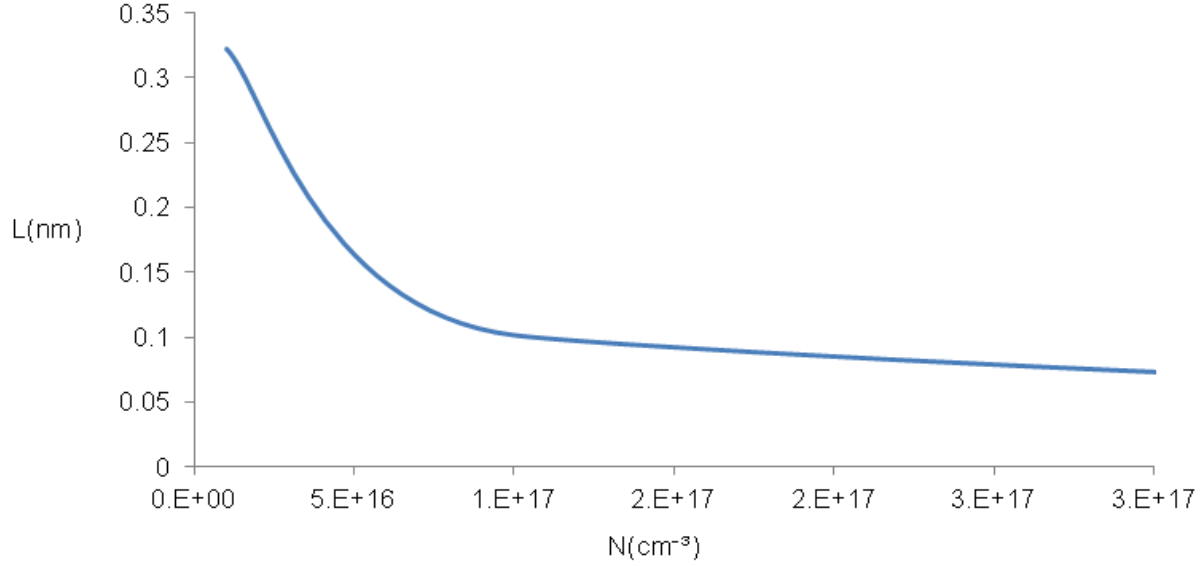


Figure 10: Debye length for silicon in doping density of more than 10^{16}cm^{-3} (calculated from equations (21) and (22)).

By integration of equation 19 along x , the electrostatic potential in the depletion region is given by equation 25, also shown in figure 9(c).

$$\begin{aligned}\phi_p(x) &= \frac{qN_A}{2\epsilon_0\epsilon_s} x(2W_p + x) & (-W_p \leq x \leq 0) \\ \phi_n(x) &= \frac{qN_D}{2\epsilon_0\epsilon_s} x(2W_n - x) & (0 < x \leq W_n)\end{aligned}\quad (25)$$

At the depletion region edge, and the quasi neutral regions beyond, the potential takes the constant values $\phi_p(-\infty)$, for the p-type region, and $\phi_n(\infty)$, for the n-type region. The potential difference, at the depletion region edges, is denoted by:

$$V_J = \phi_n(\infty) - \phi_p(-\infty) = \phi_n(W_n) - \phi_p(-W_p), \quad (26)$$

For equilibrium conditions, V_J is called the diffusion voltage, or built-in potential, V_D , of the p-n junction as in figure 9. By substituting $\phi_n(W_n)$ and $\phi_p(-W_p)$ in to equation 27, we find:

$$V_D = \frac{q}{2\epsilon_0\epsilon_s} x(N_D W_n^2 + N_A W_p^2), \quad (27)$$

The interface as a whole must be electrically neutral so

$$N_D W_n = N_A W_p, \quad (28)$$

Using equations 27 and 28, the depletion region width at equilibrium conditions follows as

$$W_n = \left(\frac{2\epsilon_0\epsilon_s V_D}{q} \frac{N_A / N_D}{N_A + N_D} \right)^{1/2}$$

$$W_p = \left(\frac{2\epsilon_0\epsilon_s V_D}{q} \frac{N_D / N_A}{N_A + N_D} \right)^{1/2}, \quad (29)$$

The characteristics of the equilibrium situation can be found in the 'Fermi levels'. The energy of the highest filled state at 0K is called the Fermi level, and a system in thermal equilibrium can have only one Fermi level. Referring to figure 11, this means that there must be a transition region near the junction, in which there is a potential change, ϕ_0 . The value of ϕ_0 can also be found from figure 11:

$$q\phi_0 = E_g - E_1 - E_2, \quad (30)$$

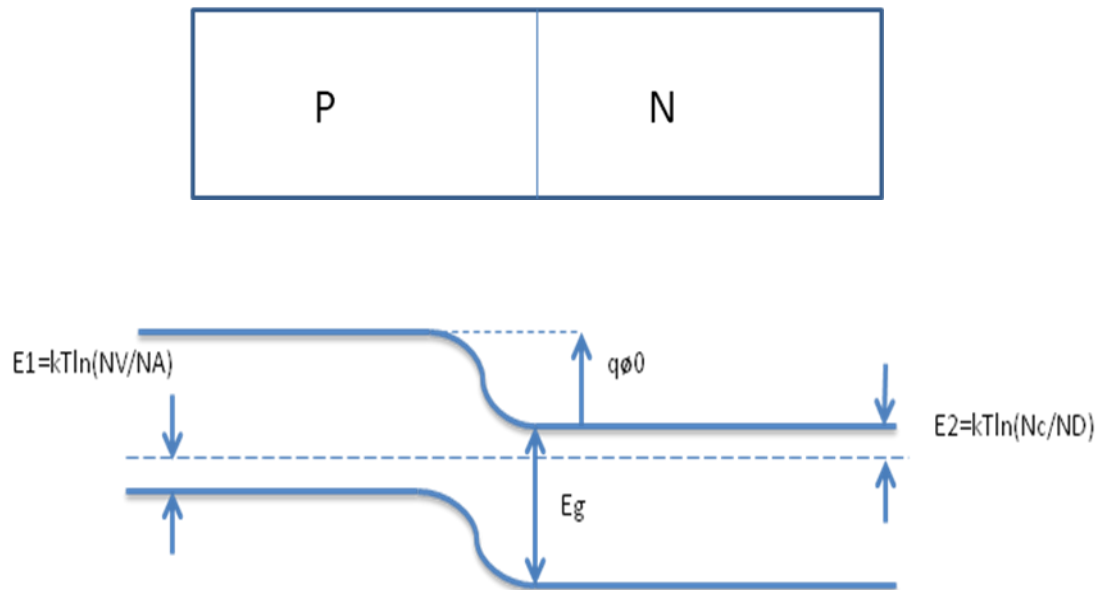


Figure 11: A p-n junction formed by bringing the isolated p-type and n-type regions together. Also shown is the corresponding energy-band diagram at thermal equilibrium which is an amended version of figure 9c to indicate the relevant quantities [27].

The expressions for E_1 and E_2 are indicated in figure 11

$$q\phi_0 = E_g - kT \ln\left(\frac{N_v}{N_A}\right) - kT \ln\left(\frac{N_c}{N_D}\right) = E_g - kT \ln\left(\frac{N_c N_v}{N_A N_D}\right), \quad (31)$$

$$n_i^2 = N_c N_v \exp\left(-\frac{E_g}{kT}\right), \quad (32)$$

$$\phi_0 = \frac{kT}{q} \ln\left(\frac{N_A N_D}{n_i^2}\right), \quad (33)$$

An applied voltage, V_a , will change the potential difference between the two side of the diodes by V_a . Hence, the potential across the transition region will become $(\phi_0 - V_a)$ with the approximation that the system is in equilibrium. It is simple to find the electric field and potential distribution across the depletion region, as shown in figure 11. The electric field is the negative gradient of potential, as explained before in Poisson's equation. The result of the maximum field strength in the depletion region, E_{\max} , the width of the depletion region, W , and the distance this region extends on either side of the junction, W_n and W_p , is given by

$$E_{\max} = -\left[\frac{2q}{\epsilon}(\phi_0 - V_a)\left(\frac{1}{N_A} + \frac{1}{N_D}\right)\right]^{1/2}, \quad (34)$$

$$W = W_n + W_p = \left[\frac{2q}{\epsilon}(\phi_0 - V_a)\left(\frac{1}{N_A} + \frac{1}{N_D}\right)\right]^{1/2}$$

$$W_p = W \frac{N_D}{N_A + N_D}, \quad (35)$$

$$W_n = W \frac{N_A}{N_A + N_D}, \quad (36)$$

2.5. Generation of electron-hole pairs

The principal means of carrier generation in solar cells is the absorption of light. A photon entering the semiconductor generates electron-hole pairs in a thin layer, at a depth $x \rightarrow x + \delta x$. The generation function, $G(x)$, is given by:

$$G(x) = \int_0^{\lambda_{\max}} [1 - R(\lambda)] \alpha(\lambda) N_{ph}(\lambda) e^{-\alpha(\lambda)x} d\lambda, \quad (37)$$

where $\alpha(\lambda)$ is the absorption coefficient, $N_{ph}(\lambda)$ is the incident photon/cm²/s per unit bandwidth, and $R(\lambda)$ is the fraction of these photons reflected from the surface. The generation rate of electron and hole pairs, as a function of distance into the cell, is shown in figure 12.

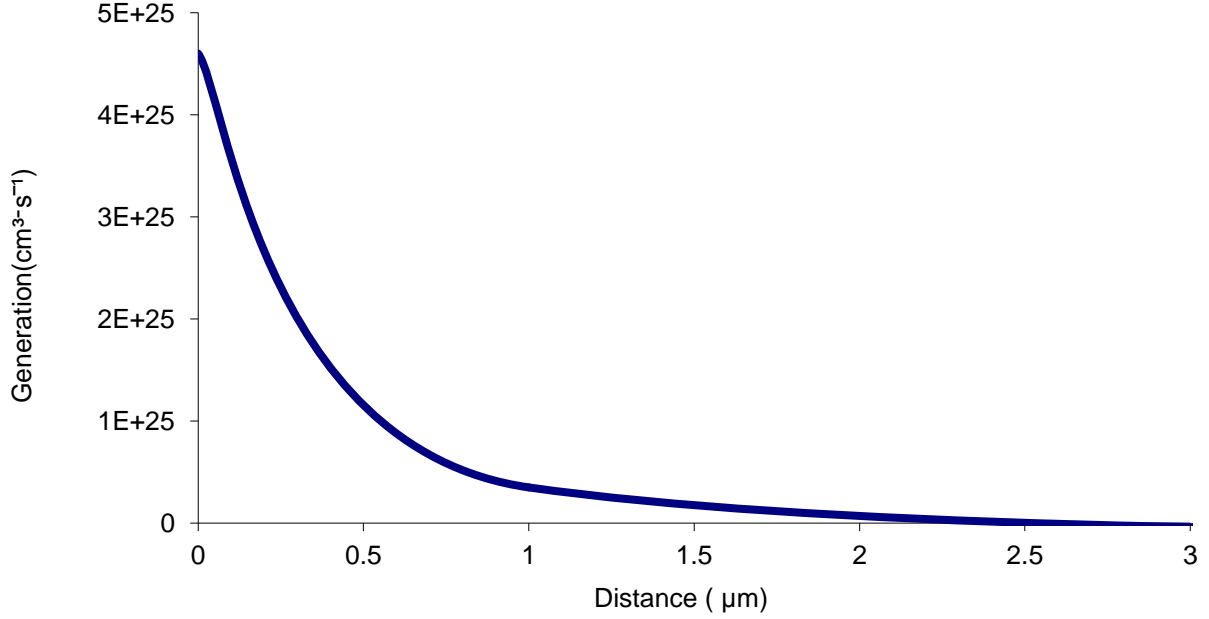


Figure 12: Generation rate of electron-hole pairs, calculated from equation (37) as a function of distance into the cell when illuminated by sunlight.

The generation rate has a very strong peak at short distances to the surface, and the recombination rate, $R(x)$, is described by the lifetime of electrons (τ_n) and holes (τ_p) as follows [23]:

$$R_n(x) = \frac{\Delta n(x)}{\tau_n}, \quad (38)$$

$$R_p(x) = \frac{\Delta p(x)}{\tau_p}, \quad (39)$$

where, $\Delta n(x)$ and $\Delta p(x)$ are the excess electron and hole concentrations respectively.

Under the influence of an applied electric field, E , a random moving electron with an acceleration, a , in a direction opposite to the field, will see its velocity in this direction increase with time (t). The average velocity increase of electrons between collisions caused by the field is called the drift velocity, or v_d , and is given by:

$$v_d = \frac{1}{2} at, \quad (40)$$

while the electron carrier mobility is defined by the ratio

$$\mu_n = \frac{v_d}{E}, \quad (41)$$

The corresponding current density flow due to the conduction band electron is given by equation 42.

$$J_n = q\mu_n v_d = q\mu_n nE, \quad (42)$$

where the n is the electron concentrations respectively. Similarly, an analogous equation for holes in the valence band is:

$$J_p = q\mu_p v_d = q\mu_p pE, \quad (43)$$

where μ_p is the mobility of the hole, E is an applied electric field, and p is the hole concentrations respectively. The total current flow is simply the sum of these two components.

The current density was obtained by the solution of the electron and hole in a continuity equation:

$$-\frac{1}{q} \frac{dJ_n(x)}{dx} = G(x) - R(x), \quad (44)$$

where

$$J_n = q\mu_n n(x)E(x) + qD_n \frac{dn(x)}{dx}, \quad (45)$$

$$J_p = q\mu_p p(x)E(x) - qD_p \frac{dp(x)}{dx}, \quad (46)$$

are the electron and hole conduction current densities. $G(x)$ is the generation rate, $R(x)$ is the recombination rate, $\frac{dn(x)}{dx}$, $\frac{dp(x)}{dx}$ are the concentration gradients of electrons and holes, D_n and

D_p are the diffusion coefficients of electrons and holes respectively by the Einstein relations, shown in equation 47:

$$D_n = \frac{kT}{q} \mu_n, \quad D_p = \frac{kT}{q} \mu_p, \quad (47)$$

Under the diffusion effect, which is the excess concentration of particles such as gas molecules, it will tend to dissipate itself unless constrained. The basic cause of this effect is the random thermal velocity of the particles involved. The electric field within the neutral region of the p and n layer is zero, hence using equations 42 and 43, equations 45 and 46 can be reduced into second-order differential equations of the form:

$$D_n \frac{d^2 \Delta n(x)}{dx^2} - \frac{\Delta n(x)}{\tau_n} + G(x) = 0, \quad (48)$$

$$D_p \frac{d^2 \Delta p(x)}{dx^2} - \frac{\Delta p(x)}{\tau_p} + G(x) = 0, \quad (49)$$

Equations 48 and 49 are solved with appropriate boundary conditions [28]. The current densities due to diffusion of charge carriers are analysed using

$$J_n = qD_n \left. \frac{d\Delta n}{dx} \right|_{x=x_n}, \quad (50)$$

and

$$J_p = qD_p \left. \frac{d\Delta p}{dx} \right|_{x=x_p}, \quad (51)$$

The electric field is generally high within the depletion layer, and we assume that the photo generated carriers are accelerated out of the depletion layer before they can recombine. Thus, the current density due to the depletion layer is

$$J_{dep} = q \int_0^{\lambda_{max}} [1 - R(\lambda)] N_{ph}(\lambda) e^{-\alpha(\lambda)x_p} [1 - e^{-\alpha(\lambda)W}] d\lambda, \quad (52)$$

The total photocurrent density is then:

$$J_{ph} = J_n + J_p + J_{dep}, \quad (53)$$

and the total current density is

$$J(V) = J_{ph} - J_{dark}, \quad (54)$$

where

$$J_{dark} = J_s \left[e^{\frac{qV}{kT}} - 1 \right], \quad (55)$$

J_s is the current saturation density.

2.6. The quantum efficiency and spectral response

The quantum efficiency of a solar cell is defined as the ratio of the number of electrons in the external circuit to the incident photon of a given wavelength. Thus, one can define external and internal quantum efficiency (EQE(λ) and IQE(λ), respectively) [23]. External Quantum Efficiency (EQE) is the ratio of the number of charge carriers collected by the solar cell to the number of incident photons of a given wavelength. Internal Quantum Efficiency (IQE) is the ratio of the number of charge carriers collected by the solar cell to the number of incident photons of a given wavelength and absorbed by the cell.

If the internal quantum efficiency is known, the total photon generated current is given by [23]

$$I_{ph} = q \int_{\lambda} \Phi(\lambda) \{1 - R(\lambda)\} IQE(\lambda) d\lambda, \quad (56)$$

where the $\Phi(\lambda)$ is the photon flux incident on the cell at wavelength λ , $R(\lambda)$ is the reflection coefficient from the top surface, and the integration is carried out over all the wavelengths, λ , of light absorbed by the solar cell. The values of the internal and external quantum efficiencies are routinely measured in order to assess the performance of a solar cell, by using interference filter, or monochromators.

The spectral response (denoted by $SR(\lambda)$, with the unit of A/W) is defined as the ratio of the photocurrent generated by the solar cell under the monochromatic illumination of given

wavelength, to the value of the spectral irradiance at the same wavelength. Since the number of photons and irradiance are related, the spectral response can be written in terms of the quantum efficiency [23]:

$$SR(\lambda) = \frac{q\lambda}{hc} QE(\lambda) = 0.808\lambda QE(\lambda), \quad (57)$$

where λ is in micrometers. The spectral response can be either internal or external, depending on which value is used for the quantum efficiency.

Conclusion

The essence of the solar cell operation has been the subject of this chapter, and the importance of the depletion layer of an abrupt p-n junction, and the current density in the p-n junction silicon solar cells, have been highlighted in this chapter.

The ideal solar efficiencies discussed in this chapter refer to the single junction semiconductor devices, with the limitations considered in the ultimate efficiency due to the fact that the simplest semiconductor cannot absorb below band gap photons. Furthermore, it is because the portion of energy of the absorbed photons in excess of the band gap is lost as heat.

The next chapters introduce the concept of scattering theory and the fluorescent solar collector, which makes use of the excellent electronic characteristics of c-Si, bypassing the absorption issue by separating absorption from electron generation.

Chapter 3

Scattering theory

Introduction

The purpose of this chapter is to review various scattering theories, and Mie scattering theorem and Fraunhofer diffraction in far-field, Bi-directional surface distribution function (BSDF) and the theory of the integrating sphere, based on radiation exchange within an enclosure of diffuse surfaces, are discussed in this chapter.

In scattering theory, elastic scattering is one of the specific forms of scattering. In this process, the kinetic energy of the incident particles is conserved, only their direction of propagation is modified by interaction with other particles. Reflections that undergo scattering are often called diffuse reflections, and un-scattered reflections are called specular (mirror-like) reflections. In specular reflection, the light from a single incoming direction is reflected into a single outgoing direction. Such behaviour is described by the law of reflection, in which the direction of incoming light (the incident ray), and the direction of outgoing light reflected (the reflected ray) make the same angle with respect to a normal surface, thus the angle of incidence equals the angle of reflection ($\theta_i = \theta_r$).

This is in contrast to diffuse reflection, where incoming light is reflected in a broad range of directions, the most familiar example of the distinction between specular and diffuse reflection being glossy surfaces compared to rough surfaces, where the reflected light is not specular (e.g. matt paint).

Even when a surface exhibits only specular reflection, with no diffuse reflection, not all of the light is necessarily reflected. Some of the light may be transmitted through the surface. Additionally, depending on the type of material into which the light passes, some of the light may be absorbed as it passes through the material. For most interfaces between materials, the fraction of light that is reflected increases with an increasing angle of incidence, θ_i . If the light is propagating in a material with a higher refractive index than the material whose surface it strikes,

total internal reflection may occur (if the angle of incidence is greater than a certain critical angle, or θ_c).

In unpolarised light, there is no preferred direction: the waves come in with electric and magnetic field vectors in random directions. Light in the form of a plane electromagnetic wave is said to be linearly polarised. In polarised light, the transverse electric field wave is accompanied by a magnetic field wave.

3.1. Radiance and Irradiance for a laser beam

Radiance, with unit: watts/(m².sr), describes the amount of light that passes through, or is emitted from, a particular area, and falls within a given solid angle in a specified direction. . Irradiance, or light intensity, is the power per unit area of electromagnetic radiation, and has the unit: watts/m². The definition of the radiant quantities is based on the emissive power, defined as the total amount of thermal energy emitted by radiation, from the surface, in all directions and at all wavelengths per unit surface area.

3.2. Scattering coefficient and the scattering efficiency

Consider a scattering particle idealised as a sphere with a particular geometrical size, and that redirects incident photons into new directions; this process constitutes scattering. However, it does provide a concept that captures the essence of the scattering coefficient.

The size of the scattering shadow is called the effective cross-section (C_{sca} [cm²]) and can be smaller or larger than the geometrical size of the scattering particle (A [cm²]), related by the proportionality constant known as the scattering efficiency, η_{sca} [dimensionless] (figure 13):

$$C_{sca} = \eta_{sca} A_s, \tag{58}$$

In other words, the total scattering energy in all directions is equal to the energy of incident wave falling to the area, C_{sca} , and therefore, we can write [29].

$$C_{sca} = \int_0^\pi \frac{I}{I_0} r^2 \sin(\theta_s) d\theta_s, \quad (59)$$

where I and I_0 are the intensities of scattered light, incident θ_s is the scattered light detected in different angles, and r is the distance between the particle and the detector.

If the particle has a geometrical cross section, $A = \pi a^2$, where a is the radius of the particle, the scattering efficiency can be calculated as:

$$\eta_{sca} = C_{sca} / A, \quad (60)$$

The scattering coefficient $\mu_{sca} [cm^{-1}]$ describes a medium containing many scattering particles, at a concentration described as a volume density, $\rho_s [cm^{-3}]$. The scattering coefficient is essentially the cross-sectional area per unit volume of the medium:

$$\mu_{sca} = \rho_s C_{sca}, \quad (61)$$

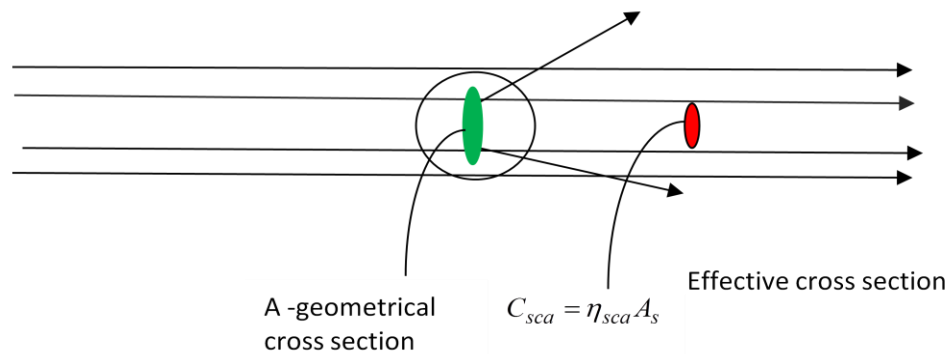


Figure 13: Scattering of light in a particle as a sphere.

Experimentally, the units [cm^{-1}] for μ_{sca} are of inverse length, such that the product $\mu_{sca}L$ is dimensionless, where $L[cm]$ is a photon's path length of travel through the medium. The probability of transmission of the photon, without redirection by scattering (specular transmittance), after a path length, L , is:

$$T = \exp(-\mu_{sca}L), \quad (62)$$

where μ_{sca} is called the scattering coefficient. The inverse of the scattering coefficient is the mean free path of the ray in the material.

3.3. Mie scattering

The scattering loss can be measured by the loss of energy in the light beam as it passes through the medium. In absorption, the light energy is converted into the internal energy of the medium, and in scattering, the light energy is reradiated in other directions. The scattering of light depends on the size of the particle that caused the scattering and, in general, scattering depends on the wavelength of light; for example, red light is scattered the least, while violet is scattered the most.

Scattering of light by particles suspended in a medium can be differentiated into different types: Mie scattering is the straightforward application of Maxwell's equations into an isotropic, homogeneous, dielectric sphere (non absorbing or absorbing). Mie scattering is applicable to spheres of all sizes, refractive indices and for radiation at all wavelengths. Rayleigh scattering is the Rayleigh limit of Mie scattering by particles much smaller than the wavelength of incident photons, spherical or dielectric. It is also well known that the geometrical optics approximation (ray optics) is correct for large particles at a large phase shift [29, 30, 31, 32].

Goniometer calibration (chapter 6) was done by using the Mie scattering theory and, therefore, the theory was discussed in the following detail.

The classical solution for the electromagnetic fields, scattered from an electromagnetic plane wave by a sphere of arbitrary size relative to the wavelength, is commonly referred to as Mie

theory. The optical properties are defined through Mie theory with the following input parameters:

- (a) the complex refractive index, $m=n+ik$, of a material relative to the surrounding medium
- (b) the dimensionless size parameter

$$x = \frac{2\pi r}{\lambda}, \quad (63)$$

where λ is the wavelength of incident electromagnetic radiation, and r is the particle radius.

In the following, a brief overview of the scattering process and different quantities, which can be written with Mie, is given in [30].

In unpolarised light, there is no preferred direction: the waves come in with electric and magnetic field vectors in random directions. In polarised light, the property of a certain type of waves describes the orientation of their oscillations.

The intensity of scattered light depends on the form and size of the scattering particle. The intensity and state of polarisation of the scattered light depends on the intensity and state of polarisation of the incident light, given by the Stokes vectors and Müller matrix, and matrix equation [29, 30, 31]:

$$\{I, Q, U, V\} = \frac{1}{k^2 r^2} \begin{bmatrix} S_{11}(\theta) & S_{12}(\theta) & S_{13}(\theta) & S_{14}(\theta) \\ S_{21}(\theta) & S_{22}(\theta) & S_{23}(\theta) & S_{24}(\theta) \\ S_{31}(\theta) & S_{32}(\theta) & S_{33}(\theta) & S_{34}(\theta) \\ S_{41}(\theta) & S_{42}(\theta) & S_{43}(\theta) & S_{44}(\theta) \end{bmatrix} \{I_0, Q_0, U_0, V_0\}, \quad (64)$$

where I, Q, U and V are the Stokes parameters of scattered light, and I_0, Q_0, U_0 , and V_0 are the corresponding parameters of incident light [29]. The S_{ij} (with $i, j=1,2,3,4$) are the elements of the Müller matrix that characterises the optical properties of the scattering.

The scattering of the radiation, by spherical particles, is described by [29, 30]

$$\hat{S}(\theta) = \begin{bmatrix} S_{11}(\theta) & S_{12}(\theta) & 0 & 0 \\ S_{12}(\theta) & S_{11}(\theta) & 0 & 0 \\ 0 & 0 & S_{33}(\theta) & S_{34}(\theta) \\ 0 & 0 & -S_{33}(\theta) & S_{34}(\theta) \end{bmatrix}, \quad (65)$$

Here, θ is the angle between the direction of the incident and scattering radiation (scattering angle), and the element of the scattering matrix can be written as below [29, 30]:

$$S_{11} = \frac{1}{2}[|S_2(\theta)|^2 + |S_1(\theta)|^2], \quad (66)$$

$$S_{12} = \frac{1}{2}[|S_2(\theta)|^2 - |S_1(\theta)|^2], \quad (67)$$

$$S_{33} = \frac{1}{2}[S_2^*(\theta)S_1(\theta) + S_2(\theta)S_1^*(\theta)], \quad (68)$$

$$S_{34} = \frac{1}{2}[S_1(\theta)S_2^*(\theta) - S_2(\theta)S_1^*(\theta)], \quad (69)$$

The amplitude function can be calculated as per the following:

$$S_1(\theta) = \sum_{n=1}^{\infty} \left(\frac{2n+1}{n(n+1)} \right) [a_n \pi_n(\theta) + b_n \tau_n(\theta)], \quad (70)$$

and

$$S_2(\theta) = \sum_{n=1}^{\infty} \left(\frac{2n+1}{n(n+1)} \right) [a_n \tau_n(\theta) + b_n \pi_n(\theta)], \quad (71)$$

The complex scattering (Mie) coefficients, a_n and b_n , depends on the size parameter, x , and the complex refractive index, m , of the material.

The angular function π_n , τ_n are dependent on $\cos\theta$, and can be found as below:

$$\pi_n(\theta) = \frac{2n-1}{n-1} \cos\theta \pi_{n-1}(\theta) - \frac{n}{n-1} \pi_{n-2}(\theta), \quad (72)$$

and

$$\tau_n(\theta) = n \cos\theta \pi_n(\theta) - (n+1) \pi_{n-1}(\theta), \quad (73)$$

The initial values are:

$$\pi_0(\theta) = 0 \text{ and } \pi_1(\theta) = 1$$

The value of a_n and b_n are usually transformed to a form convenient for calculations.

$$a_n = \frac{\psi_n'(mx)\psi_n(x) - m\psi_n(mx)\psi_n'(x)}{\psi_n'(mx)\xi_n(x) - m\psi_n(mx)\xi_n'(x)}, \quad (74)$$

$$b_n = \frac{m\psi_n(x)\psi_n'(mx) - \psi_n(mx)\psi_n'(x)}{m\xi_n(x)\psi_n'(mx) - \psi_n(mx)\xi_n'(x)}, \quad (75)$$

By replacing the Riccati-Bessel [30] functions, $\psi_n(x)$ and $\xi_n(x)$, and their first derivatives $\psi_n'(k)$ and $\xi_n'(x)$ by the spherical Bessel function, the first and second kind, $J_{n+\frac{1}{2}}(x)$ and $Y_{n+\frac{1}{2}}(x)$

:

$$a_n = \frac{[A_n/m + \frac{n}{x}]J_{n+\frac{1}{2}}(x) - J_{n-\frac{1}{2}}(x)}{[A_n/m + \frac{n}{x}]J_{n+\frac{1}{2}}(x) - J_{n-\frac{1}{2}}(x) + i[A_n/m + \frac{n}{x}]Y_{n+\frac{1}{2}}(x) - Y_{n-\frac{1}{2}}(x)}, \quad (76)$$

$$b_n = \frac{[mA_n + \frac{n}{x}]J_{n+\frac{1}{2}}(x) - J_{n-\frac{1}{2}}(x)}{[mA_n + \frac{n}{x}]J_{n+\frac{1}{2}}(x) - J_{n-\frac{1}{2}}(x) + i[mA_n + \frac{n}{x}]Y_{n+\frac{1}{2}}(x) - Y_{n-\frac{1}{2}}(x)}, \quad (77)$$

$$A_n \equiv \frac{\psi_n'(nx)}{\psi_n'(mx)} = \frac{-n}{mx} + \frac{J_{n-\frac{1}{2}}(x)}{J_{n+\frac{1}{2}}(x)}, \quad (78)$$

If $x \leq 5000$ value of $(A_n=0)$ is chosen on the recommendation of Loskutove, according to Voschinnikov [30], the calculation of the Bessel function of a real argument is based on the upward recursion for the function of the second kind, $Y_{n+\frac{1}{2}}(x)$, which is known to be stable. This

is given by the relation:

$$Y_{n+\frac{5}{2}}(x) = \frac{2n+1}{x}Y_{n+\frac{3}{2}}(x) - Y_{n+\frac{1}{2}}(x), \quad (79)$$

with initial values

$$Y_{\frac{1}{2}}(x) = -\sqrt{\frac{2}{\pi x}} \cos x, \quad (80)$$

$$Y_{\frac{3}{2}}(x) = \sqrt{\frac{2}{\pi x}} \left(\frac{-\cos x}{x} - \sin x \right), \quad (81)$$

The Bessel function of the first kind

$$J_{n+\frac{1}{2}}(x) \quad n \geq 1$$

is determined by:

$$J_{n+\frac{1}{2}}(x) = \left[\frac{2}{\pi x} + Y_{n+\frac{1}{2}}(x) J_{n-1}(x) \right] / Y_{n-\frac{1}{2}}(x), \quad (82)$$

$$J_{\frac{1}{2}}(x) = \sqrt{\frac{2}{\pi x}} \sin x, \quad (83)$$

The extinction, scattering, and back scattering efficiency factors (η_{ext} , η_{sca} , η_{bk}) are written by [30]

$$\eta_{\text{ext}} = \frac{2}{x^2} \sum_{n=1}^{\infty} (2n+1) \operatorname{Re}\{a_n + b_n\}, \quad (84)$$

$$\eta_{\text{sca}} = \frac{2}{x^2} \sum_{n=1}^{\infty} (2n+1) (|a_n|^2 + |b_n|^2), \quad (85)$$

$$\eta_{\text{bk}} = \frac{1}{x^2} \left| \sum_{n=1}^{\infty} (2n+1) (-1)^n (a_n - b_n) \right|^2, \quad (86)$$

The Mie scattering cross section for $A = \pi r^2$ is

$$C_{\text{sca}} = \pi r^2 \eta_{\text{sca}}, \quad (87)$$

and, therefore, the Mie scattering coefficient is

$$\mu_{sca} = \rho_a \pi r^2 \eta_{sca}, \quad (88)$$

where ρ_a is the particles per unit of volume.

In multiple scattering media, the value of the particle density is:

$$\rho_a = \frac{3V}{4\pi r^3}, \quad (89)$$

where V is the volume fraction and r is the particle radius.

The value of the Mie phase function scattering can be found as [29]:

$$p(\theta) = \frac{(|S_1|^2 + |S_2|^2)}{(\pi r^2 \eta_{sca})}, \quad (90)$$

3.4. Scattering in particles that are very large compared to the wavelength

For large particles, geometrical optics approximation (GOA) of light scattering is considered a good method of avoiding the Mie coefficient calculations, and studies on the GOA of light scattering by large particles have been of interest to many researchers during the past several decades [31, 32]. For a particle with a size of 20 (or more) times the incident wavelength, it is possible to mark off the difference between the rays reflected or refracted *on* the particle, and the rays diffracted *along* the particle. Also, it is possible to mark off the difference between the rays hitting various parts of the particle's surface.

In experiment it is possible to place a screen in the incident beam light with a hole in a position such that a particular part of the particle is exposed to this light. The rays hitting the particle and passing along it give two distinct phenomena:

- 1) Reflection and refraction. Rays hitting the particle's surface are partially reflected and partially refracted. Refracted light may emerge after another refraction, possibly after several internal reflections. The light so emerging, and the light directly reflected from the outer surface, both contribute to the total scattering of the particle. The energy that does not emerge is lost by absorption inside the particle. The amounts of energy scattered or absorbed, and the angular

distribution and polarisation of the scattered light, depends on the form and composition of the particle, and on the condition of its surface.

2) Diffraction. The rays passing along the particle from a plane wave front, in the form and size of the geometrical shadow of the particle, are missing. This incomplete wave front gives rise by Huygen's principle [31] to a certain angular distribution of intensity at a very large distance. Although the term 'diffraction' is often used for the entire scattering process, it can be reserved for the Fraunhofer diffraction [31, 32]. The intensity distribution in this diffraction pattern depends on the form and size of the particle, but is independent of its composition, or the nature of its surface. The diffracted light has the same polarisation as the incident light, and its pattern is independent of the polarisation.

The two parts just described are dependent on the angular distribution of the scattered light, and assuming the size of the particle is fixed, and the wavelength gradually decreasing, the scattering pattern due to reflection and refraction follows from rays that can be more and more sharply localised, and will, eventually, follow the theory of geometrical optics [32]. At the same time the diffraction pattern will be more and more compressed, forming narrow, but very intense, lobes around the forward direction, $\theta=0$. In fact the separation is strictly possible, only if the particle is very large. The entire pattern in this limit consists of two parts: a very narrow and very intense central lobe due to diffraction (2), and, less intense radiation in all directions, dependent on the optical properties of the particle (1).

In this work we assume that the diffraction pattern is much more intense, and much narrower, than the reflection and refraction pattern.

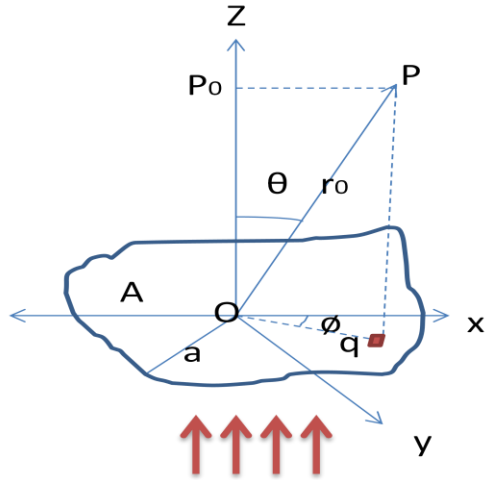


Figure 14: Diffraction by a large body with geometrical shadow area A.

Figure 14 shows a large particle with a geometrical shadow area of A, and therefore, the diffracted light is separable from the remaining scattering pattern as it is confined to very small angles, θ .

Here, let the Z-axis be in the direction of propagation of the incident light, and the origin O, be in the shadow area of the wave front. The disturbance may be sought at a distance point, P, which has the polar coordinates, (r, θ, ϕ) .

The distance from P to a point $(x, y, 0)$ of the shadow area is

$$r = r_0 - (x \cos \phi + y \sin \phi) \sin \theta, \quad (91)$$

The disturbance at P, caused by the diffraction about the particle, is

$$u_p = u_0 e^{-ikz} - \frac{i u_0}{r \lambda} e^{-ikr_0} \iint_A e^{-ik(x \cos \phi + y \sin \phi) \sin \theta} dx dy, \quad (92)$$

Here, u_0 is the disturbance, in the original wave, on the plane wave front through O.

In this formula, the double integral appears by:

$$A.D(\theta, \phi)$$

where $A = \iint dx dy$ is the geometric area of the shadow and

$$D(\theta, \phi) = \frac{1}{A} \iint e^{-ik(x \cos \phi + y \sin \phi) \sin \theta} dx dy, \quad (93)$$

$D(\theta, \phi)$ is 1 for $\theta=0$. This function essentially describes the amplitude of the diffraction pattern.

According to Van de Hulst 1957 [31], the approximations to which this diffraction theory holds are that $S_3(\theta, \theta)$ and $S_4(\theta, \theta)$ are zero, and $S_1(\theta, \theta)$ and $S_2(\theta, \theta)$ are equal, and given by:

$$S(\theta, \phi) = \frac{k}{\lambda} AD(\theta, \phi) = \frac{k^2}{2\pi} AD(\theta, \phi), \quad (94)$$

If the particle has the circular shadow (Fraunhofer diffraction at circular aperture) of radius, a , and area of $A = \pi a^2$, the function $D(\theta, \theta)$ is found by direct integration, and has the form

$$D(\theta, \phi) = \frac{2J_1(x \sin \theta)}{x \sin \theta}, \quad (95)$$

where $x = ka$, J_1 is the Bessel function of the first order, and the value of the $S_1(\theta, \theta)$ and $S_2(\theta, \theta)$ are:

$$S_1(\theta) = S_2(\theta) = x^2 \frac{J_1(x \sin \theta)}{x \sin \theta}, \quad (96)$$

The corresponding angular distribution of the radiation intensity is given by [31, 32, 33]

$$I'(\theta) = \frac{I(\theta)}{I(0)} = \left[\frac{2J_1(ka \sin \theta)}{ka \sin \theta} \right]^2, \quad (97)$$

where $I(\theta)$ is the irradiance at point P , and $I(0)$ is the irradiance at P_0 .

Further, the value of the intensity of the scattered light to the incident is:

$$I = \frac{|S_1(\theta)|^2}{k^2 r^2} I_0, \quad (98)$$

for the perpendicular polarisation:

$$I = \frac{|S_2(\theta)|^2}{k^2 r^2} I_0, \quad (99)$$

for the parallel polarisation; and for the incident natural light, is:

$$I = \frac{1/2(|S_1(\theta)|^2 + |S_2(\theta)|^2)}{k^2 r^2} I_0, \quad (100)$$

3.5. Bi-directional surface distribution function

The Bi-directional surface distribution function (BSDF) is a generalisation of the BRDF (Bi-directional reflectance distribution function) and the BTDF (Bi-directional transmittance distribution function). The BRDF or BTDF are the ratio between the outgoing light power (reflected or transmitted) and the incident light energy power for a given pair of angles (figure 15). Therefore, BRDF or BTDF are the ratios of the scattered radiance, $L_s(\lambda, \Phi, \theta)$, per unit of incident irradiance, $I_0(\lambda)$. The BRDF has units of $1/sr$ (inverse steradian) and is given by: [34, 35, 36]

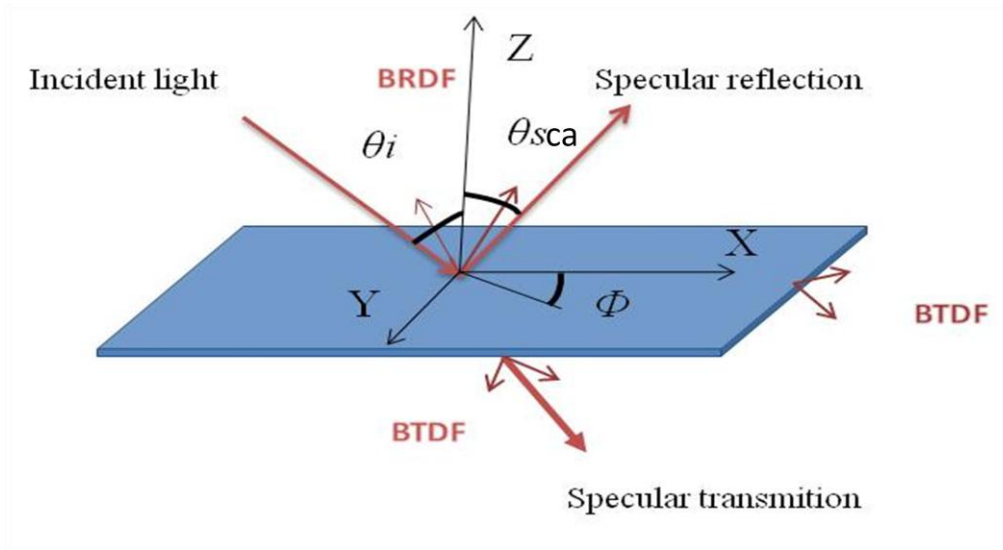


Figure 15: BRDF and BTDF geometry in a glass substrate.

$$BTDF(1/sr) = \frac{L_s(\lambda, \Phi, \theta)}{I_0(\lambda)} = \frac{\text{power of scattered light} / \Omega}{\text{power of incident light} * \cos \theta_{sca}}, \quad (101)$$

where Ω is the solid angle.

The TIS (total integrated scattering) can also be defined as an integral of the BSDF (Bi-directional surface distribution function) over all angles (the scattering angle, θ_{sca} , and the azimuthal angle, ϕ). TIS measurements are made by integrating the BSDF over a portion of the sphere surrounding the scatter source. This is usually done with instrumentation that gathers (integrates) the scattered light signal. The TIS can also sometimes be calculated from the BSDF

$$TIS = \int_0^{2\pi} d\phi \int_0^{\pi/2} BSDF(\theta_i, \theta_{sca}, \phi, \phi) (\sin \theta_{sca} \cos \theta_{sca}) d\theta, \quad (102)$$

3.6. Radiation exchange within a spherical enclosure

The integrating sphere is a device for measuring optical radiation, and the function of an integrating sphere is to spatially integrate radiant flux.

The theory of the integrating sphere originates in the principles of radiation exchange within an enclosure of diffuse surfaces, and although the general theory can be complex, the sphere is a simple solution to understand. Consider the radiation exchange between two differential elements of diffuse surfaces (figure 16), the fraction of energy that arrives at dA_2 from dA_1 is known as the exchange factor, dF_{d1-d2} . It is given by [37]:

$$dF_{d1-d2} = \frac{\cos \theta_1 \cos \theta_2}{\pi S^2} dA_2, \quad (103)$$

where θ_1 and θ_2 are measured from the surface normal.

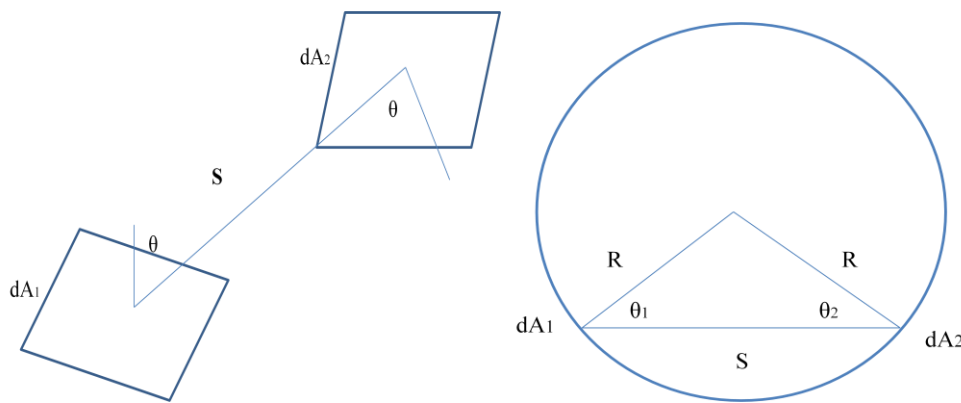


Figure 16: Radiation exchange within an enclosure of diffuse surfaces.

Consider two differential elements, dA_1 and dA_2 , inside a diffuse surface sphere. Since the distance, $S = 2R\cos\theta_1 = 2R\cos\theta_2$,

$$dF_{d_1-d_2} = \frac{dA_2}{4\pi R^2}, \quad (104)$$

The result is significant since it is independent of the viewing angle, and the distance between the areas. Therefore, the fraction of flux received by dA_2 is the same for any radiating point on the sphere surface. If the infinitesimal area, dA_1 , instead exchanges radiation with a finite area A_2 , then:

$$dF_{d_1-d_2} = \frac{1}{4\pi R^2} \int_{A_2} dA_2 = \frac{A_2}{4\pi R^2}, \quad (105)$$

Since this result is also independent of dA_1 :

$$F_{d_1-d_2} = \frac{A_2}{4\pi R^2} = \frac{A_2}{A_S}, \quad (106)$$

where A_S is the surface area of the entire sphere. Therefore, the fraction of radiant flux received by A_2 is the fractional surface area it consumes within the sphere.

Conclusion

Different scattering theory, scattering efficiency and far-field Fraunhofer diffraction theory for circular aperture were discussed in detail, these theories used in the following chapters.

Radiation exchange within a spherical enclosure, the main principle in integrating sphere measurement, was explained, and used for transmittance and reflection measurements in double beam mode (chapter 6).

Chapter 4

Fluorescent Solar Collectors

Introduction

A fluorescent solar collector (FSC) is a waveguide device that can concentrate both diffuse and direct sunlight onto a solar cell, which is then converted to electricity. The structure of the device consists of a flat fluorescent collector plate, a solar cell, and optical mirrors. A solar cell is coupled to one edge of the FSC with silver mirrors attached to the remaining edges. The electrical output of the device depends strongly on the photon flux which is absorbed, emitted, and trapped inside the FSC plate. For this reason, it is important to study the photon transport losses inside the collector [38-51].

The intention of this chapter is to investigate an overview of fluorescent solar collectors, the Weber and Lambe model, and self absorption, the effect of the non-ideal coupling between the solar cell and the collector.

4.1. Overview of a fluorescent solar collector

In a typical fluorescent solar collector (FSC), the luminescent light is trapped by the total internal reflection (TIR) and guided onto a solar cell at the edge of the plate. One objective of the collector's design is to reduce the size of the solar cell with respect to the area that collects light. Unlike their geometric counterparts, fluorescent collectors can accept light from a wide angle of incidence, and are thus able to make use of the diffuse light [40]. The photon flux at the edge of an idealised FSC is the product of the absorbed solar flux, the fraction of the trapped luminescence, and the geometric ratio of the area of the face directly exposed to sunlight, A_f , divided by the area, A_e , of the edge covered by the solar cell. The geometric gain, G_{geom} , of the FSC is then given by:

$$G_{geom} = \frac{A_f}{A_e}, \quad (107)$$

Weber and Lambe (1976) initially suggested the concept of luminescence trapping for solar concentrators, which they named the luminescent greenhouse collector. The term, ‘greenhouse’, was suggested because of the similarity between the FSC’s visible sunlight absorption, and its emission in the high wavelength. Since the luminescent material selectively absorbs radiation at a certain energy wavelength, a number of different luminescent materials, each in separate FSC plates, can separate light into its spectral components. Goetzberger, Greubel and Baur, in Germany, proposed the multi-layered FSC structure to increase the overall efficiency [52]. This technique splits the concentrated sunlight using a dichroic mirror, so that a higher energy flux can be converted by gallium arsenide cells, and a lower energy flux can be converted by silicon cells.

Organic laser dyes tend to be generated by photons in sunlight, these attached to plastic or glass substrates. The rectangle FSC used in this work, and the geometric gain of the plate, must focus the output light onto the edge.

4.2. Weber and Lambe model for luminescent collector for solar radiation

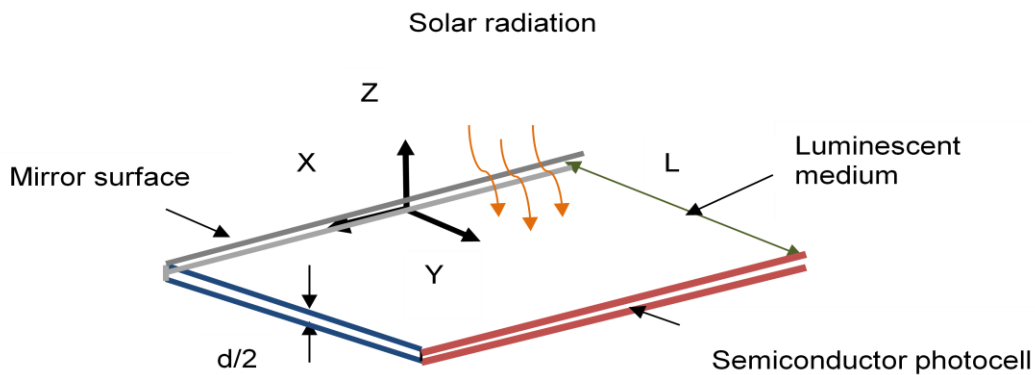


Figure 17: Schematic of a luminescent solar collector. The solar radiation is normally incident upon the collector surface, which is in the xy plane. A perfect reflecting mirror is placed in $y=0$ and the photocell is at $y=L$.

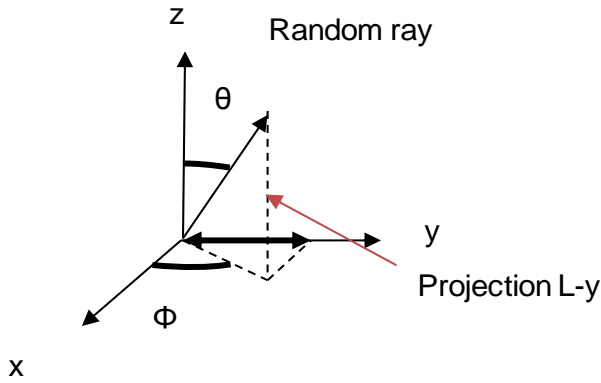
This model assumes a uniform distribution of excited molecules throughout the collector, a perfectly flat specular reflection surface, no scattering of light inside the collector, and no absorption of light, except by the dye as shown in figure 17. The edge assumed at $y = 0$ has a reflectance of one, and the structure has an infinite length in the x direction. The structure can be terminated with a perfect reflector in the xz direction, and each volume element emits light

uniformly into 4π sec. The collection efficiency, or Q_c , is defined as the amount of light collected at the edge, per unit of length at $y = L$, divided by the amount emitted per unit length, and is given by [41]:

$$Q_c = \frac{1}{2\pi L} \int_0^L dy \int_0^{\pi/2} d\phi \int_{\theta_c}^{\pi/2} \sin\theta d\theta \{ \exp[-\alpha_e(L-y)/(\sin\theta\sin\phi)] + \exp[-\alpha_e(L+y)/(\sin\theta\sin\phi)] \} [2 - |r_s(\theta,\phi)|^2 - |r_p(\theta,\phi)|^2], \quad (108)$$

where θ and ϕ are the usual spherical, polar angles defining the direction of emission, θ_c is the critical angle for total internal reflection, α_e is the attenuation coefficient at emission wavelength, and $r_{s,p}(\theta,\phi)$ is the amplitude Fresnel reflection coefficient for s , or p polarisation, at $y=L$.

In equation 108, the value of $(L \pm y)$ is the path length of a random ray within the collector, and can be estimated using the projection onto the y -axis.



$$(L \pm y) = X \sin(\theta) \sin(\phi), \quad (109)$$

$$X = \frac{(L - y)}{\sin(\theta) \sin(\phi)}, \quad (110)$$

$$X = \frac{(L + y)}{\sin(\theta) \sin(\phi)}, \quad (111)$$

Equation 110 refers to the path length of a light ray emitted towards the cell, while equation 111 refers to the path length of a random ray towards the mirror.

The exponentials in equation 108 represent the Beer-Lambert law, used to estimate the absorption over the path length of a random ray within the collector, over a distance ($L \pm y$). By using the Batchelder photon flux diagram [43, 44], equation 108 is related to the reabsorption probability, and is given by:

$$(1 - R) = \frac{Q_c}{(1 - P)}, \quad (112)$$

where P is $P = 1 - \cos \theta_c$

4.2.1. Modified Weber and Lambe model for non-ideal coupling

The practical efficiencies are significantly lower due to several loss mechanisms, and a modified model, based on Weber and Lambe's theory which will take the non-ideal coupling between the collector and the solar cell mounted at the edge, is explained below.

The structure of the collector considered in this model has three mirror covered edges, and one edge with the solar cell as shown in figure 18. The bottom surface of the collector is not coupled with a mirror, while an air gap is assumed to exist between the collector and the solar cell. This is the real situation when the edge fluorescence is detected by an optical fibre in the experiments. The reflective index of the matrix is higher than that of air (PMMA, $n \approx 1.5$, air, $n = 1$), and hence light can be totally internal reflected. The escape cones (figure 18, cone 1 and cone 3) are located at the edge, and only photons emitted in these two cones can be collected by the solar cell, if there is not any reabsorption. In this model, the photons emitted in the other two cones (figure 18, Cones 2 and 4), are considered as losses.

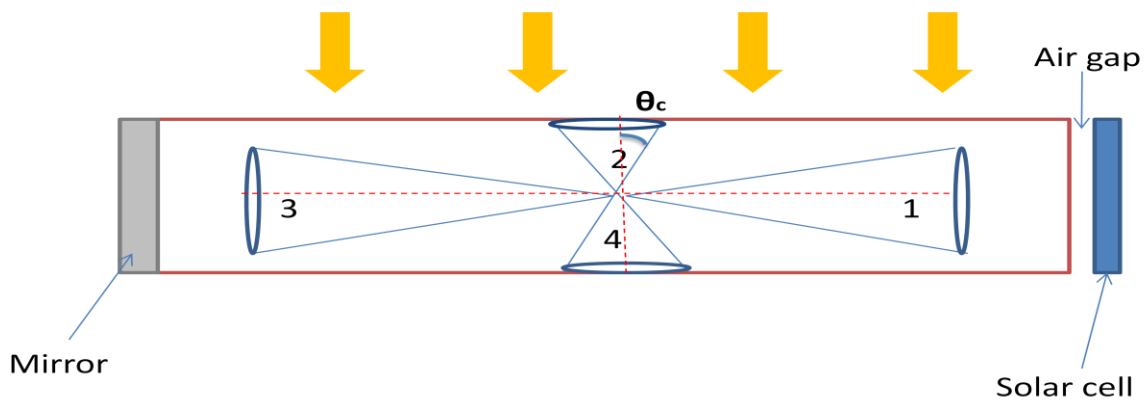


Figure 18: Collector structure and escape cones. θ_c is the critical angle for total internal reflection.

The fluorescence photon collection efficiency of the collector is defined to be the number of photons collected by the solar cell divided by the number of photons absorbed by the dye inside the collector. Assuming the fluorescent photons emitted are isotropic, and using the Beer-Lamber Law, the spectral reabsorption probabilities, $r(\lambda)$, are given by[53]:

$$\{1-r(\lambda)\}_{MWL} = \frac{1}{4\pi(1-P)} \int_0^\pi d\phi \int_{\theta_c}^{\pi-\theta_c} \frac{\sin\theta \sin\phi}{\alpha_e(\lambda)L} \{1-\exp(\frac{-2\alpha_e(\lambda)L}{\sin\theta \sin\phi})\} \sin\theta d\theta, \quad (113)$$

$$\{1-r(\lambda)\}_{MWL} = \frac{1}{2P\alpha_e L} \int_0^{\theta_c} [1-\exp(-2\alpha_e L/\cos(\theta))] \cos(\theta) \sin(\theta) d\theta, \quad (114)$$

where $\{1-r(\lambda)\}_{WL}$ is the spectral reabsorption probability for Weber and Lambe's theory, $\{1-r(\lambda)\}_{MWL}$ is for the Modified Weber and Lambe's theory, and $P=1-\cos\theta_c$ is the fraction of photons emitted inside cone 1 and cone 3, or cone 2 and cone 4. Figure 19, meanwhile, compares the numerical calculation results of the two spectral reabsorption probabilities.

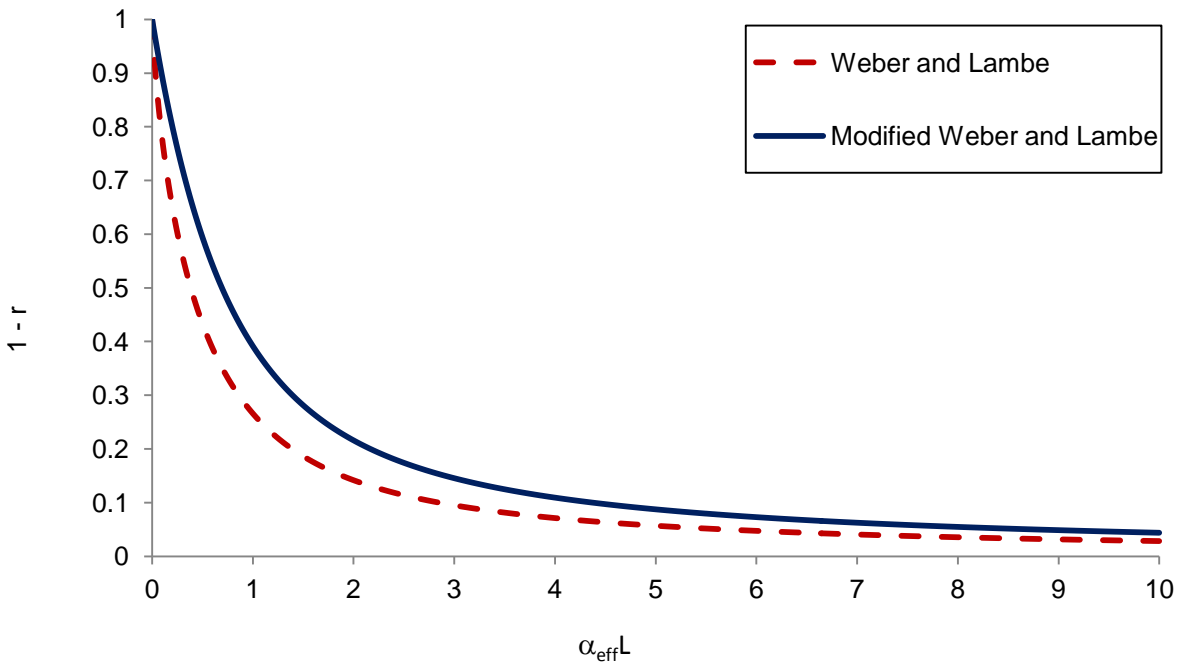


Figure 19: Comparison of reabsorption probabilities calculated from Weber and Lambe's theory and the Modified Weber and Lambe's theory.

A similar feedback loop occurs during self absorption of trapped light, where the probability that a trapped photon will be self absorbed, before it reaches the FSC-cell interface, is R [50].

4.4. Solar absorption

The solar flux per wavelength, denoted by $L = (\bar{\nu})$, and the total flux by L , is:
$$L = \int_0^{\infty} I(\bar{\nu}) d\bar{\nu}$$

This could be extended to include angular variation in spectrum and intensity, as is explained in chapter 1.

The reflection coefficient R_{ref} for vertical incidence on an uncoated plate with an index of reflection n is [44]:
$$\frac{(n-1)^2}{(n+1)^2}$$

The absorption path length for incidence on a plate, with an angle, θ , is:

$$l_s = \frac{D}{\sqrt{1 - \sin^2(\theta)/n^2}}, \quad (115)$$

where D is the thickness of the plate. If a back mirror is used, the length is double the expression. If the matrix material has an absorption coefficient, $\alpha(\bar{\nu})$, the attenuation of light of wave number, ν , over a distance, l_s , is given by $10^{-l_s \alpha(\bar{\nu})}$. The reflection of the usual matrix material is quite low, so the reflection loss tends to be low also. Further, as the angle of incidence increases, the apparent area of the plate decreases, as the cosine of the angle of incidence, and the reflection coefficient, also increases [50]. The probability, P , that luminescence will escape out of the critical cones, is the sum of the solid angles of the upper and lower critical cones divided by the solid angle of emission.

$$P = 1 - \cos \theta_c, \quad (116)$$

4.5. Self absorption effect R, \bar{R}

A phenomenon of an overlap between the absorption and emission spectra, for most of the dyes, or ions, to be used in FSC, is called self-absorption. The observed overlap allows a fluorescent photon to be reabsorbed by another dye molecule of the same type, such a reabsorption being

termed self-absorption, and actually has a dominant effect over the long path lengths travelled by light trapped in the FSC. The calculation of this self-absorption process is via a collection efficiency, Q_c , and is a generalisation of the collection efficiency used by Weber and Lambe. Q_c is defined as a fraction of the absorbed solar photons that succeed in being transported to the FSC-PVC interface.

In this case the solar photons absorbed by the dye, and the fraction, η , will be luminescence, and of those, the fraction $(1-P)$ will be trapped via total internal reflection and transported to the FSC-PVC interface, so that in this idealised case, Q_c , when we ignore the self, and matrix, absorptions, is given simply by:

$$Q_{idealized} = (1-P)\eta, \quad (117)$$

If the absorption and emission bands are now overlapping, the dye is capable of absorbing its own luminescence and the FSC acts like a filter that attenuates the luminescence, resulting in the absorption of solar photons. Thus in an FSC the light absorbed can then re-luminesce in an arbitrary direction. Most of this will again be trapped within the plate and generate a number of different generations of luminescence: the first generation is the luminescence that results from the initial absorption of the solar photons; the second generation is the luminescence resulting from the self absorption of the first generation photons; the third generation is the luminescence resulting from self absorption of the second generation photons; and so forth. So, the fluorescence was divided into various components Q_1 , Q_2 , Q_3 , etc, depending on how many times the photons had been absorbed. The fraction Q_1 , known as the first fluorescence, is given as:

$$Q_1 = \eta(2\pi L)^{-1} \int_0^{\infty} f(\bar{\nu}) d\bar{\nu} \int_0^L d\phi \int_{\alpha}^{\Pi/2} \sin(\theta) d\theta \{ \exp[-\alpha(\bar{\nu})(L-y)/\sin(\theta)\sin(\phi)] + \exp[-\alpha(\bar{\nu})(L+y)/\sin(\theta)\sin(\phi)] \}, \quad (118)$$

This equation is similar to that given by Weber and Lambe in equation 108, except that we have defined Q_1 to include the dye's quantum efficiency, and the normalised fluorescent spectrum $\int_0^{\infty} f(\bar{\nu}) d\bar{\nu}$ included in this equation, but not included the Fresnel reflection that can take place at the luminescent solar collector's photovoltaic cell interface [50]. The fraction of fluorescence emitted from the higher generation introduces two parameters: R : the average probability that

luminescence outside the critical cones will be self absorbed over a path length, L , and, \bar{R} , the average probability that luminescence inside the critical cones will be self absorbed.

These parameters are related to the n^{th} order generation of fluorescence as follows:

$$Q(n) = (1-P)(1-R)[\bar{R}P + (1-P)R]^{n-1}\eta^n, \quad (119)$$

The total collection efficiency of the system which includes all components from higher generation emission is given by:

$$Q_{c,Bat} = Q_1 + Q_2 + Q_3 + \dots = \frac{\eta(1-R)(1-P)}{1-\eta[\bar{R}P + R(1-P)]} = \frac{Q_1}{1-\eta[\bar{R}P + R(1-P)]}, \quad (120)$$

4.6. Spectroscopic measurement of reabsorption losses

The first generation spectrum is obtained by the front fluorescent spectra of dye that is free from the reabsorption. When normalised to unit intensity, this spectrum will be denoted by $f_1(\lambda)$, with:

$$\tilde{f}_1(\lambda) = \int_0^{\infty} f_1(\lambda)d\lambda = 1, \quad (121)$$

The reabsorption loss is the spectral overlap between the absorption and fluorescence bands, this mechanism resulting in a distortion of the first generation fluorescence spectra, known as the red-shift effect [40].

Theoretically, the reabsorption loss, $r(\lambda)$, can be determined by comparing the first generation fluorescence spectra with the emission spectra measured at the edge of the collectors. It can be written as:

$$(1-r(\lambda)) = \frac{f_e(\lambda)}{\tilde{f}_1(\lambda)}, \quad (122)$$

where $f_e(\lambda)$ is the edge fluorescent spectrum.

In this study, the $\tilde{f}_1(\lambda)$ spectra was obtained through measuring of the fluorescence light emitted from the front surface of the low concentration sample. The low concentration sample means it

has a small amount of absorbing molecules, and therefore has less chance of re-absorbing the emitted light. Additionally, the front fluorescence detection provides the minimum level of reabsorption losses, the detected signal emitted from the sample with a very small optical path length.

Therefore the overall reabsorption probability, R , is:

$$R = \int_0^{\infty} r(\lambda) \tilde{f}_1(\lambda) d(\lambda), \quad (123)$$

Conclusion

The analytical models reviewed in this chapter demonstrate the fundamental limitation of re-absorption loss. It has been shown that the photon collection efficiency depends mainly on the probability of reabsorption. The photon balance is based on the Weber and Lambe, and Batchelder and Zewail, models, and has led to a simple experimental technique for the characterisation of the spectral reabsorption probability in a collector.

In accordance with the edge fluorescence detection approach in the experiments, an air gap is assumed to exist between the collector edge and the solar cell, and thus only photons emitted in the escape cones (cone 1 and 3, in figure 18) could be collected by the solar cell, or observed as edge fluorescence. This Modified Weber and Lambe's theory was used in the following results chapter, and could be used to analyse the spectrum of the photons emitted out of the collector edges.

Chapter 5

Fabrication and Characterisation of Fluorescent Solar Collectors

Introduction

Spin coating is a standard technique used for many applications, whereby relatively flat substrates or objects are coated with thin layers of material. A solution of different laser dyes and PMMA was spin coated on to glass to use in the fluorescence solar collector. The solution was to spin-off a substrate, leaving a subsequently uniform layer. This process involves depositing a small amount of a liquid resin onto the centre of a substrate, before spinning the substrate at high speed (typically around 4000 rpm). The final film thickness, and other properties, will depend on the nature of the resin (viscosity, drying rate, percentage of solids, surface tension, etc) and the parameters chosen for the spin process, while factors such as the final rotational speed, acceleration, and fume exhaust contribute to how the properties of the coated films are defined. The thickness of a thin film can be measured based on different methods.

This chapter is divided into three sections. The first section describes the different stages in spin coating a material. The second provides different methods for measuring the film thickness with different thickness limits- it is very important to find a method that does not depend on the optical, or electrical properties of the film material, but is also insensitive to the processing environment. In between these methods, the con-focal laser (CL) method, scanning electron microscopy (SEM), multiple interference techniques, and profilometry method, were employed for measuring the film thickness. The third section explains the details of the characterisation techniques.

5.1. Spin coating processing stages

5.1.1. Stage one

The first step is the deposition of the coating fluid on to the substrate. During this step, the material is spread on the substrate where the centrifugal force dominates the viscous force. A typical spin process consists of a dispensing step (in which the resin fluid is deposited onto the substrate surface), a high-speed spin step (to thin the fluid), and a drying step (to eliminate excess solvents from the resulting film). Two common methods of dispensing are: static dispense, and dynamic dispense. Static dispense is simply where a small droplet of fluid is deposited on, or near, the centre of the substrate. This can range from 1 to 10cc depending on the viscosity of the fluid, and the size of the substrate to be coated. A higher viscosity and/or larger substrates typically requires a larger amount, to ensure a full coverage of the substrate during the high speed spin step. Dynamic dispensing is the process of dispensing the fluid whilst the substrate is rotating at low speeds, as demonstrated in figure 21. A speed of about 500 rpm is commonly used during this step of the process, and serves to spread the fluid over the substrate, resulting in less wastage of the resin material, it not usually being necessary to deposit as much in order to wet the entire surface of the substrate. This is a particularly advantageous method, when the fluid or substrate itself has poor wetting qualities.

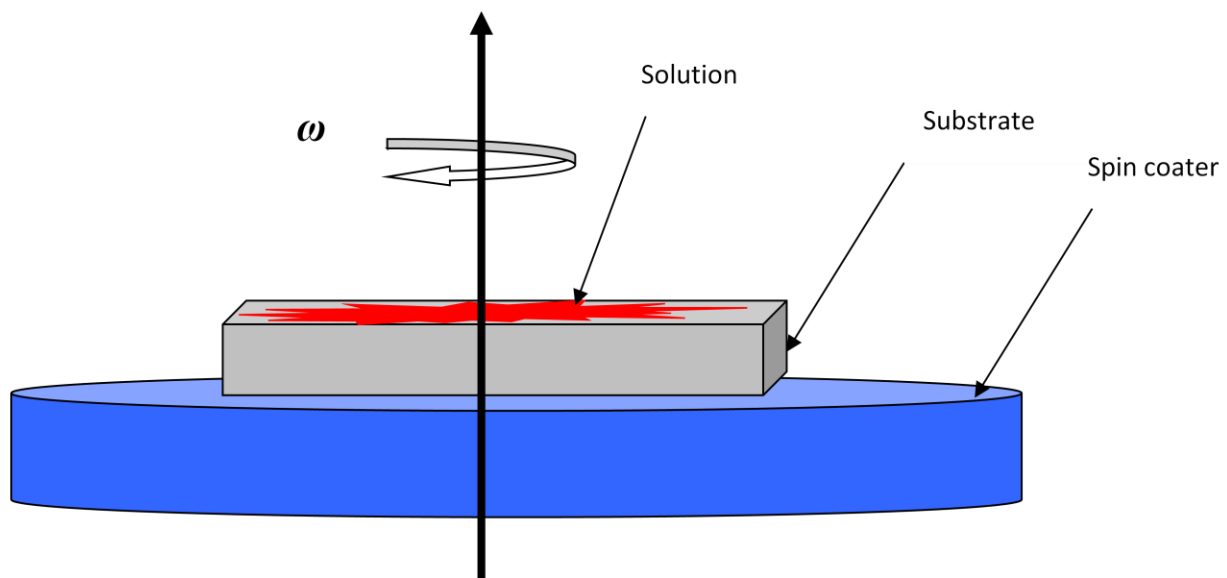


Figure 21: Stage one: dynamic dispense solution is spread on the substrate.

5.1.2. Stage two

The second stage is when the substrate is accelerated up to its final, desired rotation speed. This stage is usually characterised by fluid expulsion from the substrate, by the rotational motion. In this step, the thickness is determined by the programmed speed and time, as is shown in figure 22, and, in general, higher spin speeds and longer spin times create a thinner film. The spin coating process involves a large number of variables that tend to cancel or average out during the spin process, and it is best to allow sufficient time for this to occur.

A separate drying step is sometimes added following the high speed spin step, to further dry the film without substantially thinning it. This can be advantageous for thick films since long drying times may be necessary in order to increase the physical stability of the film prior to handling.

Film thickness is largely a balance between the force applied to shear the fluid resin towards the edge of the substrate, and the drying rate affecting the viscosity of the resin. As the resin dries, the viscosity increases until the radial force of the spin process can no longer appreciably move the resin over the surface. At this point, the film thickness will not decrease significantly with increased spin time.

The acceleration of the substrate towards the final spin speed can also affect the coated film properties. Since the resin begins to dry during the first part of the spin cycle, it is important to accurately control acceleration. In some processes, 50% of the solvents in the resin will be lost to evaporation in the first few seconds of the process.

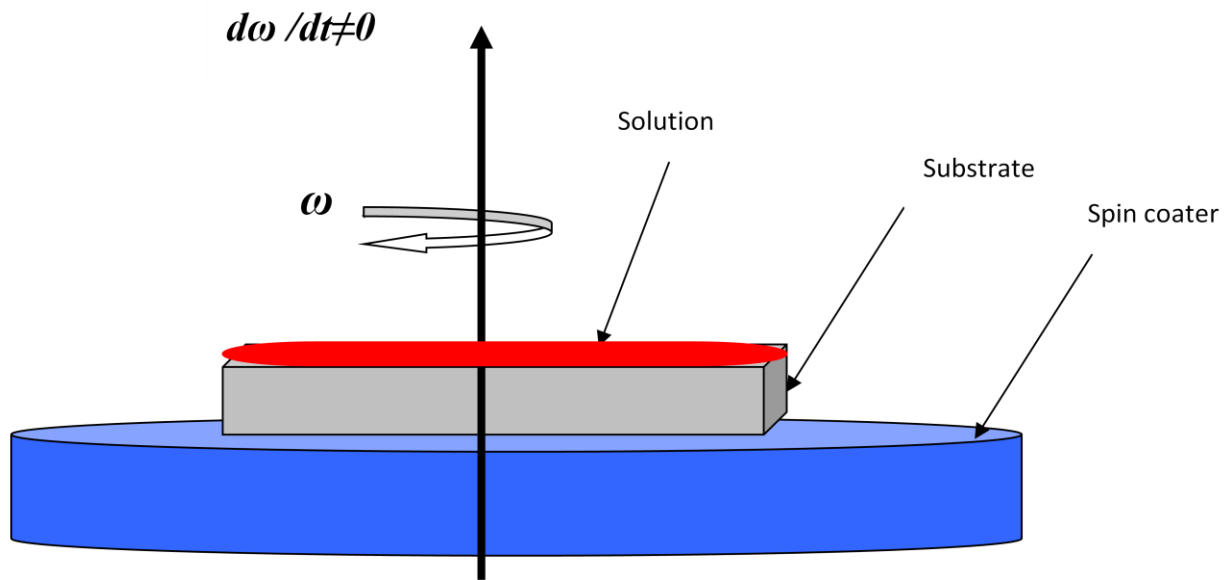


Figure 22: Stage two: the spin coater accelerates to its final speed and the solution is spun-off of the substrate.

5.1.3. Stage three

The viscous force starts to dominate the centrifugal force, a stage characterised by gradual fluid thinning through evaporation, until a film remains. The drying rate of the resin fluid during the spin process is defined by the nature of the fluid itself (volatility of the solvent systems used) as well as by the air surrounding the substrate during the spin process. The resin will dry depending on the ambient conditions around it. It is well known that factors, such as air temperature and humidity, play a large role in determining the coated film properties, and so it is also very important that the air flow, and associated turbulence above the substrate itself, is minimised, or at least held constant, during the spin process.

The slower rate of drying offers the advantage of increased film thickness with uniformity across the substrates. The fluid dries out as it moves toward the edge of the substrate during the spin process, leading to radial thickness non-uniformities, since the fluid viscosity changes with distance from the centre of the substrate. By slowing the rate of drying, it is possible for the viscosity to remain more constant across the substrate.

The drying rate, and hence the final film thickness, is also affected by ambient humidity, where variations of only a few percent in humidity can result in large changes in the film thickness. By

spinning in a closed bowl, the vapours of the solvents in the resin itself are retained in the bowl environment, tending to overshadow the affects of minor humidity variations. At the end of the spin process, when the lid is lifted to remove the substrate, solvent vapours are also released, as shown in figure 23.

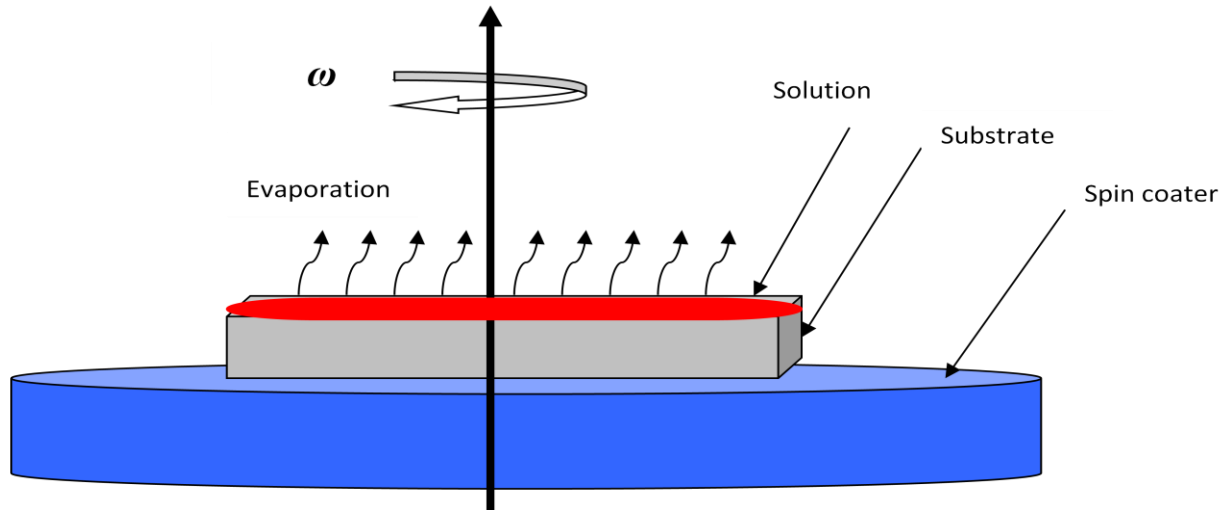
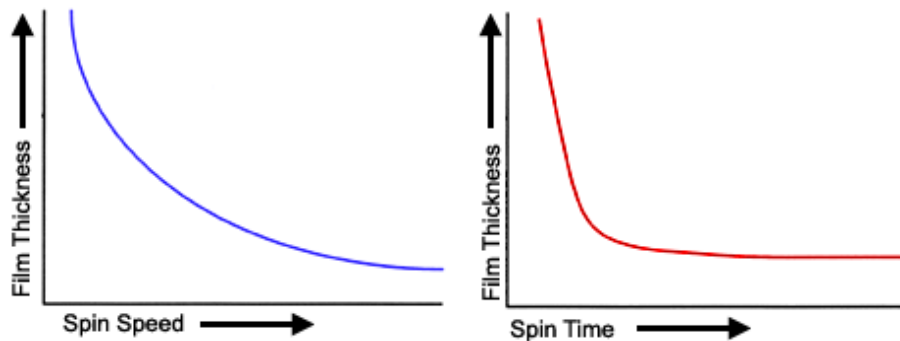


Figure 23: Stage three: excess solvent evaporates.

5.2. Process trend charts

Figure 24 represents general trends for the various process parameters. For most resin materials, the final film thickness will be inversely proportional to the spin speed and time. The final thickness will be also be somewhat proportional to the exhaust volume, although uniformity will suffer if the exhaust volume is too high, causing the film to dry non-uniformly during the spinning process



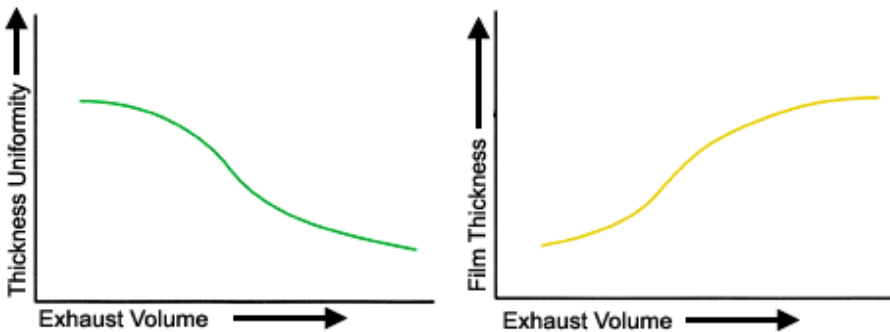


Figure 24: Effect of different parameters on the spin coating process [54].

5.3. Fluorescent material

The fluorescent materials used in this study were RhodamineB (RB) or Rhodamine 610, and Lumogen F305 Red dye (BASF, Ludwigshafen).

The RB was chosen because of its low cost and solubility in organic solvents [55, 56, 57].

The absorbance and fluorescence of RB, its chemical structure, and its important absorbance and fluorescence properties, are shown in figures 25 and 26. In ethanol, it exhibits an absorption peak at 542 nm, and a fluorescence peak at 565 nm.

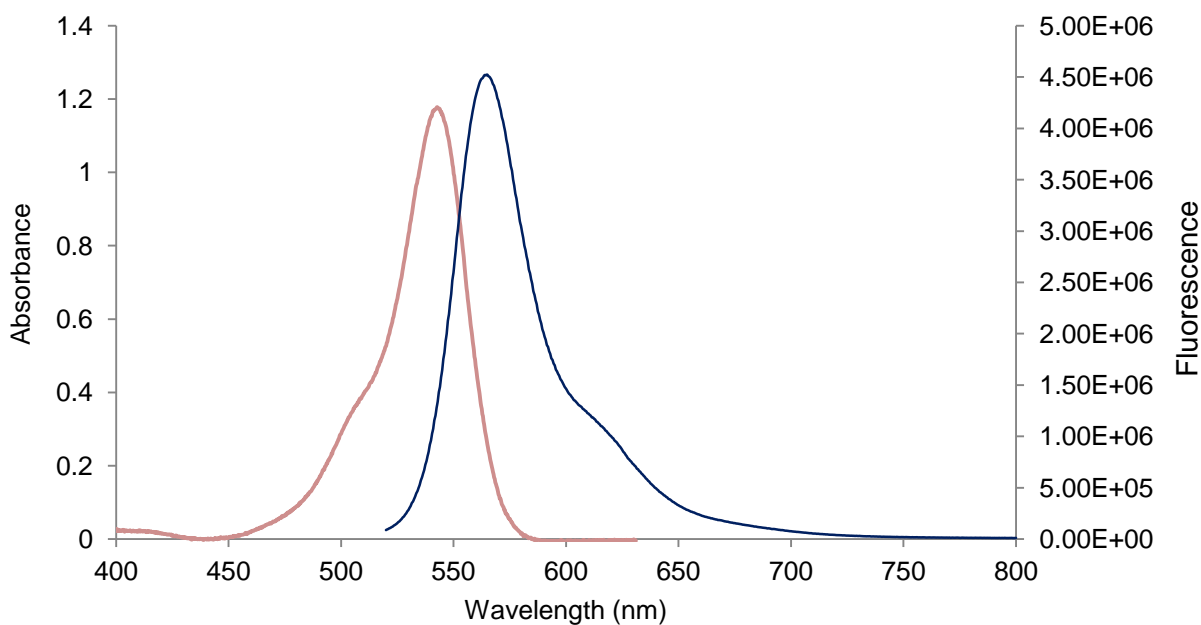
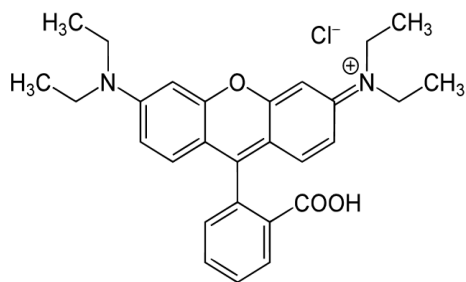


Figure 25: Absorbance and fluorescence of RB in ethanol from PhotochemCAD [55].



Maximum absorbance	542 nm
Maximum fluorescence	565 nm
Fluorescence quantum yield	0.49 in Ethanol
Molar absorption coefficient	$106000 \text{ L}^{-1}\text{Mol}^{-1}\text{cm}^{-1}$

Figure 26: The chemical structure of RB and its important absorbance and fluorescence properties, from PhotochemCAD [55].

Lumogen F Red 305 is a Perylene-based, red fluorescent dye produced by BASF. Absorbance and fluorescence, and its formula, are shown in figures 27 and 28.

These dyes seem to glow in black light, and can be excellently applied in the fluorescence solar collector.

The dye exhibits an absorption peak of 578 nm and an emission peak of 613 nm, in dichloromethane solution, and with its quantum yield of over 90%, this dye is suitable for fluorescent solar concentrators [58].

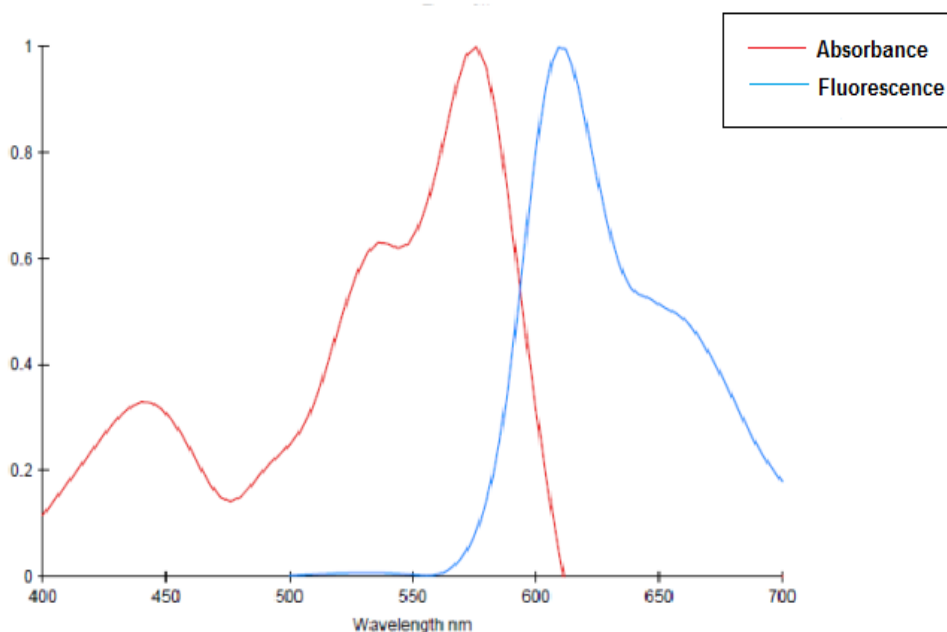
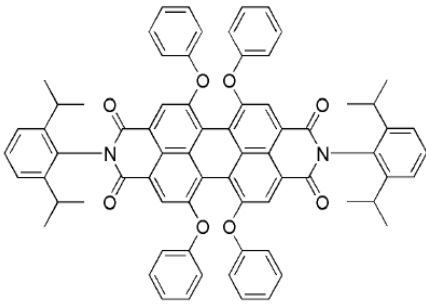


Figure 27: Absorbance and fluorescence of F Red305 in Dichloromethane (DCM) solution [58].



Maximum absorbance	578 nm
Maximum fluorescence	613 nm
Fluorescence quantum yield	>0.9 in DCM
Density	1.4 gr/cm ³

Figure 28 :The chemical structure of F Red305 and its important absorbance and fluorescence properties, from BASF Colorants for Plastics [58].

5.4. FSC (Fluorescent Solar Collector) preparation

The substrates used in this study are glass slides with two different cut edges (polished and ground) with dimensions of 26×26×1 mm³ (BK7 glass). Before depositing the layers, the slides were thoroughly cleaned, the procedure of which involved several steps: manual cleaning of the substrate with soap, a secondary clean in an ultrasonic bath for 15 minutes in the same soap, rinsing with water, and finally a 10 minute acetone clean in an ultrasonic bath. A solution of laser dyes (RhodamineB, Lumogen F305 Red dye (BASF, Ludwigshafen)) were prepared by diluting and mixing with PMMA, in different concentrations, in an ultrasonic bath for 60 minutes. The prepared mixture was spin coated (Laurell spin coater, EDC-650-15TFM) at a speed of 3000 rpm, and accelerated at a rate of 2000 rpm/s for 1 minute. The thickness of the films, measured by using a Taylor-Hobson profilometer form Talysurf-120 L, was found to be 24.85µm. The collectors were analysed by treating them as homogeneous plates, with an effective absorption coefficient of:

$$\alpha_{eff} = \alpha \frac{d_{film}}{d_{film} + d_{glass}} \cong \alpha \frac{d_{film}}{d_{glass}}, \quad (124)$$

where α is the true absorption coefficient of the dye-loaded PMMA film of thickness, d_{film} , and d_{glass} is the thickness of the glass slide [40].

5.4.1. Poly (methyl methacrylate) PMMA sample preparation

The substrate used in this study was a BK7 glass slide with dimensions of 26×26×5 mm³. Prior to depositing the layers, the slides were thoroughly cleaned. A solution of 9-10% PMMA, dissolved in Chlorobenzene (Micro Chem), was spin-coated (Laurell EDC-650- 15TFM) at a speed of 3000 rpm for 1 minute. The thickness of the spin-coated layer was measured by using a profilometer (Talysurf-120 L, Taylor Hobson Ltd.) and was found to be 24.85µm.

5.5. Con-focal laser sensor

The con-focal laser (CL) sensor is well suited to measuring general surfaces, such as metals, polymers, silicon, ceramics, etc, and measures small trenches particularly well. It has good vertical resolution, small spot size, and includes an integrated CCD camera microscope. This is recommended for the majority of applications. The con-focal white light (WL) sensor may also be used for measuring general surfaces, but is less well suited to measuring small trenches. However, it does provide superior performance when measuring curved and transparent surfaces, such as lenses and shaped mirrors.

A very small (2 micron) spot size and 10nm resolution makes this sensor ideal for measuring the smallest of features (sub micron level) [59]. It is also capable of measuring the thickness of transparent layers, featuring an integrated video microscope for targeting, and operator feedback during setup and operation (figure 29).

In a con-focal laser scanning microscope, a laser beam passes through an aperture and is then focused by an objective lens into a small focal volume within, or on, the surface of a specimen. Scattered and reflected laser light, as well as any fluorescent light from the illuminated spot, is then re-collected by the objective lens. A beam splitter separates off some portion of the light into the detection apparatus, and after passing a pinhole, the light intensity is detected by a photo detection device, transforming the light signal into an electrical one that is recorded by a computer.

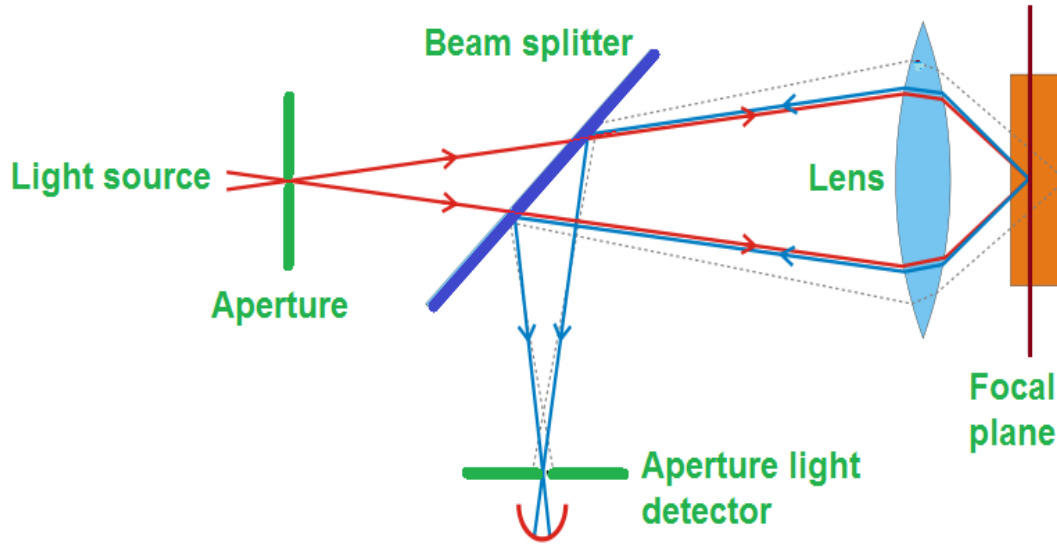


Figure 29: Schematic of the confocal operation principal. A collimator lens is oscillated over the sensors gauge range with the highest received intensity reflection corresponding to the surface height.

5.5.1. XYRIS 4000 CL (or WL) system example

The XYRIS 4000 CL is a compact, state of the art surface profiling system, using a confocal laser source that is capable of measuring form and thickness of various surfaces. It incorporates a CCD camera for on-screen viewing of the surface under investigation, which helps to identify areas, or features of interest, quickly and easily. The WL (white light) sensor offers increased performance for spherical or surface measurement, and the system includes PC software to both operate the profiler (TaiCaan STAGES), and to analyse the resultant data using the pre-installed TaiCaan BODDIES. Data can be exported from the analysis programme in 3D representations, surface profile graphs and data in spreadsheets (e.g. Microsoft Excel), by copying raw data for exporting to a spreadsheet file, or an image of the graphical display for exporting to Microsoft Word documents.

The system is characterised by a sensor in the vertical (Z) axis and a sample being scanned in the X,Y plane. The sensor selected for this application has the critical ability of measuring features below the light spot size, and through a transparent medium. This is achieved by moving the sensor, with sub-micron resolution, in the X,Y plane, and the sensor returning a value for the average height at that particular position. The thickness of RB, spin coated on to the glass with a

speed of 3000 rpm, was measured using this method, and the sample thickness was found to be approximately $25.9\mu\text{m}$, as shown in figures 30 and 31.

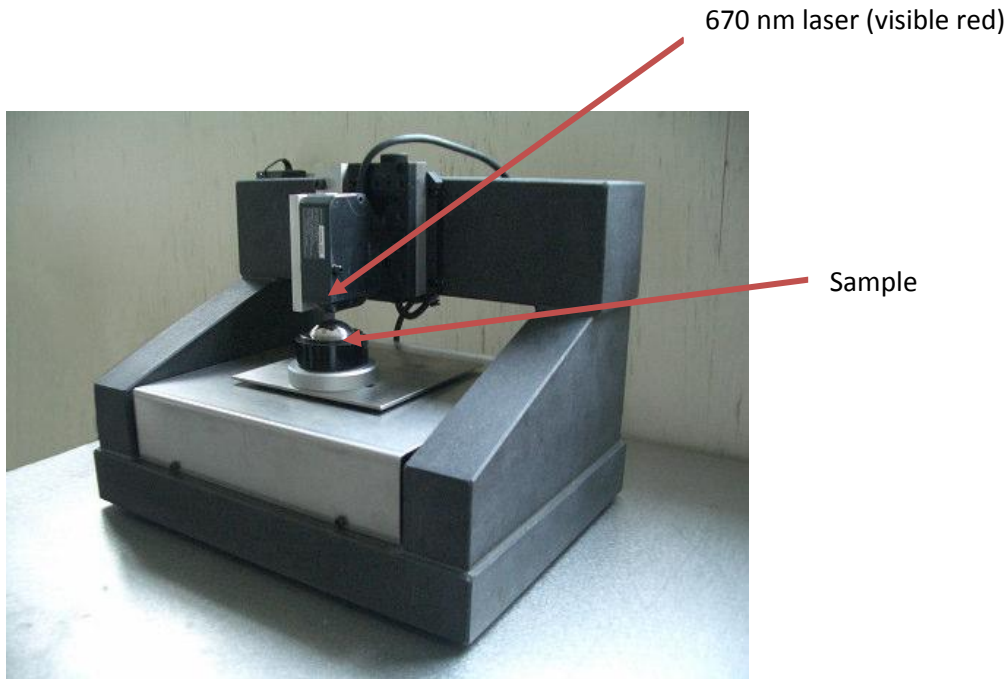


Figure 30: XYRIS 4000 CL-25 mm XYZ motion system- the CL sensor has an integrated microscope video camera, to assist in targeting the system..

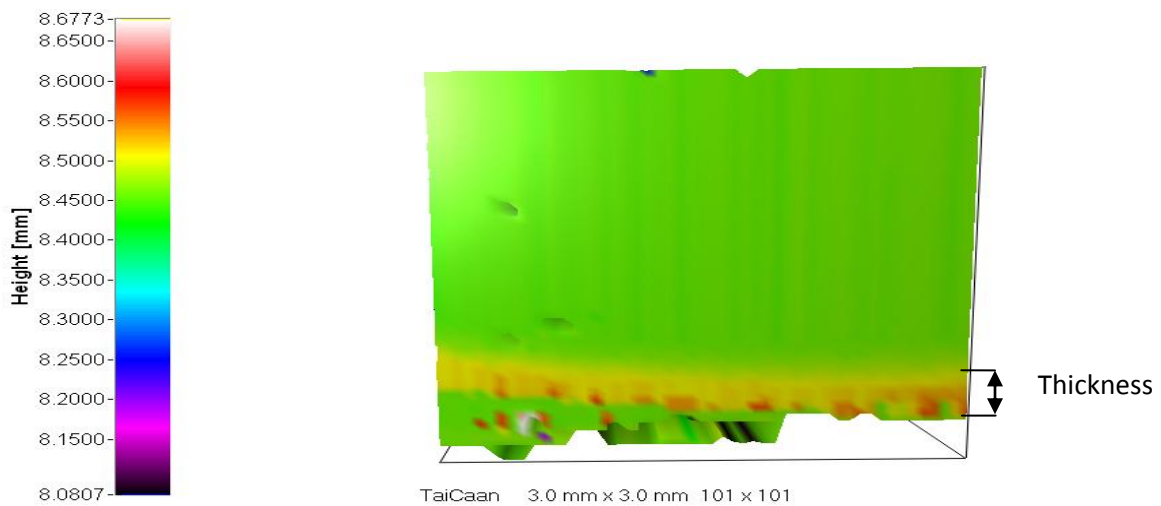


Figure 31: Thickness measurement of RB, spin coated on top of glass, using the XYRIS 4000CL (area $3\text{mm} \times 3\text{mm}$). The sample thickness is approximately $25.9\mu\text{m}$.

5.6. Scanning Electronic Microscopy (SEM)

For the study of materials, electron microscopy presents many advantages over conventional light microscopy:



Figure 32: JSM 5910 scanning electron microscope.

In this work, Scanning Electron Microscopy (SEM) (figure 32) was employed to measure the thickness of an RB solution, spin coated atop the glass. In the scanning electron microscope, a beam of electrons is rastered across the surface of a specimen. When the beam dwells at a point, the high energy electrons interact with atoms near the surface, displacing valence electrons (secondary electrons), whilst some primary electrons are reflected on collision, with the response processed and passed to a frame store. The beam then moves on to the next point on the specimen. A digital image is gradually built up in the frame store and eventually displayed on a computer screen, with the low energy, or secondary electrons, giving the best resolution topographic image, with a large depth of field. The reflected, or backscattered, electrons provide an additional compositional contrast. The electrons of the SEM beam displace valence electrons from near the surface atoms of a specimen, with these low energy, secondary electrons detected

to generate a topographic image. In a typical SEM, electrons are thermionically emitted from a tungsten filament cathode, and are accelerated towards an anode.

Tungsten is normally used in thermionic electron guns as it has the highest melting point and lowest vapour pressure of all metals, thereby allowing it to be heated for electron emission. Alternatively, electrons can be emitted using a Field Emission Gun (FEG). The electron beam, which typically has an energy ranging from a few 100eV to 100keV, is focused by one or two condenser lenses into a beam with a very fine focal spot, sized 0.4-0.5nm. The beam passes through pairs of either scanning coils or deflector plates in the electron optical column, typically in the objective lens, which deflects the beam horizontally and vertically so that it scans in a raster fashion over a rectangular area of the sample surface. When the primary electron beam interacts with the sample, the electrons lose energy through repeated scattering and absorption within the specimen. The energy exchange between the electron beam and the sample results in the reflection and emission of electrons and electromagnetic radiation, which can be detected to produce an image (figure 33) [60].

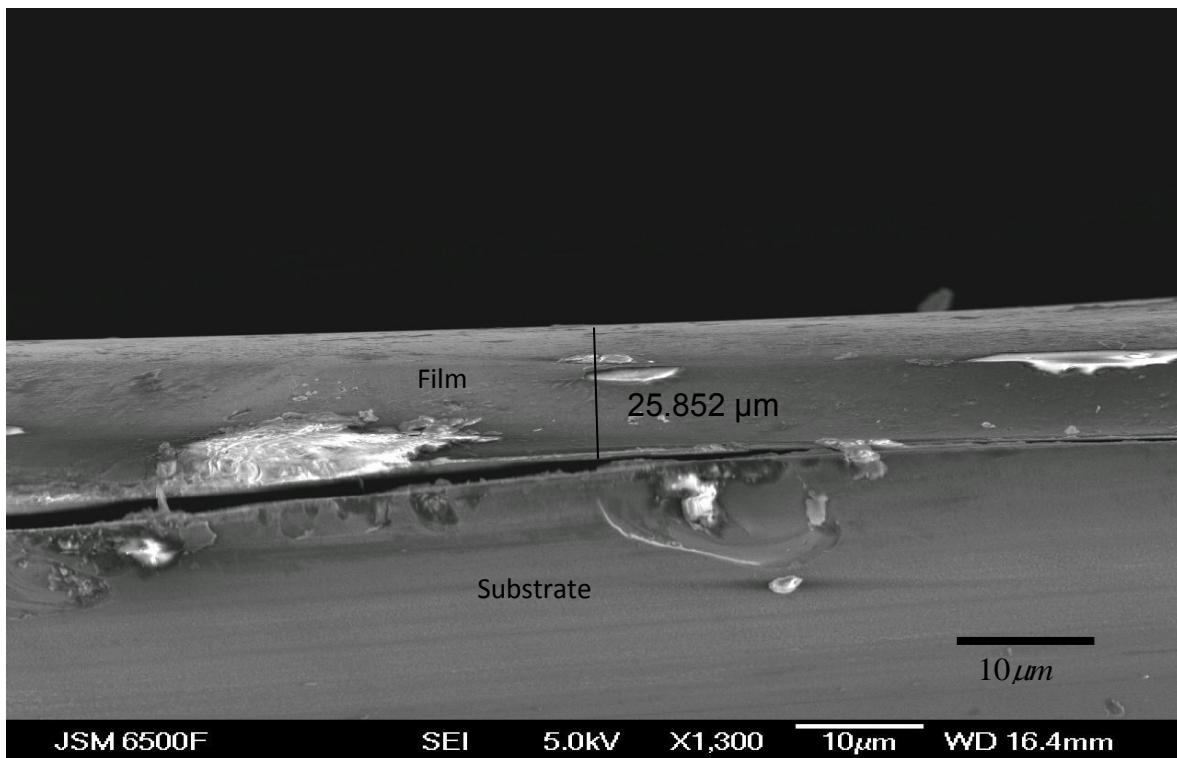


Figure 33: SEM of RB spin coated on top of glass from the edges.

5.7. Thickness measurement of transparent thin film by multiple interference technique

Thickness measurements of optically transparent thin films were achieved by employing multiple interference techniques. An Avantes spectrometer was used for wavelength scanning in the visible wavelength range, in order to obtain transmittance data on the single layer films. Spectrometer instruments generally consist of an entrance slit, a collimator, and a dispersive element (such as a grating or prism), that focuses optics, and a detector. In a monochromator system, there is normally also an exit slit, and only a narrow portion of the spectrum is projected on to a single element detector. In monochromators, the entrance and exit slits are in a fixed position, and can be changed in width. Rotating the grating scans the spectrum.

When the wavelength dependence of the refractive index of the film is negligible in the measurement range, the Fast Fourier Transform (FFT) technique can be applied to obtain film thickness. The measured thicknesses are compared with fringe counting, and the results have shown that the DFT (Discrete Fourier Transform) technique is advantageous if the film has two or more layers, or the thickness is more than 2000nm. The Fourier Transform of transmittance of a multilayer film peaks at the corresponding optical thickness of the layers, and at their harmonics; by identifying these peaks, the physical thickness of each layer is determined by the procedure given below.

5.7.1. Determination of film thickness

When a monochromatic light beam of wave number, $K_0 = 2\pi/\lambda_0$, impinges at angle, θ_i , on a dielectric film, composed of N layers, each with a particular value of refractive index $n_1; n_2; n_3; \dots; n_N$ and physical thicknesses $d_1; d_2; d_3; \dots; d_N$, between two infinite media of refractive indices n_0 and n_t , the total transmittance is derived as: [32]

$$T(K_0) = \frac{n_t}{n_0} \left(\frac{\cos \theta_t}{\cos \theta_i} \right)^{(1-2\beta)} \times \left[\frac{2\gamma}{M_{11}\gamma_0 + M_{12}\gamma_0\gamma_t + M_{21} + M_{22}\gamma_t} \right]^2, \quad (125)$$

where $\gamma_0 = n_0 \cos \theta_i$, $\gamma_t = n_t \cos \theta_t$, and $\beta = 0$ for polarisation perpendicular (TE) to the plane of incidence, and $\gamma_0 = n_0 / \cos \theta_i$, $\gamma_t = n_t / \cos \theta_t$, $\beta = 1$ for polarisation parallel (TM) to the plane of incidence. M_{kl} is the transfer matrix of the entire system, which is the product of the individual transfer matrices of various layers (the transfer-matrix is a method, used in optics, of analysing the propagation of electromagnetic waves in a medium) [61].

The transfer-matrix method is based on the fact that, according to Maxwell's equations, there are simple continuity conditions for the electric field across boundaries from one medium to the next [61]. If the field is known at the beginning of a layer, the field at the end of the layer can be derived from a simple matrix operation. A stack of layers can then be represented as a system matrix, which is the product of the individual layer matrices.

$$M = M_1 M_2 \dots M_N$$

$$= \prod_{j=1}^N \begin{bmatrix} \cos k_0 & \frac{-i}{\gamma_j} \sin k_0 D_j \\ -i\gamma_j \sin k_0 D_j & \cos k_0 D_j \end{bmatrix} = \begin{bmatrix} M_{11} & M_{12} \\ M_{21} & M_{22} \end{bmatrix}, \quad (126)$$

where $D_j = n_j d_j \cos \theta_j$, and is the optical thickness of the j th layer (θ_j being the corresponding refraction angle), $\gamma_j = n_j \cos \theta_j$ for TE polarisation and $\gamma_j = n_j / \cos \theta_j$ for TM polarisation.

The Fourier transform of transmittance, $T(K_0)$, is given by:

$$f(X) = \int_{-\infty}^{\infty} T(K_0) \exp(-iK_0 x) dK_0 \quad (127)$$

In the most common situations, transmittance spectra are obtained in a discrete sampled form, leading us to the Discrete Fourier Transform (DFT) by changing the integration in equation (127) into the summation [32]. The DFT of the N_s consecutive sampled transmittance values, $T[K_0]$, at discrete wave numbers points, $K_p = p\Delta k$ ($p = 0, 1, 2, \dots, N_s - 1$), and, Δk , being the sampling interval thus, $f(Xq)$ can therefore be written as:

$$f(X_q) = \sum_{p=0}^{N_s-1} T(K_p) \exp(-iK_p X_q / N_s), \quad (128)$$

which only takes values at discrete points

$$X_q = \frac{q\pi}{N_s \Delta k}, \quad q = -\frac{N_s}{2}, -\frac{N_s}{2} + 1, \dots, \frac{N_s}{2} \quad (129)$$

For a single-layer film, the $f(X_q)$ peaks at the corresponding optical thickness, D , of the film from which its physical thickness is shown in figure 34, and can be calculated provided that the refractive index of the film is known and non-dispersive within the sampling range of the transmittance.

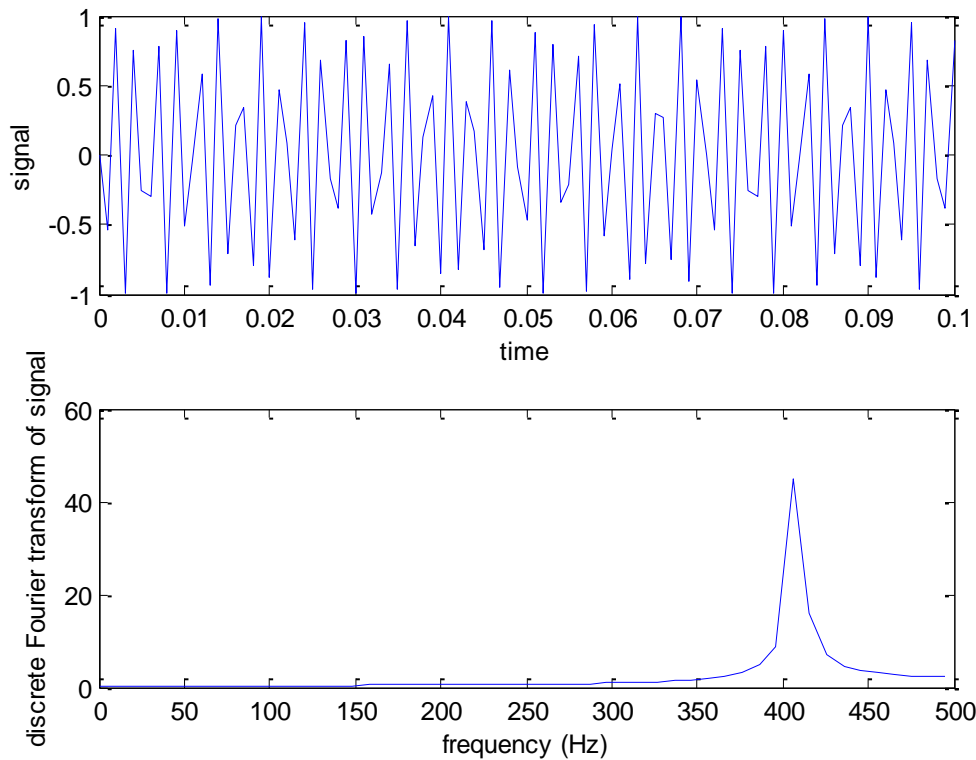


Figure 34: DFT of single layer film in Matlab, and the peak corresponding optical thickness, D , of the film, the duration of the signal equal to 1000 in this example.

In general, for an N -layer film, there would be $N(N+1)/2$ peaks in the $f(X_q)$ spectrum; N of which are positioned at the optical thickness of each layer $\{D_1, D_2; \dots, D_N\}, (N - 1)$, of which at $\{D_1 + D_2, D_2 + D_3; \dots; D_{N-1} + D_N\} (N - 2)$, of which at $\{D_1 + D_2 + D_3; D_2 + D_3 + D_4; \dots; D_{N-2} + D_{N-1}$

$+D_N)/(N-3)$, and so forth. It is worthwhile noting that, even though the refractive index of each layer is known at the outset, we cannot identify which peak position corresponds to which optical thickness from an experimentally obtained DFT spectrum. This is because the physical thickness of each layer is unknown, so a multiplicity of $n_j D_j$ combinations may result in the same optical thickness. Consequently, by pointing out that the last peak position in the DFT spectrum always corresponds to the sum of the optical thicknesses $(\sum_{j=1}^N D_j)$, the following procedure has been proposed in this work to determine the physical thickness of each layer. For an N -layer film, the DFTs of the measured transmittance spectra for N different incident angles $(\theta_i^\alpha, \alpha = I, II, \dots, N)$ lead to the following $N \times N$ matrix equation [32],

$$\begin{bmatrix} n_1 \cos \theta_1^I & n_2 \cos \theta_2^I & \dots & n_N \cos \theta_N^I \\ n_2 \cos \theta_1^{II} & n_2 \cos \theta_2^{II} & \dots & n_N \cos \theta_N^{II} \\ \cdot & \cdot & \cdot & \cdot \\ \cdot & \cdot & \cdot & \cdot \\ \cdot & \cdot & \cdot & \cdot \\ n_1 \cos \theta_1^N & n_2 \cos \theta_2^N & \dots & n_N \cos \theta_N^N \end{bmatrix} \begin{bmatrix} d1 \\ d2 \\ \cdot \\ \cdot \\ \cdot \\ dN \end{bmatrix} = \begin{bmatrix} P(\theta_i^I) \\ P(\theta_i^{II}) \\ \cdot \\ \cdot \\ \cdot \\ P(\theta_i^N) \end{bmatrix}, \quad (130)$$

where $P(\theta_i^\alpha) \equiv \sum_{j=1}^N D_j$ is the experimental value of the sum of the optical thicknesses, corresponding to the angle of incidence, θ_i^α , and the refraction angle of each layer is related to the incident angle by Snell's law:

$$n_1 \sin(\theta_1^\alpha) = n_2 \sin(\theta_2^\alpha) = \dots = n_N \sin(\theta_N^\alpha) = n_0 \sin(\theta_i^\alpha) \quad (131)$$

The physical thickness of the layers are computed from equation (130). An exemplary simulation for a one-layer film is presented in figures 35 and 36.

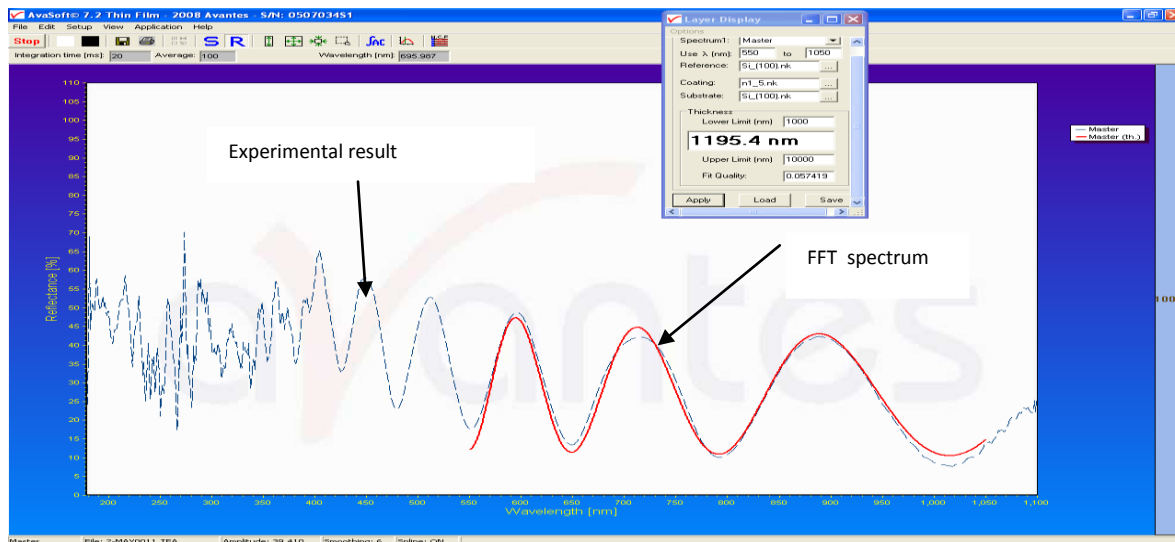


Figure 35: Thickness measurement for PMMA dissolved in Toluene (0.5gr:5ml) and spin coated on top of silicon.

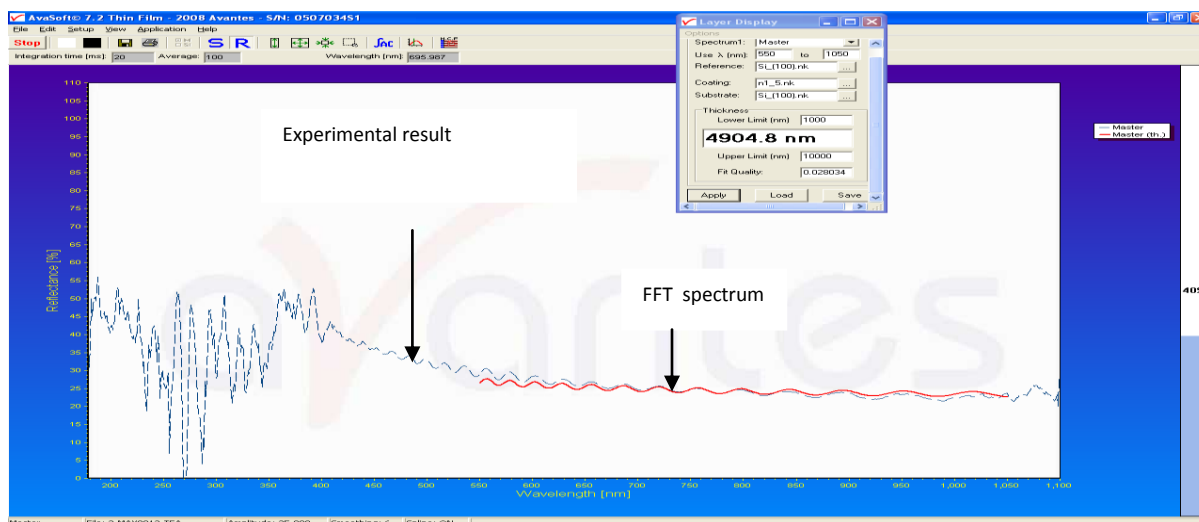


Figure 36: Thickness measurement for PMMA dissolved in DCM (0.5gr:5ml) and spin coated on top of silicon.

Figures 37 compares the results of three different techniques (Avantes, SEM and Confocal laser) where the RB was dissolved in DCM ($C=3 \times 10^{-3}$ mol/L), mixed with PMMA and spin coated on top of silicon, based on different speeds. As a result, the thickness is decreased by increasing the speed.

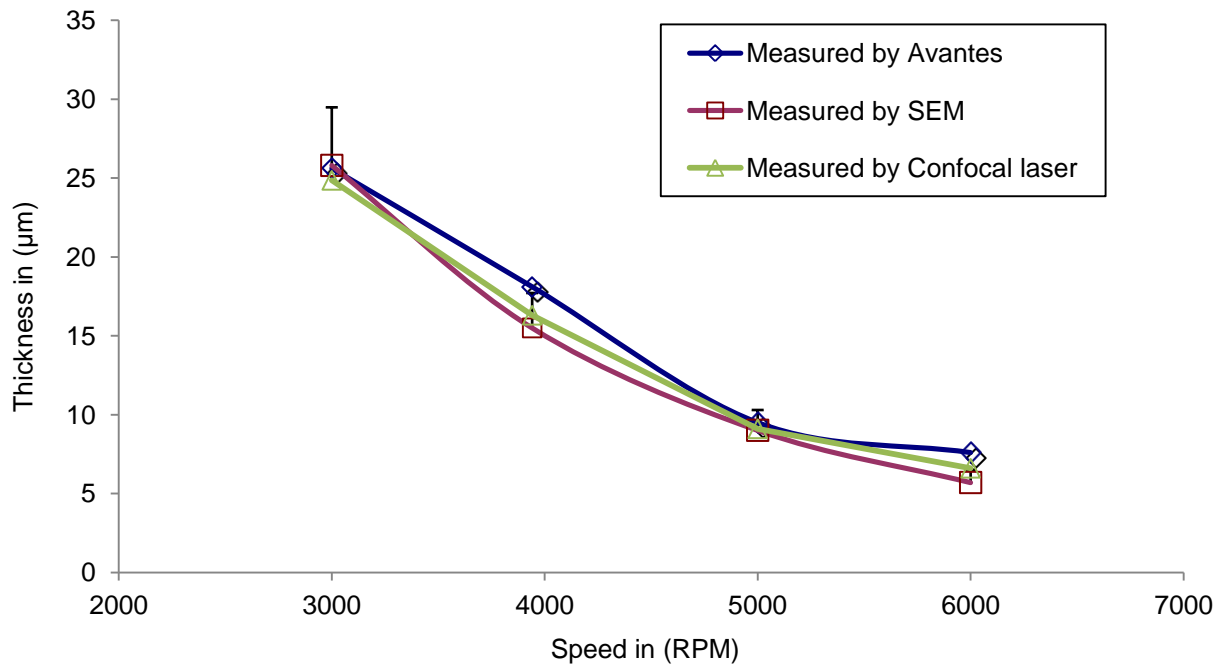


Figure 37: RB in DCM ($C=2.61 \times 10^{-3}$ mol/L), spin coated on top of silicon with different rotational speeds and measured using Avantes, SEM and Confocal laser, the error bars presenting an uncertainty of 14.26%.

The results have shown that the laser method was a very accurate method for thickness determination (more than 95% accuracy), and that SEM was also used, being similarly accurate. From the data, the thickness of the sample was difficult to determine, and when analysed and compared to the measurements produced by Avantes, it can be seen that there is an error in the data obtained in the Avantes measurements. This may be due to the type of materials used in the sample.

5.8. Taylor Hobson form Talysurf 120 stylus profiler

Profilometry is the measurement of the surface height variations of an object, and can be divided into three areas: the measurement of surface shape, or the difference of the shape from an ideal, sometimes called ‘form one’; measurement of waviness; and measurement of the roughness. The measurement of roughness requires instruments with both high lateral (in our case the X axis) and vertical (Z axis) resolution. The smoothness, or roughness, of a surface is a very important parameter in many electronic, optical and mechanical components. A diamond stylus is moved vertically, in contact with a sample, then moved laterally across the sample for a specified distance, and specified contact force. A profilometer can measure small surface variations in the

vertical stylus displacement, as a function of position. A typical profilometer can measure small vertical features ranging in height from 10 nanometres to 1 millimetre. The position of height of the diamond stylus generates an analogue signal, which is converted into a digital signal, stored, analysed and displayed. The radius of the diamond stylus ranges from 20nm to 25 μ m, and the horizontal resolution is controlled by the scan speed and data signal sampling rate. The stylus tracking force can range from less than 1, to 50 milligrams, and since the stylus is in contact with the surface, the method is not sensitive to surface reflectance. Also, contacting the surface is often an advantage in dirty environments, where non-contact methods can end up measuring surface contaminants, instead of the surface itself. The resolution of the stylus tip radius can be as small as 20nm, significantly better than white-light optical profiling.

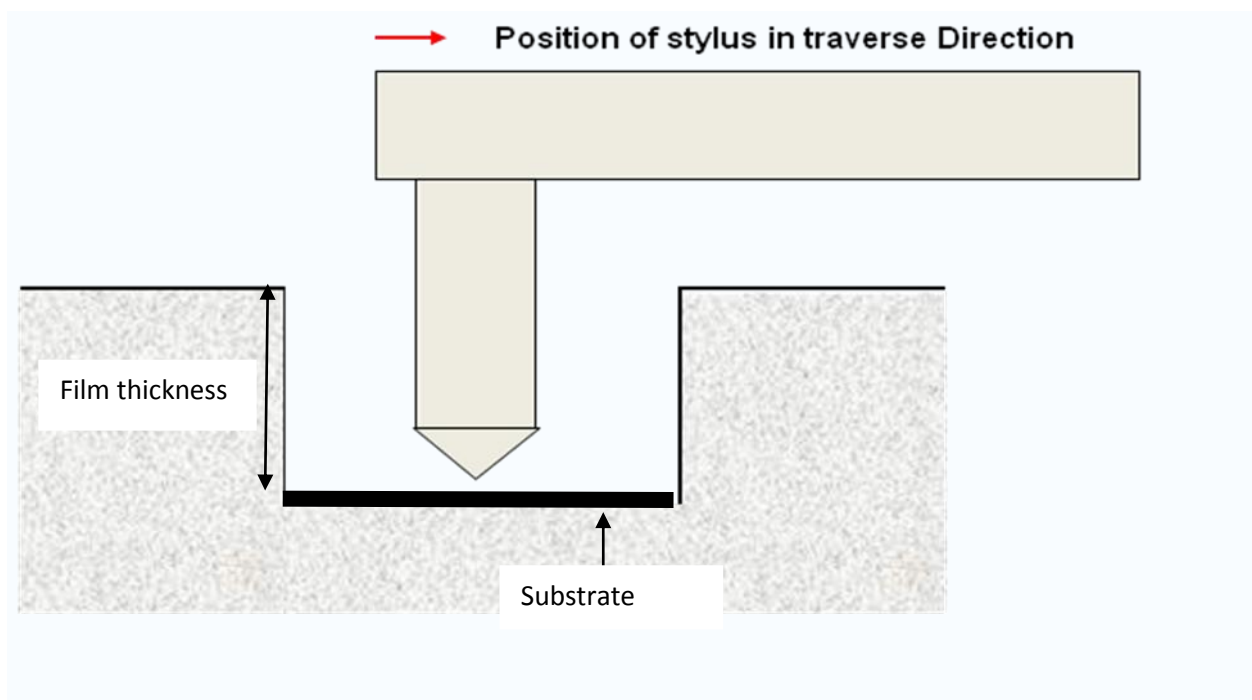


Figure 38: Contact profilometers for measuring the thin film thickness

The raw profile was measured across the dye film boundary on a glass base, and by using a reference point, it was possible to specify a value of film thickness. The thickness of the RB in DCM ($C=2.61E-03$ mol/litre), spin coated on top of glass (speed 4000 rpm) and measured by using a Taylor-Hobson profilometer of form, Talysurf-120 L (Rank Taylor Hobson Limited, Leicester, England), was found to be 11 μ m.

5.9. Characterisation techniques

This section describes two major techniques used to characterise the optical properties of the prepared samples, and a solar cell I - V characterisation of a silicon solar cell. These are the absorbance and fluorescence measurements, the former of which is very useful in quantification of the samples. The fluorescent measurement is another method used to measure the emission characteristics of the fluorescent molecules.

A Xenon lamp (75 W) was used as the excitation light, and was guided to illuminate a test sample mounted in the measurement module, the output light from the sample measured using Avantes.

The Bentham spectrometer system is composed of a grating monochromator (TM300), a photomultiplier tube (PMT: Hamamatsu type R446), and a data acquisition and control unit. The PMT is used to detect and amplify the optical signal, with the data acquisition and control unit connected to a personal computer to control the monochromator, and convert the output signal of the PMT into digital data.

5.9.1. Absorbance measurement

The absorbance of the sample, $A(\lambda)$, can be determined using the Beer-Lambert law, as shown in equation 132.

$$A(\lambda) = -\log\left(\frac{I_0}{I_i}\right), \quad (132)$$

where I_0 is the intensity of the light transmitted through a reference sample.

A schematic diagram of the system (Setup I), used to measure these light intensities, is depicted in figure 39.

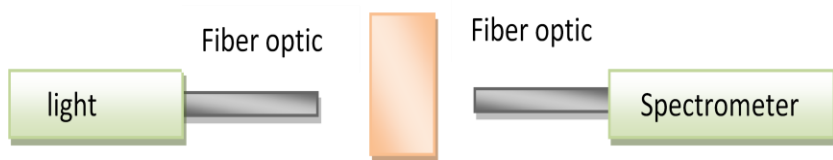


Figure 39: The optical arrangement for absorbance measurement.

A Xenon lamp was used as a light source, and guided to a device under test (FSC), either a reference or test sample, via an optical fibre. The intensity of the light transmitted through the sample was guided to the spectrometer.

5.9.2. Fluorescence measurement

To measure the fluorescence spectra, the sample is illuminated with a continuous beam of monochromatic light, and the intensity of the emission spectra recorded. Two different arrangements are used to detect the fluorescence light emitted from the test samples:

1. Front–face fluorescence detection
2. Edge fluorescence detection

The first and second arrangements were used to measure the fluorescence spectra emitted from the front surface, and from the edges of the samples, respectively. These spectra were characterised to determine the reabsorption loss of the sample, which will be discussed in chapters 8 and 9.

5.9.3. Front–face fluorescence detection

Figure 40 shows the setup of the front–face fluorescence measurement. A Xenon lamp with 500, 550 nm band pass filter was used as the excitation source, with the light guided to illuminate front surface of the sample through an optical fiber and a combination of lenses. The incident beam was fixed at 30° relative to the substrate, and the fluorescence light emitted from the sample detected using another optical fiber. The fiber was set up to detect the emission light normal to the front surface.

This arrangement enables us to measure the fluorescence signal emitted from the sample, with a minimum optical path length, in order to minimise the self-absorption

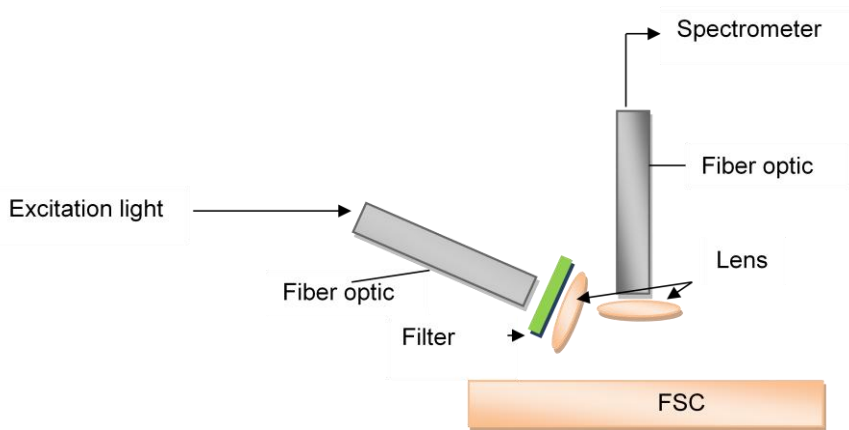


Figure 40: Setup for front Fluorescent Detection.

5.9.4. Edge fluorescence detection

Figure 41 illustrates the experimental setup used to measure fluorescence light emitted from the edges of the fluorescent collectors. For the excitation light, a Xenon lamp with excitation peak at a wavelength of 500,550 nm was used, and positioned to provide a strong intensity, as well as uniform illumination over the whole area of the sample. A fluorescence spectrum was recorded from one edge while the other three edges of the collector were covered with silver mirrors. Fluorescence spectra from the edge of the collectors were collected by an optical fiber, featuring a cosine corrector (Avantes) to collect light from a large solid angle. This eliminated optical interface problems associated with light collection sampling geometry inherent to the optical fiber.

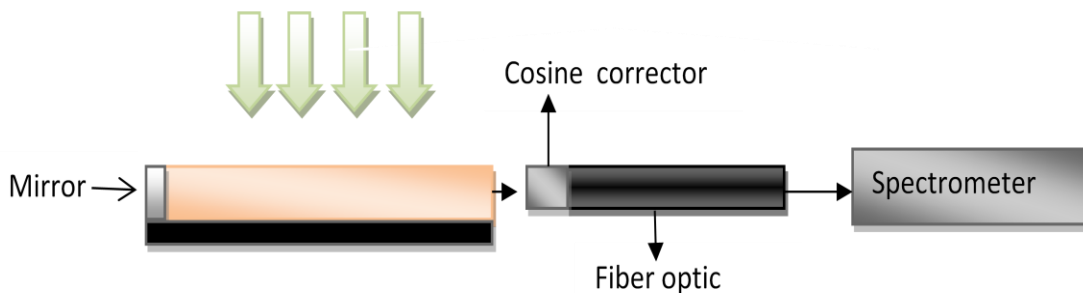
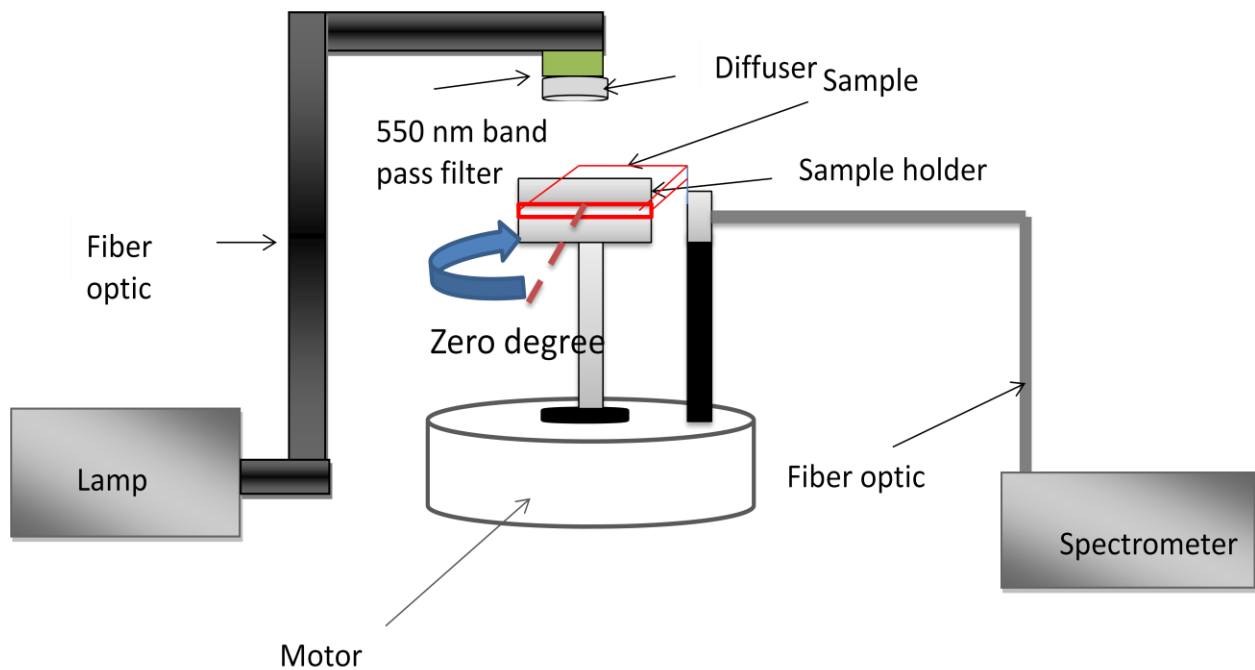


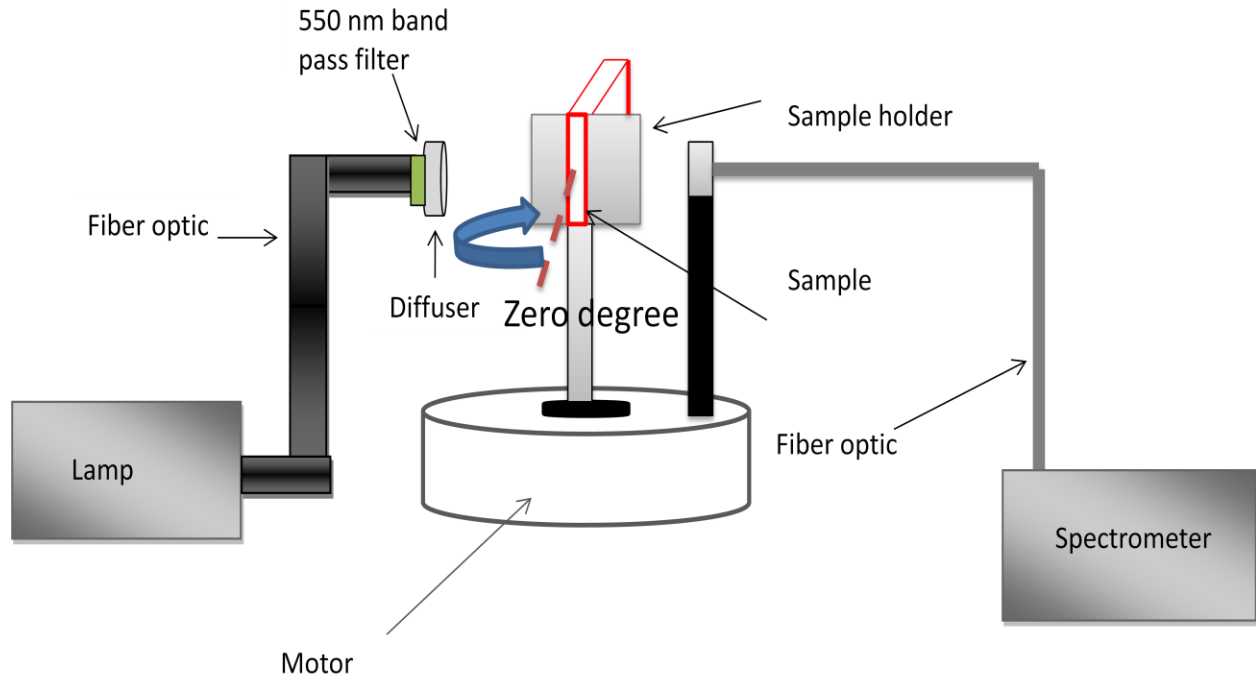
Figure 41: Setup for Edge Fluorescent Detection.

5.9.5. Edge fluorescence detection in different angles

Figure 42 illustrates the experimental setup used to measure fluorescence light emitted from the edges of the fluorescent collectors. The sample was illuminated from 2 different positions, and for the excitation light, a Xenon lamp with excitation peak at a wavelength of 550nm (by using the band pass filter in front of the lamp) and a diffuser, was positioned to provide a strong intensity and also uniform illumination over the whole area of the sample. A fluorescence spectrum was recorded from one edge at a different angle (0° - 45°). Fluorescence spectra from the edge of the collectors was collected by an optical fiber, connected to Avantes to collect light from 4.9×10^{-6} sr solid angle.



(a)



(b)

Figure 42: Setup for Edge Fluorescent Detection (a) the sample was illuminated from the top and detected from the edge at 0° to 45° (b) sample rotated 90° , illuminated from the top, and detected from the edge at 0° to 45° . 0° was chosen to be in the middle of the sample.

5.9.6. I-V characterisation of silicon solar cell measurement

The current-voltage (I - V) characteristics of fabricated solar cells were measured by illuminating the cells using a Xenon lamp. This was connected to a HP4142B DC source/monitor via a Kelvin connection, and the setup separates the channels for voltage and current measurements. Computer software controlling the HP4142B was developed as part of this work, using HP-VEE 5.0. The HP4142B was programmed to apply voltages to a solar cell, from -0.6 to $+0.7$ V in 0.01 V increments, and to sense the current from the device.

Two test conditions were used for I - V : no illumination (dark measurement), and 100 mW/cm^2 white-light standard illumination. The standard illumination was achieved with a solar simulator, T.S. Space System Solar Simulator, and in this system, a 300 W Xenon lamp was used as a light source, providing the spectrum approximating to that of sunlight. The intensity of light was adjusted from the illuminator power supply. The intensity of the light source was calibrated to 100 mW/cm^2 with the help of a standard silicon solar cell of $2 \times 4 \text{ cm}^2$ area.

5.10. Photon collection efficiency and optical efficiency measurement

A solar simulator (T.S. Space Systems), equipped with a Xenon lamp approximating AM1.5 Spectrum, was used to measure the output of the fluorescent collectors. The photon collection efficiency (Q_c) of the F305 red dye collectors were measured at 550nm by placing a silicon solar cell at one of the edges of the collector ($26 \times 26 \times 1 \text{mm}^3$), coupled with an optical gel (Thorlabs). The other three edges of the collector were covered with a silver mirror, and the cell covered with black insulating tape in order to leave an area of $3 \times 30 \text{mm}^2$ available for illumination. The same cell was also illuminated directly from the 550nm filter. The quantum efficiency of the cell is practically 'wavelength independent', in this part of the spectrum, and therefore the measured short circuit current ratio of the collector/direct illumination gives the optical efficiency.

A second important factor was the geometrical gain of a plate, which is the ratio of the area of the FSC from the top, to the area covered by the cell.

The photon collection efficiency is the ratio of photons that can reach the edge of the collector, to the number of photons that are absorbed by the plate, and, therefore, it is important to consider the geometrical gain, being the area of the top collector to the area of the solar cell.

As we know, for transparent material, absorption efficiency + reflection efficiency + transmission efficiency = 1

The absorbance of the sample, $A(\lambda)$, can be determined using the Beer-Lambert law, which was explained in chapter 6. Therefore the transmittance is $A = -\ln(T)$ or $T = 10^{-A(\lambda)}$

The value of the absorbance was measured, for all the samples, at 550nm with a Xenon lamp, and through the Benthom equipment. The reflection efficiency of the front surface was measured by using the integrating sphere (explained in chapter 6), which was around 5% at 550nm.

Therefore the value of $Q_A = 1 - \text{reflection efficiency} - \text{transmission efficiency}$.

The photon collection efficiency in the dye sample is:

$$Q_c = \text{Optical efficiency} / Q_A, \quad (133)$$

Conclusion

This chapter illustrated the spin coating method of thin film on to glass and silicon substrate, and the different methods of measuring sample thickness. It has shown the profilometry method is best for measuring the film thickness, as it is independent of the glass reflectivity. Considering the availability of the con-focal laser (CL) method, scanning electron microscopy and multiple interference technique were employed in this project for measuring the thickness of spin coated material on top of the glass and silicon. The laser method is independent of the surface and can therefore be used for any type of material. It is apparent that the laser technique provides a useful option as a non-contact probe for the localised measurement of coating thickness, even on devices with a challenging geometry. In the laser method and multiple interference techniques, it is better to use a silicon substrate instead of glass, to avoid the reflectivity problem of glass in the measurement. If the Confocal laser is compared with the SEM method, the SEM obviously provides a very high lateral resolution of the surface, with high levels of magnification, but is unable to perform basic surface parameter definitions, such as surface roughness, surface volume, area, depth or height of features. To detect these parameters it is necessary to perform a measurement of the surface where the surface is represented as 3D data (X,Y,Z).

Due to availability, the multiple interference technique was employed to measure the majority of the thickness measurements coated on top of a silicon substrate, and when the result from SEM were compared with this it, they were found to differ because of the increased accuracy of the SEM method. However, it also depends on the material, and with non-conductive materials, it was very difficult to see the thickness. It was therefore advisable to coat the sample with gold before measurement was taken, in order to reduce the static charge build up on the sample.

The optical characterisation systems were employed to measure the absorbance and fluorescence spectra. In order to obtain the absorbance spectra, the intensities of the Xenon light were transmitted through a test sample, with a reference sample measured. The absorbance spectra were obtained from these intensities by using the Beer-Lambert law. The fluorescence spectra may be characterised using two different methods, used to measure the fluorescent signal emitted from the front surface, and from the edge of the FSC, respectively.

Chapter 6

Scattering measurement setup and integrating sphere measurement

Introduction

The purpose of this chapter is to introduce the experimental setups for measuring the surface roughness of the fluorescence solar collector. , A comparison will be made between: the reflection and transmittance measurements, in double beam mode with an integrating sphere; and, the roughness of the fluorescence solar collector, measured from the total integrated scattering and angular dependence measurement. The value of the scattering coefficient from the surface, and the bulk of the fluorescence solar collector, were also measured in this chapter, by using the integrating sphere equipment.

6.1. Transmittance measurement in double beam mode

The Labsphere RT-060 integrating sphere system, with a double beam procedure, was used to measure the transmittance.

In RT series spheres, the transmittance can be recorded without the centre mount sample holder (figure 43). Port No. 1 serves as the transmittance port through which the light enters the sphere, and a sample holder is installed at the transmittance port.

The sphere was illuminated with collimated white light through the transmittance port. It was important to ensure that the beam did not clip the edge of the entrance port, and was centred on Port No. 3, where a port plug was installed. When alignment was completed, a sample was placed at Port No. 1.

The value for the total transmittance can be calculated as [37]

$$T(\lambda) = \left(\frac{S_{sample}(\lambda) - S_{dark}}{S_{ref}(\lambda) - S_{dark}} \right)_{port 1} \left(\frac{S_{ref}(\lambda) - S_{dark}}{S_{sample}(\lambda) - S_{dark}} \right)_{port 2}, \quad (134)$$

where $S_{sample}(\lambda)$ is the detector signal recorded with the sample beam switched on, $S_{ref}(\lambda)$ is the detector signal recorded with the reference beam, where the sphere is illuminated with collimated white light, and S_{dark} is the detector signal recorded for the dark measurement. For transmittance measurements, the empty transmittance port serves as the standard.

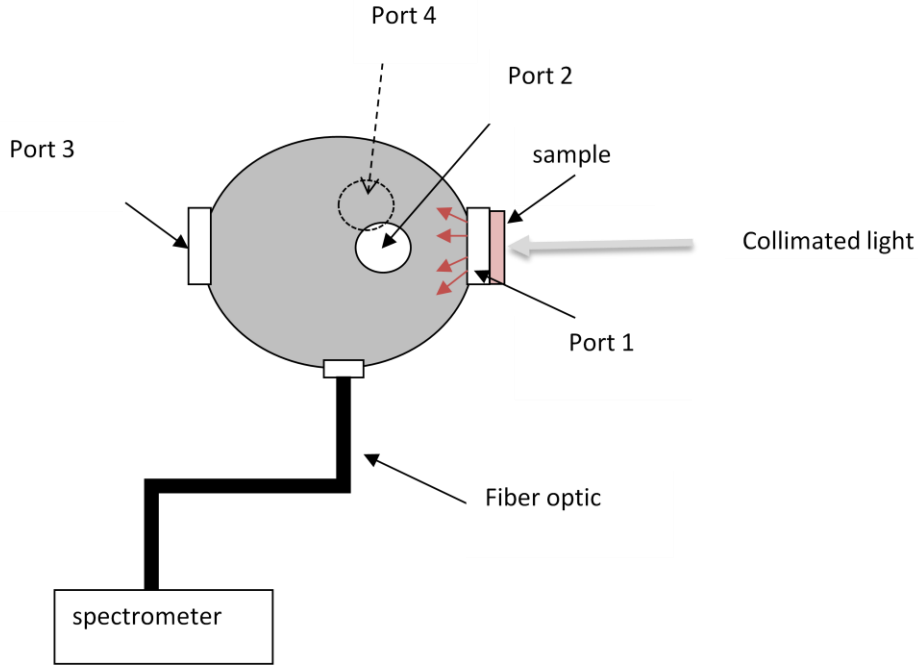


Figure 43: Integrating spheres in double beam mode for transmittance measurements.

The diffused transmittance was measured when the port plug 3, or the specular exclusion port, was removed, and its value can be calculated as:

$$T_D(\lambda) = T(\lambda) \left(\frac{S_{Dsample}(\lambda) - S_{Ddark}}{S_{Dref}(\lambda) - S_{Ddark}} \right)_{port 1} \left(\frac{S_{Dref}(\lambda) - S_{Ddark}}{S_{Dsample}(\lambda) - S_{Ddark}} \right)_{port 2}, \quad (135)$$

where the $S_{Dsample}(\lambda)$ is the detector signal recorded with the sample beam lit, $S_{Dref}(\lambda)$ is the detector diffuse signal recorded with the reference beam lit, and S_{Ddark} is the detector diffuse signal recorded for the dark measurement.

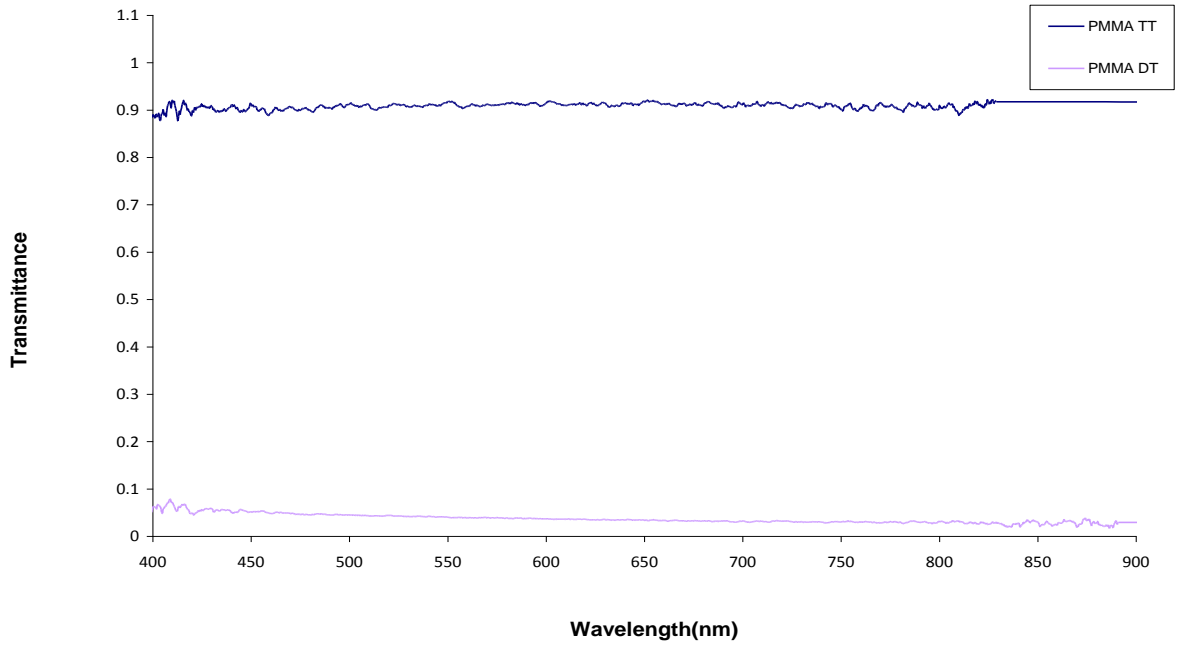


Figure 44: Comparison between the total transmittance (TT) and diffuse transmittance (DT) of PMMA spin coated on top of the BK7 glass at different wavelengths.

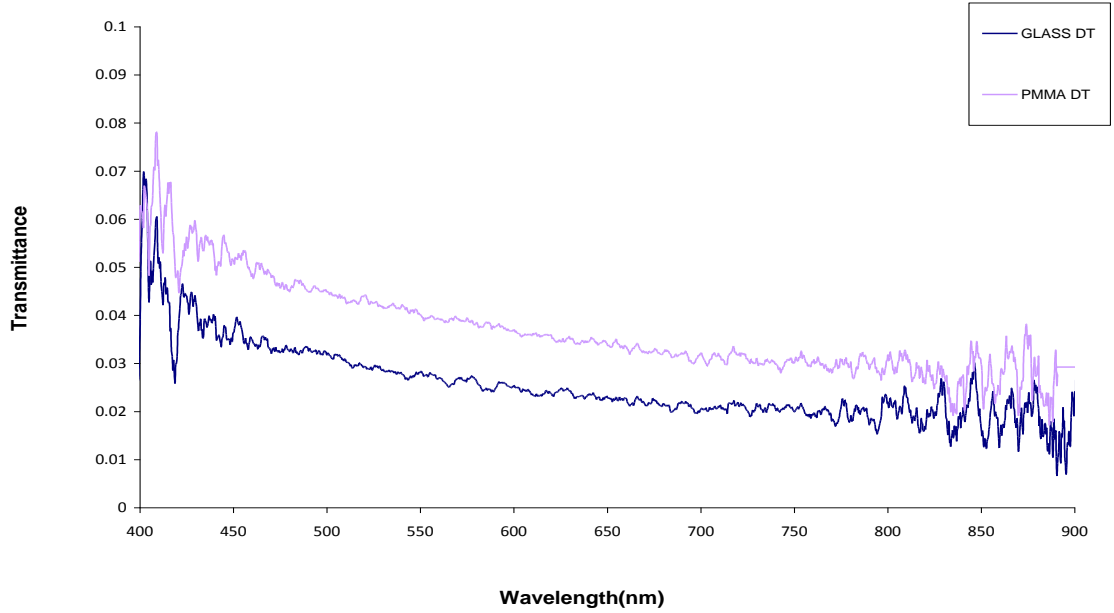


Figure 45: Comparison between the diffuse transmittance (DT) of PMMA spin coated on top of the BK7 glass and BK7 glass at different wavelengths.

Figure 44 shows the comparison between the *total* transmittance and the *diffuse* transmittance of PMMA, spin coated onto a BK7 glass slide, where it can be seen that the value of total transmittance is higher than the diffuse transmittance. Figure 45 is a comparison between the diffuse transmittance of PMMA spin coated on top of the BK7 glass, and BK7 glass. It indicates that there is some scattering from the PMMA layer on top of the glass, leading to an increase in diffuse transmittance.

6.2. Reflectance measurement in double beam mode

The reflectance standard for the Labsphere integrating sphere is calibrated in $8^\circ/h$ geometry (table 1). Therefore, the reflectance measurements carried out with the integrating sphere will be for an angle of incidence of 8° .

Wavelength	8° Hemispherical reflectance	Wavelength	8° Hemispherical reflectance
250	0.94	1300	0.95
300	0.96	1400	0.93
400	0.98	1500	0.92
500	0.98	1600	0.92
600	0.98	1700	0.92
700	0.97	1800	0.91
800	0.97	1900	0.86
900	0.97	2000	0.85
1000	0.97	2100	0.86
1100	0.96	2200	0.87
1200	0.95	2300	0.84

Table 1: Standard reflectance in different wavelengths (R_{std}) [32].

A clip-style sample holder was used to set the sample at 8° to the incoming beam. A calibrated diffuse reflectance standard, made of the same material as the inner walls of the sphere, was

installed at the reference port, with a dark current reading taken for reference, and for the sample. The sphere was then illuminated with collimated white light through port No1, and the detector current was recorded for the sample and reference sample. The 'standard' measurements are carried out on the reflectance standard, while the 'sample' measurements are carried out on the sample in port No 3.

The total hemispherical reflectance, $R(\lambda)$, can then be calculated using equation 136 [37].

$$R(\lambda) = R_{Std}(\lambda) \left(\frac{S_{sample}(\lambda) - S_{Dark}}{S_{Ref}(\lambda) - S_{Dark}} \right)_{port\ 3} \left(\frac{S_{Ref}(\lambda) - S_{Dark}}{S_{sample}(\lambda) - S_{Dark}} \right)_{port\ 2}, \quad (136)$$

$S_{sample}(\lambda)$ is the detector signal recorded with the sample beam on, $S_{Ref}(\lambda)$ is the detector signal recorded with the reference beam on, S_{Dark} is the detector signal recorded for dark current measurements, and $R_{Std}(\lambda)$ is the reflectance data for the calibrated reflectance standard. The diffused reflectance was measured when the port plug 4 or the specular exclusion port was removed.

The diffuse reflectance, $R_D(\lambda)$ can then be calculated as [37]

$$R_D(\lambda) = R_{Std}(\lambda) \left(\frac{S_{Dsample}(\lambda) - S_{DDark}}{S_{Dref}(\lambda) - S_{DDark}} \right)_{port\ 1} \left(\frac{S_{Dref}(\lambda) - S_{DDark}}{S_{Dsample}(\lambda) - S_{DDark}} \right)_{port\ 2}, \quad (137)$$

where $S_{Dsample}(\lambda)$ is the detector signal recorded with the sample beam lit, $S_{Dref}(\lambda)$ is the detector diffuse signal recorded with the reference beam lit, and S_{DDark} is the detector diffuse signal recorded for the dark measurement.

The total reflectance measure for PMMA, spin coated on top of the BK7 glass, and BK7 glass is shown in figure 46. The diffuse reflectance for PMMA was more than the diffuse reflectance of the glass, which indicates scattering caused by PMMA. However, the total reflectance was similar because the total reflectance is the sum of both the specular and diffuse reflectance, and the specular reflectance in BK7 glass was more than for PMMA.

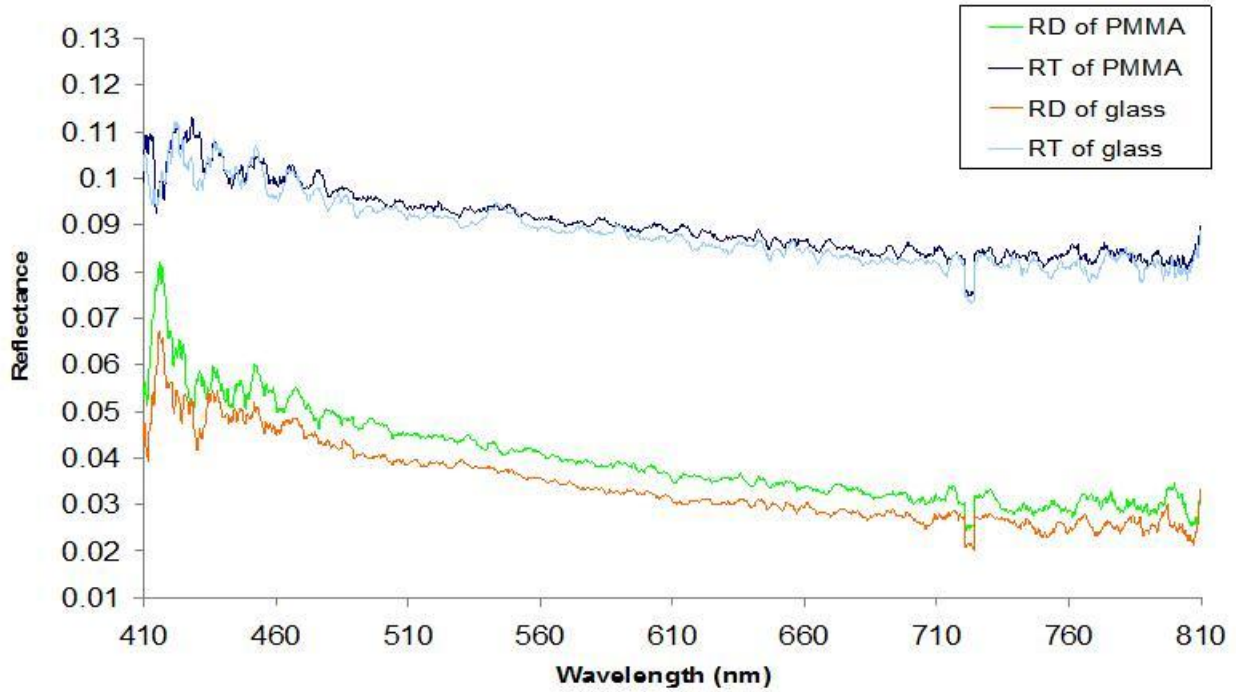


Figure 46: Comparison between the total reflectance measurement (RT) and diffuse reflectance (RD) of PMMA spin coated on top of the BK7 glass and BK7 glass at different wavelengths.

6.3. Total integrated scattering (TIS)

Total integrated scattering is well suited for measuring surface roughness [62, 63].

The Labsphere RT-060 integrating sphere system, with a double beam procedure, was used to measure the reflection and transmittance.

Scattering is assumed to originate solely from the top surface, but scattering in the bulk material, or scattering from the second surface, may influence the measurements. Furthermore, the interface effects between films in multilayer coatings are not included in the simple theory. Ideally, the TIS method includes all the theoretically possible light, scattered from the specular direction, to grazing angles along the surface. The so-called 'scalar scattering theory' [56] relates the specular reflection, R_s , of a surface, and total reflectance, R_T (which includes diffuse reflectance, R_D) to rms surface roughness, δ , and incident wavelength, λ :

$$\frac{R_s}{R_D} = \exp\left(-\left(\frac{4\pi\delta\cos\theta_0}{\lambda}\right)^2\right), \quad (138)$$

where θ_0 is the angle of incidence of light on the surface. In equation 138, it is assumed that the rms roughness is small when compared to the wavelength of the incident light.

Three types of measured reflectance are used in the calculation: specular reflectance, R_s , diffuse reflectance (all scattered light), R_D , and total reflectance, R_T . The relationship between them is:

$$R_T = R_s + R_D, \quad (139)$$

The rms is then calculated from the TIS using a rearrangement of equation 102:

$$TIS = \frac{R_D}{R_T} = \frac{(R_T - R_s)}{R_T} = 1 - \exp\left(-\left(\frac{4\pi\delta}{\lambda}\right)^2\right) \approx \left(\frac{4\pi\delta}{\lambda}\right)^2, \quad (140)$$

assuming the light to be normally incident on the surface and $\delta \ll \lambda$.

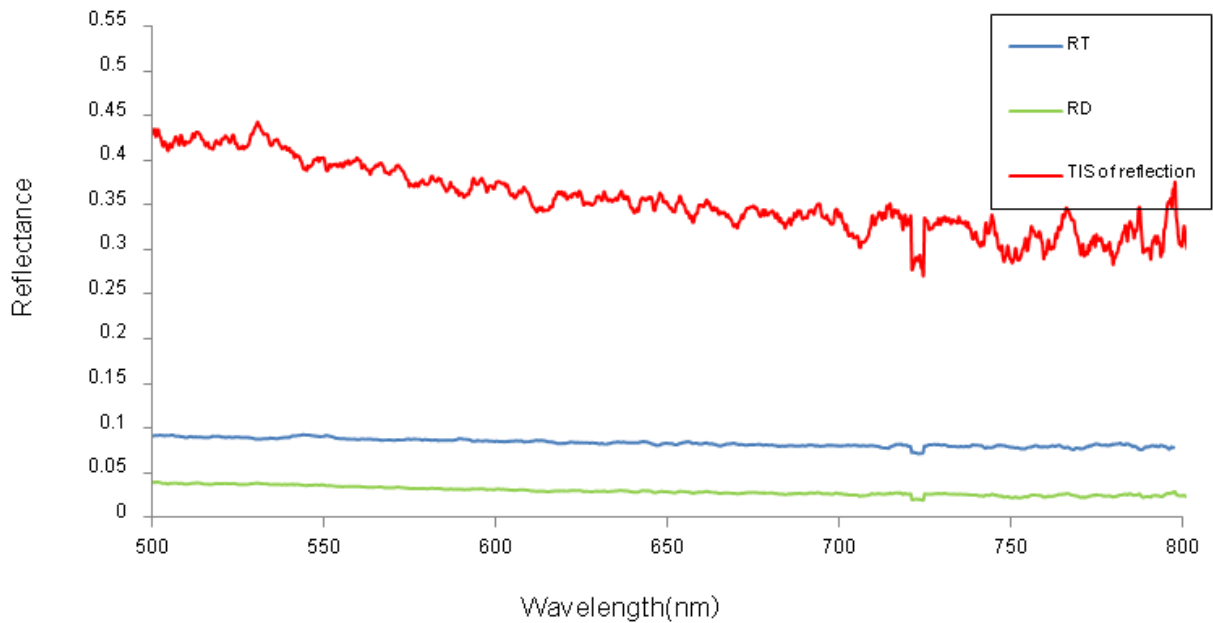


Figure 47: Comparison between diffuse reflection (RD), total reflection (RT) with TIS of reflection of PMMA spin coated on top of the BK7 glass and BK7 glass at different wavelengths.

Figure 47 shows a comparison between the diffuse reflection, and the total reflection with TIS, of reflection. The value of TIS is higher than that of diffuse reflection, RD, and total reflection, RT, showing that we have some scattering of the light, away from the reflection in the PMMA sample, spin coated on top of the glass substrate.

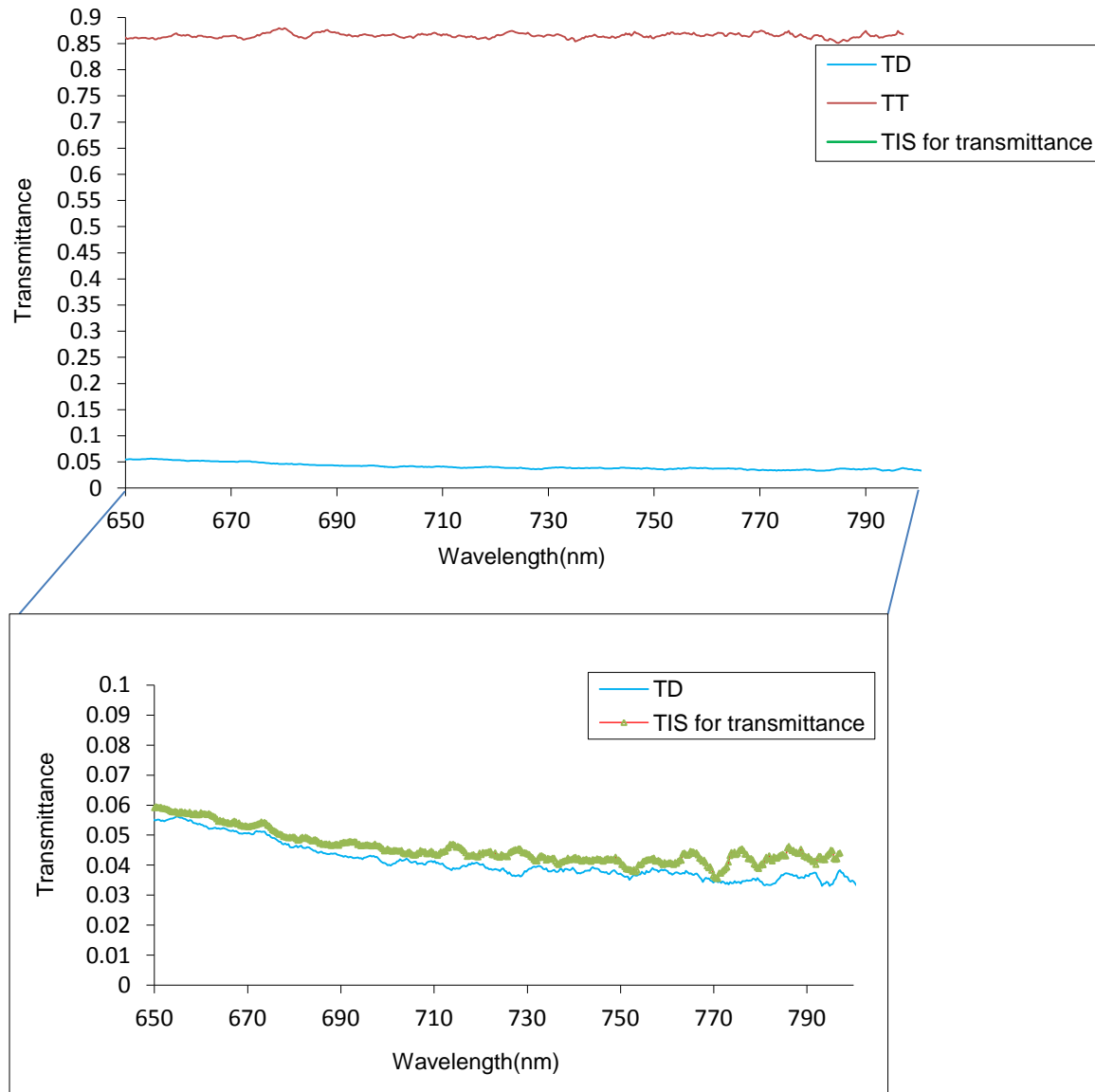


Figure 48: Comparison between diffuse transmittance (TD), total transmittance (TT) with TIS of transmittance of PMMA spin coated on top of the BK7 glass and BK7 glass at different wavelengths.

Figure 48 shows a comparison between diffuse transmittance, the total transmittance, and the TIS of transmittance, showing that the total transmittance, TT, is 17 times higher than diffuse transmittance, TD and TIS from transmittance.

Figures 47 and 48 show that there is more scattering of the light away from the reflection than in transmission.

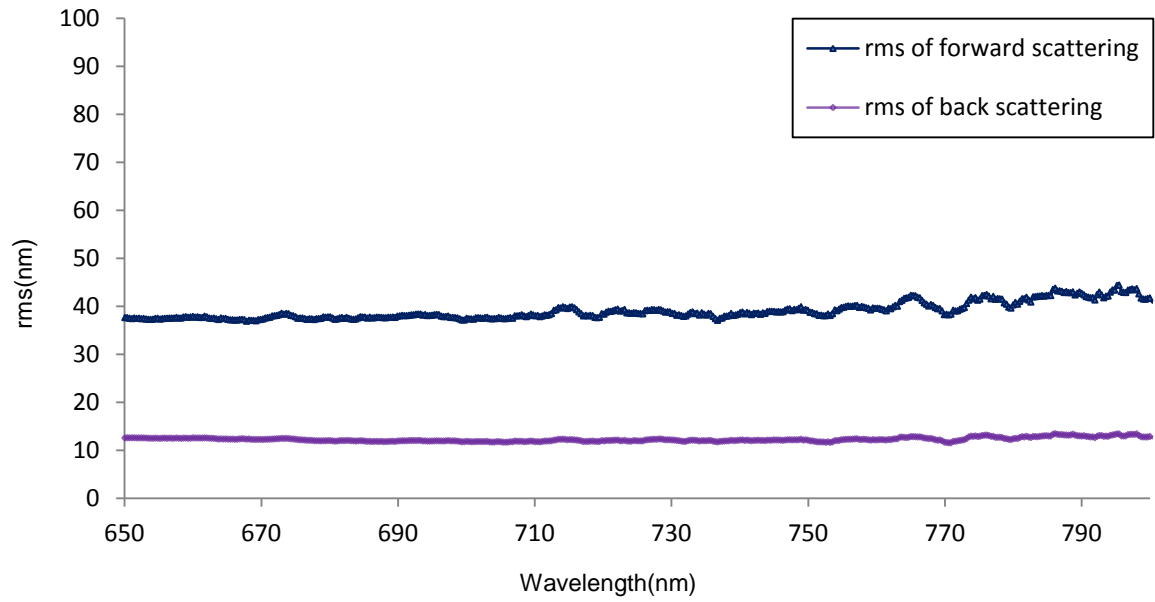


Figure 49: Comparison between rms of forward and back scattering of PMMA spin coated on top of the BK7 glass and BK7 glass at different wavelengths.

Figure 49 shows the rms of forward and backward scattering, demonstrating that the majority of the roughness in the fluorescence solar collector is caused by the roughness of the front surface. The value of the roughness was also measured by the AFM method (figure 50), and agreed well with the TIS method for roughness measurement.

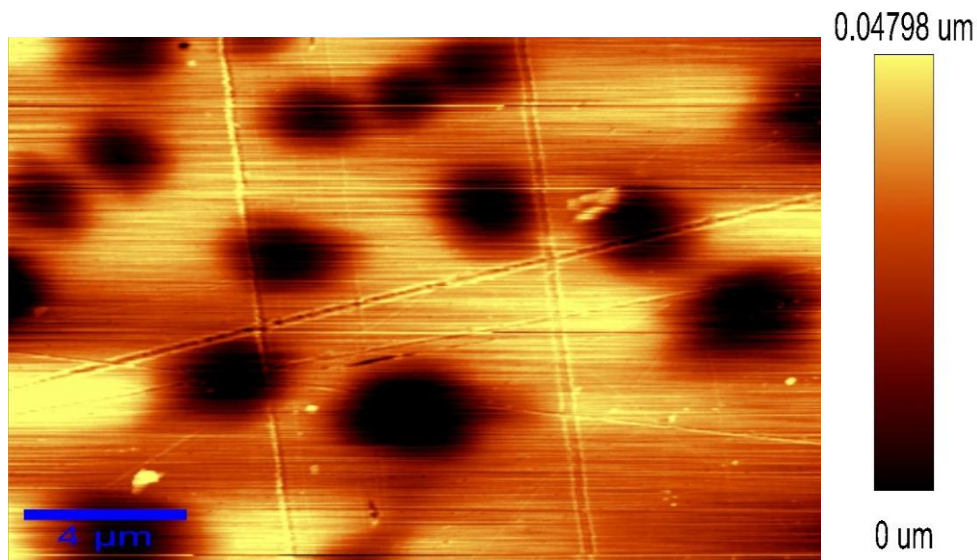


Figure 50: AFM imaging from the top surface.

6.4. Scattering coefficient measurement with an integrating sphere

In collimated transmittance, a narrow collimated beam passed through the sample in such a way that any photons scattering off the sample were undetected by the detector. The collimated transmittance can be written in terms of the absorption and scattering coefficients (bulk and surface), following Beer's law.

The intensity of this non-scattered, non-absorbed light, T_s , can thus be expressed by [64, 65, 66]

$$-\ln(T_s) = (\mu_{abs} + \mu_{sca})L, \quad (141)$$

where L is the sample thickness. If we measure T_s in the wavelength that the sample doesn't absorb, the value of $\mu_a=0$. The μ_{sca} , which includes the surface and bulk scattering (equation 141) for the spin coated dye (F305), and PMMA on top of the BK7 glass, was shown in figure 51. The thickness of the glass was 1mm. As we can see, the scattering coefficient from PMMA, spin coated on top of the BK7 glass, was similar to that of spin coated dye (F305). The result for PMMA on top of the BK7 glass, in the wavelength in which dye doesn't absorb, shows that the main problem of scattering in FSC is caused by PMMA.

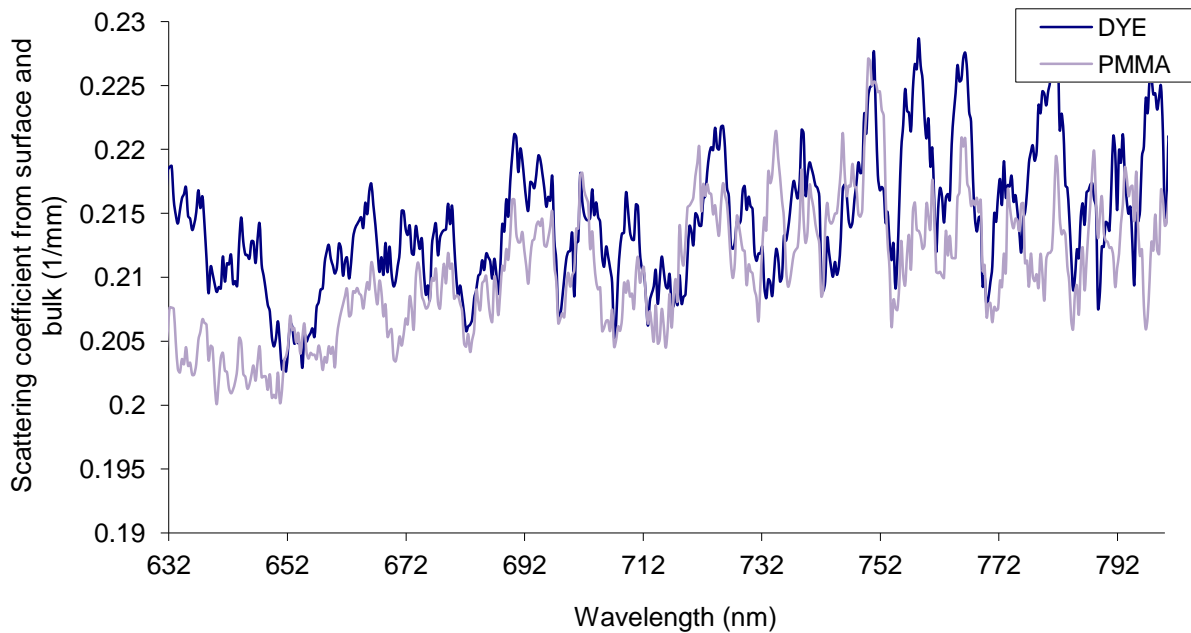


Figure 51: Scattering coefficient measurement from the surface and bulk, with the integrating sphere of dye (F305) mixed with PMMA and PMMA spin coated on top of the BK7 glass.

6.5. Roughness measurement using the angular dependence method

A surface can be considered to be slightly rough, or nearly smooth, if its rms roughness is much smaller than the wavelength, λ , of the light with which it is illuminated,

$$\delta \ll \lambda, \quad (142)$$

The intensity of the scattered light is a function of the rms roughness, whereas the angular distribution is mainly determined by angle-resolved scattering measurements.

Generally, it is sufficient to only know the rms surface roughness; this can be more easily obtained from measurements of the total integrated scattering (TIS).

The diffusely scattered portion of the light, incident on a surface, can be calculated from scalar scattering theory, which is based on the Kirchhoff diffraction integral [67].

When the surface roughness is much smaller than the wavelength, the TIS is given by [61, 63]

$$TIS = 1 - \exp[-(4\pi\delta \cos(\theta_i) / \lambda)^2], \quad (143)$$

where θ_i is the angle of incidence, and TIS can be calculated by the angular dependence of light, and by using equation 102. By expanding the exponential in equation 143, we obtain:

$$\delta = (\lambda / 4\pi \cos(\theta_i)) \sqrt{TIS}, \quad (144)$$

This relationship is independent of the height distribution function, and equations (143) and (144) are normally used for surfaces covered with a single opaque layer.

The angular dependence of reflection was detected from the top surface at different incident angles (10° , 20° , 30° , and 40°) in 670nm, as shown in figure 52. In comparing the results, it can be seen that for the peak in I/I_0 , BRDF for all measurements was shifted to zero degrees. It seems that the shape of the scattering didn't change, and the amplitude of the scattered light was increasing, from 10° to 40° .

The roughness of the surface was calculated to be $0.0105\mu\text{m}$ at a 10° incident angle, by using equation 144, and the BRDF for different incident angles (10° to 40°), shown in figure 53. The

value of the BRDF was increasing from 10° to 40° when an increased in the angle of incidence increased the reflection of light. The roughness of the surface, however, remained constant, as it was independent of the angle of incidence of light.

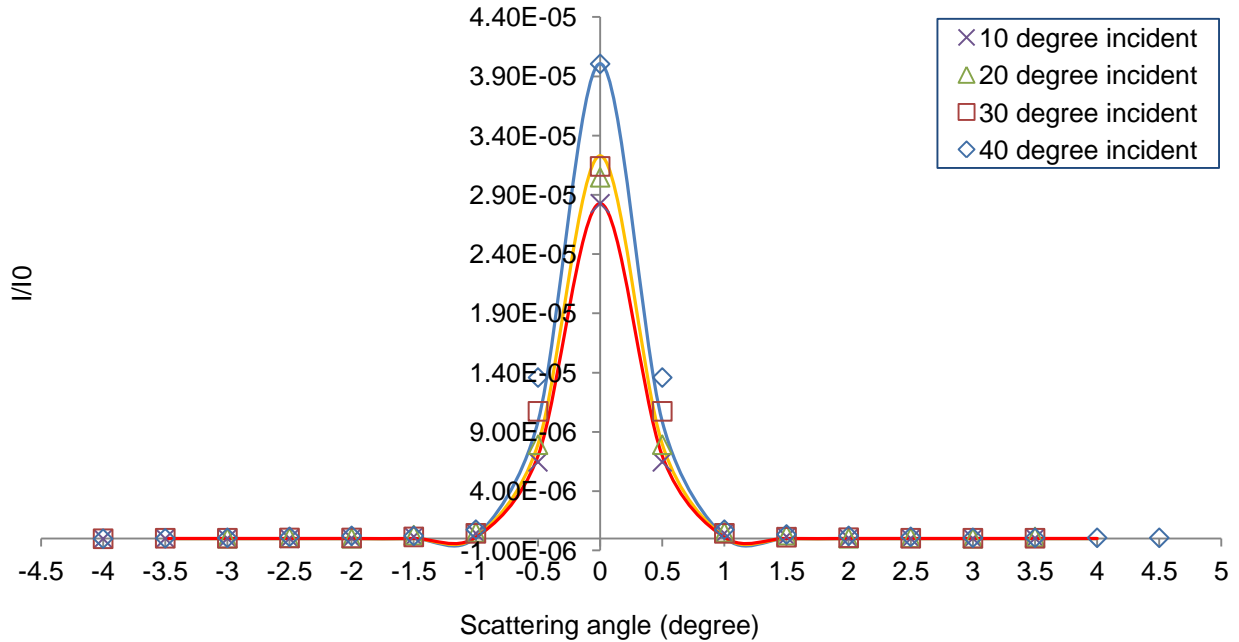


Figure 52: Angular dependence of reflection of I/I_0 for different incident angles in 670 nm.

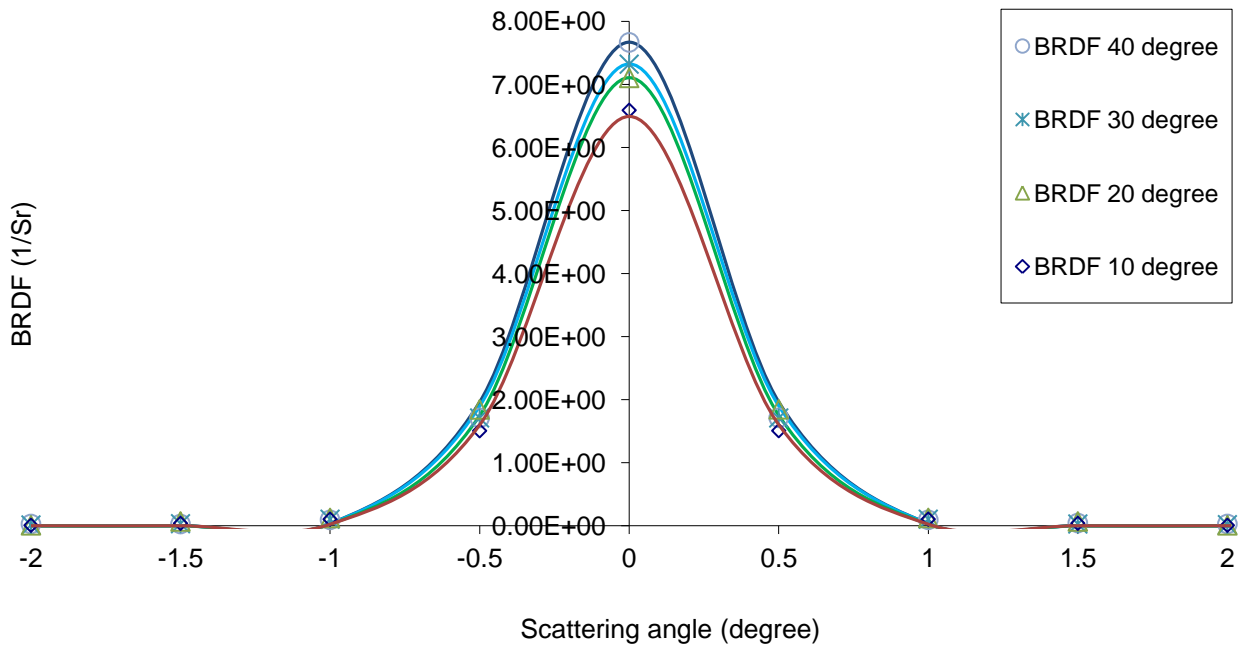
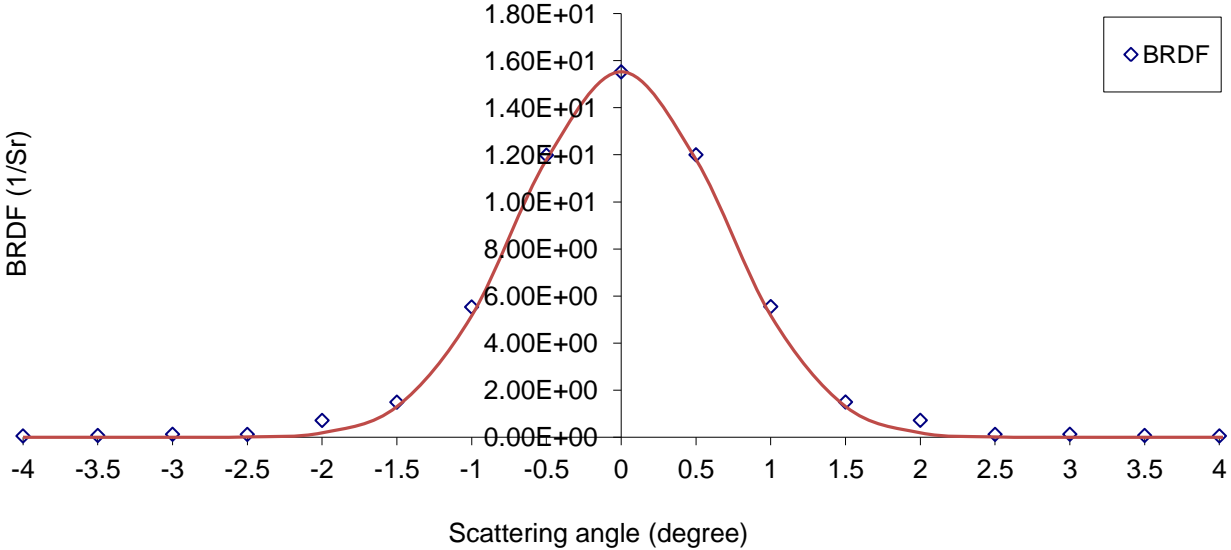
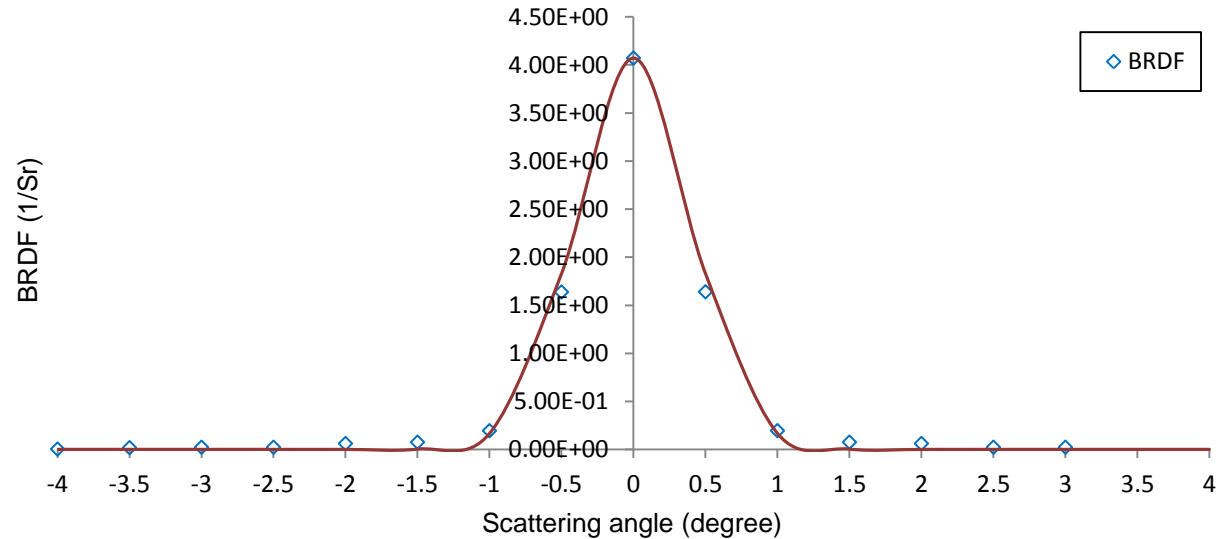


Figure 53: BRDF measurement for incident angle of 10°, 20°, 30° and 40°. The wavelength of incidence was 670 nm.

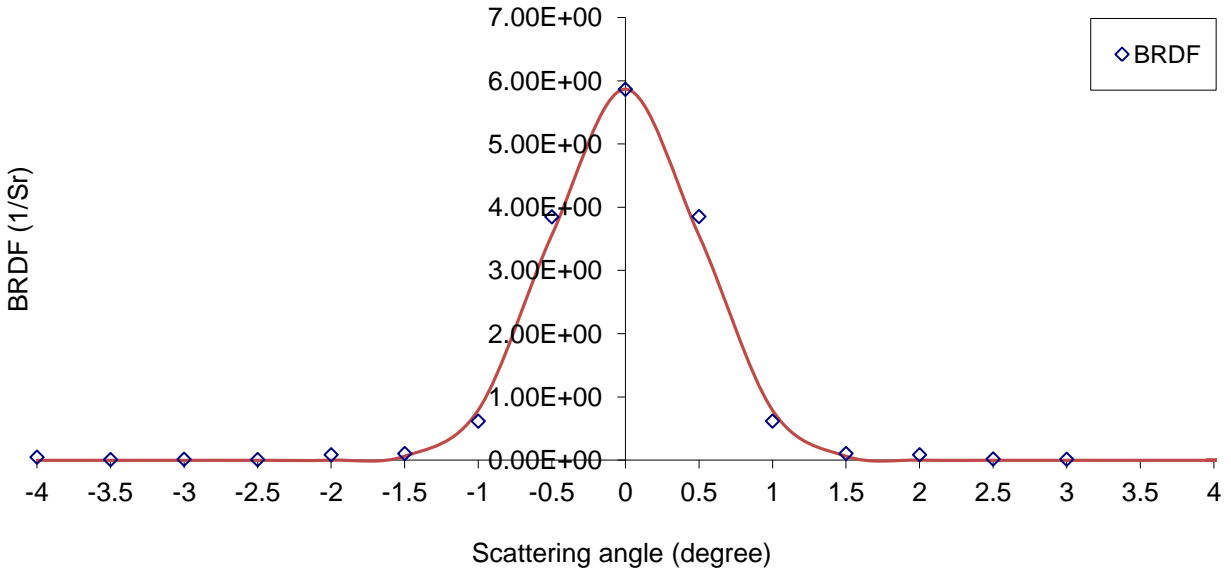
The roughness of the surface was measured at different positions on the surface, at 10° incident light (figure 54). The surface roughness was between 0.01μm and 0.030μm, and had a value similar to AFM, and the integrating sphere measurement in some positions of the sample.



(a)



(b)



(c)

Figure 54: BRDF in different positions of the surface (a) roughness was calculated to be $0.030\ \mu\text{m}$; (b) roughness was calculated to be $0.0109\ \mu\text{m}$; (c) roughness was calculated to be $0.014\ \mu\text{m}$.

Conclusion

In this chapter, the results from measurements of total and diffuse reflectance and transmittance were presented. The value of the total transmittance was around 17 times larger than that of the diffuse transmittance, and the value of diffuse reflectance was around half of the total transmittance in spin coated PMMA, on top of the glass substrate. This indicates that the scattering from the top surface was higher than that from the back surface. The measured diffuse reflectance for the PMMA coated glass, and the bare glass sample, is shown in figure 46, and indicates that the PMMA layer cause

s scattering of light.

The roughness measurement from the top surface, in spin coated PMMA on top of the BK7 glass, with an integrating sphere and angular dependence methods, was in good agreement with AFM.

Chapter 7

The role of light scattering in the performance of Fluorescent Solar Collectors

Introduction

The intention of this chapter is to investigate the effect of the bulk scattering on the performance of FSC. With bulk scattering, the Modified Weber and Lambe and Batchelder models were discussed in 3 different ways, leading us to a new theory. The experimental setups for measuring the scattering inside of the fluorescence solar collector was introduced in this chapter. Further, the angular dependence of scattering setup, and calibration technique based on Mie scattering for particle sizing measurement, will be discussed in this chapter.

7.1. Theoretical Model and Photon Balance and scattering in the Collector

The up transitions per unit time, due to photons from the incident beam, can be written as the number of photons absorbed, and must be equal to the number of photons that can leave the collector *plus* the number of photon that they can reach the edge of the collector *plus* the number of photons they are not radiative, and therefore:

$$N_{abs}^{\circ} = N_{loss}^{\circ} + N_{work}^{\circ} + N_{nr}^{\circ}, \quad (145)$$

N_{abs}° is the number of photons absorbed per unit of time by the collector, from the incident solar beam. N_{loss}° is the photon flux emitted through the front surface, which is lost from the system. N_{work}° is the useful luminescent photon flux (number of photon per unit of time due to the dye emission and scattering) that illuminates the solar cell. N_{nr}° is a non-radiative, de-excitation of the luminescent medium (figure 55).

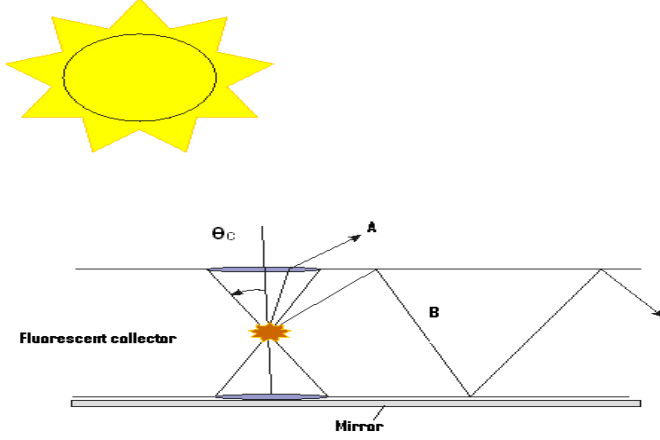


Figure 55: Schematic diagram of a fluorescent collector, showing the double escape cone with apex angle, θ_c . In the simplified theory used in this paper, rays (A) form the photon flux N_{loss}^o , which escapes from the front face of the collector, and rays (B) contribute to the flux N_{work}^o which illuminates the solar cell.

The useful photon flux, N_{work}^o , is denoted by the analyses of Weber and Lambe, and is equal to:

$$Q_1 = (1 - P)(1 - R_s) = \frac{1}{4\pi L} \int_0^L dy \int_0^\pi d\phi \int_0^{\pi - \theta_c} \sin \theta d\theta \{ \exp[-\alpha_e(L - y)/(\sin \theta \sin \phi)] + \exp[-\alpha_e(L + y)/(\sin \theta \sin \phi)] \}, \quad (146)$$

where θ and ϕ are the usual spherical, polar angles, defining the direction of emission. Considering the scattering in the form of bulk, $\alpha_e = \mu_{sca} + \alpha_{abs}$, and $(1 - P)(1 - R_s)$ is the flux trapped within the collector by total internal reflection. The μ_{sca} is the bulk scattering coefficient (chapter 3).

Bulk scattering in this model is assumed to be isotropic, and α_{abs} is the absorption coefficient. The flux, N_{loss}^o , represents photons emitted within a double 'escape cone' with a half apex angle of $\theta_c = \sin^{-1}(\frac{1}{n})$, where n is the refractive index of the collector material, as shown in figure 55.

If we have the isotropic emission by dye and isotropic scattering, P is the solid angle of the escape cone divided by 4π [40].

The photons that are lost from the FSC is given by:

$$N_{loss}^o = \frac{1}{\tau_{rad}} P(1 - \bar{R}_s) N^*, \quad (147)$$

where \bar{R}_s represents the probabilities of reabsorption of photons and re-scattered photons within the escape cone. τ_{rad} is the radiative lifetime of the dye, and N^* is the number of molecules in the excited state.

$$\frac{N^*}{\tau_{tot}} = \frac{N^*}{\tau_{rad}} + \frac{N^*}{\tau_{nr}}, \quad (148)$$

τ_{tot} is the total lifetime and τ_{nr} is the non-radiative lifetime, therefore

$$N_{abs}^{\circ} = I_0 Q_A = \frac{1}{\tau_{rad}} N^* (1-P)(1-R_s) + \frac{1}{\tau_{rad}} P(1-\bar{R}_s) N^* + \frac{N^*}{\tau_{tot}} - \frac{N^*}{\tau_{rad}} = \frac{N^*}{\tau_{tot}} - \frac{N^*}{\tau_{rad}} R_s (1-P) = \frac{N^*}{\tau_{tot}} - \frac{N^*}{\tau_{tot}} \phi_f (R_s (1-P) + P\bar{R}_s), \quad (149)$$

The R_s represents the probabilities of reabsorption of scattered photons outside the escape cone, while ϕ_f is the probability of dye emission in 4π [40].

Q_A is the absorption efficiency, given by:

$$Q_A = \frac{N_{abs}^{\circ}}{I_0}, \quad (150)$$

The photon collection efficiency in the collector can be written as:

$$Q_c = \frac{N_{work}^{\circ}}{N_{abs}^{\circ}} = \frac{Q_t}{1 - \phi_f (R_s (1-P) + P\bar{R}_s)} = \frac{(1-P)(1-R_s)}{1 - \phi_f (R_s (1-P) + P\bar{R}_s)}, \quad (151)$$

\bar{R}_s can be ignored, as it is very small for the single dye, and for the size of the collector used in this work.

The optical efficiency is given by

$$\eta = \frac{N_{work}^{\circ}}{I_0} = Q_{sca} + \phi_f \frac{N_{work}^{\circ}}{N_{abs}^{\circ}} \times \frac{N_{abs}^{\circ}}{I_0} = Q_{sca} + \phi_f Q_c \times Q_A, \quad (152)$$

and can be written as the total amount of photons that can reach the edge of the collector

$$\frac{\overbrace{\eta_{sca} (1-P)(1-R_s)}^{\text{Because of scattering}}}{1 - \phi_f R_s (1-P)} + \frac{\overbrace{\phi_f (1-P)(1-R_s) Q_A}_{\text{Because of dye emission}}}{1 - \phi_f R_s (1-P)}$$

$$= \frac{(1-P)(1-R_s)}{1-\phi_f R_s(1-P)} (\eta_{sca} + \phi_f Q_A) \quad (153)$$

Therefore, the solar photons absorbed by dye as a fraction of $(\eta_{sca} + \phi_f Q_A)$ can be luminescence inside of the collector, while the scattering coefficient is independent of the dye absorbance.

η_{sca} is the scattering efficiency and can be calculated as:

$$\eta_{sca} = \mu_{sca} T, \quad (154)$$

where T is the thickness of the sample.

7.2. Photon collection efficiency with bulk scattering in the Batchelder model

Q_c is defined as a fraction of the absorbed and scattered solar photons that succeed in being transported to the FSC-PVC interface.

If we ignore self absorption in this case, the solar photon absorbed by the dye, and the fraction $(\phi_f + \eta_{sca})$, will be luminescence, and of those, the fraction $(1-P)$ will be trapped via total internal reflection and transported to the FSC-PVC interface. As such, in this idealised case Q_c , or the first generation of emission, it is given by:

$$Q_{idealized} = (1-P)\phi_f \alpha_{abs} l + (1-P)\mu_{sca} l = (1-P)\phi_f \alpha_{abs} l + (1-P)\eta_{sca}, \quad (155)$$

If the absorption and emission bands now overlap, the dye is capable of absorbing its own luminescence, and the FSC act like filters that attenuate the luminescence, resulting in the absorption of solar photons. Thus, in FSC, the light absorbed can then re-luminescence, and be scattered in an arbitrary direction, most of which will again be trapped within the plate, generating a number of different generations of luminescence: the first generation is the luminescence resulting from the initial absorption and scattering of the solar photons; the second generation is the luminescence resulting from the self-absorption and scattering of the first generation photons; the third generation is the luminescence resulting from self-absorption and scattering of the second generation photons; and so forth. So the fluorescence was divided into various components Q_1, Q_2, Q_3 , etc. depending on how many times the photons had been

absorbed. In this model we ignore transport losses in the form of matrix absorption, and incomplete internal reflection due to the surface roughness. We can see that the fraction of the first generation, or Q_1 , that can reach the LSC-cell is $(1-P)(1-R_s)$, given by Weber and Lambe's equation 146. Those self-absorbed for the first time is $\bar{R}_s P + R_s(1-P)$.

The fraction of fluorescence emitted from the higher generation introduces two parameters: R_s , the average probability that luminescence outside the critical cones will be self-absorbed, or scattered, over a path length, L ; and \bar{R}_s , the average probability that luminescence and scattered light inside the critical cones will be self-absorbed, or re-scattered. These parameters are related to the n^{th} order generation fluorescence as follows:

$$Q(n) = Q_1 [\phi_f (\bar{R}_s P + (1-P)R_s)]^{n-1}, \quad (156)$$

The total collection efficiency of the system, which includes all components from higher generation emission, is given by:

$$Q_{c,Bat} = Q_1 + Q_2 + Q_3 + \dots = \frac{Q_1}{1 - \phi_f [\bar{R}_s P + R_s(1-P)]}, \quad (157)$$

The value of \bar{R}_s is very small for the single dye, and we can therefore ignore it.

7.3. Number of emitted photons

To calculate the number of emitted photons after I_0 , the incident photon, that are absorbed per unit time, with fraction Q_A , we consider the probability of a molecule between two energy levels in equilibrium: A, ground level, and B, excited level (figure 56).

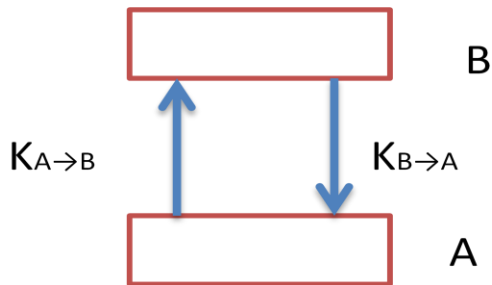


Figure 56: Two energy levels in equilibrium. A is the ground state level and B is the excited state level.

The total number of transitions between the two levels in equilibrium per unit of time can be written as:

$$k_{A \rightarrow B} = I_0 Q_A + \frac{1}{\tau_{rad}} N^* R_s (1 - P), \quad (158)$$

$k_{A \rightarrow B}$ is the number of photons that they can absorb

$$k_{B \rightarrow A} = \frac{1}{\tau_{tot}} N^* \quad (159)$$

$k_{B \rightarrow A}$ is the number of photons that can be emitted inside of the collector and be reabsorbed, or scattered, along the path to the edge.

The principle of the detailed balance gives us

$$k_{A \rightarrow B} = k_{B \rightarrow A}, \quad (160)$$

Therefore

$$\frac{1}{\tau_{tot}} N^* = I_0 Q_A + \frac{1}{\tau_{rad}} N^* R_s (1 - P)$$

$$\tau_{tot} = \phi_f \tau_{rad}$$

$$\frac{1}{\tau_{tot}} N^* = \frac{I_0 Q_A}{1 - \phi_f R_s (1 - P)}, \quad (161)$$

where Q_A is

$$Q_A = \frac{\int_0^{\lambda_g} (1 - R_{front})(1 - \exp(-\alpha(\lambda)T)) N_{ph}(\lambda) d\lambda}{\int_0^{\lambda_g} I_0(\lambda) d\lambda}, \quad (162)$$

Here, R_{front} is the reflection from the front surface, T is the thickness of the collector, and N_{ph} is the photon flux of the solar spectrum, which is the approximation of the blackbody at 5500 K, and λ_g is the cut off wavelength of the semiconductor placed at the edge of the collector.

7.4. Photon flux in the edge of the fluorescent solar collector

If we consider the fluorescent solar collector as perfectly flat and, with isotropic bulk scattering of light inside the collector, no absorption of light except of that by the dye, we can write:

Photons flux that can reach the edge of the collector from the absorption of dye =

$$\frac{N^*}{\tau_{tot}} \phi_f (1-P)(1-R_s) I_0, \quad (163)$$

where ϕ_f is the probability of dye emission in 4π , and $(1-P)$ is the $\frac{\Omega}{4\pi}$ probability outside of the escape cone. The $(1-R_s)$ can be calculated from equation 146.

The probability that the scattered photon flux can reach the edge of the collector

$$\eta_{sca} (1-P)(1-R_s) \frac{I_0}{1-\phi_f R_s (1-P)}, \quad (164)$$

where η_{sca} is the scattering probability in 4π .

Therefore, the total photon flux that can reach the edge of the collector is:

$$\eta_{sca} (1-P)(1-R_s) \frac{I_0}{1-\phi_f R_s (1-P)} + \frac{I_0 Q_A}{1-\phi_f R_s (1-P)} \phi_f (1-P)(1-R_s), \quad (165)$$

7.5. Goniometer setup

Schematic of the experimental setup

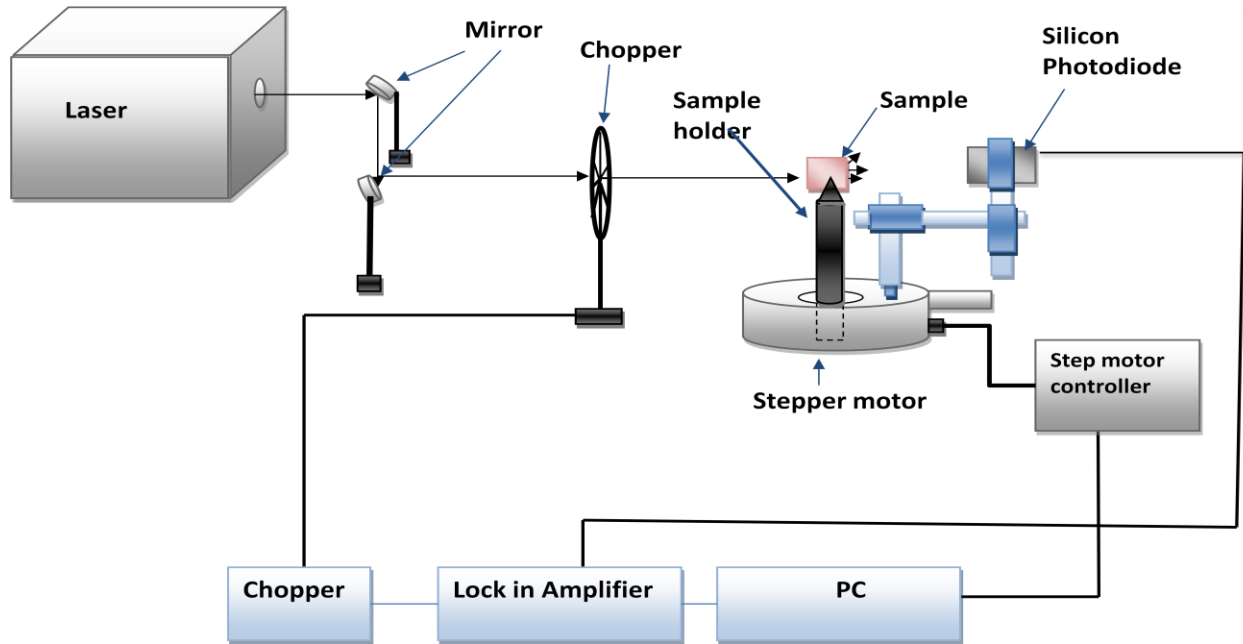


Figure 57: Schematic of the experimental setup for the measurements of scattering.

The calibration of the goniometer was carried out with a known sized sphere on top of the thin film layer of R6G dye, mixed with PMMA (6 μm diameter sphere, measured by an electronic microscope), and 2 μm diameter, standard sized PMMA dissolved in water.

For the characterisation of light scattering, the samples were illuminated with a laser beam, impinging from one side-edge of the glass. The sample was placed at the centre of a circular goniometer table illuminated with a laser. A silicon photodiode (SM05PD1A, Thorlabs) was mounted at the edge of the table, as shown in figure 57. The distance between the sample and the detector was 27cm, and a pinhole with diameter of 1mm was placed in front of the silicon photodiode, giving a solid angle for collection of 0.2°. A frequency of 185 Hz was applied, via a chopper to the beam, with the current detected by a photodiode connected via a lock-in amplifier (SR810). The lock-in amplifier was used to decrease the noise of the measurement by locking in to the chopper frequency, and the average of the two current measurements captured 1 second apart, and recorded. The interface of this setup was programmed in the Labview (8.6) software.

A sample holder was fixed to the centre of the goniometer table, while the laser beam was aligned perpendicular to the surface of the sample, with the photodiode rotatable around the table for measuring the scattered intensities at different angles. The scattered light intensity could be measured between 0° and 180°, with a scattering angle increment of 0.5°.

7.5.1. Laser beam radius measurement

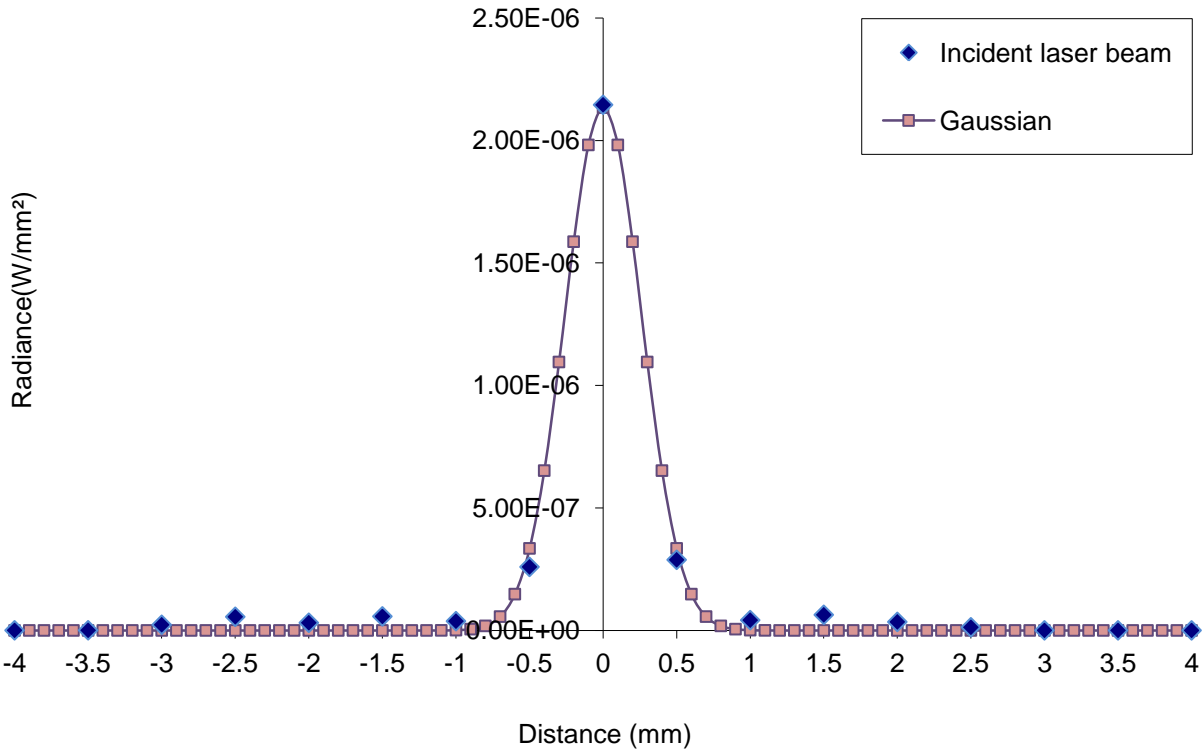


Figure 58: Irradiance intensity of the laser beam in different positions fitted with a Gaussian beam.

In optics, and particularly in laser physics, laser beams regularly occur in the form of Gaussian beams, named after the mathematician and physicist, Johann Carl Friedrich Gauß. The optical intensity of the beam, with power P , can be described with a Gaussian function [62]:

$$I(r, z) = \frac{P}{\pi w(z)^2 / 2} \exp\left(-2 \frac{r'^2}{w(z)^2}\right), \quad (166)$$

where the beam radius $w(z)$ is the distance from the beam axis where the intensity drops to 1/e of the maximum value, and r' is the distance from the centre of the beam. The optical intensity

(irradiance), I , of a laser beam, is the optical power per unit area, transmitted through an imagined surface perpendicular to the propagation direction. The units of the optical intensity (or irradiance) are W/m^2 or (more commonly) W/cm^2 .

For a laser beam with a constant intensity over some area, and zero intensity outside, the intensity is simply the optical power, P , divided by the beam area.

After fitting the irradiance of a laser beam with the Gaussian beam (figure 58), the value of the beam width was calculated to be 0.6° . This value is used as the error for the angular scattering measurements.

7.5.2. Photodiode calibration

The measurement of any unknown source with a spectroradiometer, or the response of an unknown detector, must be compared against a standard, such as those obtainable from the National Physical Laboratory.

Such measurements require a measurement of a standard, prior to measurement of the unknown device. An example of this can be seen in figure 59. The silicon detector was illuminated monochromatically with a Bentham IL1 quartz halogen light source lamp DMc150 double monochromator, and was measured with a Bentham spectrometer. The spectral responsivity of the 3.6×3.6 mm SM05PD1A silicon photodiode, and the silicon photodiode power meter, were determined with comparison to a standard device (Dh-Si calibrated photodiode) over a wavelength of 400nm to 1100nm, at an interval of 1nm and at a distance of 1mm.

Dh-Si photodiode was calibrated with a calibration traceable to the PTB, Germany, and an uncertainty of $\pm 4\%$ over the 380-900nm wavelength range.

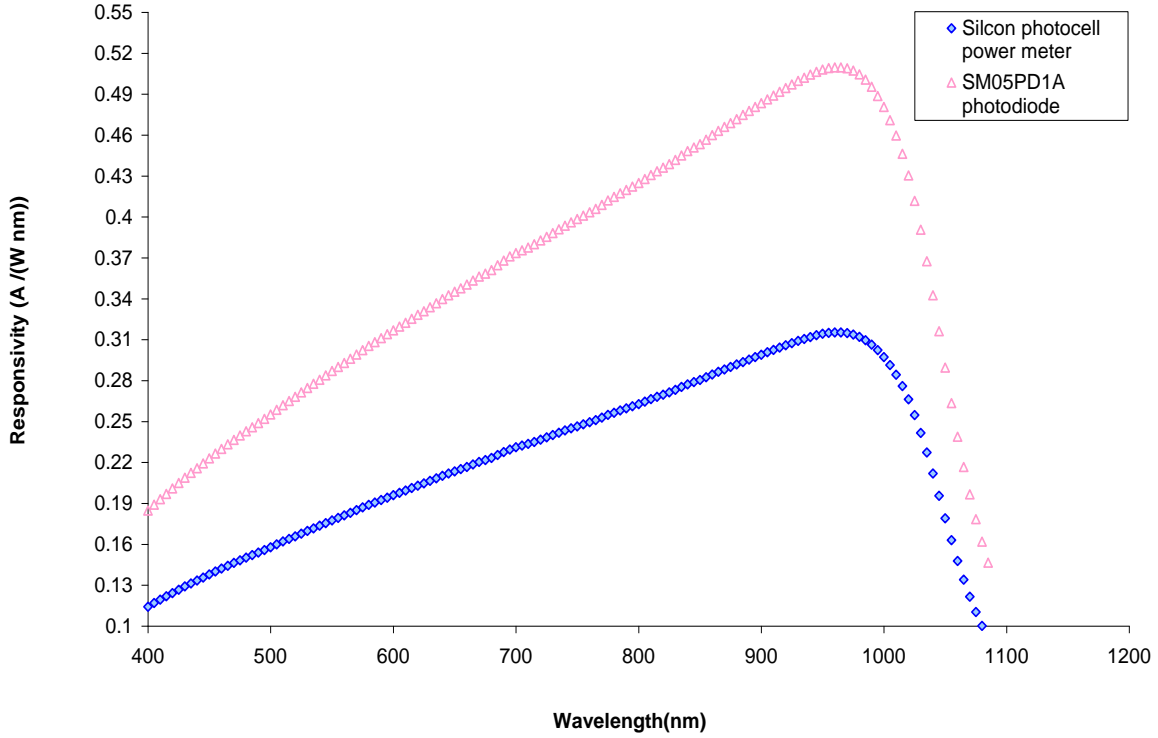


Figure 59: Spectral responsivity of DH-Si photodiode compared to calibration data, SM05PD1A mounted Si-photodiode, and a silicon photocell power meter sensor.

The responsivity, R_λ , of a photodiode is a measure of its sensitivity to light, and is defined as the ratio of the photocurrent, I_p , to the incident light power, P , at a given wavelength.

$$R_\lambda = \frac{I_p}{P}, \quad (167)$$

7.5.3. Goniometer calibration

To demonstrate that the goniometer was functioning properly, measurements were made on $2 \pm 0.08 \mu\text{m}$ average diameter Polystyrene spheres, dispersed in water to a concentration of 2 wt% (Sigma Aldrich).

The scattering phase function can be calculated, experimentally, as [29]

$$\rho(\theta) = \frac{I}{I_0} / \int_0^{2\pi} \frac{I}{I_0} \sin(\theta) d\theta, \quad (168)$$

where θ are the scattering detection angles, I is the irradiance of the scattered light, and I_0 is the irradiance of the incident.

The scattering phase function was measured and fitted with the Mie scattering model (chapter 3). A MATLAB version of Mie theory, for homogeneous spheres, by C. Maetzler in 2002, based on the appendix in Bohren and Huffman (1982), was used for the Mie theory calculations. The scattering phase function for the 2 μm spheres of PMMA in water was measured and fit the Mie theory model well, for spheres of diameter 1.9 μm (figure 60). The differences indicate the uncertainty in the measurements for this technique.

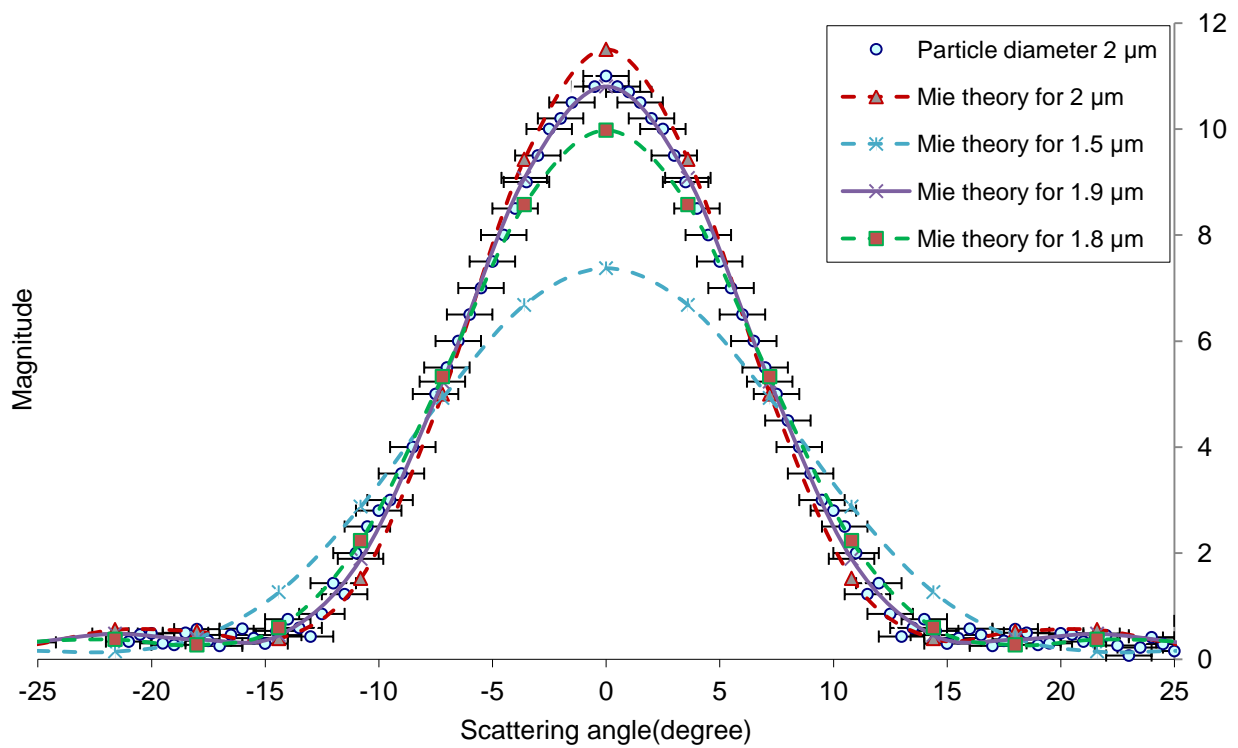


Figure 60: Particle size measurement of 2wt% aqueous suspension PMMA, with an average diameter of 2 μm , and compared with Mie scattering theory for spheres of different diameter. The error of this measurement was fixed at 0.6, with circles indicating the experimental results.

In the known sphere, on top of the thin film measurement (the R6G dye mixed with PMMA), the value of the experiment was in good agreement with the Mie scattering for the spheres of size 6.2 μm (figure 61, 62).

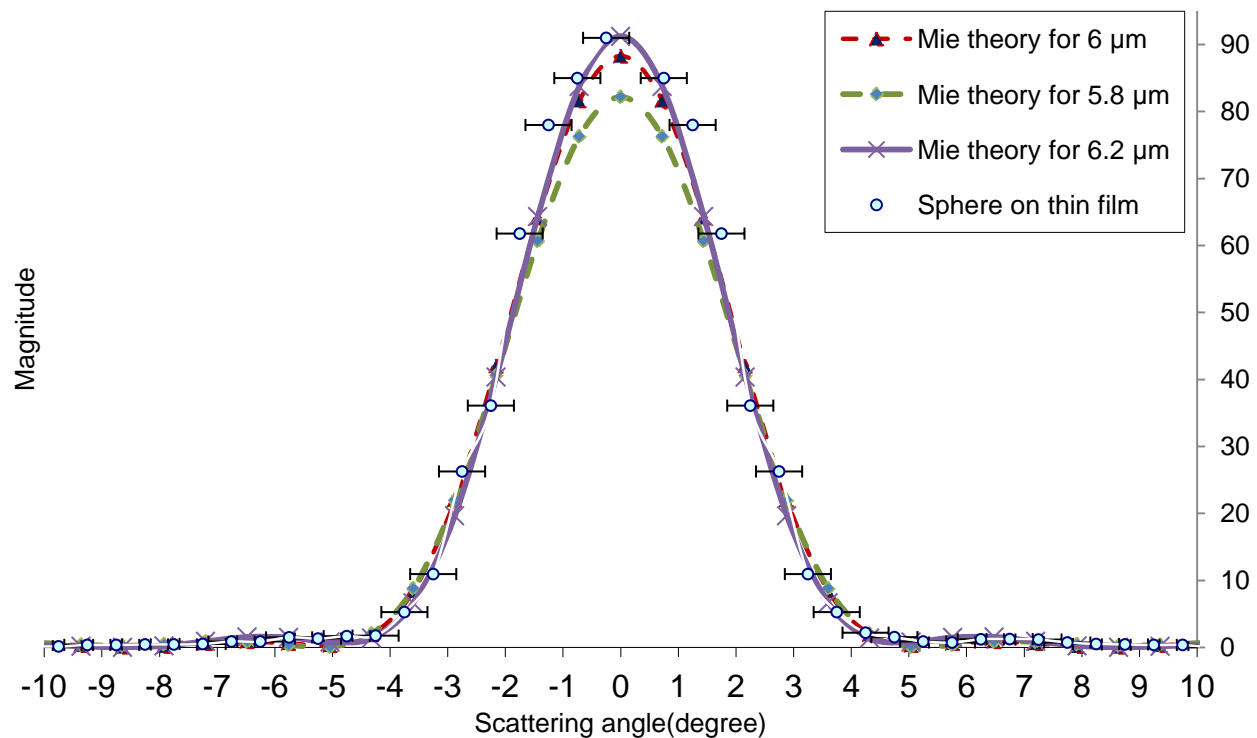


Figure 61: Particle size measurement of PMMA, with a diameter of 6 μm , and compared with Mie scattering theory for spheres of different diameter. The error of this measurement was fixed at 0.6, and the circles indicate the experimental results.



Figure 62: Image of sphere on top of the substrate, with an optical microscope (diameter 6-7 μm).

Conclusion

The analytical models reviewed in this chapter demonstrate the fundamental limitation of reabsorption, and bulk and surface scattering losses. It has been shown that the photon collection efficiency depends mainly on reabsorption probability. The photon balance, when the bulk scattering was based on the Weber and Lambe and Batchelder and Zewail models, was discussed, leading to a new theory.

In the goniometer calibration process, the measured scattering patterns, for a 2 μm average-diameter Polystyrene 2wt% dispersion in H_2O , agrees well with the theoretical Mie curve for a 1.9 μm diameter sphere. In a known sphere, on top of the thin film measurement, the value of the experiment is in good agreement with the Mie scattering, for the sphere's diameter size of 6.2 μm . The error of the measurement was 0.6, being the width of the laser beam.

Chapter 8

Results and discussion

Introduction

This work is the first time it has been carried out on a Fluorescent Solar Collector. In this chapter, we investigate the effect of surface scattering in realistic FSC devices, based on a dye-doped PMMA layer on top of a glass slide. The Modified Weber and Lambe and Batchelder models, when we have surface roughness in FSC, has led to a new theory, and is discussed in the following detail.

To characterise the photon transportation inside the collector, we monitor the angular distribution of a collimated light beam that enters the collector from the edge, after propagation and total internal reflection. We find that the surface scattering process at the surface, in homogeneities of a size of several μm , is described well by Fraunhofer diffraction. In experiments, the characterisation method consists of scaling of the edge fluorescence (figure 77) incident upon the solar cell, to the fluorescence contour, free from reabsorption losses. The edge fluorescence spectra are scaled by their relative flux of absorbed photons, and the loss-free fluorescence spectrum is approximated by the front fluorescence spectrum, as discussed in chapter 4. The reabsorption probability in this chapter is computed by the mean equation, 123, and compared to the reabsorption probability given by the Weber and Lambe model equation, and by the Modified Weber and Lambe model (chapter 4).

8.1. Scattering measurement of FSC by photon emission from the edge

From investigation, the main cause of scattering in the FSC was found to be spin coated PMMA on top of the glass sample. This section describes the method for measuring the scattering of PMMA, spin coated on top of the BK7 glass, by illumination from one edge at different incident angles, and detection from another edge (from 0° - 180°).

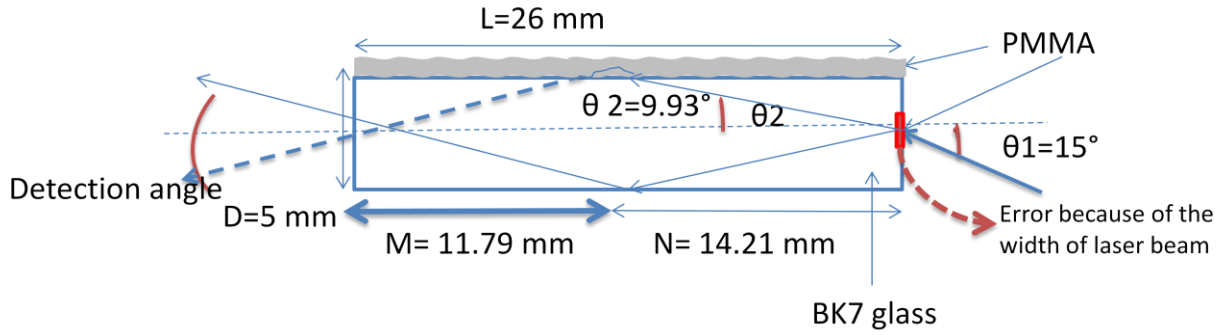


Figure 63: PMMA spin coated glass, illuminated with laser light from one edge, and the scattered light detected from another edge at different angles, $\theta_1=15^\circ$ and $N=14.21\text{mm}$, $M=11.79\text{mm}$. The error in this experiment was 0.6, which was the width of the laser beam.

BK7 glass substrates with dimensions of $26 \times 26 \times 5\text{ mm}^3$ were spin coated with PMMA, the samples then illuminated with a laser beam impinging from one side-edge of the glass. The transmitted light cone, emerging from the opposite edge of the glass, was measured using an angle scanning stage, as shown in figure 63. Several different angles of incidence were selected to vary the number of internal reflections, from zero to three.

The distance, M (distance from the detector inside of the glass) can be calculated by:

$$\frac{\sin \theta_1}{\sin \theta_2} = \frac{n_2}{n_1} \text{ for } n_2=1.5 \text{ and } n_1=1, \quad (169)$$

$$\tan \theta_2 = \frac{D}{2N}, \quad M=26-N, \quad (170)$$

and the value of N for different incident angles, from one edge, are shown in table 2.

If $N < 26\text{ mm}$, the probability that the light is totally internally reflected increases if $90-\theta_2$ is more than the critical angle.

In incident light of 0° , the light doesn't hit anywhere inside the collector. In 15° incident light, it can hit inside of the collector once, as shown in figure 63. Further, when we illuminate the glass or PMMA part from one edge, there is a probability that the light doesn't hit anywhere inside of the collector, caused by the width of the laser beam. In a 35° incident angle, the light hits the glass and PMMA once, but there is a probability of the light hitting the PMMA on the way out

from another edge of the collector. Additionally, the light can escape from the top when it hits the PMMA. At a 45° incident angle, the light can reflect three times inside of the collector. The laser beam width was 0.6°, and this number can be used as an error of the experiment.

Angle of incidence	No. of TIRs	Distance M(cm)
0°	N0	N.A.
15°	1	14.21
35°	2	6.04
45°	3	4.77

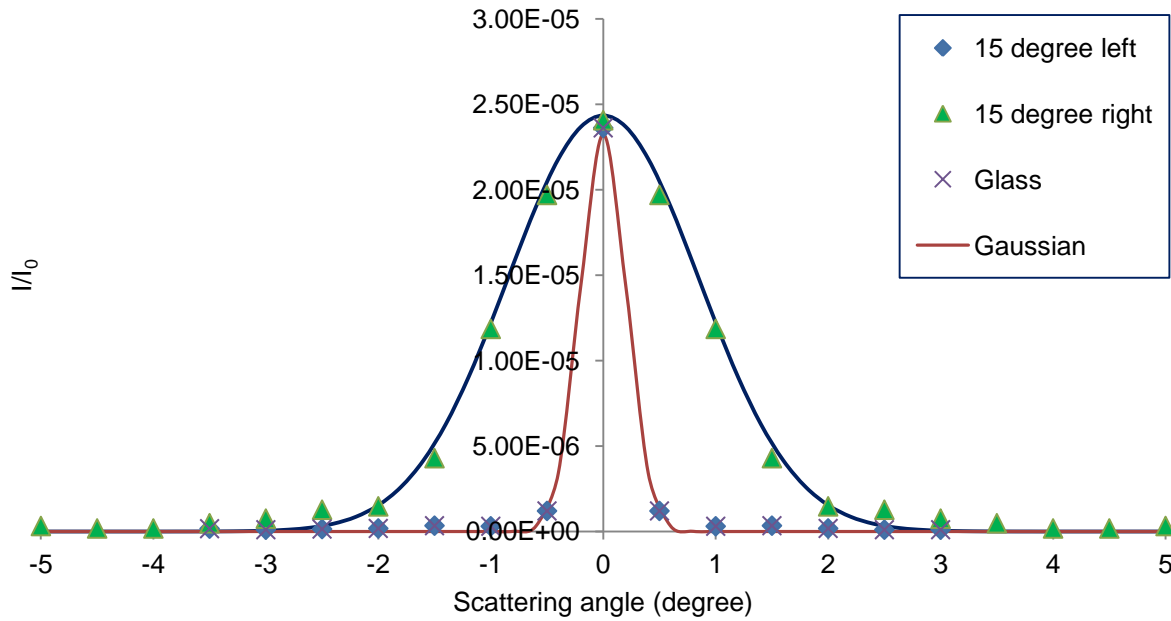
Table 2: Distance from the incident beam inside the glass for different incident angles. The error in this calculation is 0.6, which is the width of the laser beam.

In summary, for incident angles of less than 8.3 degrees, there is no reflection inside the collector. For incident angles from 8.3 to 24.6 degrees, there is one reflection inside of the collector, and for incident angles of 24.6 to 40.5 degrees, there are two reflections inside of the collector. For an incident angle of 45°, there are three reflections inside the collector.

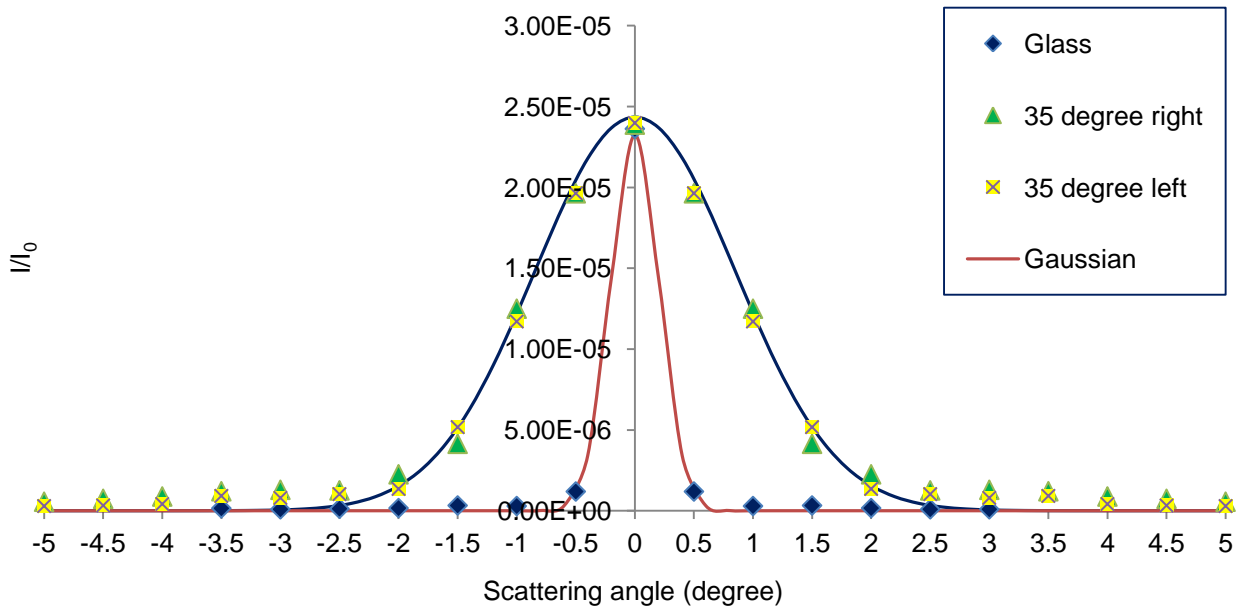
The ration of the irradiance of scattered light to the irradiance of the incident light (I/I_0), measured over a range of angles when we illuminate the sample from one edge at three different incident angles (15, 35 and 45 degrees) (see figure 64), is plotted in figure 65. To compare the results, the maximum intensity for all measurements was defined as 0°. Clearly, the light cone transmitted through the PMMA-coated FSC is considerably broadened, compared to a bare glass slide. For an incident angle of 15°, the glass part was fitted with an incident laser Gaussian function. As we can see, when the incident light angle through the PMMA portion is 15°, the I/I_0 is more than incident angle in the opposite part, which demonstrates the scattering from the PMMA layers in the fluorescent solar collector, as the light hits the PMMA once inside the collector (figure 64a).

The value of I/I_0 for 35° illumination, from the edge to the PMMA side of the glass and the opposite side, are similar, and it seems that the light can hit the PMMA and the glass side once, in both conditions (figure 64b).

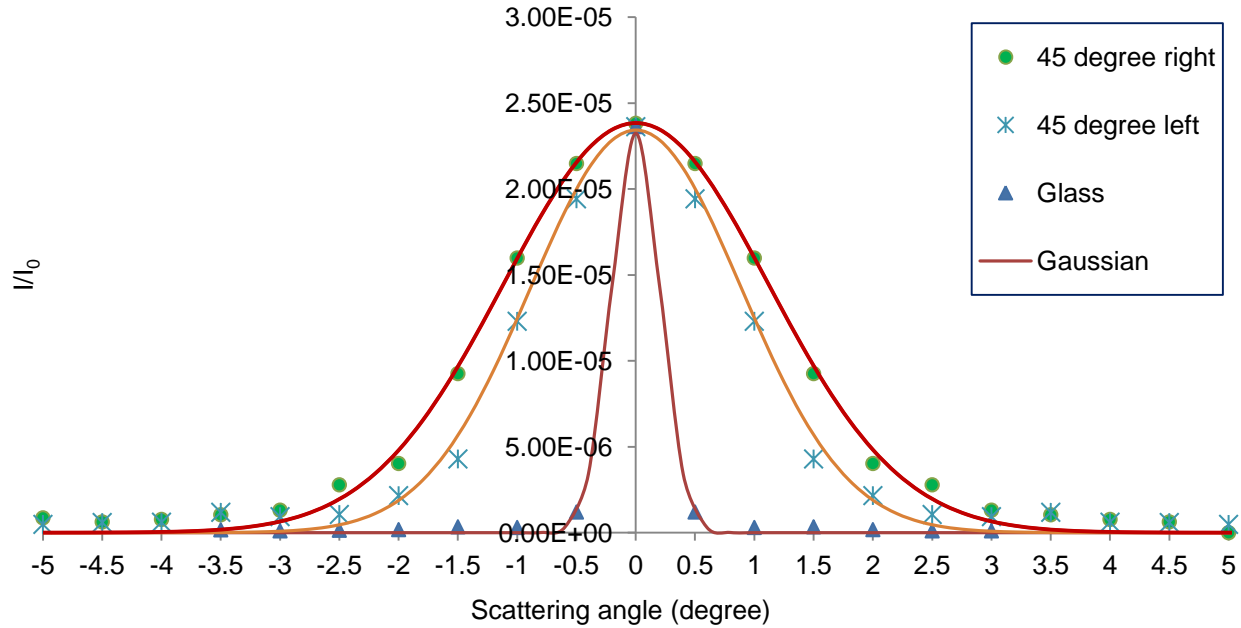
For I/I_0 at 45° incident light, the light can hit the PMMA twice and the glass once, if the incident is through the PMMA. For the incident light in the opposite part, it can hit the glass twice, and the PMMA once. Figure 64c shows that the width of the scattering increases when the light hits the PMMA twice



(a)



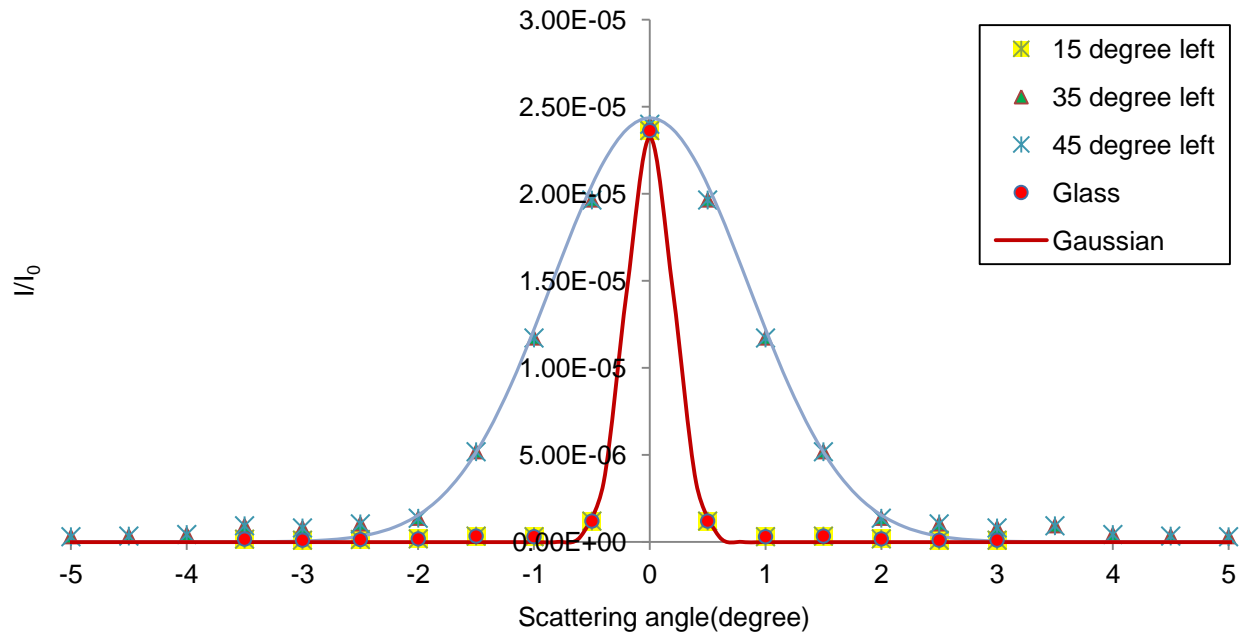
(b)



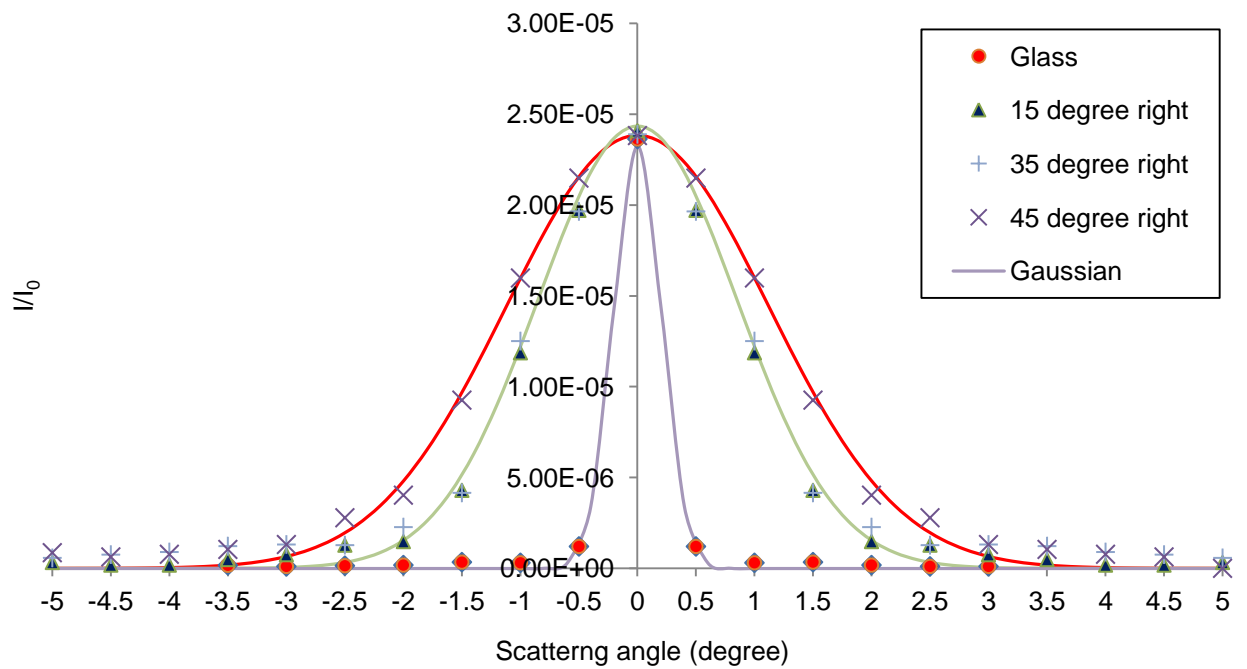
(c)

Figure 64: A comparison of I/I_0 at a wavelength of 670 nm, detected over a range of angles, with illumination from three different incident angles. The incident position labelled 'right' indicates that the light illuminated the edge to the PMMA side of the glass, while the incident position labelled 'left' indicates that the edge was illuminated from the opposite side. The incident laser beam is labelled 'Gaussian'.

The variations of I/I_0 with scattering angles, at different angles of incidence, is plotted in figure 65. Clearly, the light cone transmitted through the PMMA-coated FSC is considerably broadened, compared to a bare glass slide. As seen in Table 3, the angular width of the scattered intensity cone increases for larger angles of incidence, up to 45° . The width here is determined as the length over which the intensity drops to $1/e$ of the maximum. The measurements at 15° and 35° through the PMMA section show the same width, which can be understood from the fact that the second internal reflection takes place at the opposite glass surface without PMMA. As we will show below, the observed behaviour is consistent with diffraction of the laser beam, caused by the roughness of the PMMA layer. In a simple model, we include the diffraction by describing the reflected light as a collection of diffraction-limited cones, with an aperture given by the correlation length of the surface roughness.



(a)



(b)

Figure 65: The angular dependence of I/I_0 for different incident angles for a 670 nm incident light, (a) incident through the glass part, and (b) incident through the PMMA part.

Figure 66 shows a comparison of the intensity of scattered light at two different incident angles, indicating that at 35° the width of the scattered light is more than at 0° incident.

Incident angle=0°

Incident angle=35°



Figure 66: Intensity of scattered light at an incident angle of 0° and 35°.

Angle of incidence	Width of the scattered beam (degree)
0° laser beam	0.6
15°	1.3
35°	1.4
45°	1.6

Table 3 : Beam width for different angles of incidence.

8.2. Modelling the intensity of scattered light by diffraction

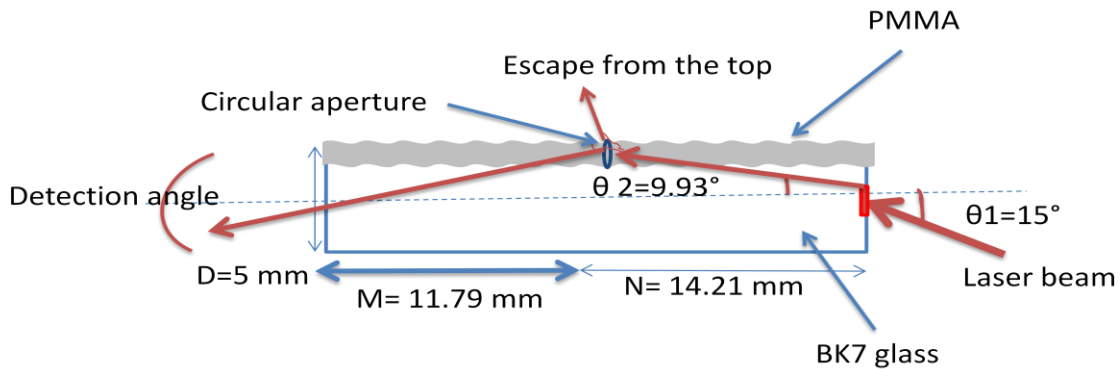


Figure 67: PMMA spin coated on top of the glass, illuminated with laser light from one edge at an incident angle of 15°, the scattered light detected from another edge at different angles. The roughness from spin coated PMMA was assumed to have the circular shadow when the laser hit it.

If we consider the PMMA surface as a collection of uncorrelated areas, the angular distribution of the reflected intensity can be fitted to the Fraunhofer diffraction formula for the circular aperture, given by [31]

$$I = I_0 \frac{G^2}{\lambda^2 r^2} \left| \frac{2J_1(ka \sin \theta)}{ka \sin \theta} \right|^2, \quad (171)$$

where $G = \pi a^2$, a is the radius of the aperture, r is the distance from the observation point to the shadow area, λ is the wavelength of the incident, J_1 is the Bessel function of the first order and k is the optical wavenumber.

Equation 171 gives us the intensity of the scattered light at different detection angles, known as the Airy pattern [32]. Good agreement is obtained for a radius of the aperture of $11 \mu\text{m}$, for the data taken at 670 nm wavelength and at 15° angle of incidence, as shown in figure 68.

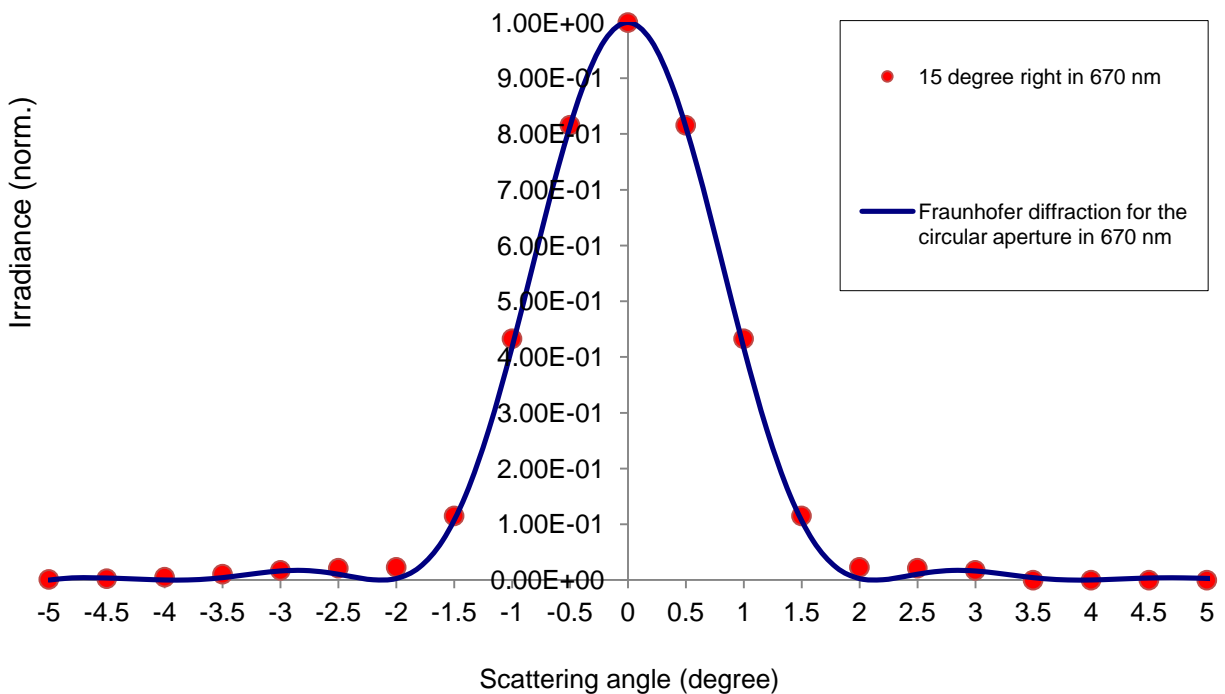


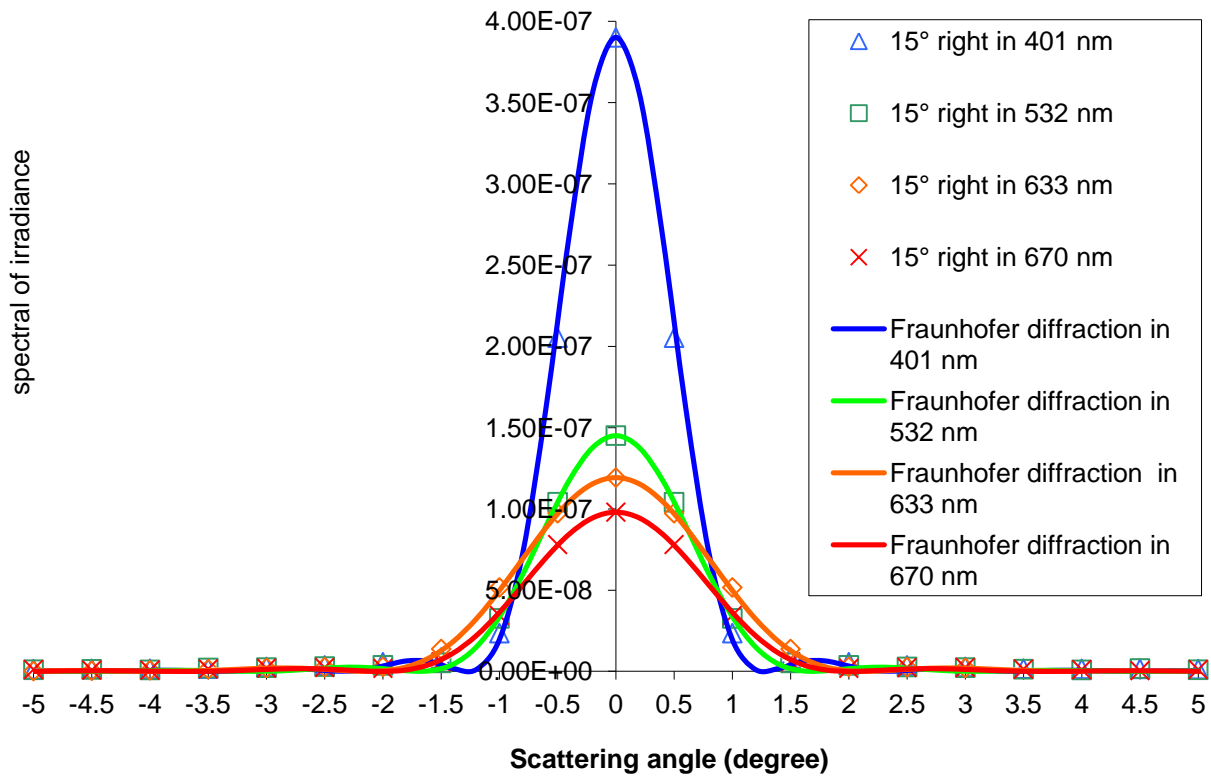
Figure 68: Normalised angular dependence of irradiance of scattering at 15° incident angles in PMMA side for 670 nm . The solid line was fitted by using equation 171, circles indicating the experimental results.

The validity of the diffraction model can be verified by changing the optical wavelength.

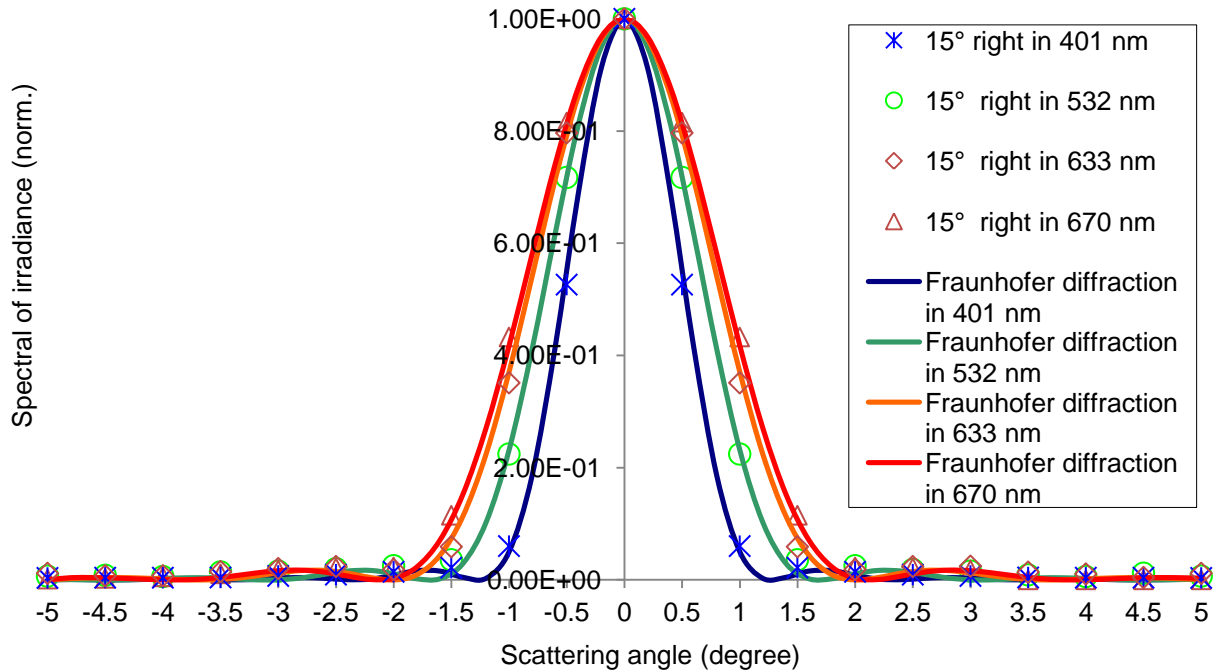
Figure 69 shows the scattered light intensity measured over a range of angles, where we illuminate the sample from one edge at 15 degrees through the PMMA part, and at different

wavelengths of, respectively, 401 nm, 532 nm, 633 nm, and 670 nm. Clearly, the scattered light cones show a decrease in width for a decreasing wavelength.

The Fraunhofer diffraction for the circular aperture was calculated when the size of the particle was fixed at $11\mu\text{m}$, while the wavelength was decreased according to the lasers used. We find a good quantitative agreement with our experimental results in figure 69 (dots), showing that the diffraction pattern gets more and more compressed into a narrow cone around the forward direction, for shorter wavelengths.



(a)



(b)

Figure 69: Comparison of irradiance of scattering (a) and normalised irradiance (b) of scattered light in wavelengths of 670,633,532,401 nm, detected over a range of angles with illumination from 15° incident angles. The incident position labelled 'right' indicates that the light illuminated the edge to the PMMA side.

To further investigate the cause of the scattering in spin coated PMMA, on top of the BK7 glass, the top surface in the PMMA ($n=1.49$) part was covered in optical gel, with a refractive index of 1.4646(THORLABS). The surface tension of the gel produced a smooth film which compensated for the surface roughness of the PMMA layer. Subsequently, the irradiance of the scattered light as a function of the angle was measured when illuminating the sample at a 15° angle of incidence. The results are compared with a measurement taken on the same sample before the gel was added. Results are shown in figure 70, and as we can see, application of the optical gel results in a decrease of the angular width of the scattering cone. This effect unambiguously shows that the cause of the scattering in spin coated PMMA, on top of the glass, is the surface roughness. Compared to the surface scattering contribution, the bulk scattering in this type of sample is negligibly small, i.e. of order 10^{-5} cm^{-1} [68].

It is relevant to consider whether diffraction effects play a role on the situation in which the illumination is provided, through mutually incoherent fluorescent molecules. To assess this, we must compare the divergence of a point source, with the diffraction provided by the surface

roughness. For example, when a point source illuminates an area of $10\mu\text{m}$ at a distance of 1mm from the source, this corresponds to a divergence angle of 10^{-2} radians, or 0.5° , i.e. smaller than the typical diffraction broadening in our samples. Surface scattering losses, therefore, are relevant for incoherent fluorescence emission at propagation distances larger than several hundred μm , which is the case in FSC.

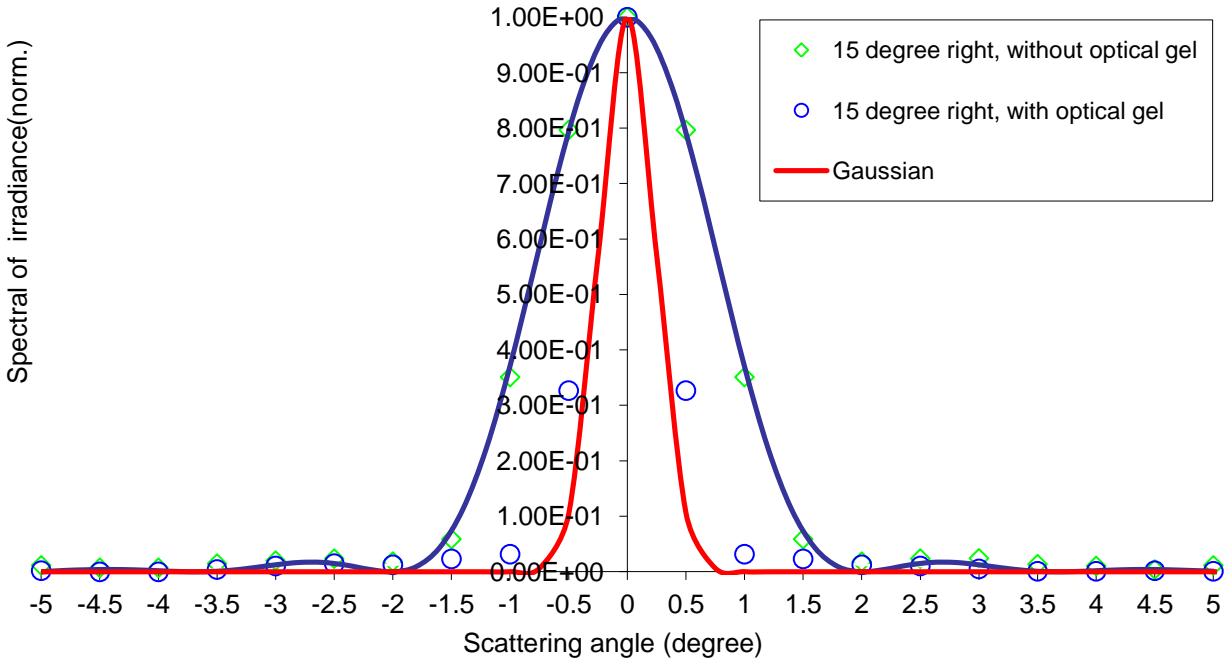


Figure 70: Comparison of the intensity of scattered light at a wavelength of 670 nm , detected over a range of angles with illumination from 15° incident angles, once when the PMMA top surface is covered with the optical gel (circles, blue), and once without optical gel (diamonds, green). The incident laser beam is labelled ‘Gaussian’.

8.3. Effect of the roughness on the performance of FSC

We can calculate the effect of diffraction, due to surface roughness, on the efficiency of FSC, using the model developed by Weber and Lamb. In their model, they included the guiding of light in the FSC at angles larger than the critical angle, for total-internal-reflection, θ_c . Attenuation of reflected light by reabsorption is taken into account through an effective absorption coefficient α_e , while Fresnel reflection losses, at the interface between the low-index FSC and the high-index solar cell, is included through Fresnel’s reflection coefficients for s- and p-polarised light.

Additionally, we include, here, losses caused by angular spread of the reflected light due to surface roughness. The effect is included as a divergence of angles, with a Gaussian profile of

1/e half-width $\Delta\theta$ (full width at half maximum (FWHM) can be calculated by taking the distance between points where the intensity falls to 1/e times the maximum value).

Around the critical angle, this additional spread in angles results in a loss of part of the light within the escape cone. The angular distribution of light after one reflection from the rough surface, can be approximated from the convolution of the unit step function, with the Gaussian diffraction function, resulting in the error function $P(\theta)=erfc[(\theta_c-\theta)/\Delta\theta]/2$. Under the condition that the scattering is only a small correction on the distribution function, the sequence of total internal reflections can be written as a multiplication of a number of error functions, where the number is given by the amount of internal reflections from the rough surface. The total collection efficiency, Q_c , is defined as the total amount of light per unit length, collected at the edge, $y=L$, divided by the amount emitted per unit length. Inclusion of the surface scattering effect in the Weber and Lambe model results in an equation for Q_c , given by:

$$\begin{aligned}
Q_c = & (2\pi L)^{-1} \int_0^L dy \int_0^{\pi/2} d\phi \int_{\theta_c}^{\pi/2} \left\{ \frac{1}{2} \operatorname{erfc} [(\theta_c - \theta) / \Delta\theta] \right\}^{N_R(\theta, \phi)} \sin\theta d\theta \\
& \times \left\{ \exp[-\alpha_e(L-y)/\sin\theta\sin\phi] + \exp[-\alpha_e(L+y)/\sin\theta\sin\phi] \right\} \\
& \times [2 - |r_s(\theta, \phi)|^2 - |r_p(\theta, \phi)|^2].
\end{aligned} \tag{172}$$

where θ, ϕ are the usual spherical polar angles defining the direction of emission, and the exponentials in equation 172 represent the Lambert-Beer law to estimate the absorption over the path length of a random ray within the collector over a distance $(L\pm y)$. The scattering losses depend on the total number of total internal reflections of light inside the collector. Here, the number of total internal reflections from the rough surface is given by:

$$N_R(\theta, \phi) = \left\lfloor \frac{2L-y}{2T} \cot\theta \cot\phi \right\rfloor, \tag{173}$$

where we have introduced the slab thickness T . The brackets indicate the floor function (the greatest integer function), which rounds N_R to the largest previous integer.

Results were calculated for the collection efficiency of the FSC, for a representative collector with index $n_c=1.5$, coupled into a semiconductor of index $n_s=3.35$, with the value of $\Delta\theta$ taken from table 3. Different values of T will only change the total amount of scattering loss, not the

qualitative response. In figure 71(A), the computed values obtained by a numerical integration of equation 172 are shown. The curve, in the absence of surface scattering (closed circles), corresponds to the Weber and Lambe result; the introduction of a surface roughness, characterised by a $\Delta\theta=1.5^\circ$ divergence, results in a reduction of several percent (open circles) in the efficiency. Also shown are the total (triangles) and relative (diamonds) scattering losses, where the latter is normalised to the efficiency, for a smooth film ($\Delta\theta=0$). Figure 71 (right) shows the absolute and relative scattering losses, as a function of the diffraction width for a value of $\alpha_e L=10^{-2}$, i.e. low reabsorption. Above $\Delta\theta=1^\circ$, the scattering loss increase is roughly linear with the diffraction width $\Delta\theta$.

The loss percentage of 5% for $\Delta\theta=2.5^\circ$ indicates the importance of surface roughness optimisation in experimental FSC. For comparison, we have also shown the results for $T=L/5.2$, which corresponds to the small-scale experimental configuration in this work. As can be seen, the scattering loss does not scale linearly with the system size, i.e. the number of internal reflections, indicating that the majority of the loss is accumulated during the first few reflections. This can be understood from the fact that the angular range around the critical angle gets depleted of photons after the first few internal reflections, and therefore the effect saturates.

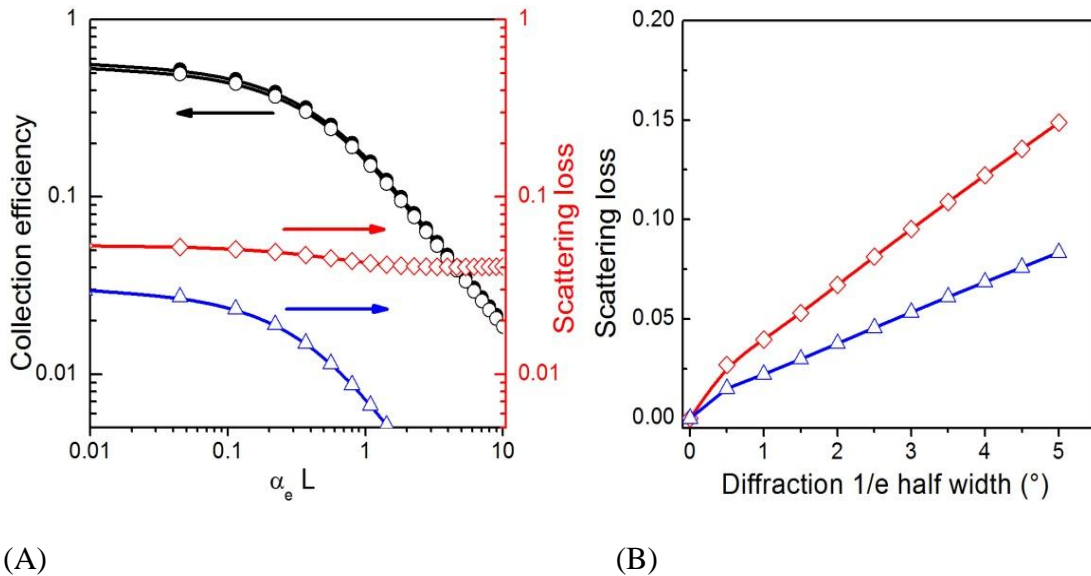


Figure 71: Collection efficiency (left) for the FSC as a function of $\alpha_e L$, calculated using the modified Weber and Lamb model equation (172), for a perfectly smooth surface ($\Delta\theta=0$, closed dots), and a surface roughness characterised by $\Delta\theta=1.5^\circ$ (open dots). The absolute scattering loss (triangles, blue), and the relative scattering loss (diamonds, red) are normalised to the result for $\Delta\theta=0$. The absolute (triangles, blue) and relative scattering loss (diamonds, red) at $\alpha_e L = 10^{-2}$ as a function of the 1/e half-width of the diffraction cone are shown on the right.

8.4. TracePro modelling

To support the experimental results, ray tracing was applied using the TracePro programme.

TracePro is a tracing programme for modelling the propagation of light in imaging and non-imaging Opto-mechanical systems [34].

Models are created through importing from either a lens design programme, or a Computer Aided Drafting (CAD) programme, or by directly creating the solid geometry in TracePro. Optical properties are assigned to materials and surfaces in the model, and source rays propagate through the model with portions of the flux of each ray, allocated for absorption, specular reflection and transmission, fluorescence and scattering [34].

The BK7 glass, modelled in the ray tracing simulation, was 2.6cm long in the X and Y axis, with a thickness of 0.5cm. A layer of PMMA, with a thickness of 0.001cm, was placed on top of the BK7 glass [69, 70].

As shown, the roughness was modelled using the BSDF measurement data, based on figure 65(b), it indicating the place that the laser hit the PMMA inside the sample at 15°, 35° and 45° incident angles.

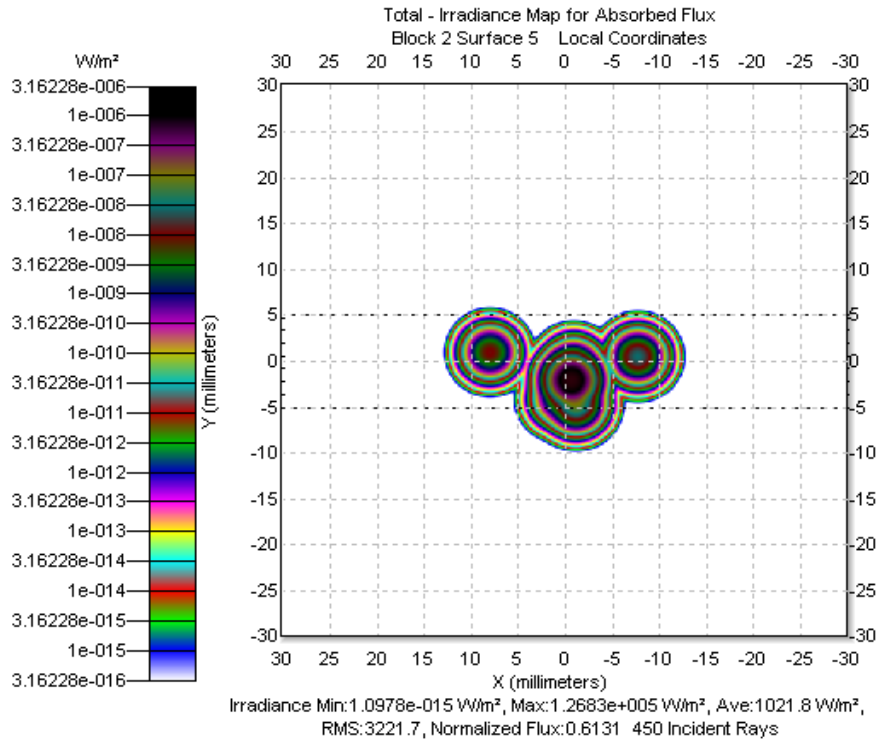
The Gaussian laser beam, in a wavelength of 0.670 μ m and a power of 5mWatt, and beam width diameter of 0.6°, was inserted, 8 cm, from the sample. The laser was placed with respect to the middle of one edge, at different angles (0°, 15°, 35° and 45°) and the scattered light was detected by using a perfect absorber in the opposite edge of the sample, at a distance of 27cm. The scattering results from ray tracing, shown in figure 72, show that the scattering width was increasing from 0° to 45°. However, the amplitude remained constant, with the flux decreasing in the perfect absorber, from 0° to 45° incident light. This indicates an increase in the scattering from 0° to 45° incident light inside the sample, in keeping with the experimental results.

For the output flux at 45° incident light, the light can hit the PMMA twice and the glass once (figure 72 a), if the incident is through the PMMA. For the incident light in the opposite part, it can hit the glass twice and the PMMA once (72 b). Figure 72a shows that the width of the

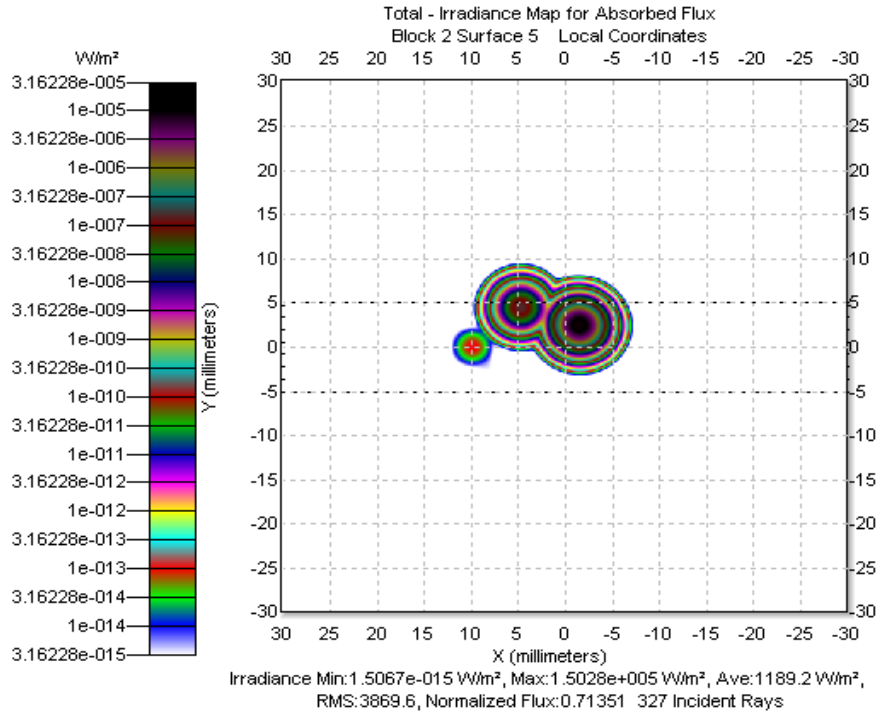
scattering was increasing, and that the output flux decreases when the light hits the PMMA twice.

The output flux at 35° illuminated light from the edge to the PMMA side of the glass, and the opposite side, are similar suggesting that the light can hit the PMMA and glass sides once, in both conditions (figure 72b).

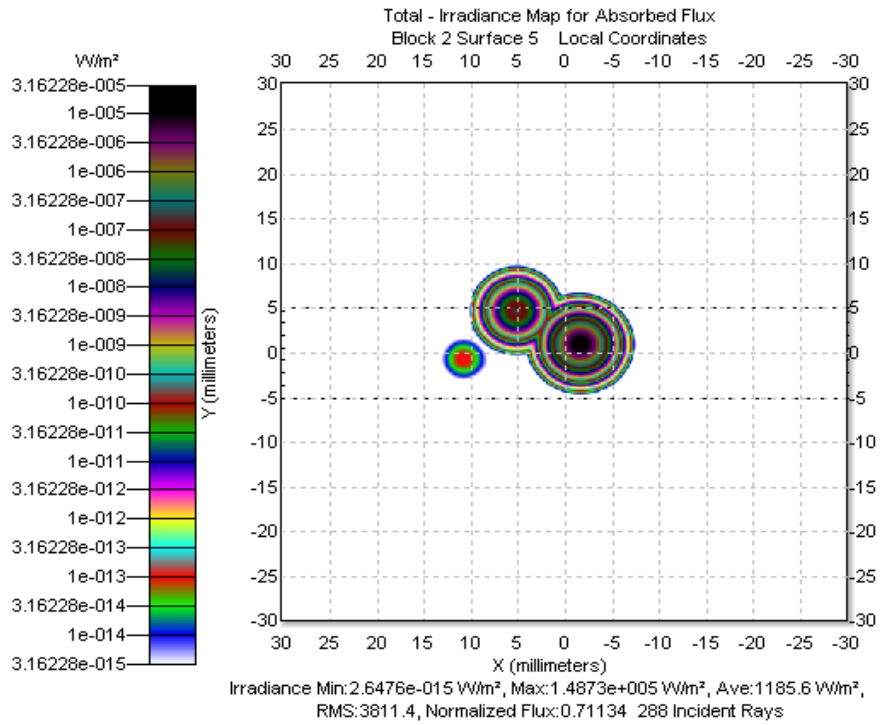
As we can see, when the incident light angle through the PMMA portion is 15° (figure 72c), the output flux decreases the incident angle in the opposite part (figure 72d). This shows the scattering from the PMMA layers in the fluorescent solar collector, as the light hits the PMMA once inside the collector.



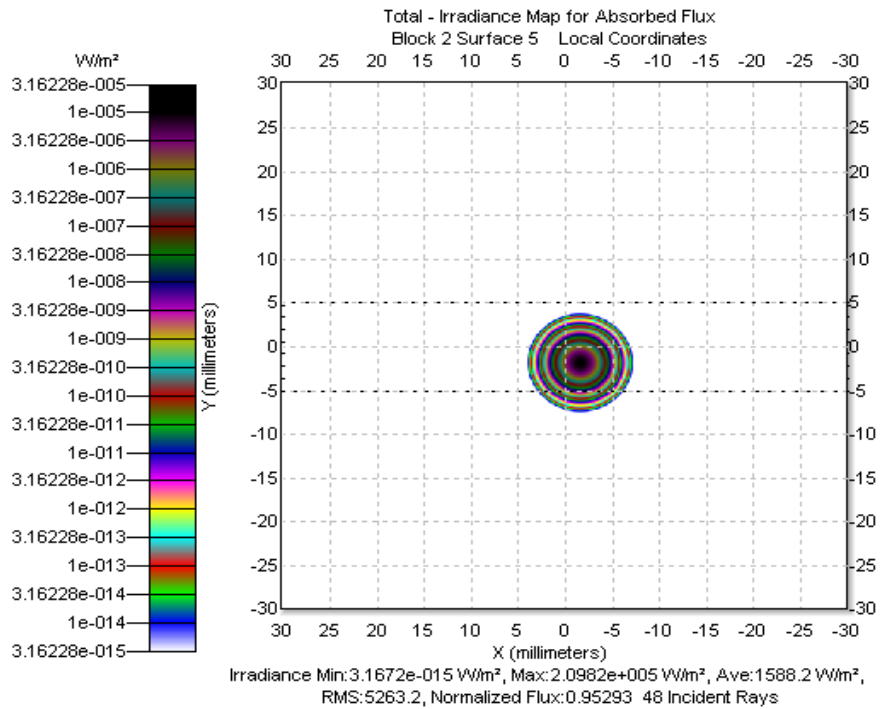
(a)



(b)



(c)



(d)

Figure 72: Gaussian laser beam in a wavelength of 0.670 μm , illuminated at (a) 45° through the PMMA part of the sample; (b) incident at 45° through the glass part of the sample, or incident at 35° through the glass or PMMA part of the sample; (c) incident at 15° through the PMMA part of the sample; and (d) incident at 15° through the glass part of the sample, or 0° through the glass. The graphs are plotted on a log scale.

8.5. Scattering measurement in Perspex /Acrylic sample

The ratio of the irradiance of scattered light to the irradiance of the incident light (I/I_0) of a Perspex/Acrylic fluorescent sample (Mars Red from Lucite solutions, with unknown dye concentration) is plotted in figure 73. The sample is taken with a diameter of 26×26×5mm³, measured in 670nm, where the dye doesn't absorb, and over a range of angles when we illuminate the sample from one edge at three different incident angles (15, 35 and 45 degrees). To compare the results, the peak in I/I_0 for all measurements, was shifted to zero degrees.

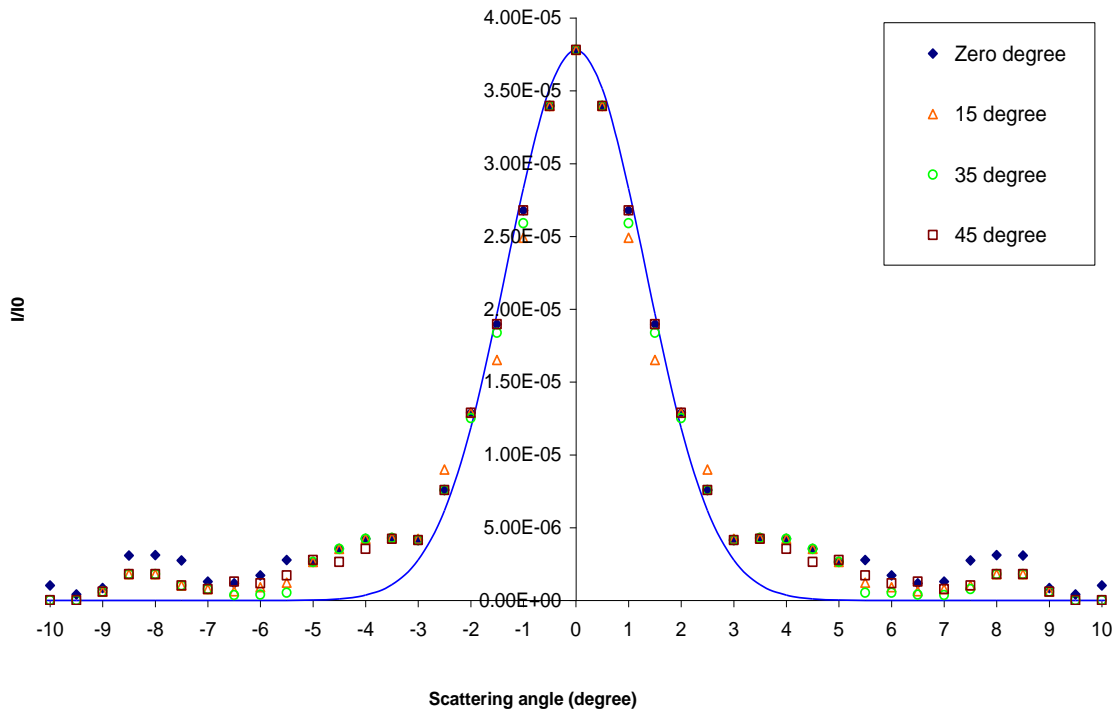


Figure 73: Angular dependence of I/I_0 for a perspex/acrylic fluorescent sample, with unknown dye concentration at different incident angles for a 670 nm incident light. The experimental data was fitted with a Gaussian (solid line) beam.

The value of the scattered light was the same for different incident angles (0° to 45°) of incident light, indicating that we have more scattering from the bulk than from the surface. In zero incident light, light doesn't hit anywhere inside the sample, and in 15 degree incident light, the light was totally internal reflected once. At 35 degrees, the light can be totally internal reflected twice, while at 45 degrees, the light can be totally internal reflected three times. As we can see, the intensity and the width of the scattered light was the same at different incident angles.

The value of the scattering phase function was obtained by directing a 5mW, 670nm laser beam, at an incident angle of 0° , through the Perspex/Acrylic fluorescent sample. Light emitted from the other end of the sample was measured by placing a silicon detector at different angles (with respect to the sample plane). The results were fitted using Mie phase function scattering theory (chapter 3), as the Gaussian fit wasn't sufficiently in agreement with the experimental data (figure 73). The experimental results fitted the Mie theory results for spheres with a diameter of $4.5\mu\text{m}$, as shown in figure 74.

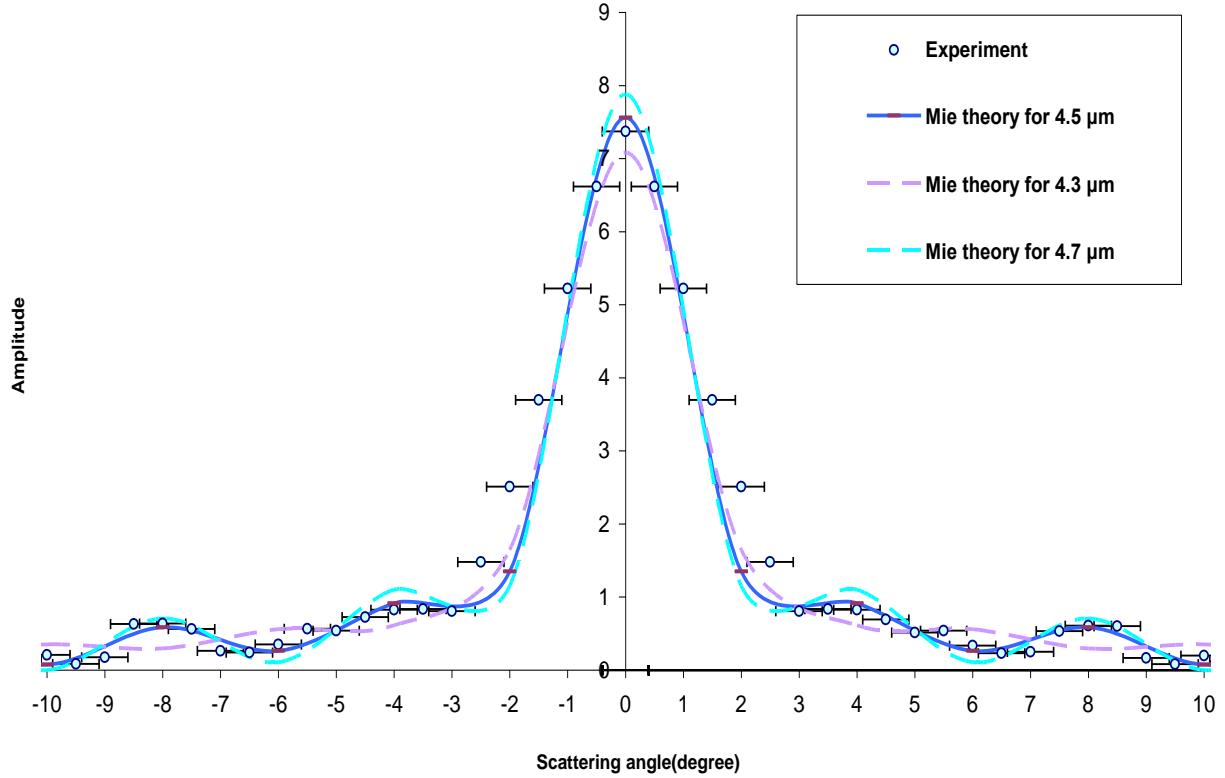


Figure 74: Scattering phase function for the perspex/ acrylic fluorescent sample, measured with the laser at a wavelength of 670 nm, and compared with Mie scattering theory for different sphere sizes. The error of this measurement was fixed at 0.6, which is the width of the laser beam, while circles indicate the experimental results.

8.6. Bi-directional surface distribution function from collector edges

The BTDFs for ground, and polished edges are shown in figure 75. The incident angle was zero degrees in 670nm to the edge of the glass, and detected in another edge at different angles. This data was used to investigate the effect of the edge roughness in the performance of the FSC. As we can see, the BTDF is higher in the ground edges collector, rather than the polished edges, indicating that we have more scattered light in the former, caused by roughness from the edge.

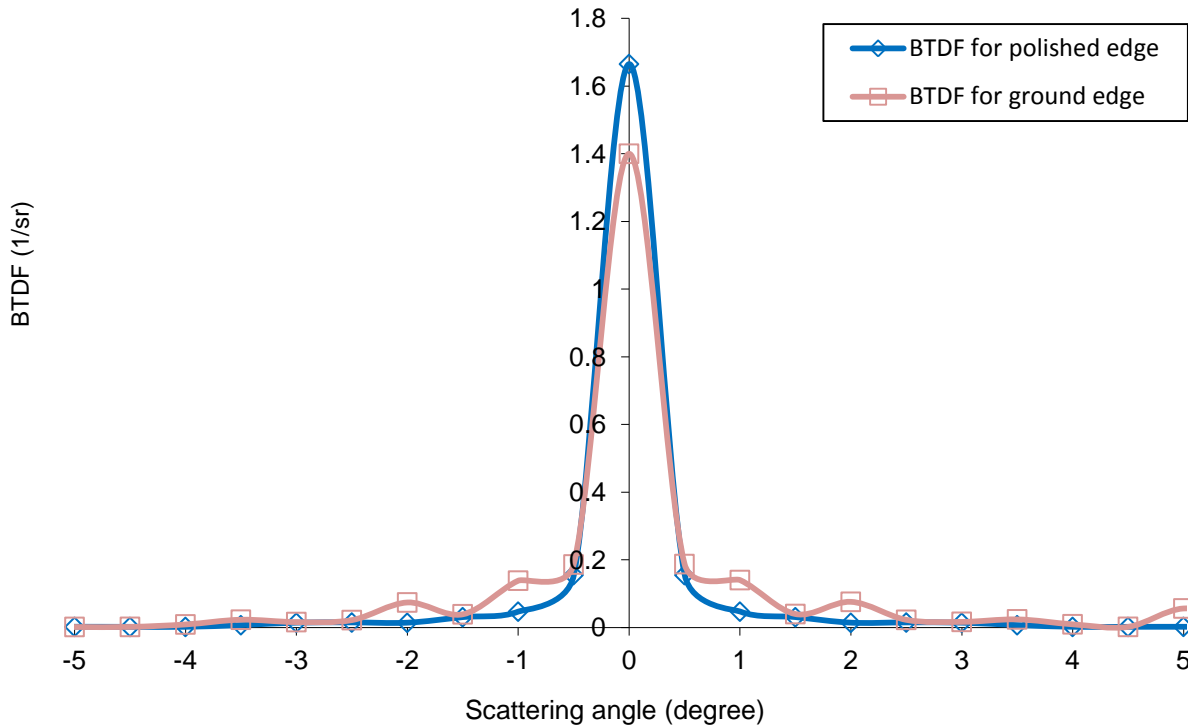


Figure 75: BTDF measurement in polished and ground edges of BK7 glass.

8.7. Results and discussion from experiment

The typical edge fluorescence spectra of fluorescent collectors with a single type of dye are shown in figure 76. The value of edge fluorescence is slightly higher for polished edges, which agrees with the BTDF measurement, since the roughness in polished edges was less than that of ground edges (figure 75).

In the red (long wavelength) region where absorption is weak, the typical optical path length inside the collector, traversed by emitted photons, is much longer than the absorption length. This part of the spectrum, therefore, corresponds to photons, which are observed in the edge fluorescence with little or no reabsorption.

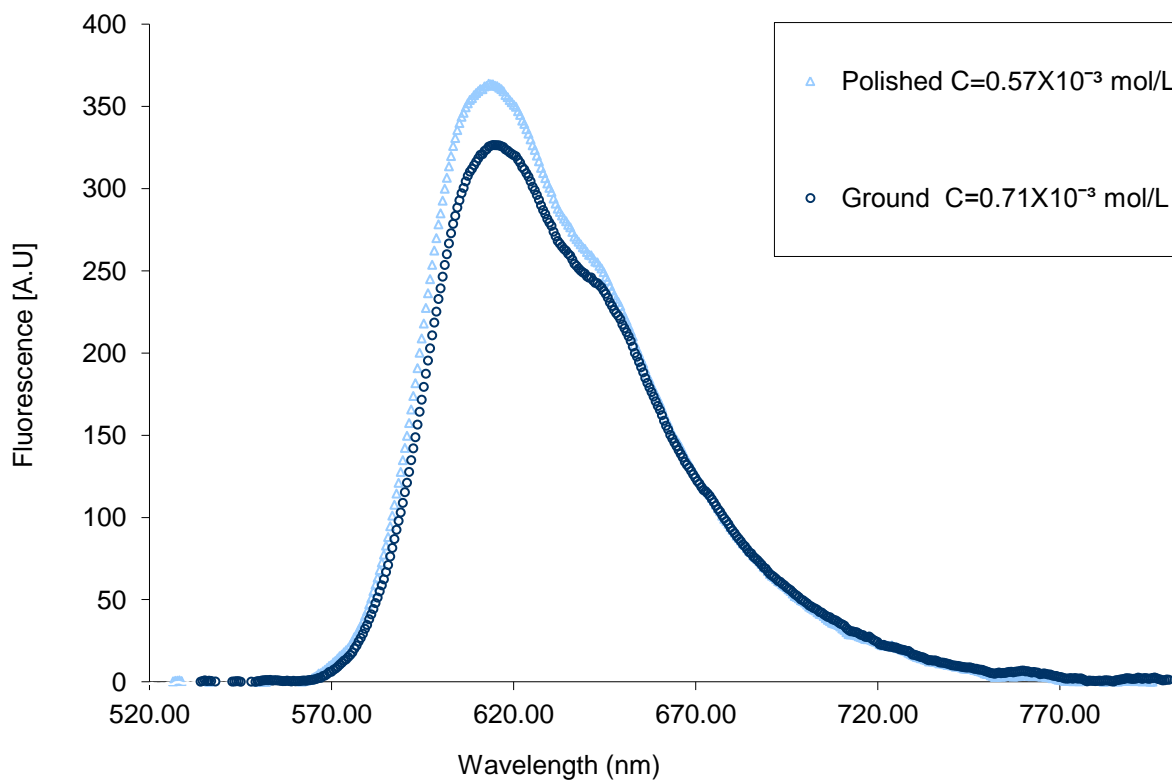


Figure 76: Typical edge fluorescence spectra of Rhodamine B collectors.

With appropriate normalisation, the shape of the edge emission spectrum in this spectral region is identical to the spectrum of first generation fluorescence. Figure 77 shows that the edge fluorescence spectra, when multiplied by an appropriate constant, coincides with the first generation fluorescence in the long wavelength region. The total probability of reabsorption, R , can then be easily determined by integration, graphically interpreted by an area between the first generation curve and the normalised edge fluorescence spectra.

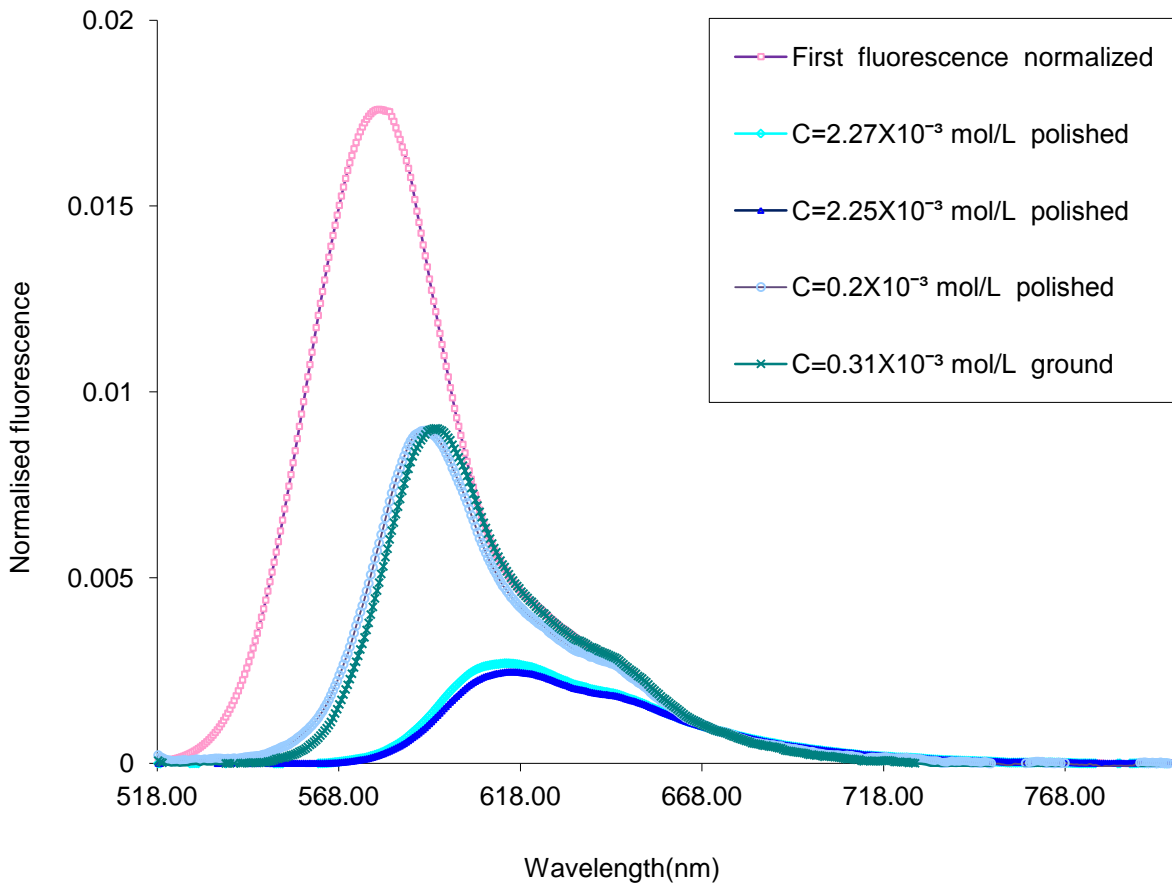


Figure 77: Edge fluorescence spectra, normalised to coincide with the first generation fluorescence spectrum in the low-absorption, long-wavelength region. The area between the first fluorescence and edge fluorescence is equal to the probability of reabsorption, R .

The reabsorption probability of Rhodamine B, as explained in chapter 4, is a function of the product, $\alpha_{eff} \cdot L$ is shown in figure 78, and compared with the Weber and Lambe, and the modified Weber and Lambe curves, and the results are in good agreement with the modified Weber and Lambe model.

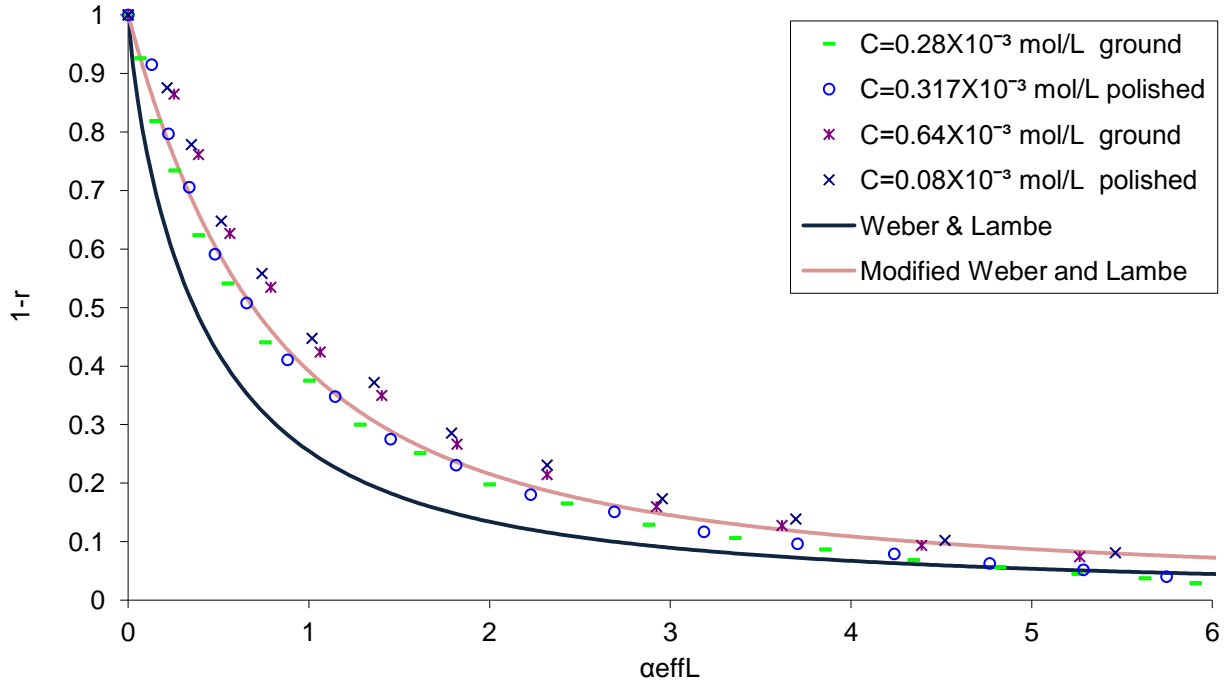


Figure 78: Reabsorption probability for thin film collectors for different absorption of RB in the film compared to the W&L model.

The value of the short circuit current detected with solar cells for different edge fluorescence of F305 dye, mixed with PMMA, is plotted in figure 79, and indicates the linear relationship between edge fluorescence and I_{sc} . The value of I_{sc} for the PMMA (edge fluorescence=0) sample indicates the scattered light that can reach the edge of the collector.

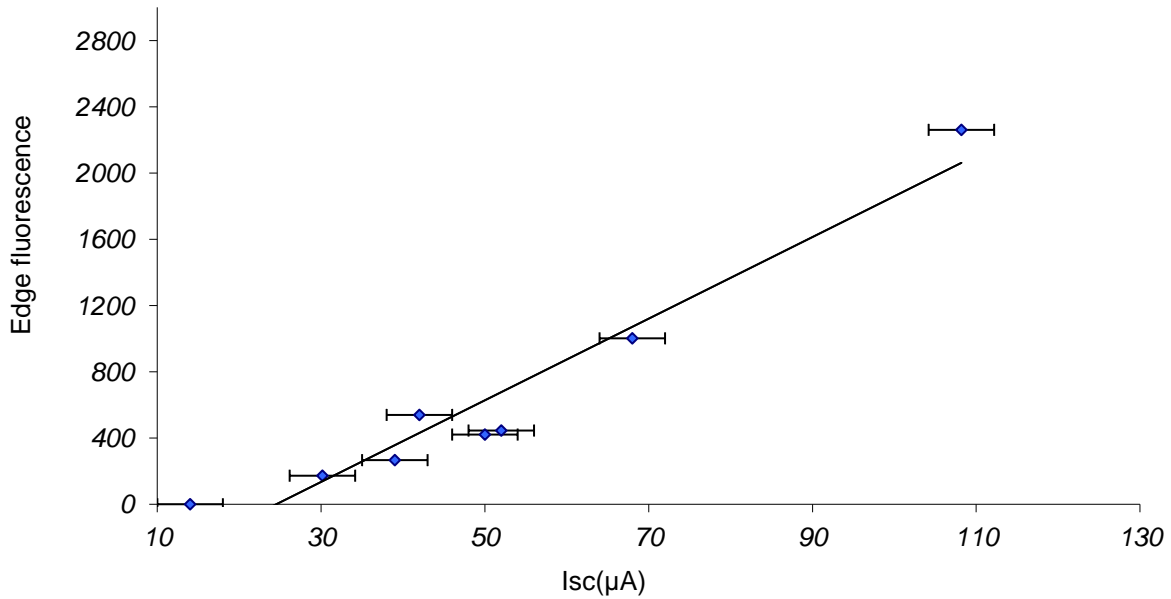


Figure 79: Short circuit current detected with a solar cell for different edge fluorescence.

8.8. Scattering efficiency measurement

To measure the scattering efficiency of the scattered light able to reach the edge of the collector caused by the PMMA layers, the value of the short circuit current, detected from the edge in the PMMA sample ($I_{sc \text{ edge PMMA}}$), was divided by the short circuit current from direct illumination in the solar cell ($I_{sc \text{ top}}$), in 550 nm, giving the scattering efficiency. In this case it was found to be 0.089 for $I_{sc \text{ edge PMMA}}=14.26\mu\text{A}$, and $I_{sc \text{ top}}=159\mu\text{A}$. It is important to find the number of scattered photons that can reach the edge of the collector, and so we illuminate the sample from the top, detecting the scattered light with the solar cell from the edge. To find the number of photons reaching the solar cell, we have to divide the scattering efficiency by the geometrical gain, which is the ratio of the collector from the top ($26\times 26\text{mm}^2$) to the area of the solar cell ($30\times 3\text{mm}^2$).

For a geometric gain of 7.5, the scattered photons able to reach the edge of the solar cell was 0.0119.

To establish the effect of the scattering in photon collection efficiency, it is important to consider the scattering from the PMMA substrate. Therefore, we can write

$$Q_c = \frac{(I_{sc \text{ sample}} - I_{sc \text{ from PMMA}})}{\text{geometrical gain} \times Q_A}, \quad (174)$$

where the $I_{sc \text{ sample}}$ is the short circuit current detected from the edge in the dye sample, and Q_A is the absorption efficiency. The $I_{sc \text{ sample}}/(\text{geometrical gain} \times Q_A)$, gives us the photon collection efficiency from the dye, and $I_{sc \text{ from PMMA}}/(\text{geometrical gain})$ gives us the photon flux of the scattered light that can reach to the edge of collector.

Conclusion

The effect of the surface scattering in a theoretical model for an FSC was discussed in this chapter.

In summary, the contribution of light scattering in fluorescent solar collectors (FSC) based on a spin-coated dye/polymer layer was investigated. Measurements of the transmission cones as a function of the total internal reflections (TIR) revealed that the predominant loss factor is surface scattering at the top layer, caused by roughness of the spin-coated PMMA. Scattering losses depend on surface roughness, the size of the sample and the number of total internal reflections of light inside the collector. Diffraction of light at surface roughness is shown to increase the escape cone losses, which are one of the most prominent factors limiting the performance of FSCs [51].

Good agreement is obtained when we consider the PMMA roughness as an coherent aperture with a circular shadow, and therefore the angular distribution of the scattering intensity can be fitted using far-field Fraunhofer diffraction. The width of the scattered beam increases when the wavelength is increased from 401nm to 670nm, in good agreement with Fraunhofer diffraction for a circular aperture at different wavelengths, where the size of the aperture is fixed at 11 μ m. This value is of the same order as the correlation length of the height variations observed in AFM measurements. The angular broadening due to surface roughness for different numbers of TIR of light inside the collector was found to be 0.6 ° to 1.6 ° (Table 2). The value of the scattering was found to decrease significantly when covering the top surface with optical gel, unambiguously showing that surface scattering is the predominant loss factor in our FCS, compared to bulk scattering effects. The reduction of angular broadening to 0.6° indicates that surface scattering losses could be reduced to below 2% according to the Modified Weber and Lambe model. Surface roughness is caused by the high level of thickness that the PMMA-dye layer requires for the operation of the FSC. Our results indicate that the performance of the FSC can be improved by using a subsequent planarisation with a thin index-matching layer of low roughness.

The effect of the surface roughness of the edges has also been evaluated and found to be relatively small.

In an acrylic fluorescent sample, the width of the intensity of scattered light was the same for the incident angle of 0° to 45°, indicating that we had more scattering from the bulk than at the surface. The bulk scattering in the acrylic fluorescent sample fitted well with the Mie theory for a 4.5 μ m sphere size.

The linear relationship between edge fluorescence and I_{sc} was shown in this chapter.

Chapter 9

Angular Dependence of edge fluorescence

Introduction

Thermal equilibrium provides a framework for measuring the actual chemical potential of the fluorescent flux escaping from the edge of the collector [70]. At thermal equilibrium, the spectrum of the edge fluorescence acts similarly to a quasi-blackbody spectrum at a temperature T , with non-zero chemical potential. The quasi-blackbody term refers to a blackbody emitter, with non-zero chemical potential.

In this chapter the effect of the angular dependence of the edge fluorescence on reabsorption probability was studied, while the chemical potential of the edge fluorescence flux, incident on the solar cell, was characterised.

The Modified Weber and Lambe model, for angular dependence of the edge fluorescence, was used to calculate the reabsorption probability of the fluorescence solar collector.

9.1. Fluorescence measurement

To measure the fluorescence spectra of F305 mixed with PMMA in a concentration of 9.5×10^{-4} mol/L, the sample was illuminated with a continuous beam of monochromatic light, with a wavelength of 550nm, and the intensity of the emission spectra was recorded. Two different arrangements were used to detect the fluorescence light emitted from the test samples:

1. Front–face fluorescence detection
2. Edge fluorescence detection

as explained in chapter 6.

The first and second arrangements were used to measure the fluorescence spectra emitted from the front surface, and from the edges of the samples, respectively. These spectra were characterised to determine the reabsorption loss of the sample.

9.2. Edge fluorescence detection

A fluorescence spectrum was recorded from one edge at different angles (0° - 45°), in 550nm, and in two different setups, as explained in chapter 6 (figure 42). Fluorescence spectra from the edge of the collectors was collected by an optical fibre, connected to Avantes to collect light from a 4.9×10^{-6} sr solid angle, as shown in figures 80 and 81. Zero degrees was chosen to be in the middle of the sample. As we can see, the edge fluorescence decreases by increasing the detection angle in both set ups.

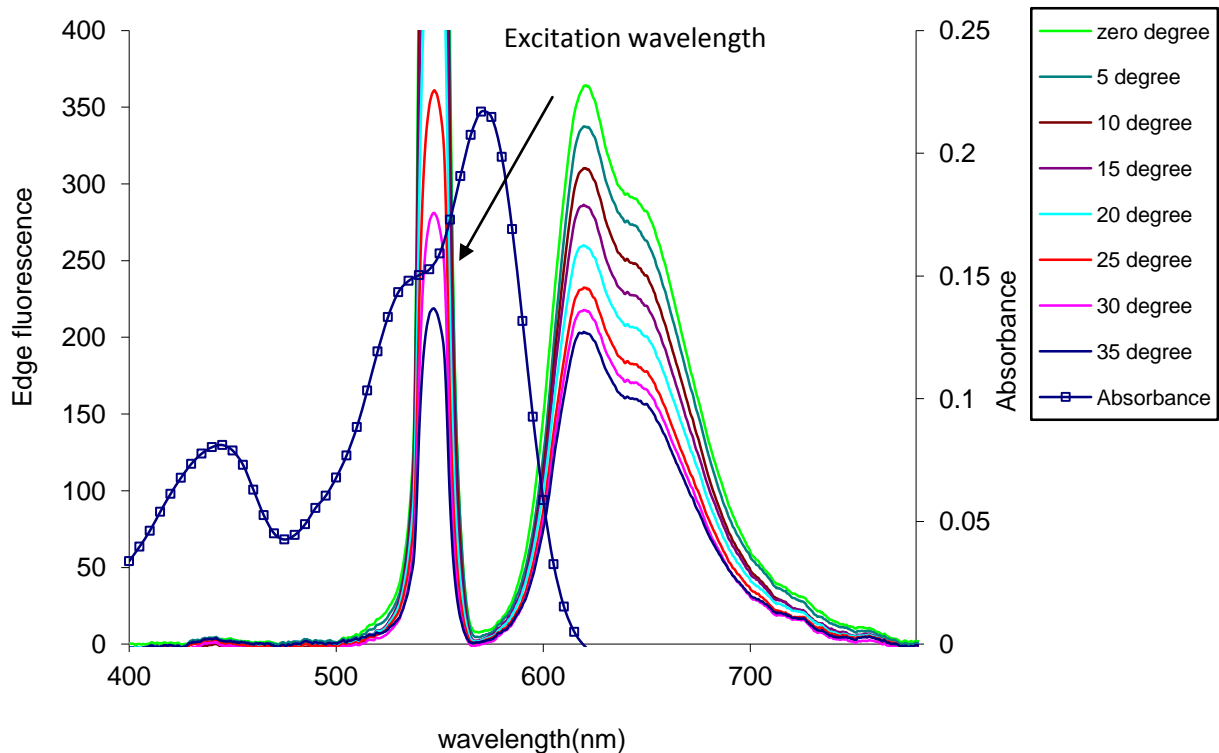


Figure 80: Typical flux of edge fluorescence spectra of F305 ($C=6.5 \times 10^{-4}$ mol/L) in an excitation wavelength of 550 nm, with the sample illuminated from the top and detected from one edge at different angles.

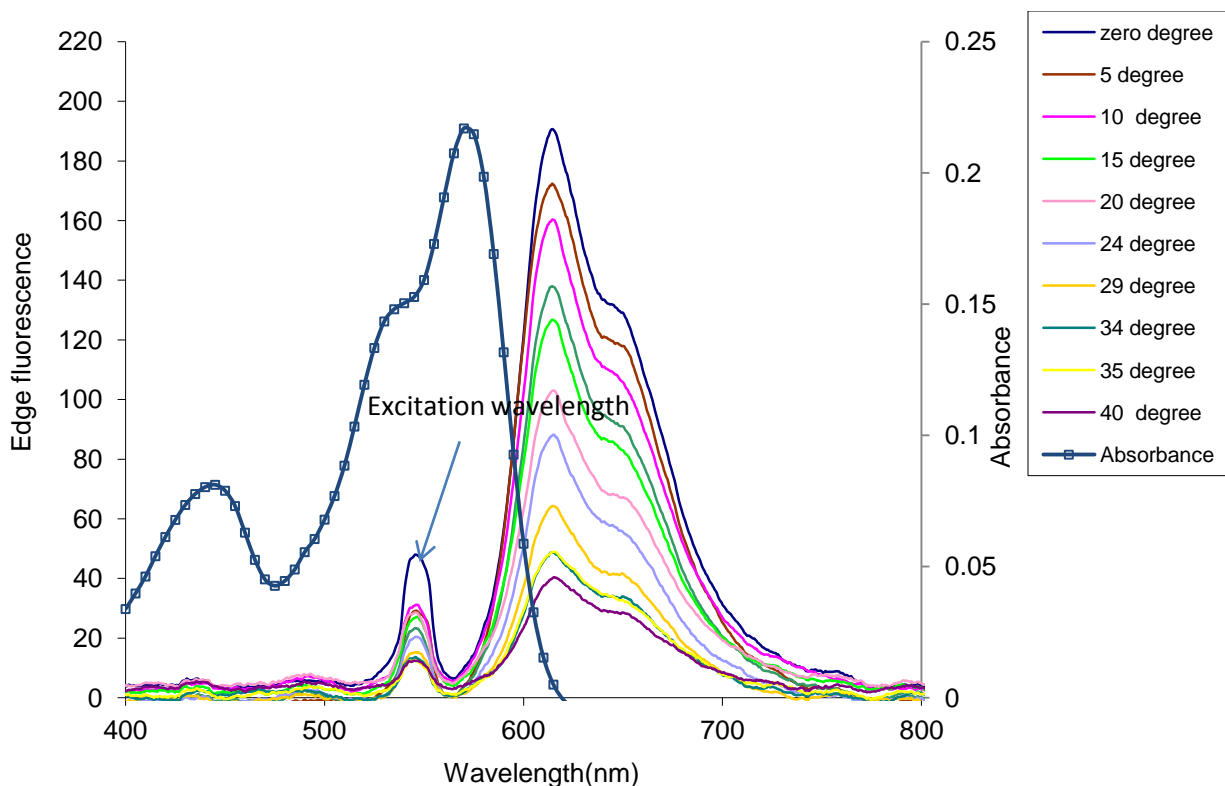


Figure 81: Typical flux of edge fluorescence spectra of F305 ($C=6.5 \times 10^{-4}$ mol/L) in an excitation wavelength of 550 nm, the sample rotated to 90° , illuminated from the top, and detected from one edge at different angles.

9.3. Determination of the first-generation fluorescence spectra

In order to minimise the reabsorption loss, the measurements were performed with low absorbance samples, and are shown in figure 82.

Figures 83 and 84 show the fluorescence spectra, observed from the front surface of the samples in a 550nm filter. It was found that the shift of the spectra was no longer observed when the absorbance of the sample was less than 0.03. This key feature suggests that the spectra detected from the front surface of the samples, which have an absorbance of less than 0.03, are not affected by the reabsorption mechanism. Hence, such spectra were considered as the first generation fluorescence of the fluorescent collectors developed in this work.

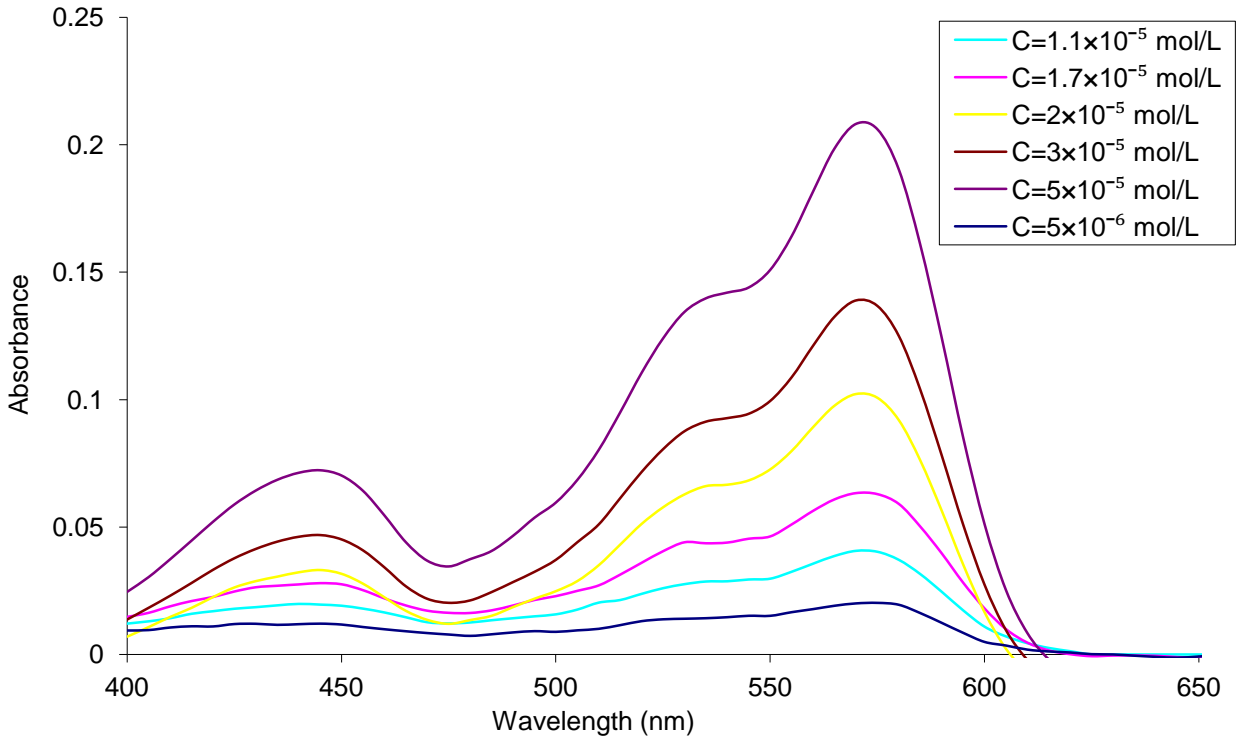


Figure 82: Absorbance of spin coated F305 on top of the glass substrate, for 6 different concentrations.

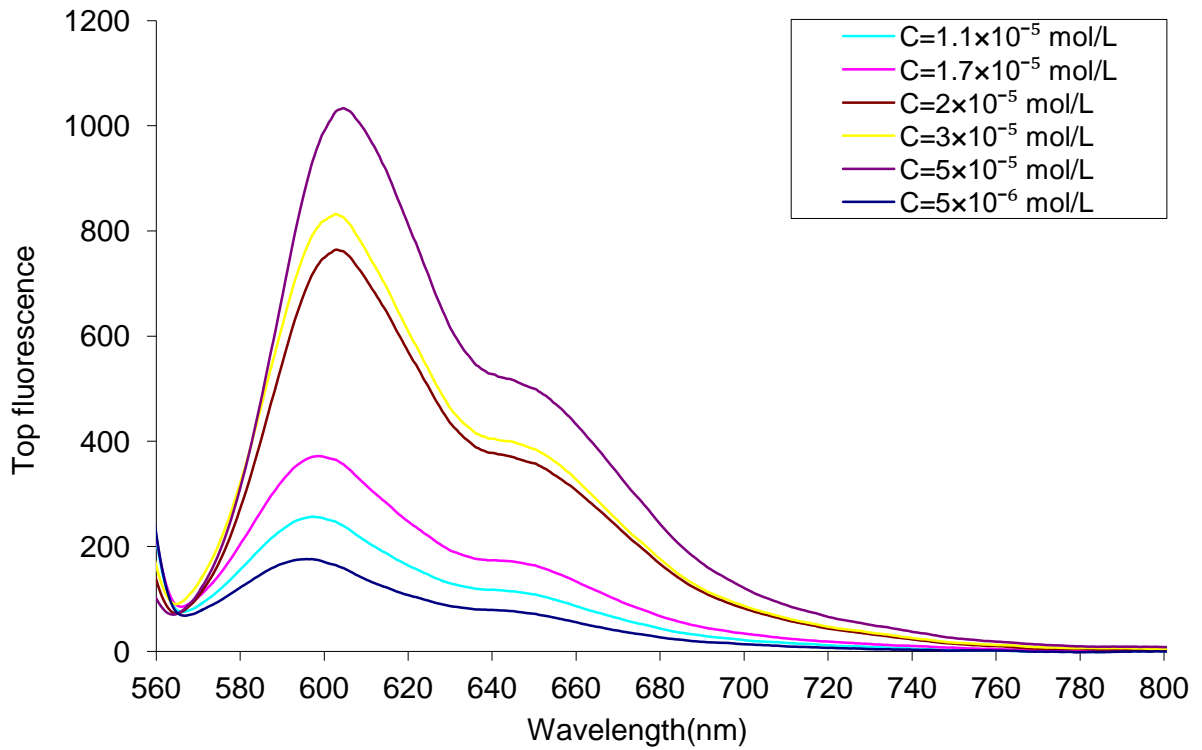


Figure 83: Top fluorescence spectra for various concentrations of spin coated F305, on top of the glass substrate.

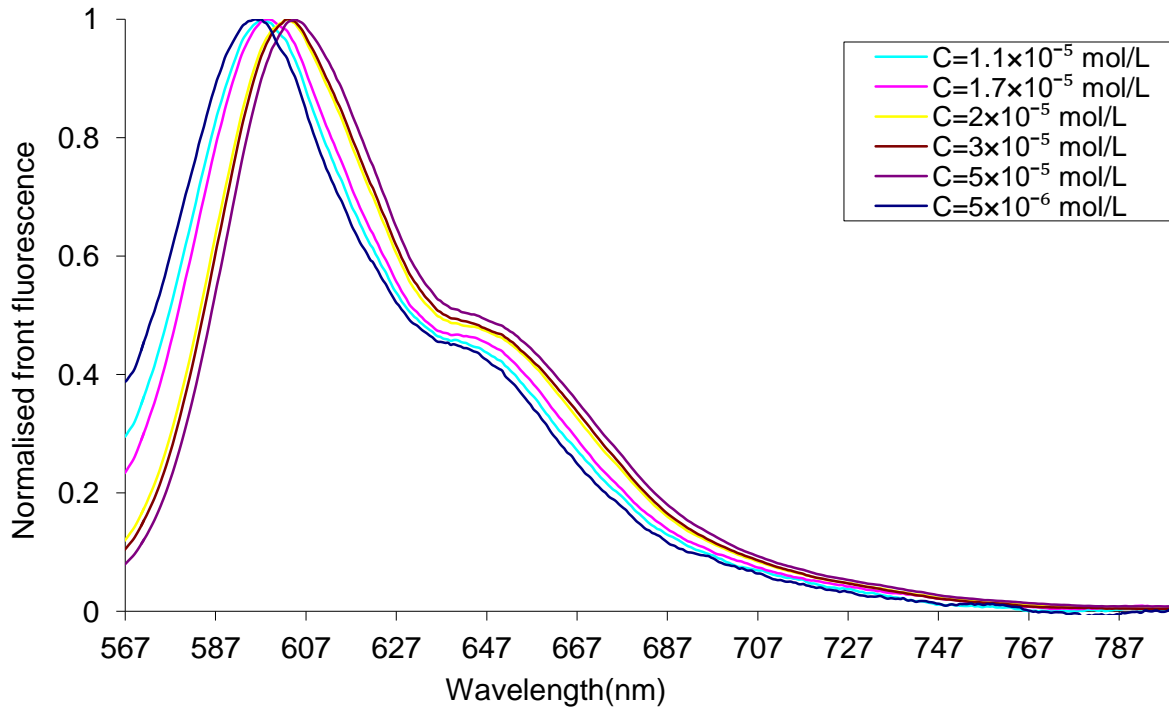


Figure 84: Fluorescence spectra detected from the front surface of fluorescence collectors at various concentrations of spin coated F305 on top of the glass substrate. The spectra were normalised to unity at their peak.

To obtain a more precise value of the reabsorption probability, it is essential to eliminate the effect of the excitation light, as well as the ‘concentration quenching’, which influenced the first fluorescence spectra. To eliminate the effect of the concentration quenching, a very low concentration of dye was used, and to eliminate the effect of the excitation light, the first fluorescence spectra at the short wavelength region were fitted to the standard Gaussian beam. The results of the Gaussian fits with the first fluorescence, and are presented in figure 85. The first fluorescence fitted results were used to determine the reabsorption loss at each wavelength.

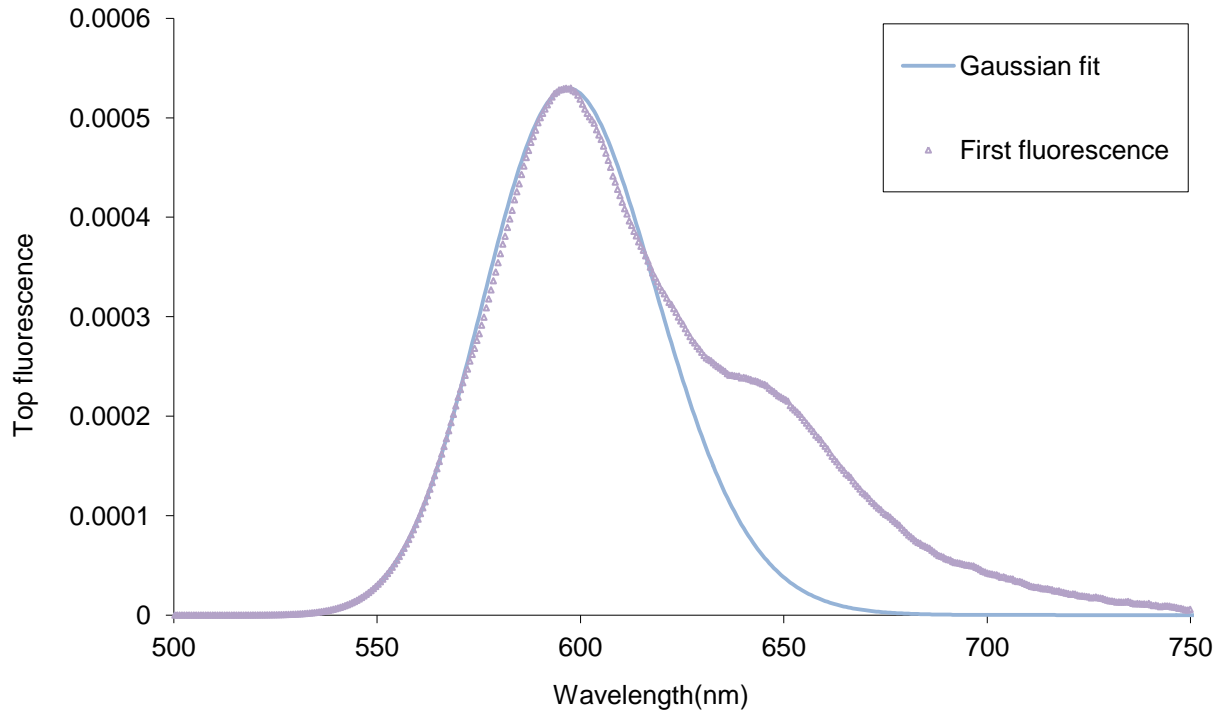


Figure 85: The spectra of spin coated F305 on top of the glass substrate with concentration of $C=5 \times 10^{-6}$, fitted with the Gaussian.

Figure 86 shows that the edge fluorescence spectra of spin coated F305, mixed with PMMA ($C=6.5 \times 10^{-4}$ mol/L), when multiplied by an appropriate constant coincides with the first generation fluorescence in the long wavelength region. The total probability of reabsorption, R , can then be easily determined by integration, graphically interpreted by an area between the first generation curve and the normalised edge fluorescence spectra. As we can see, the value of reabsorption was decreased by increasing the detection angle, up to 20° , before increasing, showing that, through increasing the detection angle close to the edge, the light has a longer path length inside the collector.

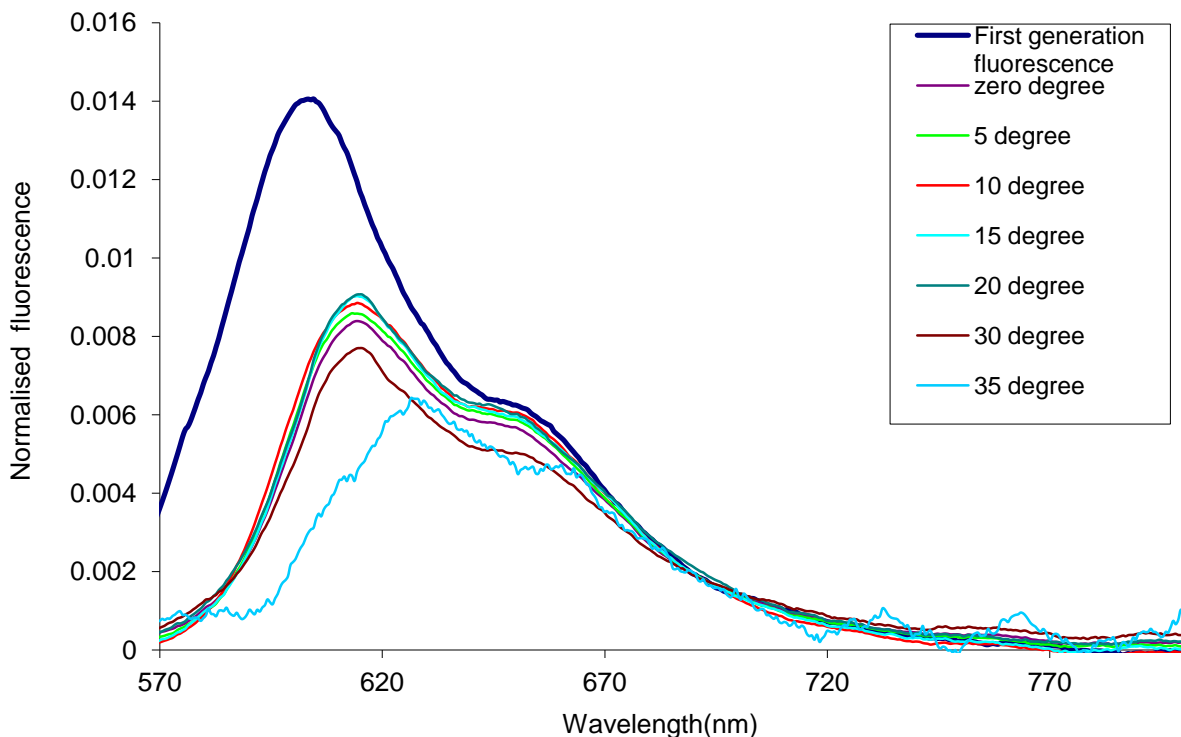


Figure 86: Edge fluorescence spectra of spin coated F305, mixed with PMMA on top of the glass substrate with concentration of $C=5 \times 10^{-6}$, normalised to coincide with the first generation fluorescence spectrum in the low-absorption, long-wavelength region. The area between the first generation fluorescence and edge fluorescence is equal to the probability of reabsorption, R .

9.4. The effective temperature measurement

The effective temperature of the dye was calculated using the Kennard-Stepanov law.

For systems with one excited electronic state, and under conditions of excited-state thermal equilibrium, the Kennard–Stepanov (KS) relation predicts a linear relationship between absorption, emission, and temperature

In this application, the general focus has been on the fit of experimental data to the linear function of frequency, suggested by equation 7 in chapter 1, to see how well the results of the excited state attained thermal equilibrium before emission.

Figure 87 presents the application of this law to the absorbance and fluorescence spectra of spin coated F305 mixed with PMMA ($C=6.5 \times 10^{-4}$ mol/L).

The effective temperature of the fluorescence was $T^*=293\pm 8$ k, and it was used to calculate the chemical potential of the angular dependence of edge fluorescence. The Kennard-Stepanov law worked well for dye with a small stokes shift, but for dyes with a large stokes shift, it is impossible to determine T^* , as the reabsorption region almost disappears.

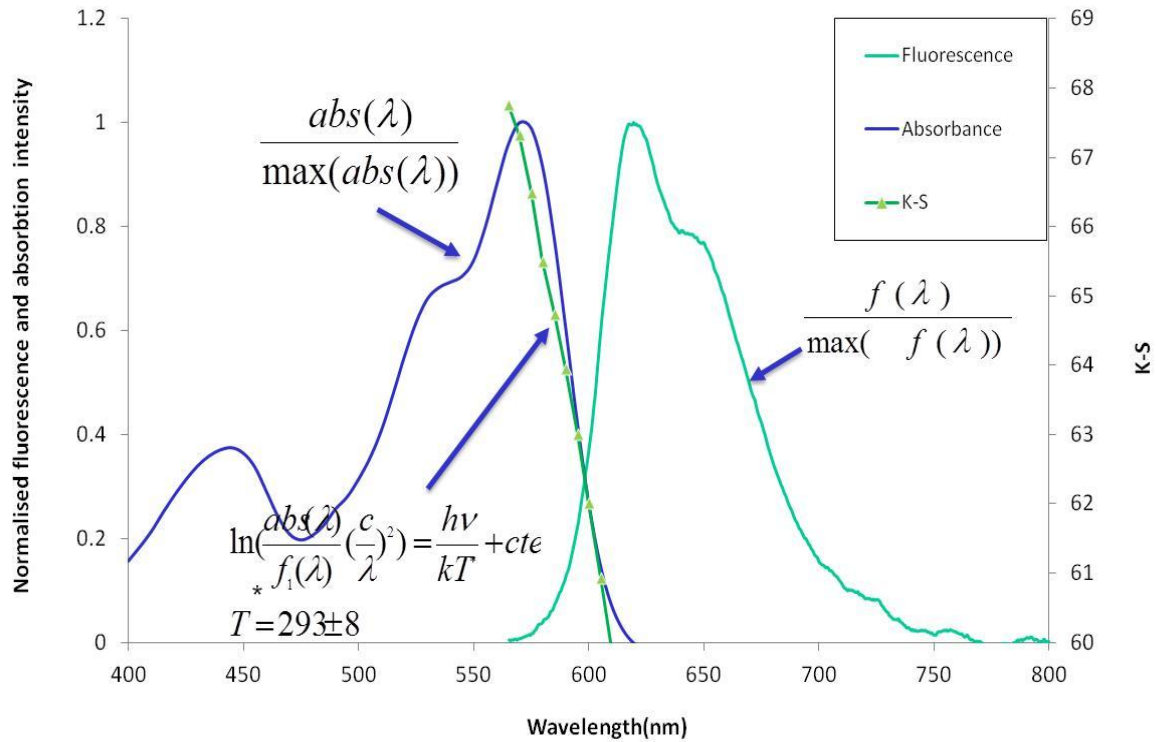


Figure 87: Kennard-Stepanov relation applied to the spectra of spin coated F305, mixed with PMMA on top of the glass substrate, with a concentration of $C=5\times 10^{-6}$ mol/L.

9.5. Chemical potential of the angular dependence of edge fluorescence

Once the contours of the fluorescence spectra were recorded, the optical fiber was replaced by the calibrated solar cell, covering the whole edge of the collector. The cell and collector were coupled using an index matching gel, and the short circuit current, I_{sc} , recorded by the cell, and used to scale the intensity of the fluorescence spectra previously obtained. The normalised fluorescence profile was multiplied by an appropriate constant, so the following relation holds:

$$J_{sc} = \int SR_{pv}(\lambda) f_e(\lambda) d(\lambda), \tag{175}$$

where J_{sc} is the current expected unit area, $SR_{pv}(\lambda)$ in Amps/ Watt is the spectral response of the cell, and $f_e(\lambda)$ (Watt/(unit area of emitting surface in the normal direction \times unit solid angle \times unit wavelength)) is the scaled fluorescence spectrum.

The edge cell short circuit current was measured with the calibrated digital DC amplifier (Bentham 487) module, and the edge cell illuminated monochromatically using a Bentham IL1 quartz halogen light source lamp DMc150 double monochromator, which was measured with a Bentham spectrometer. The spectral responsivity of the $3 \times 0.3 \text{mm}^2$ edge silicon solar cell was determined with comparison to a standard device (Dh-Si calibrated photodiode) over a wavelength of 400nm to 1100nm, and at an interval of 1nm at a distance of 1 mm, as shown in figure 88. By replacing J_{sc} and the spectral response of the silicon solar cell in equation 175, the scaled fluorescence spectrum can be calculated, and used in the following equation to calculate the chemical potential of the flux (μ_{flux}).

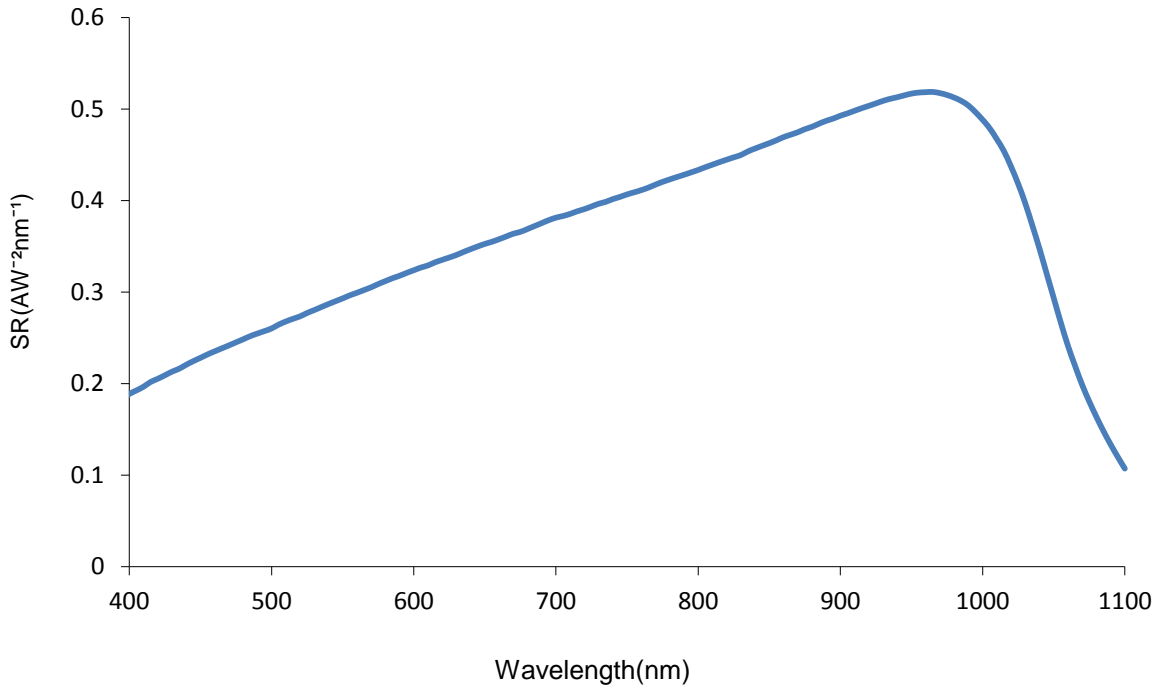


Figure 88: Spectral responsivity of the edge of a silicon solar cell.

In the wavelength region where the reabsorption affects photon transport, the edge fluorescence spectrum can be approximated by [22]:

$$f_e(T^*, \mu_{flux}, \nu) \approx \frac{2\pi h \nu^3}{c^2} \exp\left(\frac{-h\nu}{KT^*}\right) \exp\left(\frac{\mu_{flux}}{KT^*}\right), \quad (176)$$

where h is the Planck constant, c is the speed of light in a vacuum, and μ_{flux} is the chemical potential of the flux. Stimulated emission is neglected in this function. μ_{flux} indicates the flux after reabsorption and the re-emission reach to thermal equilibrium events, and is described by a specific temperature, as given by Planck's law [21, 22].

Figure 89 shows the experimental data of edge fluorescence at different detection angles, compared to the quasi-blackbody function, and we can see the value of scaled edge fluorescence was decreasing up to a 25° detection angle, before increasing again. Figure 90 shows the edge fluorescence detected at different angles, divided by the $\cos(\text{detection angle})$. As we can see in figure 90 (a, b), the edge fluorescence was decreased by increasing the detection angle, and the quasi-blackbody function agrees well with the experiment in the spectral region, where the absorption and fluorescence band of the dye overlap. From this fit, μ_{flux} can be determined.

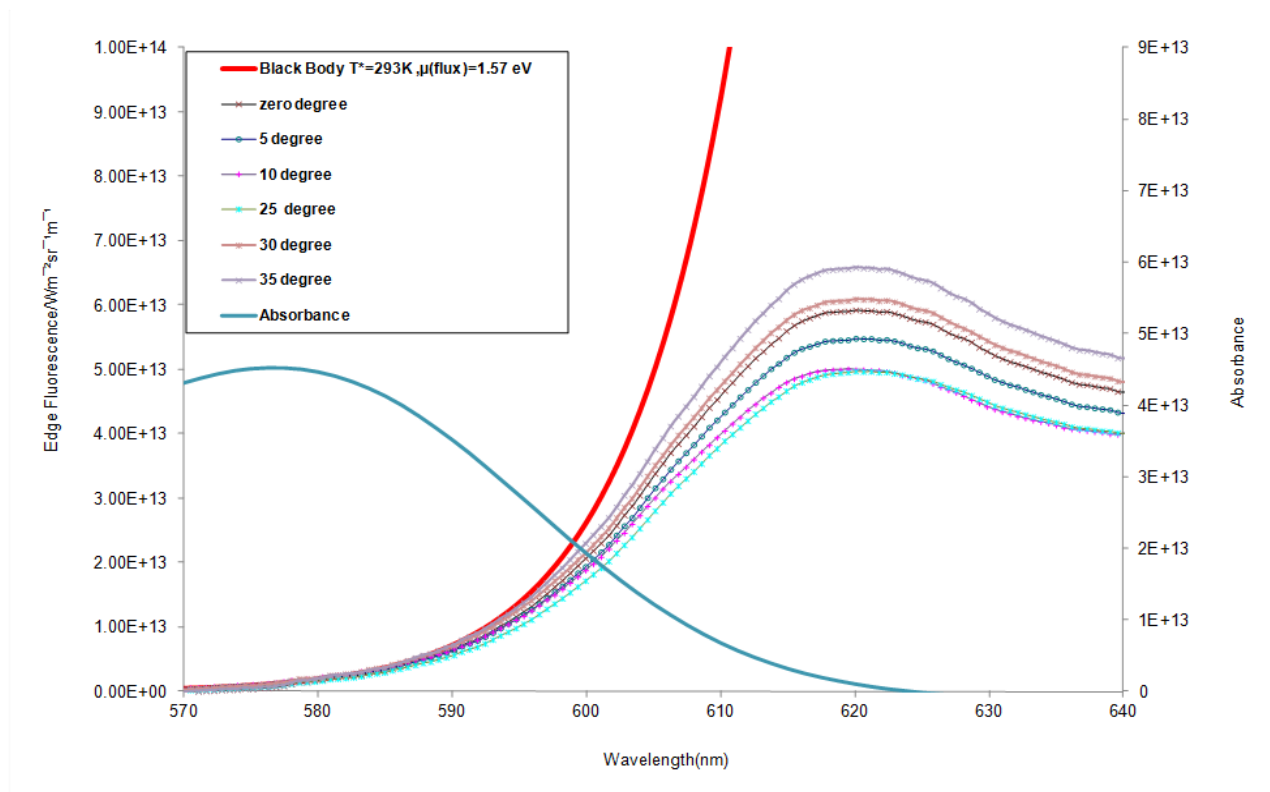
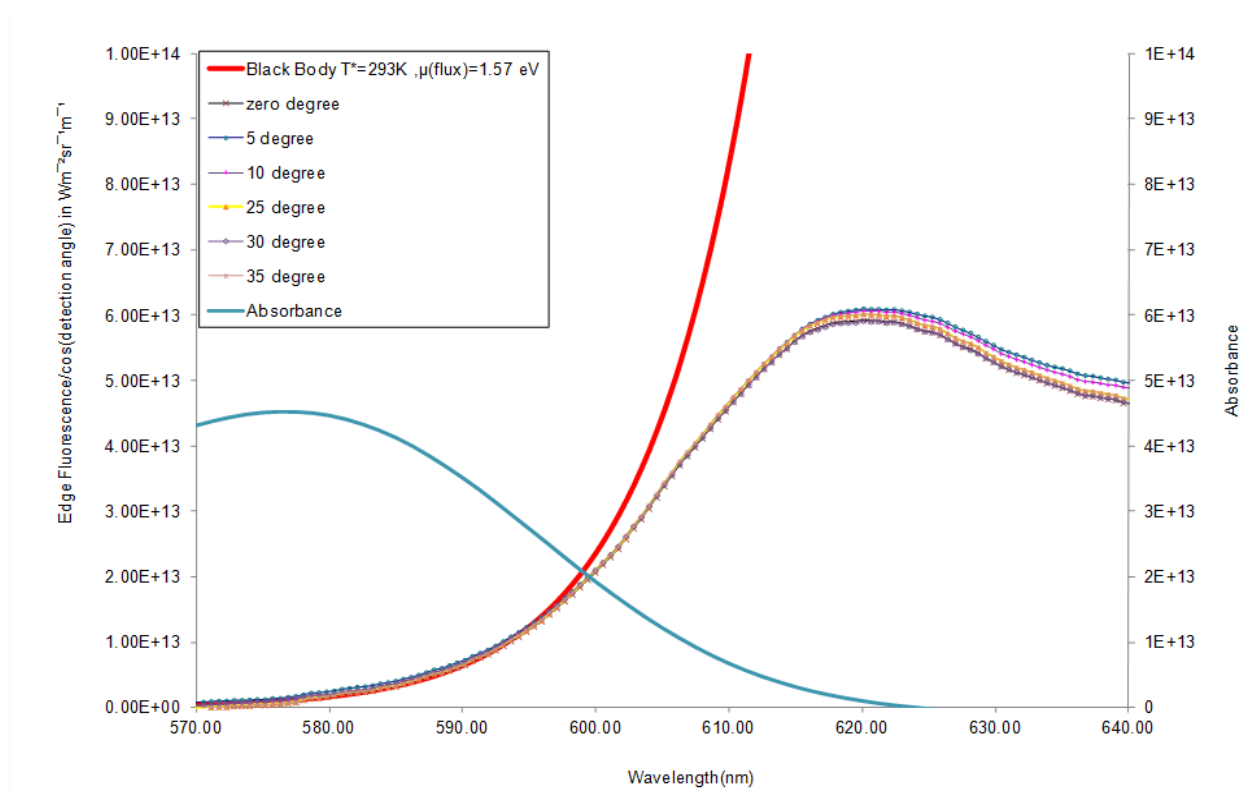
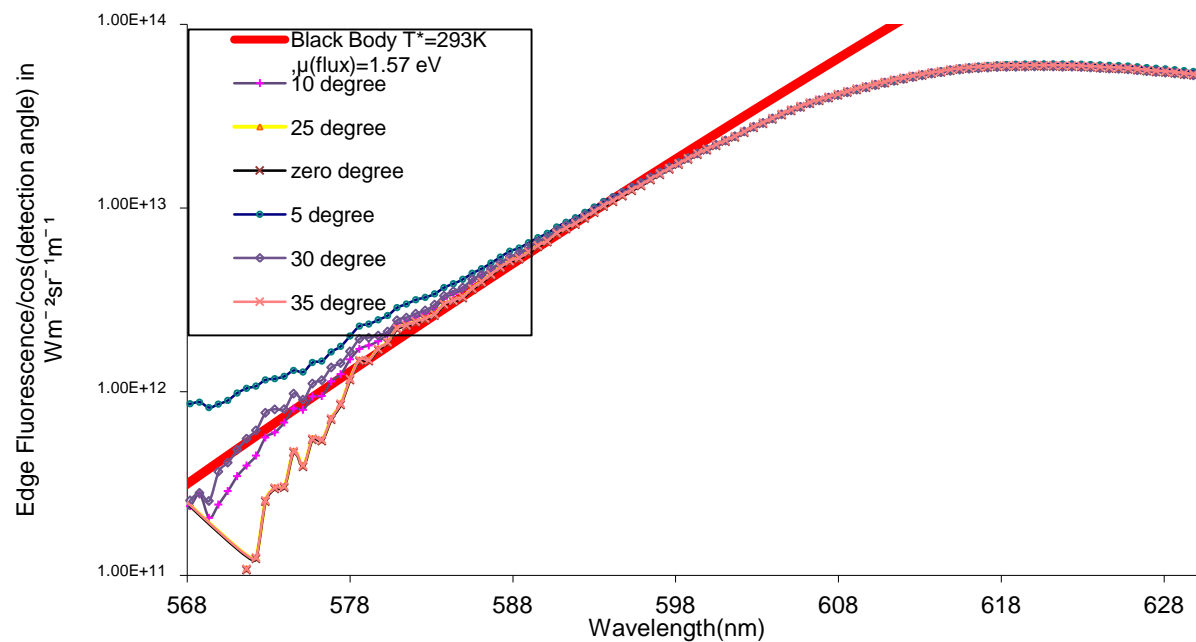


Figure 89: Edge fluorescence of F305, with concentration of $C=5 \times 10^{-6}$ mol/L, spin coated on top of the glass substrate and detected at different angle, compared with the Blackbody curve. In the spectral region where reabsorption affects photon transport, the edge fluorescence spectrum resembles a quasi-blackbody function.



(a)

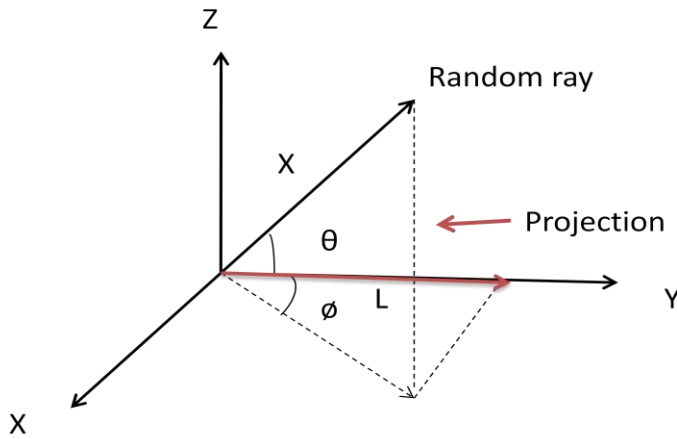


(b)

Figure 90: Edge fluorescence of F305, with concentration of $C=5 \times 10^{-6}$ mol/L, spin coated on top of the glass substrate and detected at different angles, divided by $\cos(\text{angle of detection})$, compared with the Blackbody curve. In the spectral region where reabsorption affects photon transport, the edge fluorescence spectrum resembles a quasi-blackbody function. (b) Log plot of (a).

9.6. Modified Weber and Lambe for the edge fluorescence detected at different angles from one edge of the collector

The Weber and Lambe model for luminescent collectors was discussed in chapter 4, and assumes a uniform distribution of excited molecules throughout the collector, perfectly flat specular reflection surface, no scattering of light inside the collector, and no absorption of light (except by the dye). The Modified Weber and Lambe model is assumed for the edge fluorescence detected at different angles from one edge of the collector.



$$L = X \cos(\theta) \cos(\phi), \tag{177}$$

$$X = \frac{L}{\cos(\theta) \cos(\phi)}$$

Equation 177 refers to the path length of a light ray emitted towards the cell.

Using the Beer Lambe law to estimate the absorption over the path length, L , we can write

$$\exp\left(\frac{-\alpha(\lambda)(L)}{\cos(\theta) \cos(\phi)}\right), \tag{178}$$

The value of the solid angle is very small, as we detect the fluorescence in a small solid angle, and therefore the value of $I-r$ can be written as:

$$1-r = \frac{\sin \theta \int_0^L \frac{1}{L} (e^{-\alpha L / \cos \theta \cos \phi})}{\sin \theta}, \quad (179)$$

$$1-r = \frac{\cos \theta \cos \phi}{\alpha L} (1 - e^{-\alpha L / \cos \theta \cos \phi}), \quad (180)$$

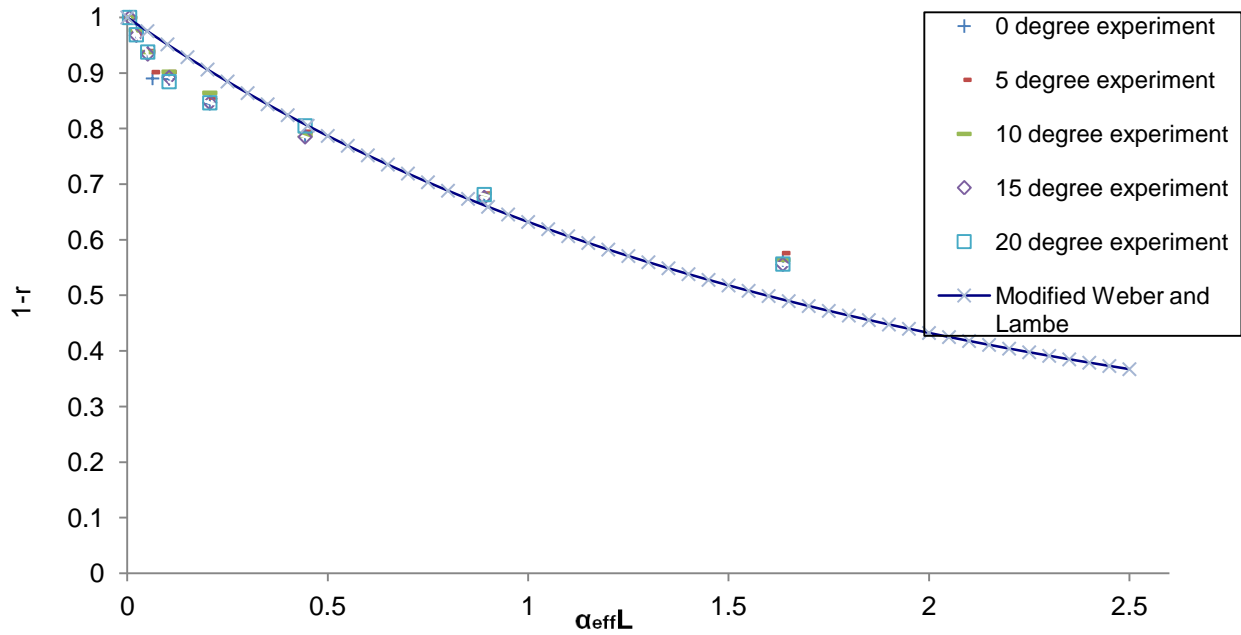


Figure 91: Reabsorption probability for thin film collectors at different detection angles of ROT305, with a concentration of $C=5 \times 10^{-6}$ mol/L, compared to the modified W&L model.

Figure 91 shows the reabsorption probability for dye (ROT 305) mixed with PMMA, with concentration of $C=5 \times 10^{-6}$ mol/L, on top of the glass substrate and compared to the Modified Weber and Lambe, indicating that the experimental results agree well with the MW&L model for reabsorption probability.

Conclusion

First generation spectra of F305 dye was measured in this chapter. We showed that the fluorescence spectra of the solid collector can be compared to a quasi-blackbody radiation, with a non-zero chemical potential (figure 89).

The angular dependence of the edge fluorescence decreases by increasing the detection angle, and the value of reabsorption also decreases by increasing the detection angle, up to 20°, increasing after that.

It showed that that the quasi-blackbody function agrees well with both the angular dependence of edge fluorescence spectral, divided by the $\cos(\text{detection angle})$ region, where the absorption and fluorescence band of the dye overlap, and also with the Modified Weber and Lambe for the angular dependence of the fluorescence, which agreed well with experimental results.

Chapter 10

Conclusion and suggested future works

Conclusion

This thesis presents the results of research carried out over 4 and a half years, with the partial support of the Supergen PV21 Consortium. The aim of the work was to study the photon collection efficiency of fluorescent solar collectors, in order to improve energy collection.

A literature review of the role of the solar radiation in the design of solar cells, and the properties of semiconductors that are important in the design and operation of solar cells, was discussed in this thesis.

Mie scattering theorem and Fraunhofer diffraction in far-field, Bi-directional surface distribution function (BSDF) and the theory of the integrating sphere, which is based on radiation exchange within an enclosure of diffuse surfaces, was discussed in detail.

A literature review of fluorescent solar collectors, including their history, operation principles, and self absorption, was discussed in this thesis.

The effect on reabsorption probability of non-ideal coupling, between the collector and the solar cell mounted at the edge, was discussed in detail.

In preparation techniques, the spin coating method was used to prepare a thin film layer of dye-doped PMMA, on top of the glass substrate. Different methods for measuring sample thickness were discussed in the 'fabrication and characterisation technique of FSC' section. It showed that the profilometry method is best for measuring the film thickness, being independent of the glass reflectivity problem.

Results from measurements, of the total and diffuse reflectance and transmittance by using integrating spheres, have been presented in this thesis. The diffuse reflectance and transmittance

measured for the PMMA coated glass sample are shown in figures 47 and 48 (chapter 6), indicating that the PMMA layer causes a scattering of light.

A roughness measurement, with TIS, was in good agreement with AFM, and the angular dependence of scattering measurements.

The effect of bulk scattering on the performance of the collector was discussed in detail, and the Modified Weber and Lambe model used when we have bulk scattering in FSC.

A goniometer was used to measure the angular dependence of scattering in the FSC. In the goniometer calibration process, the measured scattering patterns for 2 μm average diameter Polystyrene 2wt% dispersion in H₂O agreed well with the theoretical Mie curve for a 1.9 μm sphere, and in a known sphere on top of the thin film measurement, the value of the experiment was in good agreement with the Mie scattering for the sphere's size of 6.2 μm .

The contribution of light scattering in fluorescent solar collectors (FSC), based on a spin-coated dye/polymer layer was investigated. Measurements of the transmission cones, as a function of the total internal reflections (TIR), revealed that the predominant loss factor was surface scattering at the top layer caused by the roughness of the spin-coated PMMA. The angular broadening, due to surface roughness, for different numbers of TIR of light inside the collector was found to be 0.6° to 1.6° (Table 2).

Good agreement is reached when we consider the PMMA roughness as particles with a circular shadow, and therefore the angular distribution of the scattering intensity can fit with far-field Fraunhofer diffraction, for the circular aperture. The amplitude of the scattered light decreases as the wavelength increases, from 401 to 670nm; simultaneously, the width of the scattered beam increases, and is in good agreement with Fraunhofer diffraction for a circular aperture at different wavelengths, where the size of the aperture is fixed to the RMS roughness of around 11 μm . The value of the scattering was found to decrease significantly when the top surface was covered with optical gel, unambiguously demonstrating that surface scattering is the predominant loss factor in our FSC, compared to bulk scattering effects. Surface roughness is caused by the large thickness of the PMMA-dye layer required for the operation of the FSC. The reduction of angular broadening to 0.6° indicates that surface scattering losses could be reduced to below 2% according to our Modified Weber and Lambe model for the surface scattering. Surface roughness

is caused by the large thickness of the PMMA-dye layer required for the operation of the FSC. Our results indicate that the performance of the FSC can be improved by using a subsequent planarisation with a thin, index-matching layer of low roughness.

The effect of the surface roughness of the edges has also been evaluated and found to be relatively small, while in the Perspex/Acrylic sample, scattering was caused by bulk, agreeing well with the Mie theory.

The value of the scattering efficiency of scattered light that can reach the edge of the collector, caused by PMMA spin coated sample on top of the BK7 glass, was a ratio of the short circuit current detected by the solar cell from the edge to the short circuit current from direct illumination in the solar cell.

The linear relationship between edge fluorescence and I_{sc} was shown in this thesis.

First generation spectra of F305 dye was measured in this work, and by angular dependence of the edge fluorescence, we showed that the fluorescence spectra of solid collectors can be compared to a quasi-blackbody radiation, with a non-zero chemical potential.

The angular dependence of edge fluorescence was decreased by increasing the detection angle, while the value of the reabsorption was decreased up to 20°, before increasing.

It showed that that the quasi-blackbody function agrees well with both the angular dependence of the edge fluorescence spectral, divided by the $\cos(\text{detection angle})$ region, where the absorption and fluorescence band of the dye overlap. It also agreed with the Modified Weber and Lambe model for the angular dependence of fluorescence, itself agreeing with experimental results.

10.1. Future work

The optical efficiency of FSC can be increased by using the following methods:

- **Thin and smooth layer of optic gel on top of the fluorescent solar collector.**

- **Efficient light trapping in a fluorescence solar collector by 3D photonic crystal.**

The escape of photons from a fluorescence collector is substantially reduced by the addition of a 3D photonic crystal, geometrically designed for the emission wavelengths of the collector. A

photonic crystal has a spatial periodic variation in its dielectric constant, preventing light of certain energy levels propagating in certain directions [71]

The losses of photon energies can be reduced by a factor >10 by using a selective filter on top of the FSC [72], the selective filter consisting of a 3D photonic crystal on a glass substrate (refractive index $n_G=1.5$) and composed of 7-9 layers of hexagonally packed PMMA spheres of 260nm diameter (opal [11]); its stop gap emerges in Γ -L direction nominally at $\lambda = 580$ nm. Figure 92 shows an AFM-scan of the surface topology of the opal.

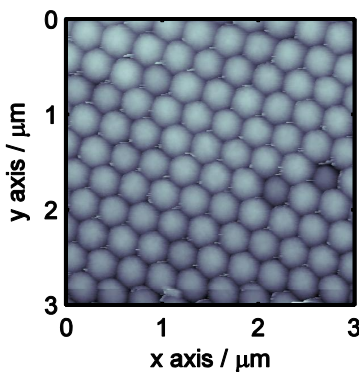


Figure 92: AFM-scan of opal surface with hexagonally packed PMMA-spheres [72].

➤ **The effect of a scattering layer on the edge output of a FSC**

To decrease the transmittance losses, the incorporation of a scattering layer to the rear of a fluorescence solar collector can have a significantly positive impact on the energy output of the FSC system. The physical distance over which the scattered light provides a positive effect depends on whether or not the waveguide is attached to the FSC (shorter range) or separated by an air gap (longer range) from the scattered layer [73].

➤ **Effect of the solar cell in 4 edges of the collector**

The optical efficiency of the fluorescence solar collector can be increased by using 4 solar cells in the edges of the FSC as we can detect all photons that can travel and reach the 4 edges of the collector. Also, the losses caused by a non-perfect mirror will be illuminated using this method.

References

- [1] W.W. Anderson and Y.G. Chai, *Energy Converse* 15 (1976), p. 85.
- [2] C.E. Backus, *J. Vac. Sci. Technol.* 12 (1975), p. 1032
- [3] N. Panchuk-Voloshina, R.P. Haugland, J. BishopStewart, M.K. Bhalgat, P.J. Millard, F. Mao, W. Leung, and R.P. Haugland. Alexa dyes, a series of new fluorescent dyes that yield exceptionally bright, photostable conjugates. *J. of Histochemistry and Cytochemistry*, 47:1179–1188, 1999.
- [4] U. Rau, F. Einsele, and G. Glaeser. Efficiency limits of photovoltaic fluorescent collectors. *Applied Physics Letters*, 87:171101, 200.
- [5] A.J. Chatten, K.W.J. Barnham, B.F. Buxton, N.J. Ekins-Daukes, and M.A. Malik. A new approach to modelling quantum dot concentrators. *Solar Energy Materials and Solar Cells*, 75:363–371, 2003.
- [6] T. Markvart, L. Danos, P. Kittidachachan, and R. Greef. Detailed balance efficiency of ideal single-stage fluorescent collectors. In *Proc. 20th European Photovoltaic Solar Energy Conference*, pages Pre–print, Barcelona, Spain, 2005.
- [7] L. Danos, P. Kittidachachan, T.J.J. Meyer, R. Greef, and T. Markvart. Characterisation of fluorescent collectors based on solid, liquid, and langmuir blodget (lb) films. In *21st European Photovoltaic Solar Energy Conference*, pages 443– 446, Dresden, Germany, 2006.
- [8] L.H. Sloof, R. Kinderman, A.R. Burgers, J.A.M. van Roosmalen, A. Buchtemann, R. Danz, M. Schleusener, A.J. Chatten, D.J. Farrell, and K.W.J. Barnham. The luminescent concentrator: A bright idea for spectrum conversion. In *Proc. 20th European Photovoltaic Solar Energy Conference*, pages Pre–print, Barcelona, Spain, 2005.
- [9] A.R. Burgers, L.H. Sloof, R. Kinderman, and J.A.M. van Roosmalen. Modelling of luminescent concentrators by ray-tracing. In *Proc. 20th European Photovoltaic Solar Energy Conference*, pages Pre–print, Barcelona, Spain, 2005.
- [10] S.T. Bailey, G.E. Lokey, M.S. Hanes, J.D.M. Shearer, J.B. McLafferty, G.T. Beaumont, T.T. Baseler, J.M. Layhue, D.R. Broussard, Y. Zhang, and B.P. Wittmershaus. Optimised excitation energy transfer in a three-dye luminescent solar concentrator. *Solar Energy Materials and Solar Cells*, 91:67–75, 2007.
- [11] M. Hammam, M.K. El-Mansy, S.M. El-Bashir, and M.G. El-Shaarawy. Performance evaluation of thin-film solar concentrators for greenhouse applications. *Desalination*, 209:244–250, 2007.
- [12] J.Beer, A. Blinov, G. Bonani, R.G. Finkel, H.J. Hofmann, B. Lehmann, H. Oeschger, A. Sigg, A. Schwander, T. Staffelbach, B. Stauffer, M.Suter, W.Wölfli. Use of ^{10}Be in polar ice to trace the 11-year cycle of solar activity. *Nature* 1990, 347, 164-166.
- [13] K. McGuffie, A. Henderson-Sellers, *A Climate Modelling Primer*, John Wiley & Sons, Mar 14, 2005.
- [14] J.Twidell, T. Weir, *Renewable Energy Resources*, London and New York, 1986.
- [15] J. L. Monteith (Author), M. H. Unsworth, *Principles of Environmental Physics*, Elsevier, 2008.

- [16] C. Gueymard. The Sun's total and spectral irradiance for solar energy applications and solar radiation models, *Solar Energy*, Vol.76,PP. 423-453.
- [17] G. S. Campbell, J. M. Norman, *Introduction to Environmental Biophysics*, Springer, 1998.
- [18] DA. Skoog; West, DM; Holler, FJ; Crouch, SR *Fundamentals of Analytical Chemistry*, 8th ed. Belmont, CA: Brooks Cole; 2004.
- [19] J.R. Lakowicz, *Principles Of Fluorescence Spectroscopy*, 3rd ed., Springer, New York, 2006.
- [20] D. A. Sawicki and Robert S. Knox, Universal relationship between optical emission and absorption of complex systems: An alternative approach, *Physical review A*, Vol.54.pp. 6.
- [21] T.J.J.Meyer, T.Markvart. The chemical potential of light in fluorescent solar collectors, *J. Applied Physics*, Vol.105,pp.063110-8.
- [22] T.Markvart. Detail balance method for ideal single-stage fluorescent collectors. *J. Applied Physics*, Vol.99,pp026101-3.
- [23] T. Markvart, L.Castañer, *Practical Handbook of Photovoltaics: Fundamentals and Applications*, 2003 Elsevier
- [24] W. Shockley and H.J. Queisser, 1961. Detailed balance limit of efficiency of p-n junction solar cells, *J. Appl. Phys.* Vol. 32, p. 510.
- [25] M.A. Green, *Solar Cells*. Prentice Hall, New York, 1982.
- [26] M.D. Archer, Robert Hill. *Clean electricity from photovoltaic vol .1*, Publisher (2001).
- [27] F. Y.r.El Faituri and A.Y.Darkwi University of Garyounis, Benghazi-Libya, Computer simulation for density in PN-silicon solar cell.
- [28] T.L.Chu.1988.Cadmium telluride solar cells, in T.J. Coutts and J.D. Meakin, Eds., *Current topics photovoltaic* , Vol.3, p.235.
- [29] C. F. Bohren, D.R. Huffman *Absorption and scattering of light by small particles*. Wiley, 1983.
- [30] S. Wolf, N.V. Voshchinnikov, Mie scattering by ensembles of particles with very large size parameters, *Computer Physics Communications* 162 (2004) 113–123.
- [31] H.C.van de Hulst, *Light scattering by small particle*, New York,1981.
- [32] E. Hecht, *4ed Optics*, Addison Wesley,2002.
- [33] L.A. Dombrovsky, Geometrical optics approximation , 10.1615/thermopedia.000158.
- [34] *TracePro User's Manual* by Lambda Research Corporation, 2007.
- [35] J. C. Stover, *Optical scattering: measurement and analysis*, SPIE Press, 1995.
- [36] J.Birn, *Digital Lighting and Rendering*, New Riders, 2006.
- [37] *Manuela of Labsphere RT-060*.
- [38] J. a Levitt, W.H. Weber, *Applied Optics* 16 (1977) 2684-9.
- [39] A. Zastrow, *Physics and applications Of Fluorescent Concentrators: A Review*, SPIE, 1994.

- [40] P. Kittidachachan, L. Danos, T.J.J. Meyer, N. Alderman, and T. Markvart. Photon collection efficiency of fluorescent solar collectors. *CHIMIA*. 61, 780 (2007).
- [41] W.H.Weber and J. Lambe. Luminescent greenhouse collector for solar radiation. *Applied Optics*, 15, 2299 (1976).
- [42] J.A. Levitt and W.H. Weber. Materials for luminescent greenhouse solar collectors. *Applied Optics*, 16, 2684 (1977).
- [43] J.S. Batchelder, A.H. Zewail, and T. Cole. Luminescent solar concentrators. 1: Theory of operation and techniques for performance evaluation. *Applied Optics*, 18, 3090 (1979).
- [44] J.S. Batchelder, A.H. Zewail, and T. Cole. Luminescent solar concentrators. 2: Experimental and theoretical analysis of their possible efficiencies. *Applied Optics*, 20, 3733 (1981).
- [45] P. Kittidachachan, L. Danos, R. Greef, T.J.J. Meyer, N. Alderman, and T. Markvart Characterisation of fluorescent collectors in terms of spectral photon collection efficiency. Proc.22nd European photovoltaic Solar Energy Conference, Milan, Italy, 2007.
- [46] L. Danos, P. Kittidachachan, T.J.J. Meyer, R. Greef, and T. Markvart. Characterisation of fluorescent collectors based on solid, liquid, and Langmuir Blodget (LB) films. Proc. 21st European Photovoltaic Solar Energy Conference, pp. 443–446, Dresden, Germany, 2006.
- [47] F. Agullo-Lopez, M. Carrascosa, and S. Unamunu. Monte Carlo simulation of the performance of PMMA luminescent solar collectors. *Applied Optics*, vol. 22, pp. 3236–3241, 1983.
- [48] B.C. Rowan, L.R. Wilson, B.S. Richards, *IEEE Journal Of Selected Topics In Quantum Electronics* 14 (2008) 1312-1322.
- [49] A.H. Zewail, J.S. Batchelder, in: *Polymers In Solar Energy Utilisation*, n.d., pp. 331-352.
- [50] J Samuel Batchelder. The luminescent solar concentrator, Dissertation (Ph.D.), California Institute of Technology, 1982.
- [51] J.C. Goldschmidt, M. Peters, L.Prönneke, L. Steidl, R.Zentel, B. Bläsi, A. Gombert, S.Glunz, G. Willekel, and U. Rau, Theoretical and experimental analysis of photonic structures for fluorescent concentrators with increased efficiencies, *phys. stat. sol. (a)* 205, No. 12, 2811–2821 (2008).
- [52] A. Goetzberger, W. Greubel, Solar-energy conversion with fluorescent collectors, *Appl. Phys.* 14, pp. 123-139, 1977. 5.
- [53] L Fang, T S Parel, L Danos, T Markvart, Photon reabsorption in fluorescent solar collectors, in *Applied Physics*. 076104.
- [54] C. Columbia, Spin coating process theory and theory of spin coating process description.
- [55] About PhotochemCAD. URL <http://www.photochemcad.com/>.
- [56] F.L. Arbeloa, T.L. Arbeloa, I.L. Arbeloa, A. Costela, I.G. Moreno, J.M. Figuera, F.A. Guerri, and R. Sastre. Relations between photophysical and lasing properties of rhodamines in solid polymeric matrices. *Applied Physics: B*, 64:651–657, 1997.

- [57] K.G. Casey, E.L. Quitevis, (1988). Effect of solvent polarity on non-radiative processes in xanthene dyes: Rhodamine B in normal alcohols. *Journal of Physical Chemistry* 92 (23): 6590–6594.
- [58] BASF Colorants for Plastics (Oct.2004) data F Red 305.
- [59] J.W. McBride, The Loaded Surface Profile: A new technique for the investigation of contact surfaces, ICEC2006 University of Southampton, United Kingdom.
- [60] G.D. Danilatos. Foundations of environmental scanning electron microscopy. *Advances in Electronics and Electron Physics* 71: 109-250 (1988).
- [61] M.Born, E.Wolf, Principles of optics, electromagnetic theory of propagation, interface and diffraction of light, Oxford, Pergamon press, 1964.
- [62] H. Kogelnik and T. Li, Laser beams and resonator, *Appl. Opt.* 5 (10), 1550 (1966).
- [63] Z. Zhenrong, Z.jing, G.peifu, Roughness characterisation of well-polished surfaces by measurements of light scattering distribution, *Optica Applicata*, Vol. XL, No. 4, 2010.
- [64] B. H. Clampitt, D. E. German, and H. D. Anspen, Techniques for Measuring Surface and Bulk Optical Properties of Polyethylene Films, *Analytical Chemistry* VOL. 41, NO.10, (1969).
- [65] D. K. Sardar , F.S. Salinas Optical properties of a laser dye in a solid-state polymeric host, *Applied Physics*, V. 91, N. 12.
- [66] G. Brooker, *Modern classical optics*, Oxford University Press, 2003 - 397 pages.
- [67] K. H. Guenther, P. G. Wierer, and J. M. Bennett, Surface roughness measurements of low-scatter mirrors and roughness standards, *Applied Optics*. Vol. 23, No. 21.
- [68] Y. Koike, N. Tanio, and Y. Ohtsuka, “Light scattering and heterogeneities in low-loss poly (methyl methacrylate) glasses”, *Macromolecules* 22, 1367-1373 (1989).
- [69] T.J.J. Meyer, J. Hlavaty, L. Smith, E.R. Freniere, T. Markvart, *Proceedings Of SPIE* (2009) 72110N-72110N11.
- [70] T.J.J. Meyer, *Photon Transport in Fluorescent Solar Collectors*, University of Southampton, 2009 (phD thesis).
- [71] S. Bailey, G. Lokey, M. Hanes, J. Shearer, J. Mclafferty, G. Beaumont, T. Baseler, J. Layhue, D. Broussard, Y. Zhang, *Solar Energy Materials and Solar Cells* 91 (2007) 67-75.
- [72] S. Knabe, N. Soleimani, T. Markvart, G.H. Bauer, Efficient light trapping in a fluorescence solar collector by 3D photonic crystal, *Physica Status Solidi (RRL) - Rapid Research Letters* 4 (2010) 118-120.
- [73] M.G. Debije, M.-P. Van, P.P.C. Verbunt, M.J. Kastelijn, R.H.L. van der Blom, D.J. Broer, C.W.M. Bastiaansen, *Applied Optics* 49 (2010) 745-51.

Appendix 1

Useful quantities and conversion factors

$$1 \text{ cm}^{-1} = 1.9864 \times 10^{-23} \text{ J} = 11.963 \text{ J mol}^{-1} = 0.12398 \text{ meV} = 2.9979 \times 10^{10} \text{ Hz}$$

$$1239.8 / (\lambda / \text{nm}) = U / \text{eV}$$

$$kT \text{ at } 298.15 \text{ K} = 0.02569 \text{ eV}$$

$$kT/q \text{ at } 298.15 \text{ K} = 0.02569 \text{ V}$$

$$(\ln 10) kT/q \text{ at } 298.15 \text{ K} = 0.05915 \text{ V}$$

$$h/2\pi = 6.582 \times 10^{-16} \text{ eV s}$$

$$1 \text{ kWh} = 3.6 \times 10^6 \text{ J}$$
